Design of a
Primary Mirror Deployment Mechanism
for a Deployable Space Telescope

Matthew Corvers

TU Delft

Design of a Primary Mirror Deployment Mechanism for a Deployable Space Telescope

Matthew Corvers
(4017994)

Master thesis

Department of Space Systems Engineering
Faculty of Aerospace Engineering
Delft University of Technology

June 2018

This thesis is confidential and cannot be made public until June 26, 2019.

Design of a Primary Mirror Deployment Mechanism for a Deployable Space Telescope

Front cover: Courtesy of André Krikken

Graduation committee:
Prof. dr. E.K.A Gill - Space Systems Engineering, Delft University of Technology
dr. J.M. Kuiper - Space Systems Engineering, Delft University of Technology
ir. M.C. Naeije - Astrodynamics and Space Missions, Delft University of Technology

"Give me a lever long enough and a fulcrum on which to place it, and I shall move the world."
- **Archimedes of Syracuse (212 BC)**

ABSTRACT

The Deployable Space Telescope developed at the TU Delft aims to develop a high resolution space telescope that is able to compete with current state-of-the-art devices at significantly reduced cost. The goal is to achieve a resolution of 25 $cm/pixel$ in the market segment of visual light Earth observation satellites. The cost reduction will be achieved by making the primary and secondary mirrors deployable. Compared to other satellites where the mirrors are fixed inside a large cylindrical structure, the stowed mass and volume of this satellite will form a fraction of what is common nowadays. This will lead to highly reduced launch costs.

To be able to deploy the Primary Mirror (M1) it is split into four M1 segments. This leads to a major challenge, because the segments not only have to be phased with respect to each other, but also with respect to the other optical elements. This phasing should be executed with a precision of 10 nm. The required calibration movements will be provided by an algorithm that analyzes wavefront errors in the optical images. This algorithm only works when certain requirements regarding the deployment precision, thermal drift, and vibration stability can be met by the deployment mechanism. The required deployment precision is less stringent than the required phasing precision. Therefore an active optics calibration system, mounted on top of the deployment mechanism, will achieve the latter requirement.

This thesis describes the development of the M1 deployment mechanism, without the calibration system. A trade-off between several concepts is made to end up with three concepts that are assessed in more detail. Based on a thermal analysis it is concluded that none of the proposed concepts will be able to meet the requirements related to the in-orbit thermal drift.

After seeking for advise, Prof.dr.ir. Just Herder proposes a novel concept that is very different from the considered options and benefits the Secondary Mirror (M2) deployment mechanism as well. A ribbon connecting the M1 and M2 deployment mechanisms will improve the structural stiffness and vibration stability of the M2 deployment mechanism, while applying the required preload to the M1 deployment mechanism to fall into a high precision kinematic interface. Applying athermalization turns out to be much less complex in this configuration and therefore it is known that meeting the thermal drift budget is feasible.

It is explained how this concept is designed in more detail. Athermalization is incorporated in the design, precision design practises are applied, and an actuated ribbon winch is developed. Although the design is not finished, it is assessed whether it is expected that the final version of this deployment mechanism will meet the requirements. It is concluded that it is feasible to meet all requirements, except for the one defining the mass budget.

It is recommended to apply two types of mass optimization during future work. Then it can be determined how far the mass budgets is exceeded. This information can be used to revise the mass budget requirements. Furthermore specific design recommendation are provided and a proposal for the upcoming work packages is suggested.

Keywords: *Deployment mechanism, precision, accuracy, exact constraint design, kinematic interface, athermalization, EMC hinge, tape spring hinge*

ACKNOWLEDGMENTS

At the moment I wrote this page to finish my thesis, two and a half year have past since I talked with Hans Kuiper about the Deployable Space Telescope project for the first time. With the challenges laying ahead I immediately became interested, especially because it felt like the thesis could be a win-win situation. This is because I started a company during my MSc-studies that could potentially benefit from this research as well. At IMSystems we invented the Archimedes Drive, a speed reducer with unparalleled precision for its weight and size. I hoped to be able to investigate whether the Archimedes Drive could turn up the performance of the primary mirror calibration mechanism. When discussing how I could fit in the team, the chaos started...

The industry suddenly started to show major interest in the Archimedes Drive, proposing projects in which we actually could generate revenue. IMSystems became an actual job, rather than a hobby on the side. I worked full-time for the company for 10 months and when I came back to start my literature study, I tried to combine it with the company. Only about a year ago, I started to see that this did not work. It was a tough choice, but I decided to step out of the company as an active employee, to fully focus on my graduation. Even when it turned out I could not apply the Archimedes Drive in the project, I decided to continue my work to graduate as soon as possible and return to the company.

So far I only talked about personal matters. The trajectory of writing this MSc-thesis was however a big challenge as well. I could not have gotten to this point without the help of some people to which I would like to show my gratitude:

First of all I would like to thank my daily supervisor, Hans Kuiper. From the start Hans was very understanding of my situation with the company. He gave me the freedom to decide on how I wanted to combine the company and the thesis research, which was really important to me. Furthermore I very much enjoyed our conversations about how the business side of the space industry works.

Second I would like to thank Victor Villalba Corbacho, the PHd-student who joined the team shortly after I decided to make my MSc-thesis a full-time occupation. We had very fruitful discussions at the moments I got stuck and I especially appreciate that he sacrificed a weekend to read my draft thesis and provide feedback.

Furthermore I would like to thank Boris Van Putten. Your thesis was a very extensive source of information that formed a strong basis for the continuation of your work.

Then I would also like to thank the rest of the MSc- and PHd-students of the team. It was very *gezellig* to work together with you in our tiny Master Room. I also liked how the group actually became a team over the course of my involvement in the project. In the beginning everyone worked one his own subsystem with little interaction towards other team members. In the meantime we developed a good sense of the dependabilities between the subsystems, which led to better communication about design changes that potentially impact other subsystems. In this regard I would like to especially thank Andre Krikken and Sean Pepper. We all required similar types of knowledge to design our subsystems, which are very much interconnected. Therefore we had a lot of discussions and brainstorm sessions where we shared our individual knowledge and found ways to make the system work as a whole.

The next person I would like to thank is Just Herder. At the point where it turned out that none of the suggested deployment mechanism concepts would meet the requirements, he was the one to jump in with an outsider perspective and proposed the ideas that led to the current design.

Other persons I would like to thank are Henk Cruijssen and Guus Borst of Airbus Defence and Space. Their knowledge and insights, based on years of experience, have been very useful during the first half of this research project.

I would also like to thank the team of IMSystems, first for accepting my absence for what turned out to be a year. Second, for pushing me to finish my MSc. At a certain point I was seriously considering quitting this study to fully focus on growing the company. This thesis would not have been written if it was not for this guys.

Finally I would like to thank my parents, John and Ina, and my brother, Brandon. Their support and advise really helped getting through this past two hectic years.

TABLE OF CONTENTS

LIST OF FIGURES

LIST OF TABLES

LIST OF ACRONYMS

ABDS	Articulated Boom Deployment Hinge	48
ACT	Avior Control Technologies, Inc	87–89
ADS	Airbus Defence and Space	9, 12, 44, 63, 64, 66, 74
BST	Berlin Space Technologies	32
CDA	CDA InterCorp	87–89
CFRP	Carbon Fiber Reinforced Polymer	12, 41, 56–58, 60, 63, 67, 74–76, 99, 101, 102, 111, 117, 132
CNT	Carbon Nano Tube	74
CTD	Composite Technology Development, Inc.	37
CTE	Coefficient of Thermal Expansion	XIX, 32, 39–42, 45, 47, 49, 56, 57, 65, 74–76, 84, 85, 97, 99, 101, 102, 105, 117
CTM	collapsible tubular mast	12
DC	Direct Current	87
DOF	Degree Of Freedom	95, 96
DPT	Deployable Petal Telescope	26, 27, 29, 44, 49
DST	Deployable Space Telescope	XII, 1, 3, 7–9, 11, 25–27, 29, 32, 35, 40, 57, 65, 67, 74, 110
ECSS	European Cooperation for Space Standardization	76
EMC	Elastic Memory Composite	25, 29, 32, 37, 38, 45, 47, 49
EO	Earth Observation	1, 3, 5–7
ESA	European Space Agency	23, 29, 66, 76
ESDM	Engineering Science Development Model	24, 25
FORTA	Fast Optical RayTrace Application	11, 20
GSD	Ground Sampling Distance	7
H-BN	hexagonal boron nitride	76
HDRM	Hold Down and Release Mechanism	12, 78, 79, 83, 86, 91, 93, 106, 110
HST	Hubble Space Telescope	23
HTS	Hoch Technologie Systeme GmbH	45, 48, 65, 66
IP	Intellectual Property	119
ISS	International Space Station	37
ITAR	International Traffic in Arms Regulations	37, 45
JWST	James Webb Space Telescope	7, 23–26, 32, 39, 44

lidar	LIght Detection And Ranging	24, 25, 29, 37
M1	Primary Mirror	VII, 9, 11–13, 18, 20, 21, 25, 35, 40, 44, 49, 57, 65, 66, 68–71, 73, 74, 77, 78, 83–86, 97, 106, 108, 110, 111, 115–118
M2	Secondary Mirror	VII, 11–13, 20, 44, 65, 67–71, 73, 78, 81, 83–87, 97, 108–111, 114, 115, 117, 118
MH	mid-hinge	51, 53, 56, 57, 60, 63, 64, 132
MTF	Modular Transfer Function	11
NASA	National Aeronautics and Space Administration	23–25, 29, 37, 38, 49, 76
NDA	Non Disclosure Agreement	47, 119
NGST	New Generation Space Telescope	23, 24, 37, 44
PSF	Point Spread Function	11
RMS	Root Mean Square	50, 132
rpm	rotations per minute	90
SL	slider	51, 53, 56–58, 60, 63, 132
SMPC	Shape Memory Polymers and Composites	37, 38
SMSS	Secondary Mirror Support Structure	26
STScI	Space Telescope Science Institute	23
TRL	Technology Readiness Level	27, 38, 45, 47, 48, 66, 67
TU Delft	Delft University of Technology	44, 67
UDM	Ultra-light Deployment Mechanism	35, 45, 47, 48
WPD	Web Plane Diagram	94–96

LIST OF SYMBOLS

Symbol	**Description**	**Unit**
Capital letters		
D	Aperture diameter of entrance pupil	$[m]$
E_x	Young's modulus of material x	$[GPa]$
F_{hd}	Hold down force	$[kN]$
F_{pl}	Preload force	$[N]$
FS_y	Safety factor for static ultimate loads	[-]
$F\#$	F-number	[-]
GR	Gear ratio	[-]
H	Altitude w.r.t. Earth's surface	$[km]$
L_x	Length described by specification x	$[mm]$
M	Radius mirror	$[mm]$
N	Number of ribbon windings	[-]
R	Radius mirror mount	$[mm]$
T_g	Glass transition temperature	$[°C]$ or $[K]$
T_{in}	Input torque	$[mNm]$
V	Volume in cubesat unit sizes (10x10x10 cm^3)	$[U]$
X_r	Spatial resolution on ground	$[m]$
Lowercase letters		
a_{launch}	Launch acceleration	$[g]$
d	Length defining path	$[mm]$
d_{x-y}	Distance between component x and y	$[mm]$
dX_{x-y}	Distance between component x and y in X-direction	$[mm]$
dY_{x-y}	Distance between component x and y in Y-direction	$[mm]$
f	Focal distance	$[mm]$
g	Gravitational constant	$[m/s^2]$
k_{sx}	Linear stiffness of component x	$[N/mm]$
k_t	Thermal conductivity	$[W/(m-K)]$
m_{mirr}	Mirror mass	$[kg]$
m_{temp}	Dimension multiplier after ΔT	[-]
r_x	Radius of component x	$[mm]$
t_x	Thickness of component x	$[mm]$
w_r	Width ribbon	$[mm]$
x_r	Detector pixel size	$[\mu m]$
Greek letters		
α	Angle between M1 and support frame reference systems around X-axis	°
α_x	Coefficient of Thermal Expansion of material x	$[\mu m/(m-K)]$
ΔL	Change in length due to ΔT	$[mm]$
ΔT	Temperature change	$[°C]$ or $[K]$
η	Worm gear efficiency	[-]
θ_r	Angular resolution	$[rad]$
λ	Wavelength	$[nm]$

1

INTRODUCTION

In today's world, Earth Observation (EO) satellites are crucial to provide information about the Earth for many different applications. As of 1962 more than 320 satellites have been launched for EO purposes, to be used for applications such as defence, land cover/land use mapping, carbon biomass assessment, food security, disaster management, water resources mapping, ocean management, and health and air quality assessment [1]. Especially for astronomers it is desirable to build satellites that achieve even higher spatial resolutions than currently possible, so they have better chances in finding exoplanets. However, also for EO there are applications that require higher spatial resolutions. Within the commercial domain, the state of the art satellites WorldView-3 and WorldView-4 both achieve the highest spatial resolution ever achieved, of 31 $cm/pixel$ in the panchromatic band [2][3].

When designing for high resolutions, one should choose an aperture diameter of the entrance pupil which leads to the appropriate diffraction limit. The diffraction limit is the physical limit one can have for the resolution angle, the minimum angle for which two point sources can be distinguished at a given wavelength, according to the Rayleigh criterion [4]. For a given wavelength the criterion says that the resolution angle is inversely proportional to the aperture diameter of the entrance pupil. In other words, the higher the required resolution, the larger the aperture diameter should be. Another limitation in high resolution designs is that the minimum required focal length is often determined by the minimum achievable detector pixel size. In high resolution satellites this leads to the necessity of relatively long focal lengths. Summarizing, high resolution can be achieved by having a large aperture diameter of the entrance pupil and a long focal length.

In space design it is preferred to use passive systems, not moving and not requiring active control, over active systems, because everything that moves or needs control, can break or lose contact with the controller. Since it will usually not be possible to repair damage in space, protection of the mirrors is required as well. Due to the need for large aperture diameters and long focal lengths, the preference to use fixed mirrors for passivity, and the need to protect the mirrors, high resolution satellites conventionally look like a long and wide cylinder. Unfortunately this type of design also has disadvantages. Big and relatively expensive launchers are needed to fit the volume and the big mass of such a system, which adds a lot of costs.

This thesis forms a part of the DST project. A project where the challenge is to overcome the named disadvantages of conventional telescopes, by developing a system of which the primary mirror consists of several segments that fold open and the secondary mirror extends away after launch. At the same time the goal is to achieve a resolution comparable to WorldView-3 and WorldView-4. This is very challenging, because one needs to actuate the mirrors with extreme precision to align the primary mirror segments. The required precision is in the order of 10 nm.

When starting this thesis project a conceptual design had been made by several PHd-students and MSc-students. However, the design was insufficiently detailed and did not meet every requirement yet. The challenge lays for a big part in the achievable precision in positioning of the deployment mechanisms. It is important to make the next steps towards a final design in a high pace, because the DST team got an offer to piggy back along with a launch of another project, once a breadboard prototype is developed. The author of this thesis is responsible for the primary mirror deployment mechanism and will present a detailed design that is expected to meet the requirements once further developed.

This is done by first providing more background information on the project in chapter 2. Thereafter relevant literature and theories are discussed in the fields of comparable space missions, high precision design, and hinge and latch design, in chapter 3. Then chapter 4 discusses the concept selection for the deployment mechanism, followed by chapter 5 where the selected concept is developed into a detailed design. Afterwards chapter 6 will elaborate on what steps to take from this point to be able to design a breadboard prototype. Finally chapter 7 will present the conclusions and recommendations.

2

GENERAL PROJECT OUTLINE AND THESIS FIT IN THE PROJECT

This chapter will provide the reader with the required background information on the DST project and discusses the work performed by other team members until the start of this thesis research. From there it follows how this thesis will contribute to the further development of the DST.

The chapter starts by describing the EO market in section 2.1. From here it can be concluded what the market actually needs. This, and how this project can help providing those needs is discussed in section 2.2. In section 2.3 the needs of the real world are translated into requirements, to be able to look at the project from an engineering point of view. The progression in the engineering practises of the other team members so far, is discussed in section 2.4. The chapter then concludes with the project needs and corresponding thesis goals in section 2.5.

2.1. THE EO MARKET

As a rule, companies can only exist if they make more money then they spend. This also holds for companies in the EO sector. Luckily companies in this sector can often limit their spending, because the data of one satellite can often be used for many different applications by processing it in a different way. It is usually too costly to design, build, and operate a satellite for, for example, only one scientific research experiment. Hence, the market developed such that there are operators that assign third parties to develop and build satellites, but afterwards operate the satellites themselves, harvesting all the data. They sell this data to companies and institutes that want to use it, mostly in differently priced packages, going from raw data to processed data, where the quality is adjusted to the price one pays. The current amount of EO data sold per application is shown in fig. 2.1 with a total market value of 1.6 billion dollars per year [5]. As can be seen, defence applications dominate the market with 61% of the bought data. Defence systems are usually bought for observations where the spatial resolution, i.e. the number of pixels projected per unit area on the ground, should be as high as possible. However, also other applications are found that benefit from, or even require a high resolution. This leads to the trend shown in fig. 2.2, where one can clearly see the EO market grows rapidly, but only for the less than 1 m resolution data. The absolute sizes of the other market segments are relatively stable [5].

Due to the drive for higher resolutions, the market of EO satellite operators changed drastically over the past decade. Back in 2011 the market was very divided with several small and three big players, of whom no one had a market share higher than 33%, as shown in fig. 2.3 [6]. As can be seen in fig. 2.4 the market now has two major players of which DigitalGlobe is by far the market leader [7]. Notable is that in 2013 DigitalGlobe and GeoEye, both known for building the satellites with the highest resolutions, merged, resulting in them controlling a worldwide constellation of high resolution satellites. Astrium was a division of EADS, which restructured into the Airbus Group, which led to Astrium becoming part of Airbus Defence and Space. In February 2017 DigitalGlobe merged again, now with the third player in the market at that moment. Combining this information it seems that becoming market leader depends on how high the resolution of one's satellites is.

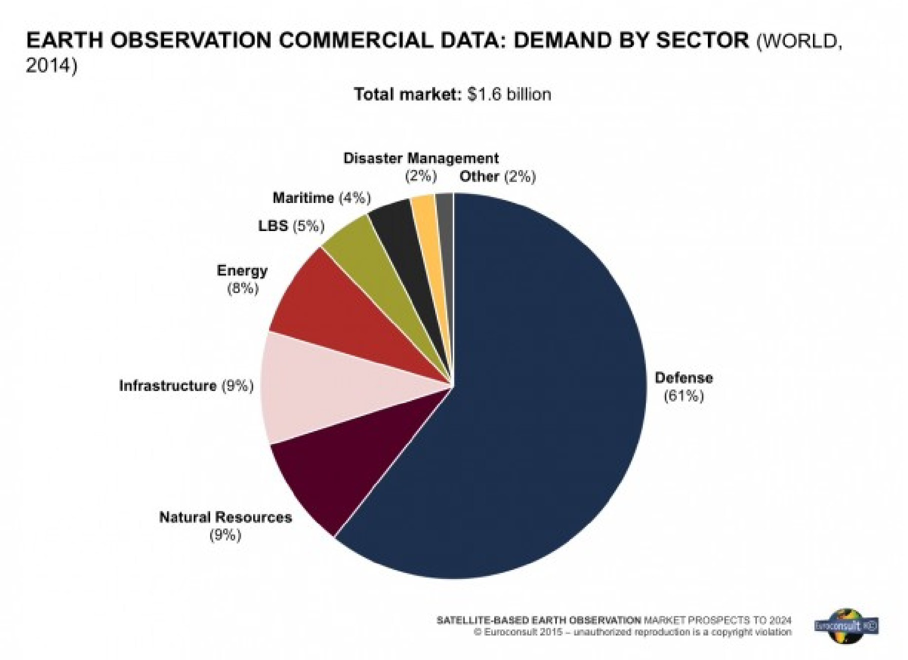

Figure 2.1: EO data sold per application in 2014 [5]

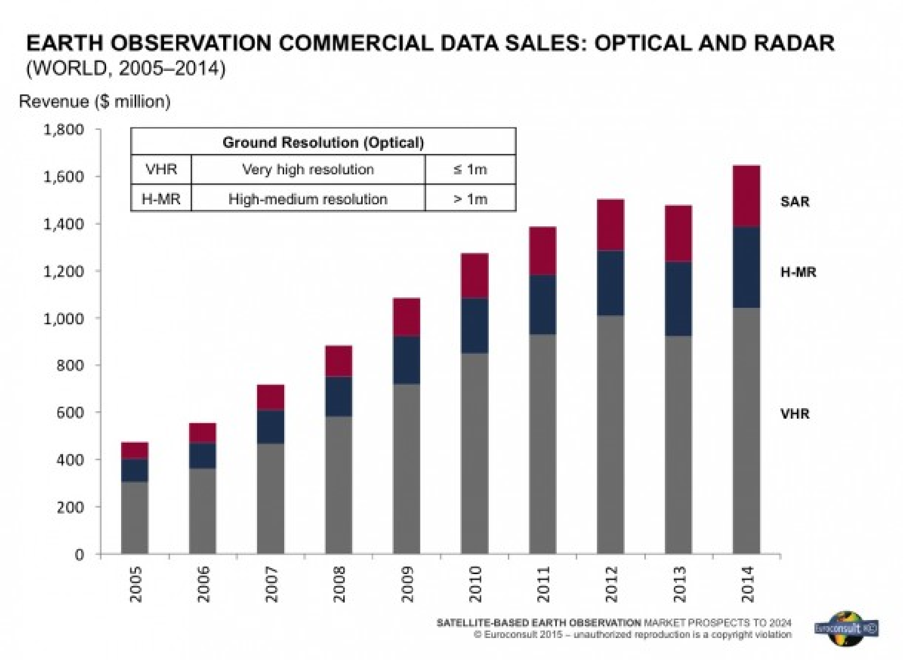

Figure 2.2: Amount of EO data sold between 2005 and 2014, divided in different resolutions [5]

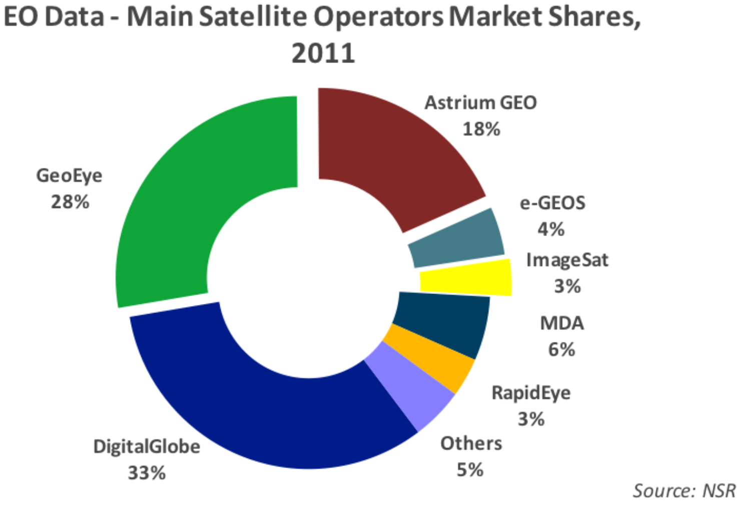

Figure 2.3: Market shares per operator in 2011 [6]

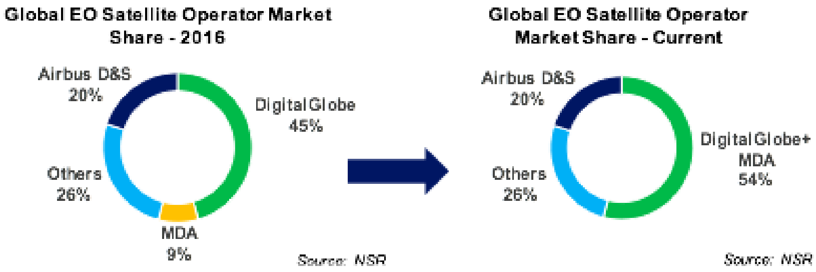

Figure 2.4: Market shares per operator in 2017 [7]

For defence applications little imagination is needed to explain why high resolutions are necessary. For other applications this might not be that clear. A good explanation of new applications that were made possible with the 31 $cm/pixel$ resolution of the WorldView-3 has been provided at the Geospatial World Forum 2014 by DigitalGlobe [8]. An example is that it becomes easier to remove atmospheric effects, because clouds become more distinguishable from snow. Another example is related to mineral and oil exploration. Oil and minerals do not often occur as one big chunk on the surface, but rather small mineral rocks or groups of oil particles that have risen to the surface. With the high resolutions it becomes possible to distinguish these rocks and particle groups from the general ground layer.

To end this section the price of high resolution satellites will be discussed. Operators tend to share little details about satellite costs. However, Walter Scott, founder and CTO of DigitalGlobe, once said that WorldView-3 cost $650 million, including building and launch [9]. For WorldView-4 it is only known that the original costs were estimated at $835 million [10], although Scott later said the price is comparable to the price of WorldView-3 [11]. The costs involved for building and launching this satellites are rather large, and a significant portion of the price is in the launch. The satellites are big and heavy, meaning a big launcher is required, such as the Atlas V for both WorldView-3 and WorldView-4. Today the basic cost of such a rocket is $109 million, but with the additional costs for the required solid rocket boosters and additional services, the price goes up to over $150 million rather easily [12]. A lot of costs can be saved when a lighter launcher such as a VEGA rocket can be used. Depending on the amount of launches per year it is estimated a launch will cost between €22 million and €32 million [13], for a payload of at most 1430 kg that fits in a cylinder of 1.7 m high, with a diameter of 1.9 m [14]. With this in mind a lot of research is conducted nowadays in making smaller and lighter EO satellites.

2.2. MARKET NEEDS AND PROJECT GOAL

The market research of previous section, clearly shows that the market share of the big companies depends for a big part on how much high resolution data a company can deliver, but that on the other hand the satellites that can provide this data are too expensive to make a constellation. This is summarized in the following need statement:

Need statement
The Earth observation market has a need for satellites with high ground resolutions for a drastically decreased price.

There is a trend in research to investigate the feasibility of making smaller and lighter high resolution EO satellites, to reduce the launch costs by a large amount. The introduction of chapter 1 already described some basic knowledge, required for reaching high resolutions. This discussion will continue below.

The angular resolution, θ_r, is the smallest angle from the image center to two different point sources for which these point sources can be distinguished. The terminology might come in a bit strange, because the lower the value of the angular resolution, the higher one says the resolution is. Even if there are no aberrations in the optical system, there still is a physical limit for the achievable angular resolution, which is caused by diffraction. The diffraction limit is defined by the Rayleigh criterion, which says that θ_r in rad is proportional to the wavelength of interest, λ, divided by the aperture diameter of the system, D, as shown in eqn. 2.1. Since this angle provides the radius of the so called Airy disk, one needs to double the right-hand side of eqn. 2.1 to relate to the diameter and find the equation for the spatial resolution on the ground, X_r, as shown in eqn. 2.2. Here H is the height of the satellite. Since the detector pixel is approximately located at the focal distance, f, of the lens, the detector pixel size, x_r,can be derived by eqn. 2.3 [4].

$$\theta_r = 1.22\frac{\lambda}{D} \tag{2.1}$$

$$X = 2.44\frac{H\lambda}{D} \tag{2.2}$$

$$x = 2.44\frac{f\lambda}{D} \tag{2.3}$$

$$F\# = \frac{f}{D} \tag{2.4}$$

From the equations it becomes clear that better resolutions are achieved with bigger aperture diameters. Also one can see that in general it is more difficult to achieve high resolutions at longer wavelengths. This however does not hold for this project, because longer wavelengths relax the phasing budgets of the mirrors, which is more critical in this design. In eqn. 2.3 an important characteristic of an optical system comes by, namely the f-number or F#, as shown separately in eqn. 2.4. It indicates how sensitive the system is to aberrations, but is also a measure of how bright an image will be. As a rule a low F# results in high order aberrations, while for a high F# first order optical equations are reliable [15]. On the other hand it holds that the brighter the image, the less exposure time is needed. The The square of the F# is inversely proportional to the brightness, so with an F# of 2, the image is four times as bright as with an F# of 4. Since satellites move fast over the ground, a low required exposure time is beneficial, which can be achieved best by designing for the physical minimum limit of the F# of 0.5. In other words an optimum needs to be found for enough brightness with minimal aberrations. There is however another limit that often defines the minimum F#. When looking to eqn. 2.3 for a chosen wavelength, the detector size x_r is proportional to the F-number, and so one is limited by how small detector pixels can be made. Andor, an Oxford Instruments company, says the smallest detector pixel sizes are currently 4 μm x 4 μm [16]. This means for example that if one wants to observe blue light with a wavelength of 500 nm and an aperture diameter of 1 m, the focal length would still need to be at least 3.28 m, leading to a minimal F# of 3.28. In short, high resolutions are achieved by:

- Maximizing the aperture diameter;
- Finding the minimum focal length defined by the detector pixel size, which is often quite long;

- Finding the optimal focal length for the required brightness and minimal aberrations, taking the boundary defined by previous point into account.

The first two points of this summation are the reason most EO satellites are big. As explained before, passive systems are preferred, because they form much less risk to fail than active systems. This means that the satellite usually has a large primary mirror, and a secondary mirror placed far away from it via legs or a cylinder, so the required focal length is achieved. A typical image is provided in fig. 2.5, with next to it fig. 2.6 showing the size relative to a human.

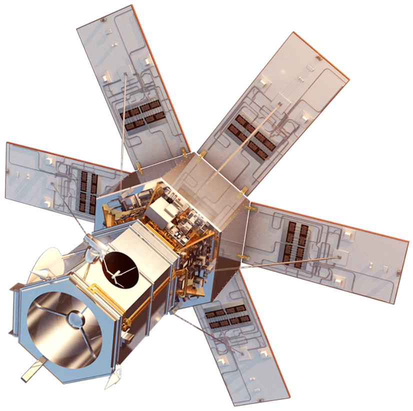

Figure 2.5: Artist impression of WorldView-4 [17]

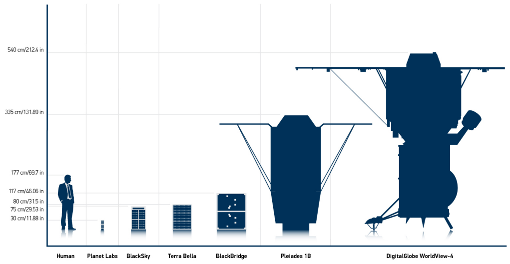

Figure 2.6: Relative size of an average human vs. WorldView-4 on the far right [18]

These days a lot of companies and institutes investigate the option of active telescopes that can be deployed. Some of them are discussed in detail in chapter 3. One of the most well-known deployable telescopes, is the James Webb Space Telescope (JWST). It is still under development and planned to be launched in spring 2019. The JWST is seen as the successor of the Hubble Space Telescope and has a much larger primary mirror with a diameter of 6.5 m, versus 2.4 m for the Hubble. This gives the JWST the option to observe mainly in the far-infrared and mid-infrared, but also part of the visible spectrum (wavelengths between 0.6 μm and 28 μm) with a high resolution, where the Hubble could observe in the near-infrared, but mainly focused on the visible and UV wavelengths [19]. For both the mirrors and the sun-shield, with roughly the size of a tennis court, it was necessary to make both systems deployable to fit the JWST into a launcher. As explained in subsection 3.1.1, the JWST is not completely comparable with EO satellites, but it gave a lot of inspiration. During the development a lot of useful science is conducted that can be applied to EO satellites.

In the projects discussed in chapter 3 that are comparable with the DST project, often only the secondary mirror will be deployed and sometimes only the primary mirror unfolds. Also, these telescopes often go for high resolutions of less than 3 m, but not a single one tries to break the record of WorldView-3 and WorldView-4 with their panchromatic ground resolution of 0.31 m. Under the supervision of Dr.ir. J.M. Kuiper, ir. D. Dolkens graduated on designing a first concept of a synthetic aperture telescope able to achieve a sub-meter Ground Sampling Distance (GSD) [20]. The main focus was on the optical design, but also the mechanical design, calibration strategy, and image processing strategy are discussed on a conceptual level. The design of fig. 2.7 was the result, and afterwards Dolkens and Kuiper felt confident that it is possible to achieve even higher resolutions than currently available, while still being cheaper, by making a satellite where both the primary mirror and secondary mirror unfold. Dolkens is now a PHd-student. Together with Kuiper they created a project to develop this idea involving industry partners, MSc-students and another PHd-student. The goal of the DST project became as follows;

Mission Statement *The goal of this project is to design and develop a Deployable Space Telescope (DST) that is capable of achieving the same GSD as state-of-the-art Earth Observation satellites for a fraction of the costs, by making it able to achieve a relatively very low stowed volume and mass.*

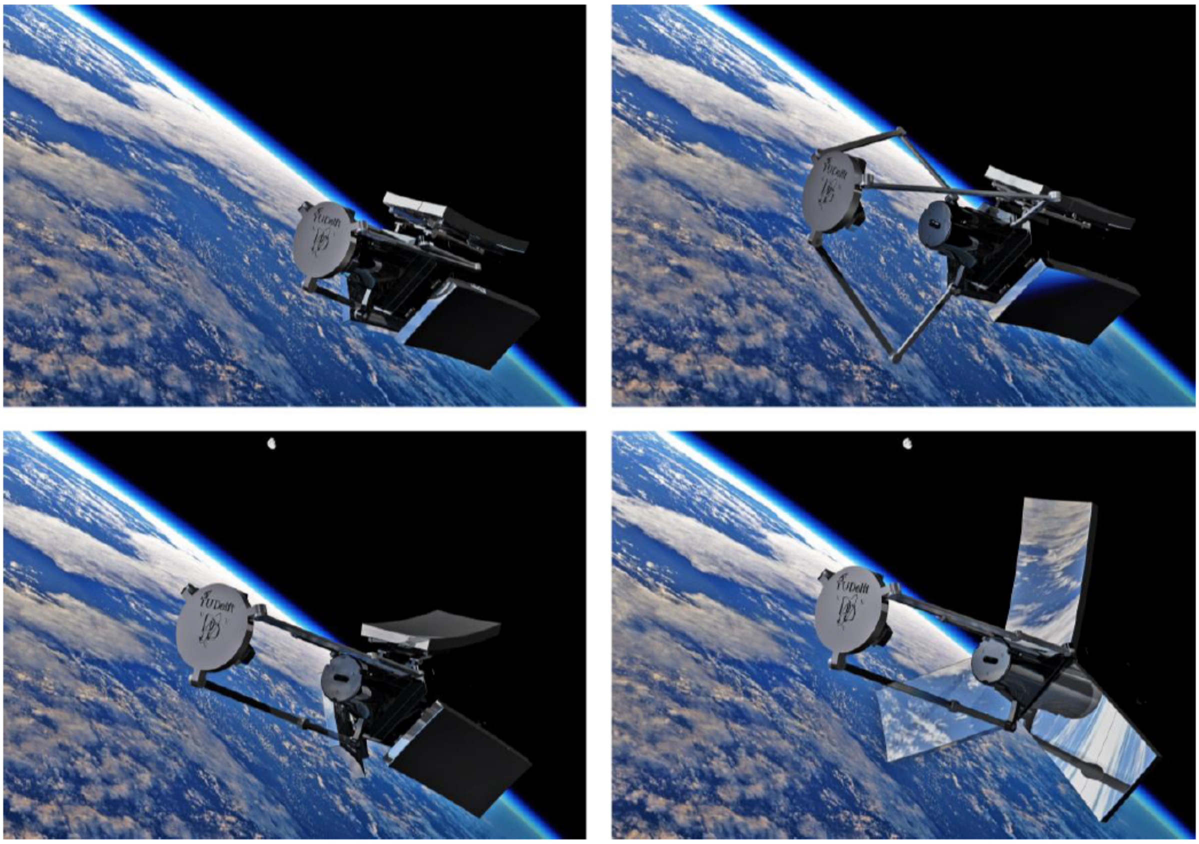

Figure 2.7: Deployment sequence of the initial DST design developed for the masters thesis of Dolkens in 2015 [20]

2.3. REQUIREMENTS

In the meantime the project has evolved and rough time lines are determined. The original plan was to fulfill the mission statement by launching the satellite in roughly 5 years, although it currently seems that the development time needs to be extended. Also, Airbus Defence and Space (ADS) provided an opportunity at a meeting in June 2016, to launch a small mock-up satellite that will piggy back with one of their test payloads within a time frame of two years. At the moment it is exactly two years ago this was agreed. ADS however had some delays, so now the plan is to launch in early 2019. Also the DST project progressed slower than expected, to such an extend that it is expected the mock-up will not fly on the flight in 2019. Although a general concept of the mock-up satellite has been made by the previous person working on the Primary Mirror (M1) subsystem, for now the focus is back towards the real satellite design. This fits the current design philosophy that only when the design is mature enough to know with a reasonable certainty that certain components will be used, it is possible to define what critical components should be tested in space. Furthermore the current plan is to actually build a first breadboard prototype for ground testing, before a second one will be designed and build that will be sent to space.

In general, testing is a way of verifying whether requirements are met. Therefore it is important to first define requirements before making a design. This project mainly works with a bottom-up systems engineering approach. This means that a top-down start is made by deriving requirements that describe the required performance of the output data, followed by the technical requirements for the optical system. Based on these requirements, one starts to develop the subsystem that allows to fulfill them. In this case the optical design requirements flow down on the required performance of the mirror positioning mechanisms, which will be designed thereafter. During this design it becomes clear the requirements can only be met in a certain thermal environment, meaning that requirements flow down on how to design the baffle, which will be designed thereafter, etc.

In reality this is not a serial process, as described above, but one starts with the next subsystem once enough requirements are known to make a start. The design of the subsystem they flow down from is not necessarily finished yet. Also one will find that sometimes the imposed requirements are unfeasible. In that case one goes back to the subsystem design that led to the requirement and tries to find an alternative solution or compromise.

In the work of the team members so far, each of them made their own table of requirements with their own ID tag system. This is confusing and makes one lose track of where certain subsystem requirement flow down from. Between the start and end of this thesis, the team expanded from 3 people working on 3 subsystems to 11 people working on 6 subsystems. Therefore it was necessary to create one document to keep track of all requirements with a uniform coding and a system to track mother requirements [21]. This document is too extensive for placement in (the appendix of) this thesis, but the top level requirements and the primary mirror subsystem requirement tables are shown in appendix A.

The most challenging requirements that are a very important factor in the design choices of this thesis work are M1-MEC-01, M1-MEC-04, M1-MEC-07, and all of the daughter requirements of these 3. They are summarized in a more clear format that was used for a presentation in fig. 2.8. Requirement M1-MEC-01 tells the values in the first row of the 'Deployment and Coarse Alignment Tolerances' section shall be met with a confidence level of $> 2\sigma$. The daughters of this requirement, M1-MEC-01-01 to M1-MEC-01-06, provide the values of the first 6 columns in this row, respectively. In the same fashion M1-MEC-04 corresponds to the section called 'In-Orbit Drifts' and M1-MEC-07 corresponds to the section called 'Stability Budget'. The last two titles may need some explanation, since it is not immediately clear what the budgets stand for. The In-Orbit Drifts budget refers to the allowable deformations due to temperature changes allowed per orbit. The stability budget refers to the maximum allowable deformations due to vibrations. Note that only the In-Orbit Drift budget is time bounded as an allowed error per orbit. The two axis reference systems used in this thesis are defined in fig. 2.9. The budgets apply to the M1 reference system. Note that the full satellite reference system used by the DST team is actually located at the vertex of the parabola described by the primary mirror with the axial directions parallel to the ones of the M1 reference system. This axis system is however not relevant for the work described in this thesis.

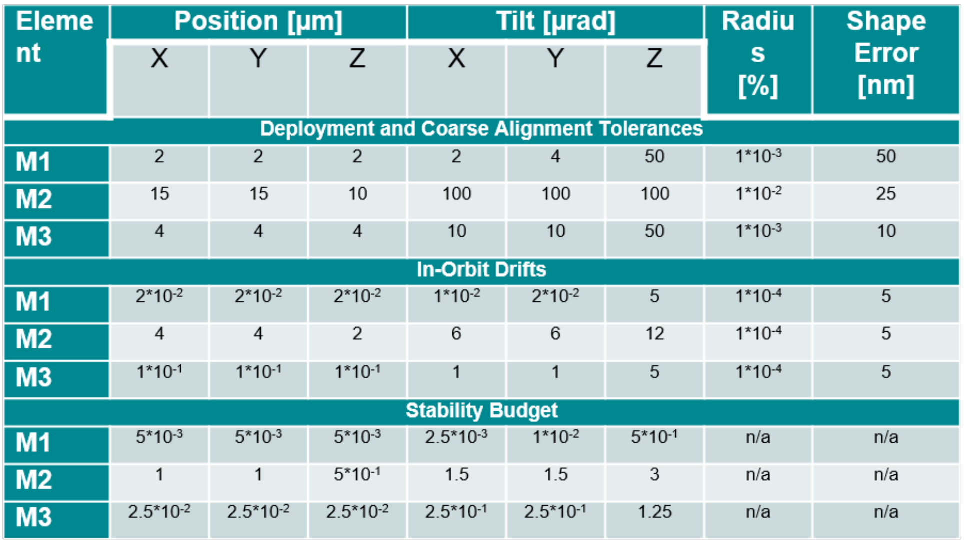

Element	Position [μm]			Tilt [μrad]			Radius [%]	Shape Error [nm]
	X	Y	Z	X	Y	Z		
Deployment and Coarse Alignment Tolerances								
M1	2	2	2	2	4	50	$1*10^{-3}$	50
M2	15	15	10	100	100	100	$1*10^{-2}$	25
M3	4	4	4	10	10	50	$1*10^{-3}$	10
In-Orbit Drifts								
M1	$2*10^{-2}$	$2*10^{-2}$	$2*10^{-2}$	$1*10^{-2}$	$2*10^{-2}$	5	$1*10^{-4}$	5
M2	4	4	2	6	6	12	$1*10^{-4}$	5
M3	$1*10^{-1}$	$1*10^{-1}$	$1*10^{-1}$	1	1	5	$1*10^{-4}$	5
Stability Budget								
M1	$5*10^{-3}$	$5*10^{-3}$	$5*10^{-3}$	$2.5*10^{-3}$	$1*10^{-2}$	$5*10^{-1}$	n/a	n/a
M2	1	1	$5*10^{-1}$	1.5	1.5	3	n/a	n/a
M3	$2.5*10^{-2}$	$2.5*10^{-2}$	$2.5*10^{-2}$	$2.5*10^{-1}$	$2.5*10^{-1}$	1.25	n/a	n/a

Figure 2.8: Requirements on several budgets for the positioning of the different mirrors

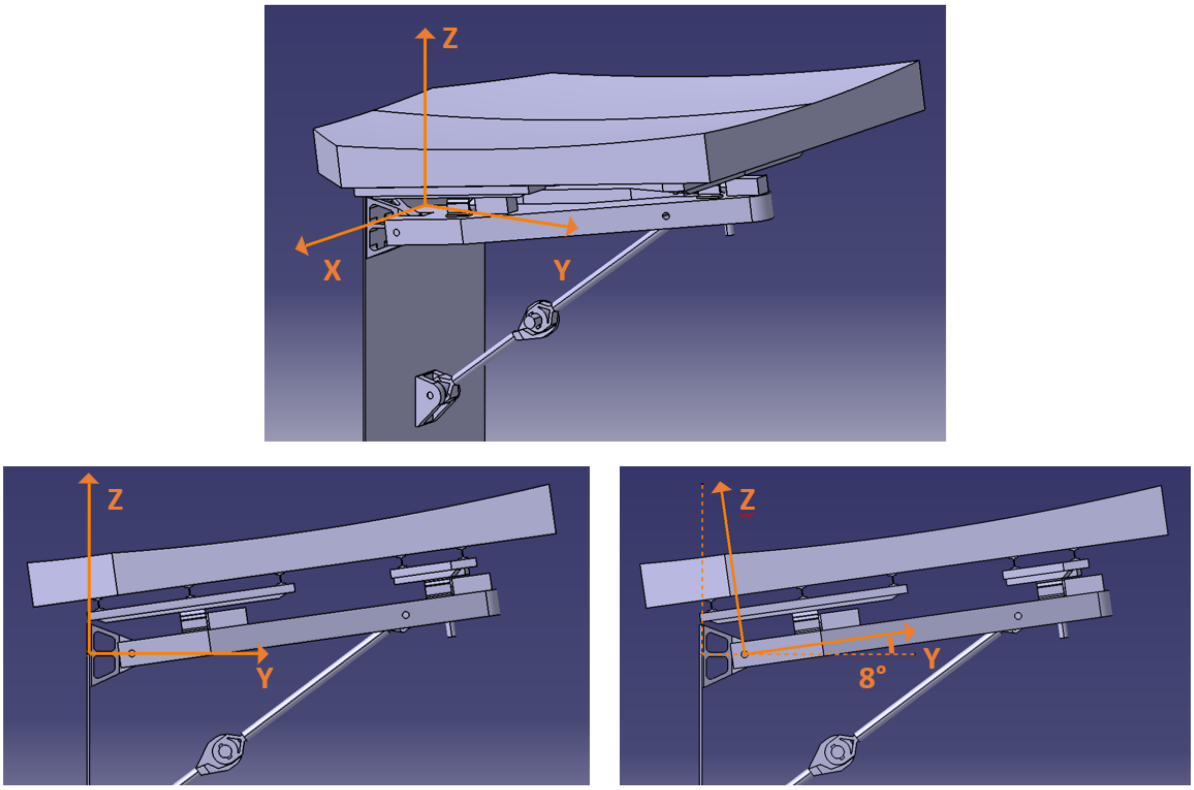

Figure 2.9: Top: M1 reference system in 3D - Bottom left: M1 reference system as seen in YZ-plane - Bottom right: Support frame reference system as seen in YZ plane, consisting out of a 50 mm translation in Y-direction and an 8° rotation around the X-axis with respect to the M1 reference system

2.4. PREVIOUS WORK

As said before, at the start of this thesis only three people worked on this project on three different subsystems. It started with PHd-student Dennis Dolkens, who worked already for some years (and currently still works) on the optical system design. Then MSc-students Boris van Putten and Jessy Lopes Barreto developed the M1 and Secondary Mirror (M2), respectively. They both graduated around the time this thesis research started. At this point the design of fig. 2.7 evolved to the one of fig. 2.10. During the literature study preceding this thesis more team members joined. They did not provide any results yet, but it is useful to discuss the matters they started to work on, because this in this thesis some design choices are made based on the preferences of the team members working on other subsystems. Below first an overview is provided on the work of Dolkens and Lopes Barreto to get familiar with the bigger context of the project. Then the thesis of Van Putten will be discussed in more detail, since this thesis is a continuation of that work. Finally the new team members are introduced together with the topics they work on.

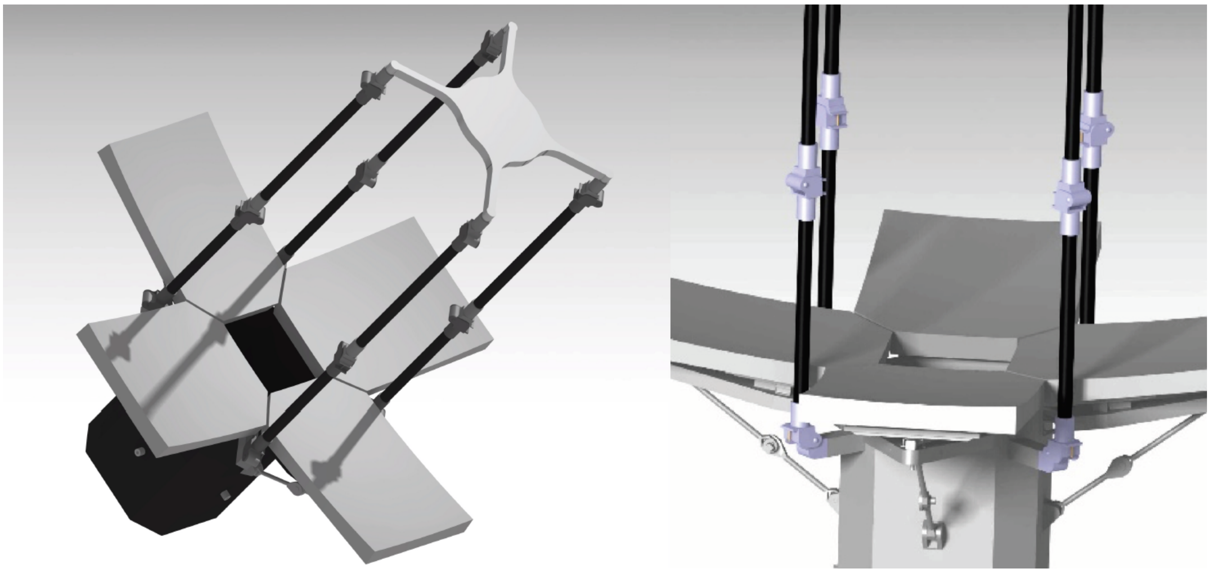

Figure 2.10: Render of DST design after the thesis work of Van Putten and Lopes Barreto [22]

2.4.1. WORK OF DOLKENS AND LOPES BARRETO

As explained in section 2.2, Dolkens initiated this project with a feasibility study during the MSc-thesis preceding his PHd-study [20]. After the positive outcome one of the main achievements of Dolkens is the ray tracing software he developed, called Fast Optical RayTrace Application (FORTA). Since existing ray tracing software is hard to adept for the use of segmented mirrors, this unique software had to be developed for this project. FORTA, first described in [23], supports ray tracing for not only spherical and aspherical mirrors and lenses, but also for freeform surfaces described by Zernike polynomials. These elements can be described by user defined functions, meaning that other optical systems than the one of the DST can also be analyzed. This capability is used to validate the software by comparing the results for optical systems that are suitable for both FORTA and Zemax, a commercially available ray tracing software.

The main capability of FORTA is to calculate the wavefront, Point Spread Function (PSF), and Modular Transfer Function (MTF) given a certain positioning of the optical components. When providing an image it will simulate how it is seen by the detectors. As a follow-up, calibration algorithms have been developed that detect the wavefront errors, which is used to calculate how the M1 segments and deformable mirror can be altered to improve the image quality. This is not only useful for defining the ideal positioning during the design phase of the project, but also for autonomous mirror calibration during operation. By performing several case studies Dolkens found the most optimal lay-out of the optical system, which is shown in fig. 2.11. After this, more case studies have been performed to find which errors can be tracked and calibrated by the algorithm to end up with the desired image quality. This resulted in many of the requirements for the mirror subsystems, which are summarized in the budgets of fig. 2.8.

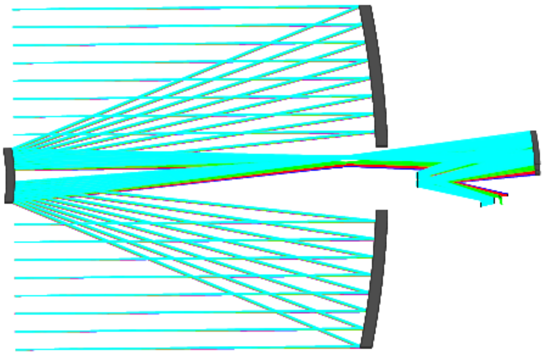

Figure 2.11: Optical lay-out of Annular Field Korsch Telescope design with the wide mirror section representing two M1 segments, the far left mirror representing the M2, the far right mirror representing a folding mirror, and the small mirror near M1 representing the deformable mirror [23]

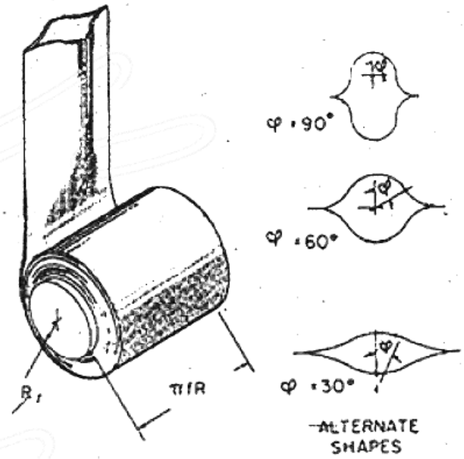

Figure 2.12: Sketch of the working of a CTM boom [24]

Lopes Barreto was the first person to look into detail to the thermo-mechanical design of the M2 subsystem, since the design with the deployment by articulated booms as shown in fig. 2.7 was the result of a conceptual design where little thought was put into the deployment mechanisms. In his thesis Lopes Barreto investigated multiple types of deployment mechanisms such as articulated booms, coilable booms, collapsible tubular mast (CTM) booms, telescopic booms, inflatable booms, and deployable truss structures [22]. After a trade-off and discussions with experts from ADS it was decided to work out the concepts of the articulated booms and the CTM booms in more detail, before a final decision would be made. A CTM boom is flat when coiled up during stowage. Comparable to a measuring tape it gets a stiffer curved shape once it is rolled out, but in this case it actually has two opposing tapes that form a closed cross section. This is shown in fig. 2.12.

Now first a trade-off on the material for the articulated booms led to the selection of Carbon Fiber Reinforced Polymer (CFRP) as the material of choice. After this models that measure the deflection for different load cases were applied to the two concepts. A first effort proved that it was quite challenging to meet the stability requirements (especially concerning that the required boom length was 1.6 m at this time). Therefore iterations were made to optimize both designs. For the articulated boom this was done by changing dimension, applying different lay-ups to change the material properties of the CFRP, and experimenting with the amount of boom segments. For the CTM boom this was done by varying the many dimensional parameters and by optimizing the design of the Hold Down and Release Mechanism (HDRM) of the boom, which provides a significant amount of stiffness. Even though the final CTM design scored better in all properties related to the stability, the final choice was to go for the articulated booms, mainly because the HDRMs of the CTM booms add a lot of mass and complexity.

Finally the articulated boom concept was designed in more detail. Only the spring loaded hinges lacked detail. However, even with simplified and probably too relaxed assumptions for the hinges the design could not meet the requirements. Two main reasons were the long length of the boom and the impact of thermal effects on the unprotected booms. This is the point where the required boom length has been brought down from 1.6 m to 1.3 m and where it was decided that a baffle will need to be implemented in the design. It should be noted that there was already a push towards the use of a baffle, since the thesis of Van Putten [25], which was finished a month before these conclusions, also indicated that the M1 would not work without thermal shielding.

2.4.2. WORK OF VAN PUTTEN ON M1 DESIGN

In the MSc-thesis of Dolkens the mechanical design of the M1 subsystem was out of the main focus of the work. Therefore the resulting design was more of a first suggestion than actual design, by using components and mechanisms copied from comparable space projects, without comparing multiple options. The design is shown in fig. 2.13. Only the material for the mirror surface (SiC) has been selected after an extensive trade-off. The useful information for the mechanical design that resulted from the thesis and later work of Dolkens consisted of the shape of the mirror surface, the position of the mirror surface with respect to M2 and the satellite bus, and the budgets defining the allowed alignment errors of the mirror.

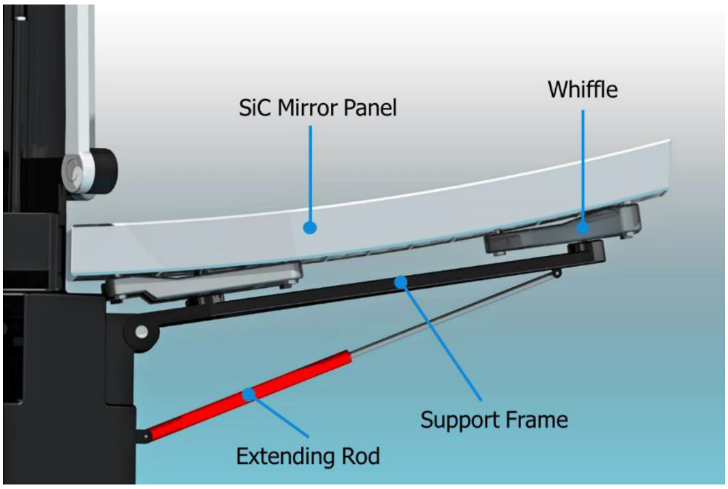

Figure 2.13: Conceptual M1 subsystem design described in the MSc-thesis of Dennis Dolkens [20]

Based on this information Van Putten started working on the mechanical design from a clean slate. Since the M1 subsystem comprises many components and a lot of considerations needed to be taken into account, the thesis was rather a broad work on the complete subsystem design than a detailed study into (some of) its components.

A first thing that became clear from looking at the provided information of Dolkens was that the required calibration precision would form a difficult challenge. Therefore the calibration mechanism and the deployment mechanism, that should deploy with a precision that falls into the range of the calibration mechanism, were seen as the critical components of this subsystem. After studying deployment mechanisms of comparable satellite designs, first a trade-off was performed to find the most suitable deployment mechanism. The strutted and strutless concepts assessed are shown in figs. 2.14 and 2.15, respectively. They underwent a trade-off with weights as shown in tab. 2.1, resulting in the trade-off results of tab. 2.2.

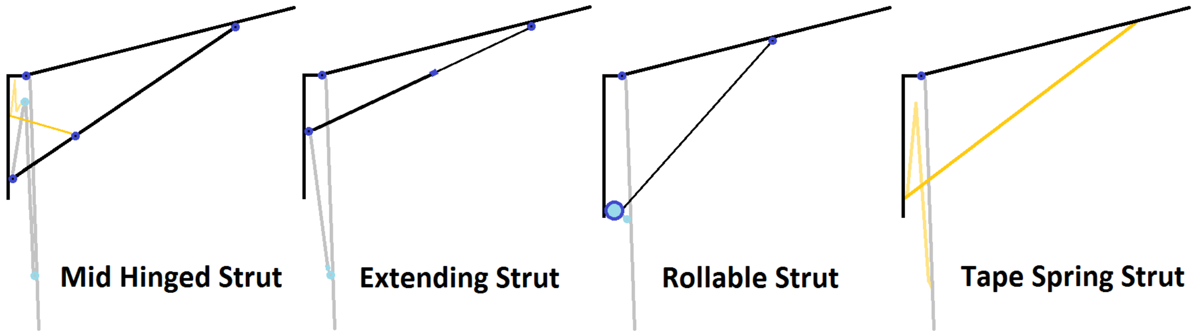

Figure 2.14: Concepts of the assessed M1 deployment mechanisms that involve a strut [25]

Based on the outcome of tab. 2.2 it was decided to make a preliminary design of the motor resistance, mid hinged strut, and kinematic interface concepts. These design were analyzed in ANSYS to find the eigenfrequencies of the mechanisms. The results for the first five eigenmodes of each concept are shown in tab. 2.3.

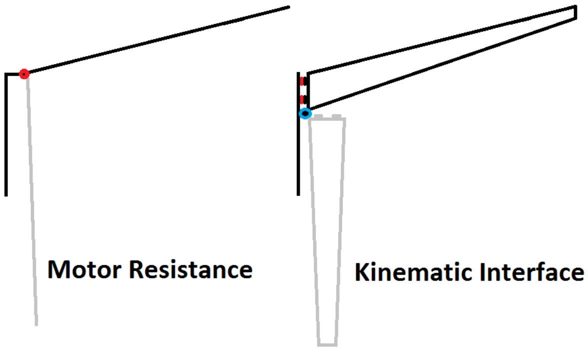

Figure 2.15: Concepts of the assessed M1 deployment mechanisms that do not involve a strut [25]

Criteria	**Weight**
Accuracy	5
Readiness	4
Repeatability	3
Stability	3
Compactness	2
Mass	2

Table 2.1: Weights for strut concept trade-off in the work of Van Putten [25]

Table 2.2: Trade-off between the different strut concepts in the work of Van Putten [25]

Concept	**Kinematic Interface**	**Motor Resistance**	**Mid Hinged Strut**	**Extending Strut**	**Rollable Strut**	**Tape Spring Strut**
Accuracy	4	3	4	4	1	2
Readiness	4	4	4	3	3	3
Repeatability	4	5	4	4	2	3
Stability	4	2	4	3	3	3
Compactness	3	4	3	3	3	4
Mass	2	4	3	3	3	4
Weighted total	70	68	72	65	44	56

Table 2.3: First five eigenmodes of the top concepts [25]

Eigenmode	**Frequency** $[Hz]$		
	Motor resistance	**Mid Hinged Strut**	**Kinematic Interface**
1	8.42	78.45	19.74
2	102.67	114.98	66.11
3	160.56	143.73	139.10
4	267.10	154.63	198.27
5	394.90	245.67	233.95

Since the mid hinged strut came out as the best option in both the first trade-off and the vibration analysis, the logical step was to select this concept for further development. The next design step was to find the right strut length and select the appropriate location of the hinge along this length. This was done along with designing the support frame, mostly referred to as the A-frame due to its shape, since the strut has to move through the A-frame when stowed. This is shown in the render of fig. 2.16.

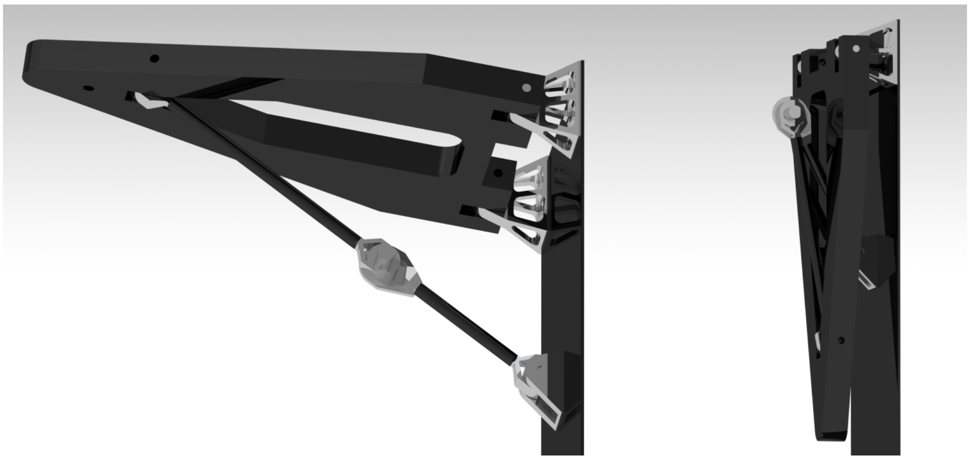

Figure 2.16: Render of the deployed and (left) and stowed (right) configuration of the A-frame and strut [25]

Then the mirror was designed, since the optical design of Dennis only provided the parabolic shape of the mirror surface and the preferred material. Taking the weight, resistance to gravity sag, and fundamental eigenfrequency into account it has been decided that the mirror will consist of triangular hollow pockets at the bottom, as shown in fig. 2.17, with a bottom that is flat instead of parabolic. This makes it easier to design the whiffles. The size and geometry of the pockets and the location of the whiffle nodes (shown as circles in fig. 2.17), were determined by optimizing iteratively for certain gravity and thermal load conditions. In the end the maximum modelled deformation was 58 nm for the gravity off-loading and 25 nm for the thermal deformation.

The whiffles are mechanisms that can distribute mechanical loads in the system evenly and can reduce stresses in the mirror due to deformations. Each mirror segment has three whiffles with each three points that connect to a node of the mirror pockets. Each whiffle is actuated for calibration purposes. A trade-off was made between different calibration actuators and a certain actuated flexure was found to be the most suitable. The working of this actuated flexure is shown in fig. 2.18. A motor of choice will be connected to the hole in the middle of the flexure via an eccentric bearing. This leads to relatively large up and down motions of the cross-beam, which results in a small up and down motion of the top of the flexure. Assuming a stepper motor with a precision of 200 $steps/revolution$ in combination with an harmonic drive with a reduction ratio of 50:1, the flexure has been designed to have a range of 34 μm (see left of fig. 2.19) and a precision per step of at least 10.72 nm (see right of fig. 2.19). As the figure shows, the displacement per step is not equal over the full range, so the worst precision of 10.72 nm, only holds for actuation near the starting position in the middle of the range. Assuming an actuator resolution of 10.72 nm over the whole range, it can conservatively be calculated how precise the actuation in tip, tilt, and piston is. Also one can find the allowable deployment error of the A-frame by calculating the errors that would fall just within the range of the actuated flexures. The results are shown in tab. 2.4. Optimizing the design for a high eigenfrequency and minimal displacement due to gravity off-loading, a final design for the mirror, including the whiffles and actuation, came out as shown in fig. 2.20. The estimated mass of these parts is 3140 g.

Table 2.4: Calibration actuator precision and the allowable deployment error for which these actuators can correct in tip, tilt, and piston [25]

	Tip	**Tilt**	**Piston**
Actuation precision	51.05 $nrad$	32.58 $nrad$	10.72 nm
Allowable deployment error	15.50 μrad	9.90 μrad	13.02 μm

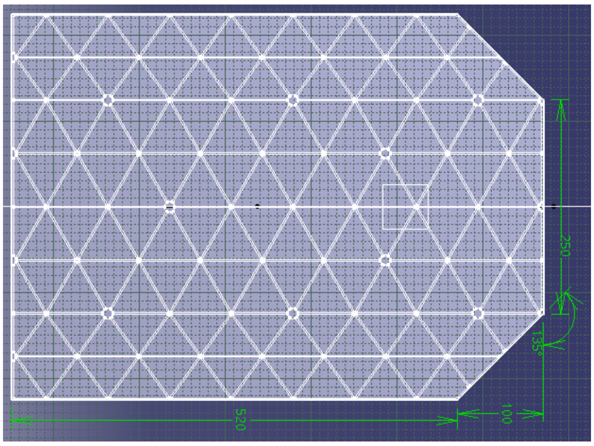

Figure 2.17: Pocket geometry of the primary mirror segments as designed by Van Putten [25]

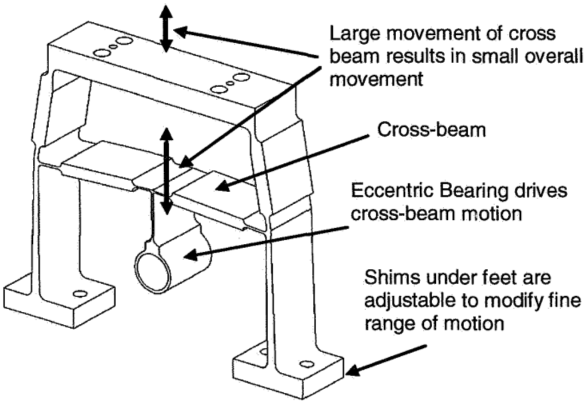

Figure 2.18: Explanation of the working of the actuated flexure [26]

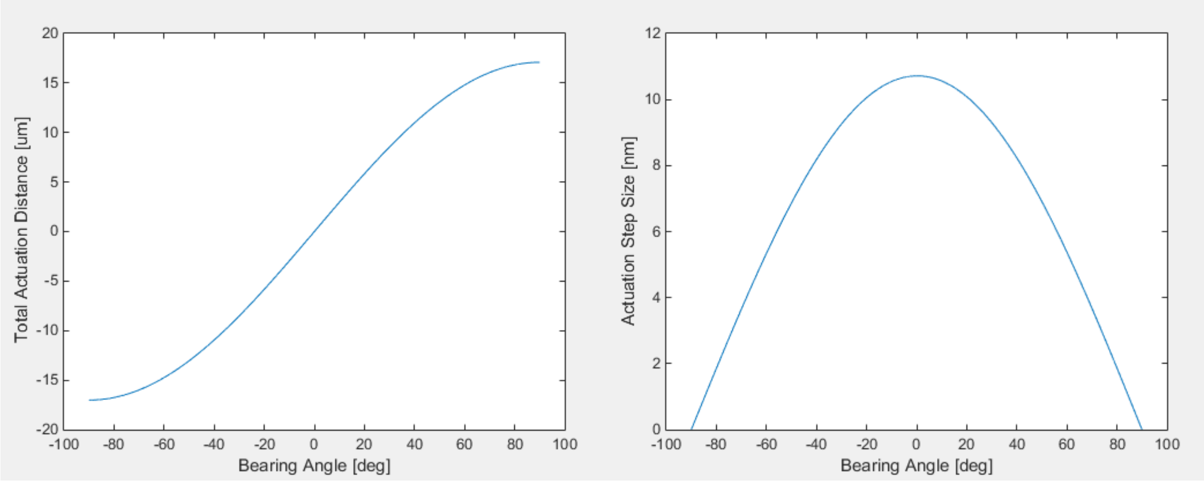

Figure 2.19: Left: accumulated vertical displacement of the top of the flexure per *deg* of motor rotation - Right: vertical displacement of the top of the flexure per step for each motor position in *deg* [25]

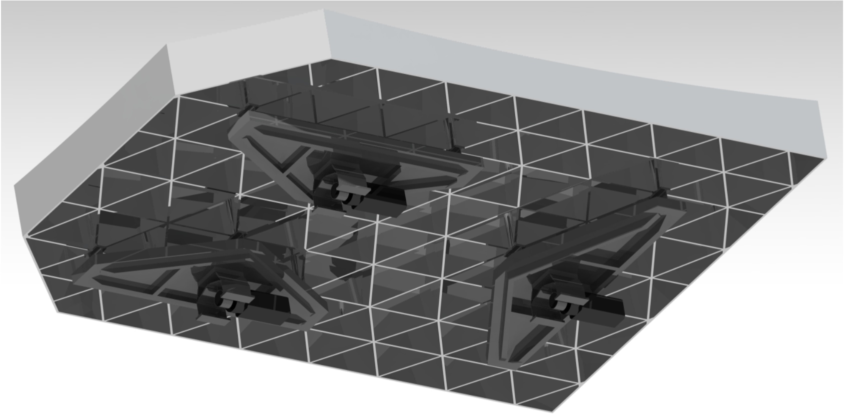

Figure 2.20: Render of the Van Putten's final mirror design, including the whiffles and calibration actuators [25]

Knowing the required precision of the deployment mechanism, the elements affecting this precision were designed. These elements are all hinges and latches involved in the positioning of the A-frame, to be more specific: the self-latching hinge joint in the middle of the strut, the hinges at the ends of the strut, and the support hinges connecting the A-frame with the bus. To achieve a high deployment precision it is important that freeplay, nonlinear elasticity and hysteresis are reduced as much as possible in the hinges and the latch. Van Putten got most of his inspiration from literature written by by Mark Lake, Lee Peterson, and Peter Warren. Together with different co-authors they wrote many papers on the development of several deployment systems that required high precision to support the optics. The project started in 1994 and from then to the late zeros they published papers and reports describing ideas [27], experiments [28][29], production drawings [30], and also a document combining the gained knowledge with guidelines on how to reduce hysteresis in mechanisms for deployable optical instruments [31]. The focus in these documents is mainly on hinges and latches. In subsection 3.1.1 of this thesis the theory from this literature is discussed in more detail.

The guidelines [31] suggest a design with hinges as shown in fig. 2.21 when designing for high precision. Van Putten translated this to support hinges for the A-frame as shown in fig. 2.22, and into hinges for the strut ends as shown in fig. 2.23. The triangular cut-out in the tang (clearest shown on the left of fig. 2.23) is to achieve constant tang stiffness, regardless of stresses imposed by thermal expansion of the bearings.

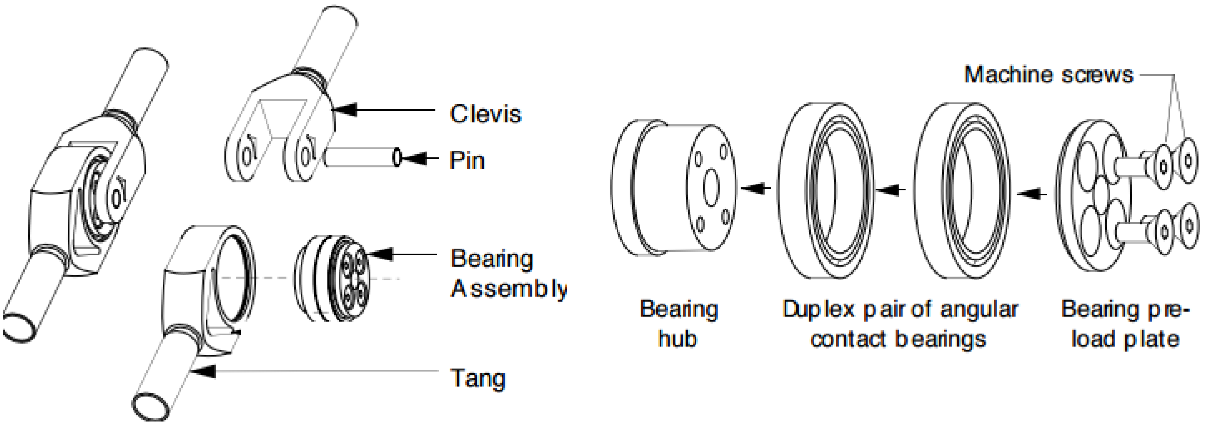

Figure 2.21: Exploded view of high precision ball bearing hinge applied in the design [31]

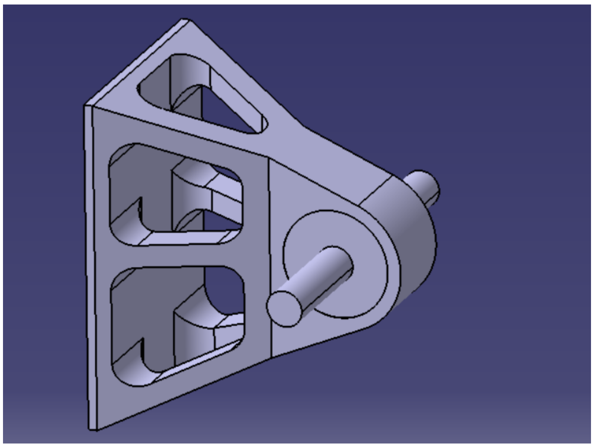

Figure 2.22: Support hinge connecting the satellite bus and the A-frame as designed by Van Putten [25]

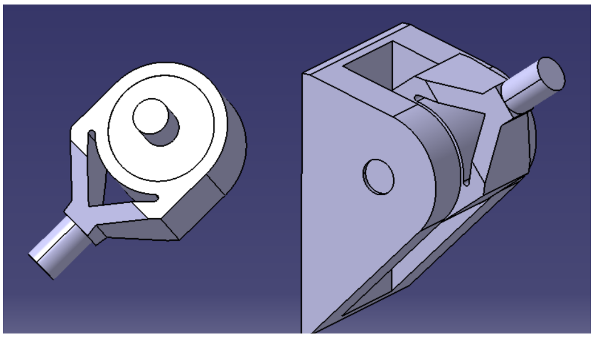

Figure 2.23: Hinge designs that connect the strut with the A-frame (left) and the satellite bus (right), respectively [25]

Finally the self-latching hinge in the middle of the strut was designed in more detail. It is based on a design described in [32] and the production drawings can be found in [30]. A sketch is provided in fig. 2.24. The descriptions of the mechanism in the papers of Lake, Peterson, and Warren is vague, no videos or step by step descriptions of the mechanism in working are available, the few black and white photographs of systems containing the supposed self-latching hinge are of too low quality to observe the latches, and the referencing in the literature to documents describing multiple hinges and latches, made it very difficult to verify the exact working of the mechanism. Van Putten assumed that the hinge can rotate with high precision until the point where the strut halves make a 180° angle and a spring driven device locks the rotational movement. Van Putten translated the sketch of fig. 2.24 into the low-detail design of fig. 2.25. He did not know the exact working of the spring mechanism yet, but recommended to continue the search for this information.

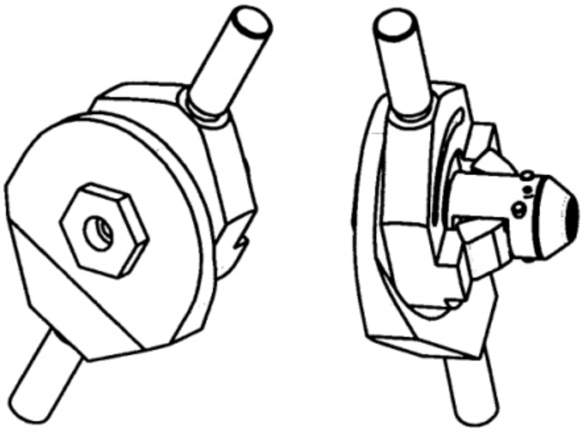

Figure 2.24: Sketch of a deployed self-latching hinge. The pin sticking out of the two latch halves is a spring driven locking mechanism [30]

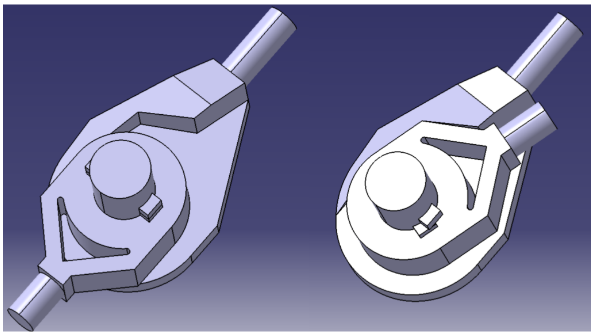

Figure 2.25: Self-latching hinge design made by Van Putten. Due to the lack of required knowledge, the spring driven locking mechanism is not designed in detail [30]

The literature study preceding this thesis describes that the assumptions about the working of the self-latching hinge are unfortunately found to be incorrect. The actual working of the device is explained in more detail in subsection 3.1.1. This working is so different that the concept is completely useless in the current design. Since the use of this device was already assumed for the mid hinged design during the concept trade-off, it has been decided that the concept selection for the deployment mechanism should be conducted all over again. This will have a big impact on the design and performance of the system. This makes the remainder of Van Putten's work irrelevant and it will therefore not be discussed in this thesis.

In the thesis of Van Putten it is not yet acknowledged that the deployment mechanism does not work as assumed. Therefore an analysis was performed to verify the compliance of the design with the requirements. A summary of the results is shown in tab. 2.5. Note that the requirements are provided according to the old ID tag system. The requirements [R-M1D-03] and [R-M1D-08] were soft requirements, meaning adjustment can be negotiated if they cannot be met. Therefore it was concluded that it was feasible to make a design that meets the requirements, as long as the recommendations of the last column of tab. 2.5 are incorporated in the design.

Since quite some design considerations are still relevant in the future design (regardless of the concept), the recommendations of Van Putten regarding these considerations are also relevant for the future design of the M1 subsystem. They are listed below:

- The soft criterion concerning the weight was not met in the current design and the biggest contributors to the weight are the whiffle plates and the support structure. It is recommended to look into optimizing them for weight. A suggestion is to do this by looked into the use of other materials, especially in the strut (if still applicable in the future concept). At the moment simple materials with conservative properties are used.
- A pressing recommendation is that a way needs to be found to lower the thermal fluctuations, for example by using a baffle. It is even claimed that the design is unfeasible if it is not controlled to a certain extend. However, even with a baffle the temperature will fluctuate, resulting in a slight rotation of

the mirror around the X-axis (if the new concept still involves a strut). The design should be made to counteract this thermal deformation. Without a baffle not only the precision of the mirror position is a concern. The local stresses in the mirror due to thermal fluctuations are currently too close to the yield stress.

- It is recommended to take a further look into the ability to withstand launch loads. Especially the effect of vibrations needs to be analyzed.

- The actuated flexure should be designed in more detail. This includes the motor, the speed reducer, the eccentric bearing, and the flexure itself. Little research is done into the availability of parts on the market, weight optimization, and the precision of the whole assembly. Especially backlash in the speed reducer can become a problem.

- According to Van Putten it is important to start building and testing some of the components in the near future. Especially tests that verify the precision requirements after deployment are important, because existing models cannot exactly predict the microdynamic effects that have a significant impact on the achieved precision at the scale used. Van Putten suggests the following component tests: a hinge hysteresis test, a self-latching hinge locking and accuracy test, and an actuated flexure behaviour test. Also the following system tests are suggested: a deployment accuracy repeatability null test, a shaker table test, a deployment accuracy repeatability test, and a thermal deformation test. Due to the need to redo the concept selection it is not expected testing will start anytime soon.

Table 2.5: Requirement Compliance Matrix based on the design of Van Putten. Note that the requirements are presented in the phrasing and with the ID tag that applies to Van Putten's thesis. The corresponding new ID tags and rephrased requirements can be found in appendix A [25]

Code	**Requirement**	**Compliant**	**Comments**
[R-M1D-01]	*The deployment mechanism and primary mirror calibration system shall be able to bring the mirror elements within the allocated position and orientation tolerances.*	Yes	Assuming 1 [μm] accurate assembly of crucial parts.
[R-M1D-02]	*There shall be a confidence level of >2 that the deployment accuracy tolerances of all 6 degrees of freedom of the mirror support structure are met.*	TBD	To be verified by testing.
[R-M1D-03]	*The mechanism shall position the mirror segments parallel to the telescope bus with a clearance of ≤10[cm] in stowed configuration.*	No	Current design 12 [cm]. Further optimization is possible.
[R-M1D-04]	*The stowed mechanism shall be able to withstand launch conditions.*	Yes	Larger safety margin would be preferable.
[R-M1D-05]	*The stowed mechanism shall conform with CSG safety regulations.*	Yes	No comment.
[R-M1D-06]	*Mirror position and orientation drifts due to thermal cycling shall be smaller than the allocated position and orientation tolerances for the mirror elements.*	Yes	If a baffle is included in the design. More detailed thermal modelling recommended.
[R-M1D-07]	*The deployed mechanism, when under influence of platform vibration, shall remain able to allow for the acquisition of diffraction limited images.*	Maybe	More advanced mission design and vibration analysis required.
[R-M1D-08]	*The mechanisms shall have a maximum total mass of 16[kg].*	No	Current design is 31.5[kg] including 20% margin.
[R-M1D-09]	*The mechanism shall be designed for a minimal operational lifetime of 5 years.*	Yes	Actuated flexure fatigue must be investigated.

2.4.3. UPCOMING RESEARCH TOPICS

Based on the theses of Van Putten and Lopes Barreto and the PHd work of Dolkens up to this point, the research topics and time line were evaluated. It became clear that some existing topics needed to be brought up to speed by assigning more people to the topic. Also the creation of new research topics was required. The topics are discussed below:

- **Optical design:** The FORTA software needs to be improved in several ways. Next to optimizing the existing algorithm further, a calibration algorithm needs to be developed that can calculate the required shape of the deformable mirror for better image quality. A comparable algorithm is required to steer the M1 segments. Furthermore, after optimizing the existing algorithm case studies need to be performed to find out whether the budgets of fig. 2.8 can be relaxed, since this will make the job of the other subsystem designers easier. Gijsbert van Marrewijk started the development of a phase-diversity algorithm that will be used for the calibration of the deformable mirror. He started around the time Van Putten and Lopes Barreto finished their work and graduated recently as well [33]. His work is currently continued by Dirk Risselada. Dolkens is tasked with the other aspects of the optical design.
- **M1 subsystem design:** From the work of Van Putten it became clear that the M1 subsystem consists of many aspects that cannot all be developed further by one person. It seemed that the deployment mechanism is currently the limiting factor for feasibility. Therefore it was decided to split the M1 subsystem design in two work packages. The first one was the design of the deployment mechanism, including the design of the support frame and the design of the interfaces between the satellite bus, support frame, and the TBD actuation device. The other work package is concerned with the design of the mirror and its calibration actuators. The boundary between the two design units is the interface between the support frame and the calibration actuators. This thesis is focused on the first work package and started around roughly two months before Van Putten and Lopes Barreto graduated. In the meantime Matys Voorn joined the team to continue the work described in this thesis. His main focus will be on designing and ordering test components and executing several types of tests. Roughly halfway the duration of this thesis project Sean Pepper joined the team to work on the mirror calibration design.
- **M2 subsystem design:** The work of Lopes Barreto needed continuation and roughly one month after his graduation Andre Krikken agreed on becoming his successor. It has been decided that one person suffices for this work package. Andre started slightly later than the start of this thesis and will finish his work in the upcoming weeks. No successor has been appointed, since the design is in a stage where parts can be ordered for testing. Matys Voorn will be responsible for the testing of this subsystem as well.
- **Baffle design:** Based on the theses of Van Putten and Lopes Barreto it was decided a baffle is required. Three months after they finished, Essi Korhonen joined the team to design this. Initially it was expected she could create thermal models and design a baffle that achieves the required performance according to this model. It was however found this is too much work for one student. Since the satellite deploys to dimensions much larger than what can be fitted in the stowed volume, a baffle is required that can deploy as well. The deployment ratio is much larger than what is commonly required and therefore the mechanical design of the baffle is a task for one MSc-thesis alone. Therefore it was decided to treat thermal modelling as a separate research topic.
- **Thermal modelling:** 9 months ago, soon after Korhonen started on the baffle, Victor Villalba Corbacho joined the team as a PHd-student. It was decided that he would start with the creation of a thermal model for the satellite to later grow into a role where he oversees the work of the MSc-students focused on the thermo-mechanical design of the several subsystems. 3 months ago Tim van Wees joined the team to work on the development of the thermal model. He just finished his literature study and is currently starting his modelling work. Since thermal modelling is fairly complex and because it turned out active thermal control is needed to meet the M1 thermal drift budgets (see section 4.3), an extra team member was added. Stefan Leegwater joined the team a couple of weeks ago.

2.5. THESIS NEED AND GOALS

As discussed in previous section, the work of Van Putten and Lopes Barreto left the project at that time with certain needs. Without going into too much technical detail these needs can be stated in terms of required human resources:

- **PN-1** The project has a need for additional manpower to design a deformable mirror control algorithm
- **PN-2** The project has a need for additional manpower to continue the work on the M1 subsystem design
- **PN-3** The project has a need for additional manpower to continue the work on the M1 subsystem design
- **PN-4** The project has a need for additional manpower to work on the design of a baffle

At the moment the author wanted to start his literature study, fulfilling PN-2 and PN-3 had the highest priority in order to delay the project as little as possible. The author choose to continue the work on the M1 subsystem, because it was expected that some optimization was need for the deployment mechanism and support frame design, while the main focus would be on the detailed design of the calibration actuation. This matched the skill set of the author, since he co-founded a company that invented a high precision drive during his MSc. A drive, also called speed reducer or gear box (latter one does not apply to the invention, because the design is gearless), in combination with a motor is the most common type of actuator used in moving mechanical applications. Possibly the so called 'Archimedes Drive' would be a suitable device to implement in the design.

During the literature study the the design flaw of Van Putten was discovered and it was realized that it was necessary to start all over with the concept selection of the deployment mechanism, delaying the development of the M1 subsystem substantially. To get back up to speed it was decided that the project needed one person dedicated to the design of only the deployment mechanism rather than the complete M1 subsystem. This led to PN-5, which now had the highest priority:

- **PN-5** The project has a need for one MSc-student, dedicated only to the design of the deployment mechanism of the M1 subsystem in order to synchronize its development with the development of the other subsystems

This thesis aims to fulfill the need of PN-5. The need statement does however not provide clear boundaries indicating how far the development should go for the acceptance of a MSc-thesis. Knowing that in space projects usually many years or even decades are needed to design, build, and test a space system, it is unrealistic to expect a completed M1 subsystem design. Therefore the author decided to think about a research framework that defines the research activities up to the point where a first breadboard design can be tested. With these test results the predicted performance can be verified and valuable lessons will be learned that can be implemented in the final design. The design of the breadboard prototype and the design of the test setup are research activities after which a natural development stop is formed in the project, because after ordering breadboard components, ordering test equipment, and booking test facilities there will be a lead time until the project can continue with the actual testing. Some major design steps to get to this point are defined and led to the research objective and corresponding research framework (fig. 2.26) below:

Research objective To provide the information required to build and test a breadboard version of a primary mirror deployment mechanism for a deployable space telescope, by completing the preliminary design of the full scale mechanism, identifying the high risks components, making a breadboard design including these components, and defining the required tests to assess the behaviour resulting from the high risk components.

Since a lot of knowledge is already gathered with the Thesis of Van Putten, it seems feasible to finalize the improved design and model the expected behaviour in the first half of the thesis. The remainder of the work consists of more, but less time consuming research activities and will be completed in the second half of the thesis. The research objective can be split in the following central research questions:

Central research question 1 What improvements of the primary mirror deployment mechanism are needed to meet the requirements?

Central research question 2 What should a breadboard design, designed with the purpose to verify the performance of critical components, look like?

Central research question 3 What test methodology is required to verify the compliance of the breadboard design with the breadboard requirements?

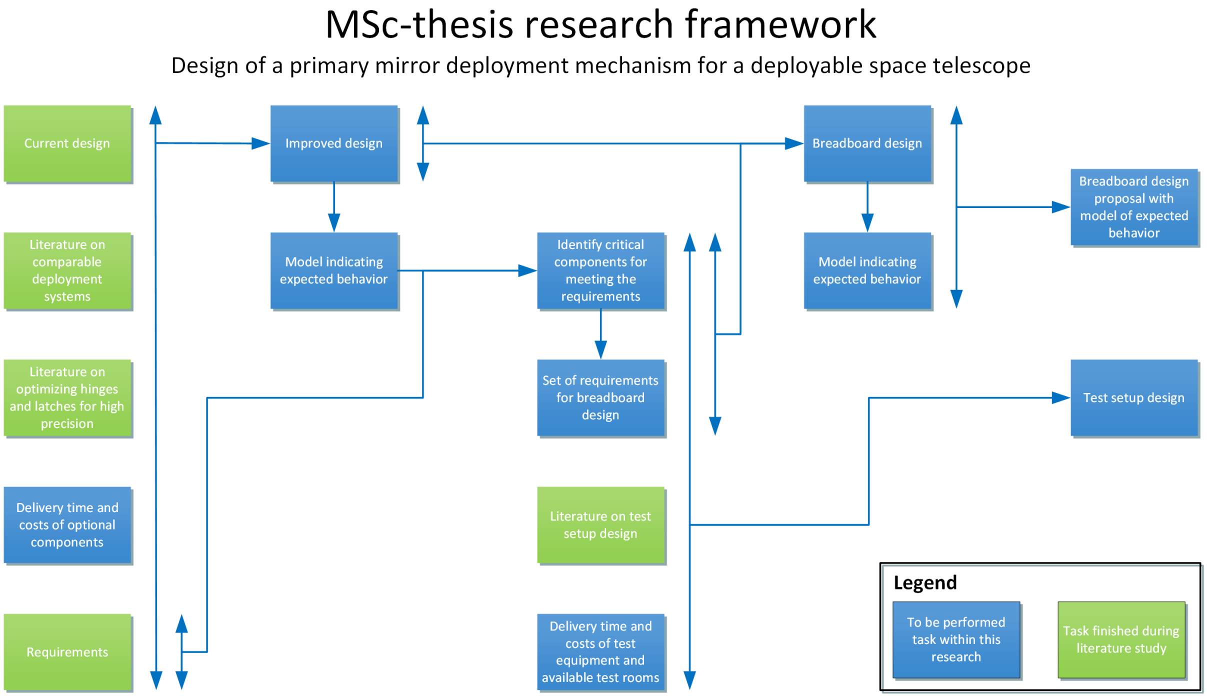

Figure 2.26: Research framework of this thesis. The logical order of the research activities is structured from left to right. Vertical lines indicate that the combination of this information is required as input for the next research activity

3

THEORY FROM LITERATURE

This chapter will discuss the relevant literature for this thesis. This means it will be discussed what satellites of comparable projects look like to get familiar with the state of the art, but also that the working of potentially useful components and theories applied in the design practises are discussed. First the literature on comparable space systems is discussed in section 3.1. Second, the working of and theory behind the hinges and latches assessed in a trade-off later in this work is provided in section 3.2. Finally literature describing preferred design practises for the development of high precision mechanisms, including kinematic interface design and athermalization, is presented in section 3.3.

3.1. LITERATURE ON COMPARABLE TECHNOLOGIES

This section will describe a couple of telescope concepts that contain a deployable primary mirror, a deployable secondary mirror, or both. Subsection 3.1.1 will dive into the deployment mechanisms developed as of 1994 for what is now known as the JWST, but was still called the New Generation Space Telescope (NGST) at the start. Afterwards the Deployable Petal Telescope will be discussed in subsection 3.1.2. In 2007 European Space Agency (ESA) requested proposals for 'Advanced LIDAR Concepts' and a group of six companies responded to this request with a concept discussed in subsection 3.1.3. Finally the Dobson Space Telescope is treated in subsection 3.1.4.

3.1.1. DEPLOYABLE MIRROR DESIGNS FOR THE NGST/JWST

Already in 1989, a year before the Hubble Space Telescope was launched, the Space Telescope Science Institute (STScI) organized the first workshop that resulted in a mission concept for the next major space telescope after the Hubble Space Telescope (HST) [34]. Some years of assessing science proposals and investigating what is feasibility from a technology perspective went by up to 1993. At this moment the STScI appointed a committee to study 21-century space astronomy missions and generate recommendation reports on the required capabilities of the NGST. In 2002 the project was renamed to the JWST and after some delays the launch is currently scheduled to take place in 2020[19].

Soon after the NGST committee was formed, companies and research institutes started the development of the required technology. As of 1994 the people who mainly worked on the development of high precision deployment mechanisms were Mark Lake, an employee of National Aeronautics and Space Administration (NASA) Langley Research Center, and Lee Peterson and Peter A. Warren, both researchers of the University of Colorado [35]. These developments started early, because NASA knew the primary mirror would be so big that making precisely foldable mirror segments was inevitable. During the period from the mid 90s to the early zeros the researchers developed two conceptually different deployment mechanisms that were based on classical hinge and latch designs, optimized for precision. They developed a precision hinge joint that is used in both designs, and two precision latches, a different one for each design. It seems information on the latches is purposely kept vague for a patent filing. A patent number has not been found, but a statement confirming the lack of detail because of a patent filing can be found in [32]. Next to this paper, also the papers in [27, 30] provide 'invention disclosure case numbers' used for submission to the internal patent counsel of NASA. In the big amount of papers written on the topic, a lot of cross-referencing takes place. The combination of the cross-referencing and vagueness caused the confusion that led to the false assumptions about the working of the self-latching hinge in the thesis of Van Putten (see subsection 2.4.2) [25]. The details on the two concepts, followed by the final concept of the JWST, are discussed separately below.

ESDM CONCEPT

The first concept made was a deployable truss structure that was called the Engineering Science Development Model (ESDM). Among other papers the development of the complete system and some of the components is described in [27–29, 36]. Due to the camera quality at that time, no clear figures are available, but a photo of the fully deployed configuration and a sketch of the partly deployed configuration, are presented in figs. 3.1 and 3.2, respectively. When stowed, the tip is folded upwards in the z-direction indicated on the photo. The aim of the research was to make the deployment mechanism very precise and to this end a new high precision hinge was developed. The hinge is described in quite some detail in [27–29]. In a later stage the production drawings were published in [30]. Information on the latch and the actual working of the deployment mechanism is scarce. Only [36] provides some level of detail. Here a sketch of the latch, depicted in fig. 3.3, can be found from which it becomes clear that the deployment is caused by one half of the latch, sliding towards the other latch half via a rail.

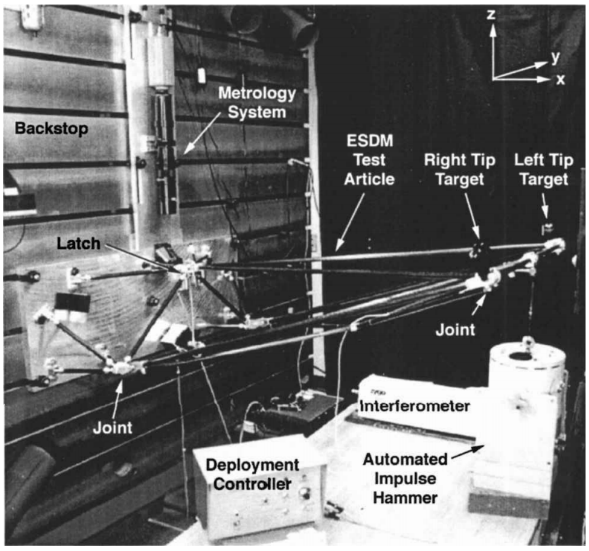

Figure 3.1: Photo of the fully deployed ESDM design in a test set-up for absolute static shape testing [36]

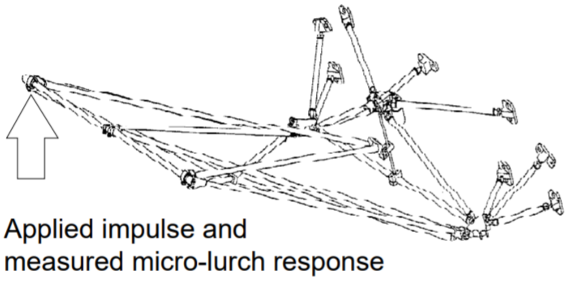

Figure 3.2: Sketch of the partly deployed ESDM design indicating where impulses where applied to measure the micro-lurch response [27]

NASA LIDAR PROTOTYPE CONCEPT

The second concept, often referred to as the NASA lidar prototype (the LIght Detection And Ranging (lidar) project was decided to be an intermediate step towards developing precision mechanisms for the NGST [35]), deploys in a different fashion and is among other papers described in [32, 37]. The mirror is mounted on an A-frame of which the tip is connected to a strut. The other side of this strut is connected near the base of the A-frame in stowed configuration. During deployment this strut connection slides down via a rail until it falls into a latch. Photos of the whole structure and the latch are depicted in figs. 3.4 and 3.5, respectively. Although the same hinge is used that was designed for the ESDM, a different latch has been developed. Both papers describe a self-latching hinge, as shown in figs. 2.24 and 3.7, with a reference to the production drawings [30]. However, when looking to fig. 3.5, one can see that only the spring driven locking mechanism of the self-latching hinge is used, which is presented in an exploded view in fig. 3.8. One of the questions that follow from watching the production drawings is how the self latching hinge works. Rotation of the hinge will not cause an automated latch without a force pressing the latch halves together. In the NASA lidar prototype design the strut end is also pushed until it locks, in what would be the direction of the rotational axis for the self-latching hinge. This is not explained in any paper. Also no application can be found where this self-latching hinge is used. Knowing this, a second question is what the purpose of this design is, followed by why it is described in the papers. An

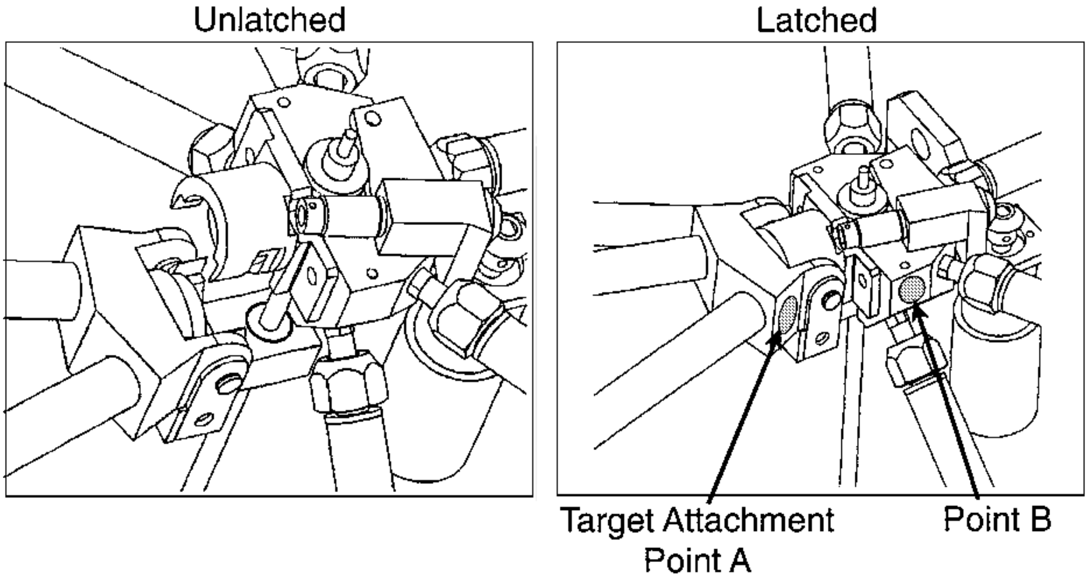

Figure 3.3: Sketches of the ESDM latch in unlatched and latched position [36]

answer has not yet been found, but the author of this thesis hypothesizes that it is designed only to compare the post-deployment microdynamic response of the self-latching hinge with the one of a normal precision hinge. Reasons for this hypothesis are listed below. It is concluded that the standalone latching component may be suitable for the DST project and that the self-latching hinge is not.

- The papers only discuss the properties in the latched (post-deployment) configuration
- In [32] experiments are described that compare the differences in hysteresis between the normal and self-latching hinge
- Not a single photo or sketch can be found where the self latching hinge is not in a latched 180° position
- Nowhere a description can be found of how the hinge latches after rotation

The M1 subsystem designed by Van Putten consists of high precision hinges and is mainly based on the design practises described about the development of the ESDM and NASA lidar prototype concepts. Descriptions of the conducted research and the most important conclusions on both designs up to 1998, are summarized in [35]. A year later, a set of guidelines was published that elaborates in detail on the lessons learned [31]. Furthermore it provides recommendations on best design practices to reduce the microdynamic response. This information will be treated in section 3.3. Around the start of this century the researchers continued their work on the NASA lidar prototype, by replacing the sliding strut with smart material hinges. A paper of 2002 describes tests performed on tape spring hinges in [38]. A couple of other papers describe how the use of Elastic Memory Composite (EMC) hinges was investigated in [39–41] between 2004 and 2007. The theory behind those hinges will be discussed in section 3.3 as well.

FINAL JWST CONCEPT

The final design of the M1 deployment mechanism of the JWST is completely different from the previous concepts. As shown in fig. 3.9 the M1 consists of a core section containing 18 mirror segments and two wings containing 9 mirror segments each. Rather then rotating away from the pointing direction of the optical axis (as is the case for the previously discussed concepts), these wings fold towards the pointing direction of the optical axis. This corresponds to the deployment direction of the M1 segments of the current design in this thesis project. According to [42], the guidelines [31] written after developing the previously described concepts were carefully followed to end up with the current design. An important note from these guidelines is that a kinematic interface is always preferred over other mechanisms, such as precision hinges, to transmit operational

Figure 3.4: Photo of the deployment mechanism of the lidar prototype design [37]

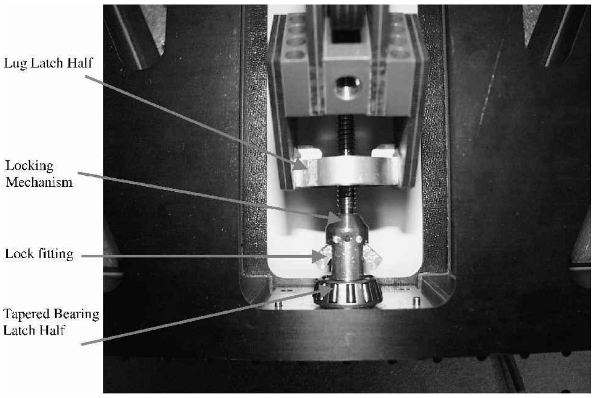

Figure 3.5: Close-up photo of the latch used in the lidar prototype design [37]

loads in high precision designs. This recommendation led to a design where the wings are deployed into a kinematic interface by a motorized and a passive 'sloppy hinge' that drop out of the load path after deployment. The preload is provided by a specially designed latch. Details about the exact working of the kinematic interface are provided in section 3.3.

Where the previously described concepts focused on the deployment mechanisms of primary mirror segments, the final JWST design also has a deployable secondary mirror. In [42] this deployment mechanism is referred to as the Secondary Mirror Support Structure (SMSS). The deployment sequence shown in fig. 3.10 reveals that this design makes use of five hinges. Three at the feet of the struts, one in the middle of the 'single strut', and one at the tip of the single strut. All of them are latched. For the mid hinge this is done with a highly complex preloaded device, which was required because it was impractical to follow the best practises of the guidelines. The rest of the hinges is latched by heat fitting the lug and clevis, after the desired position is reached.

Some aspects of the final deployment mechanisms of the JWST are discussed in more detail in section 3.3, but not every mechanism is taken along in this discussion. One should keep in mind that the JWST in designed for a completely different mission. With an aperture diameter of 7 m this primary mirror is almost 5 times as big as the one of the DST. Besides, there was a huge financial budget and a team of top notch engineers that designed this satellite over the course of almost three decades. None of these resources is available for this project and therefore it is assumed unfeasible to include the highly complex mechanisms that are especially present in the SMSS within the DST project.

3.1.2. Deployable Petal Telescope

The Deployable Petal Telescope (DPT) is a telescope cubesat with a 2-3 U stowed size and a ground resolution of 1.5 m, currently under development by the Space Dynamics Laboratory of the Utah State University [43]. As shown in fig. 3.11, this satellite consists of four deployable primary mirror segments and a secondary mirror that deploys away from the primary mirror, like the current design of the DST. A video of the test version

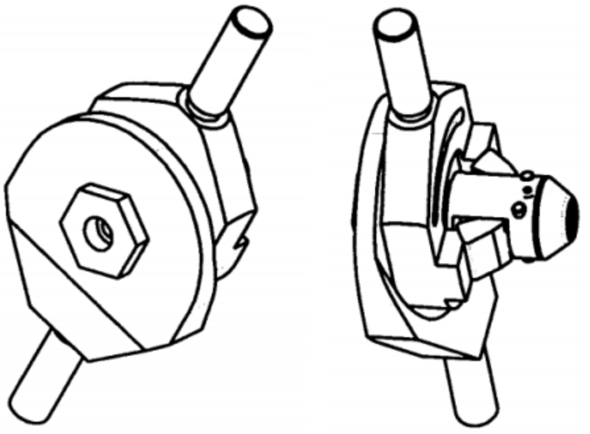

Figure 3.6: Sketch of a deployed self-latching hinge (copy of fig. 2.24) [30]

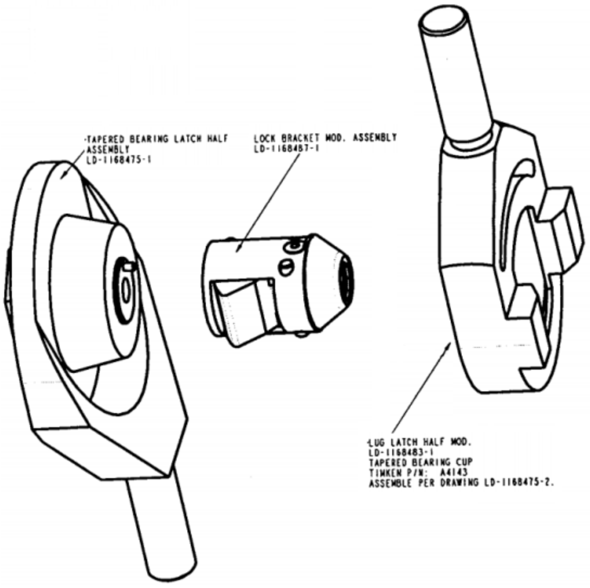

Figure 3.7: Exploded view of the self latching hinge with the three main components [30]

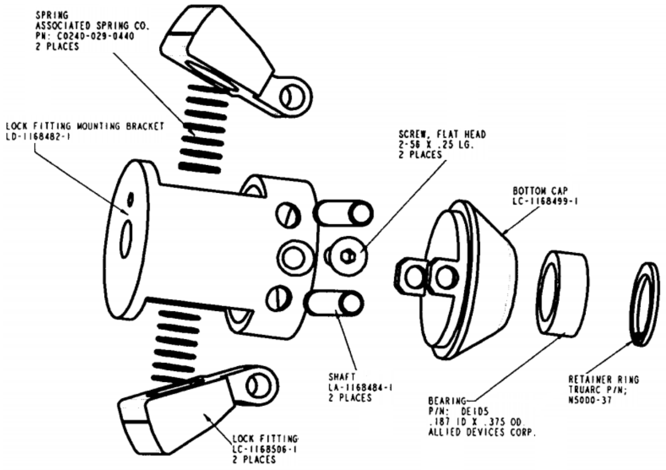

Figure 3.8: Exploded view of the locking mechanism of the self latching hinge [30]

[44] also shows some major differences. In this design the primary mirror is folded upwards when stowed, so deployment is generated by pulling the segments downward, rather than pushing the segments upward as in the DST design. Another difference is that the secondary mirror of the DPT design is carried by one boom that slides over a rail in one of the corners of the satellite.

There is not much literature available on the details of the design. A presentation from 2014 [43] indicates that back then, they were at Technology Readiness Level (TRL) 4, and that they were expecting to move into TRL 5 soon. Next to a news article from 2015 [45] that does not provide a single technical detail, the only further information can be found in a patent that is by now internationally granted [46]. This patent protects only the deployment mechanism of the primary mirror and reveals useful information about its working. On the left side of fig. 3.12 one can see the backside of the mirror with the eight holes in it. In between these holes is a strut that hinges at the outer part of the mirror. The strut slides down along the bus by pulling a line. The sliding stops when the strut couples with a hard stop. Fig. 3.13 shows the satellite when partly deployed for a better understanding. Here one can see a conic hole the strut slides towards to. Fig. 3.14 shows the sliding end of the strut, with in the middle a sphere that will fall into the conic hole, and two pins on the outside that will surround the block with the conic hole.

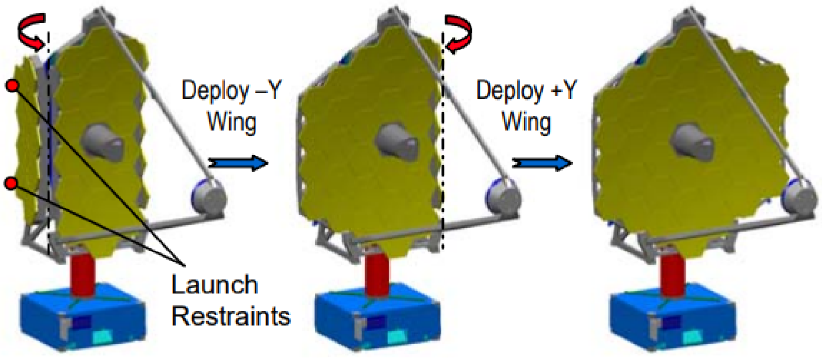

Figure 3.9: Deployment sequence of the M1 wings of the JWST [42]

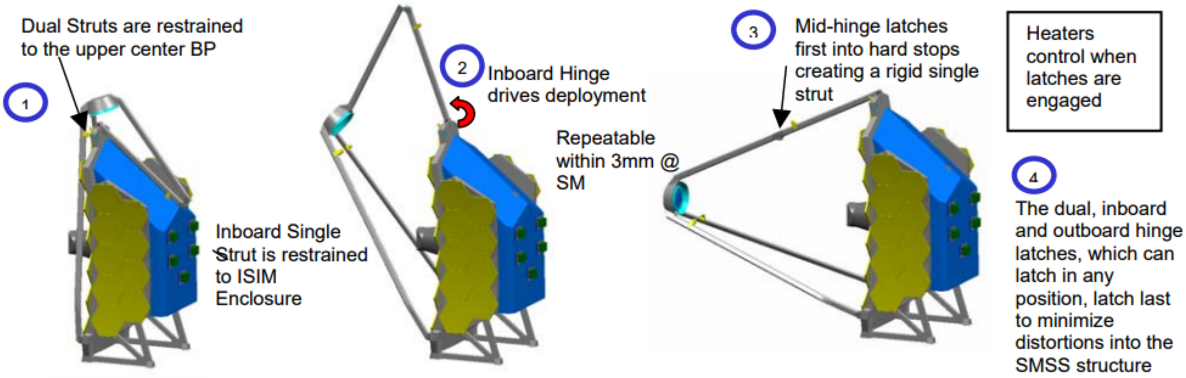

Figure 3.10: Deployment sequence of the SMSS of the JWST. BP: undefined - ISIM: Integrated Science Instrument Module - SM: Secondary Mirror - SMSS: Secondary Mirror Support Structure - Dual struts: the struts without a mid hinge - Single strut: strut with mid hinge [42]

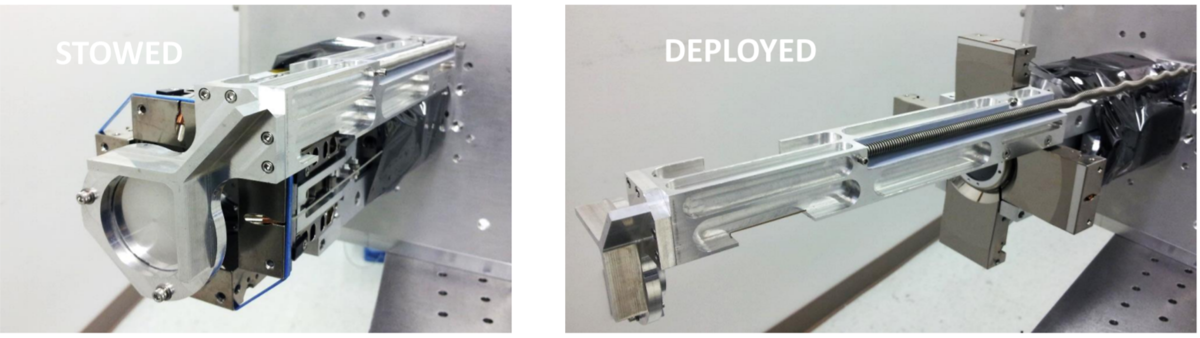

Figure 3.11: Photos of a test version of the DPT in stowed and deployed configuration [43]

Since the current deployment mechanism needs to be redesigned, the DPT deployment mechanism design might be a good alternative. Although the DPT does not achieve the required resolution, its design is similar to that of the NASA lidar prototype concept. Combining elements of both concepts may lead to satisfying design. In that case it is however important to remember that either, a way should be found to work around the patent, or that license fees should be discussed with the patent holder.

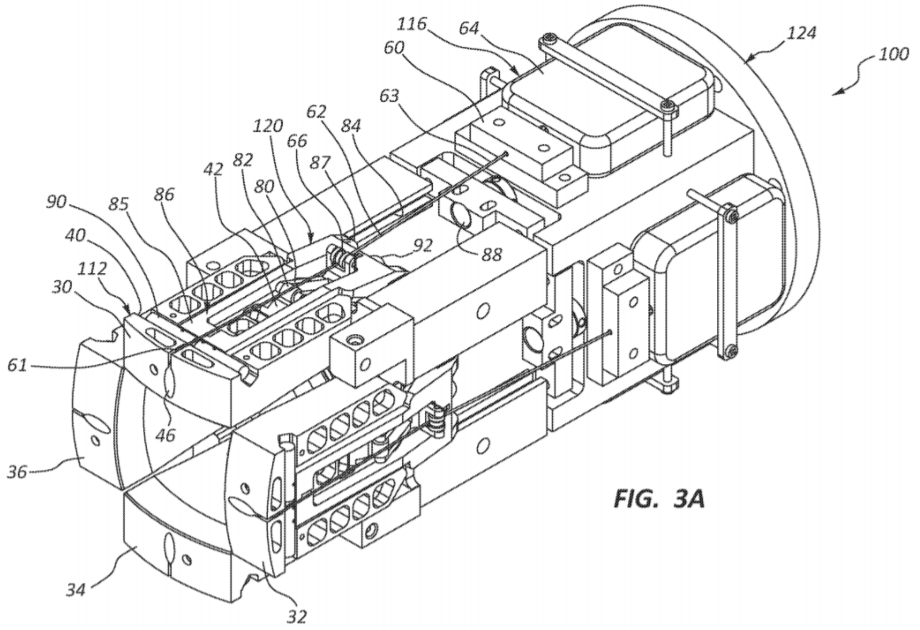

FIG. 3A

Figure 3.12: Patent drawing showing the primary mirror deployment system of the DPT when stowed [46]

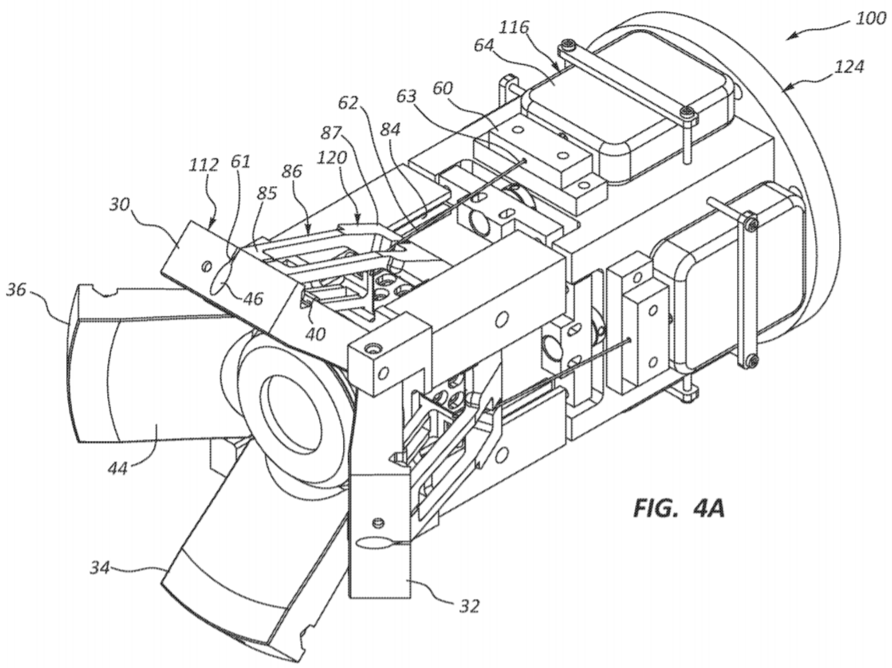

FIG. 4A

Figure 3.13: Patent drawing showing the primary mirror deployment system of the DPT when partly deployed [46]

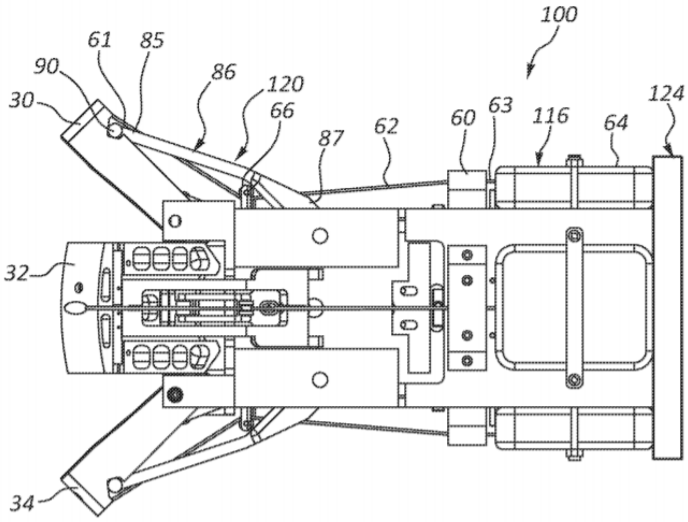

Figure 3.14: Patent drawing showing the primary mirror deployment system of the DPT when partly deployed in side view [46]

3.1.3. ADVANCED LIDAR CONCEPT PROPOSAL

An interesting study has been conducted by a group of scientists of multiple European space companies and institutes as a response to ESA's call for proposals on 'Advanced LIDAR Concepts'. Under ESA contract AO/1-4629/NL/CP a concept was developed that uses some interesting technology that might be useful for the DST [47]. There are no plans to continue with this proposal in the future. The secondary mirror is placed on a fixed structure and does not deploy, but the primary mirror unfolds in the same direction as the DPT. This is shown in fig. 3.15. An interesting feature is that EMC actuators are used for deployment. These actuators, as shown in fig. 3.16, can be bend in a random angle above a certain temperature to stay frozen in this shape when the temperature is lowered again. If no load is applied when heated again, they fold back to their original shape over the course of minutes. In this way they can be seen as self-latching hinges. In general the repeatability of EMC hinges is too low for applying them in the DST deployment mechanisms. Recent developments however showed major improvement. This is discussed in section 3.2.

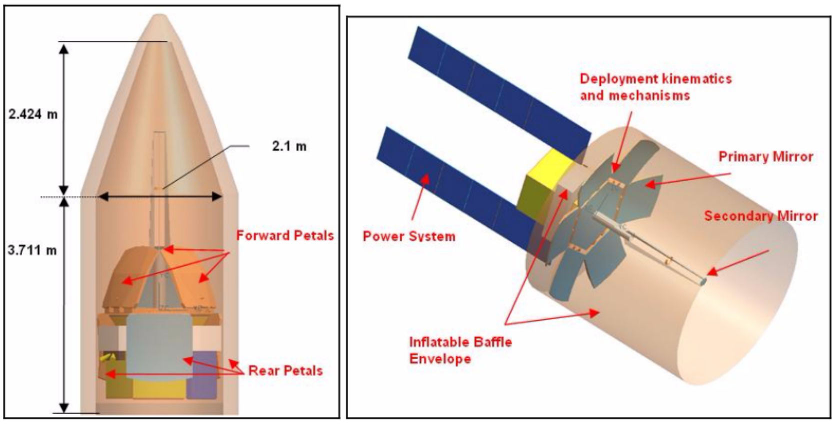

Figure 3.15: Concept for a proposed lidar satellite for an ESA mission [47]

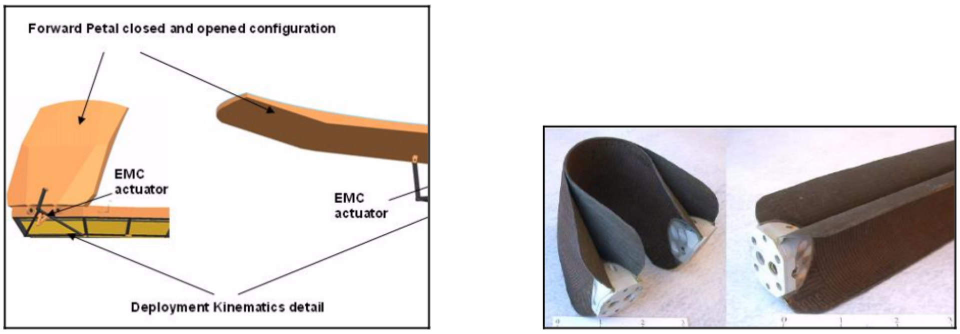

Figure 3.16: Left: usage of EMC actuator in the concept - Right: photo of an EMC actuator in stowed and deployed configuration [47]

3.1.4. DOBSON SPACE TELESCOPE

The Dobson Space Telescope, or LEOS satellite as it is called nowadays, was a project of the Technical University of Berlin. This might be the satellite that is most comparable with the Deployable Space Telescope. To avoid confusion with the abbreviations, which are the same for both projects, Dobson Space Telescope will always be written out completely in this report, while the abbreviation DST always refers to the Deployable Space Telescope. The Dobson Space Telescope project started in 2002 with the goal to develop a deployable satellite telescope with a ground resolution of 1 m and a weight of 100 kg [48]. Up to 2007 several papers have been published [48–51], but none of them reveal even the slightest technical detail on the deployment mechanism. Fig. 3.17 shows the conceptual idea of the deployment, where first the solar panels deploy, followed by the deployment of the secondary mirror together with a baffle. This however does not reveal anything about the mechanism behind it.

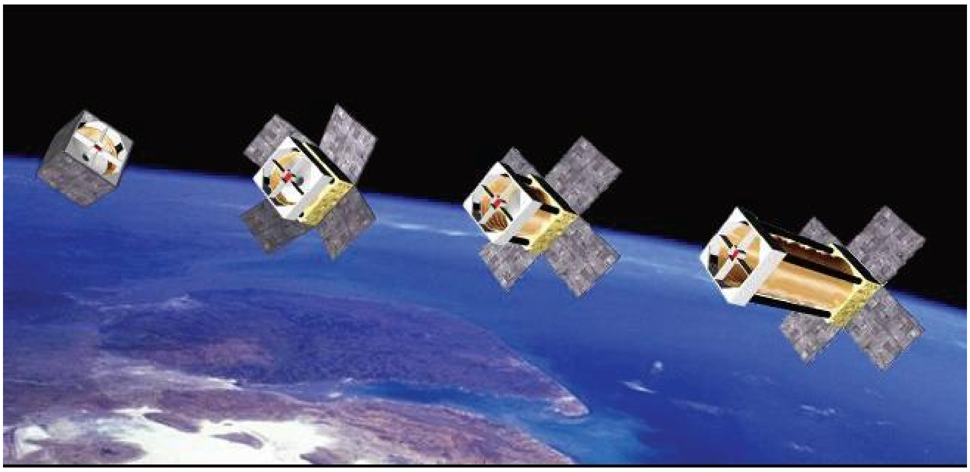

Figure 3.17: Artist impression of the Dobson Space Telescope during different phases of deployment [52]

Although the project looked promising, even reaching a phase with zero gravity tests via parabolic flights with results that turned out better than expected [48], no papers can be found on the Dobson Space Telescope after 2007. Even their website [53], which was still referred to as a source in [52], now redirects to the website [54] of a company called Berlin Space Technologies (BST). However, searching the website for their products, one can find the LEOS-100 satellite. It looks very different from the artist impression in fig. 3.17 and does not look like it is deployable. On the other hand the specifications are comparable to what was aimed for with the Dobson Space Telescope, with a mass of 90 kg and a ground resolution of 1.5 m. Contact with an employee of BST, learned that the company is a spin-off of the university project, and that the LEOS-100 is indeed the further developed version of the Boston Space Telescope. Also, he provided a link to the German patent [55] (no English version available) of the deployment mechanism, which was granted in 2007. The papers did not describe any detail, because the patent was not yet in the public domain when they were published, so it was best to keep the details internal. The patent however never went into the PCT-phase, meaning that it only holds in Germany and that one can reproduce the technology, as long as one does not sell or produce it in Germany. Although there are no resources available within the DST team to have the patent translated, the figures of the deployment mechanism (figs. 3.18 and 3.19) explain the basic principle very clear. When the struts hinge together, the cones on both ends stack on top of each other. They are pulled together by a rope that moves through the struts and generates the required preload. This principle might be of use for either the primary mirror or secondary mirror deployment mechanisms of the DST.

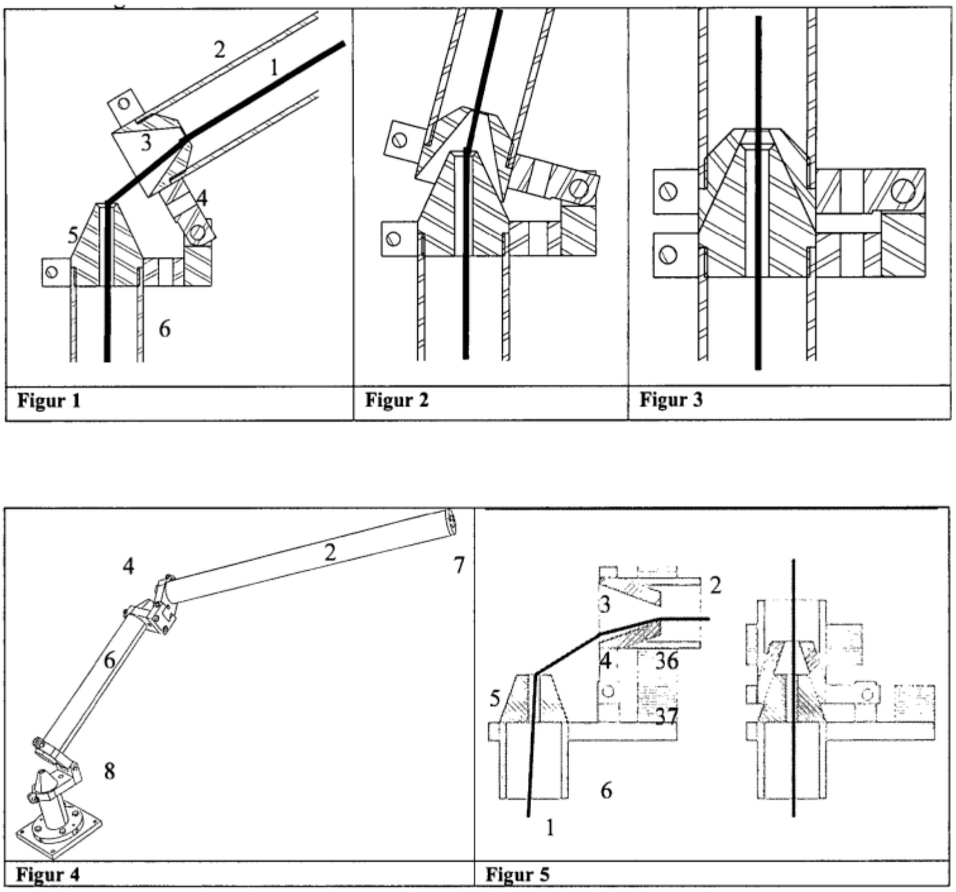

Figure 3.18: Patent drawings of hinges of the deployment mechanism of Dobson Space Telescope [55]

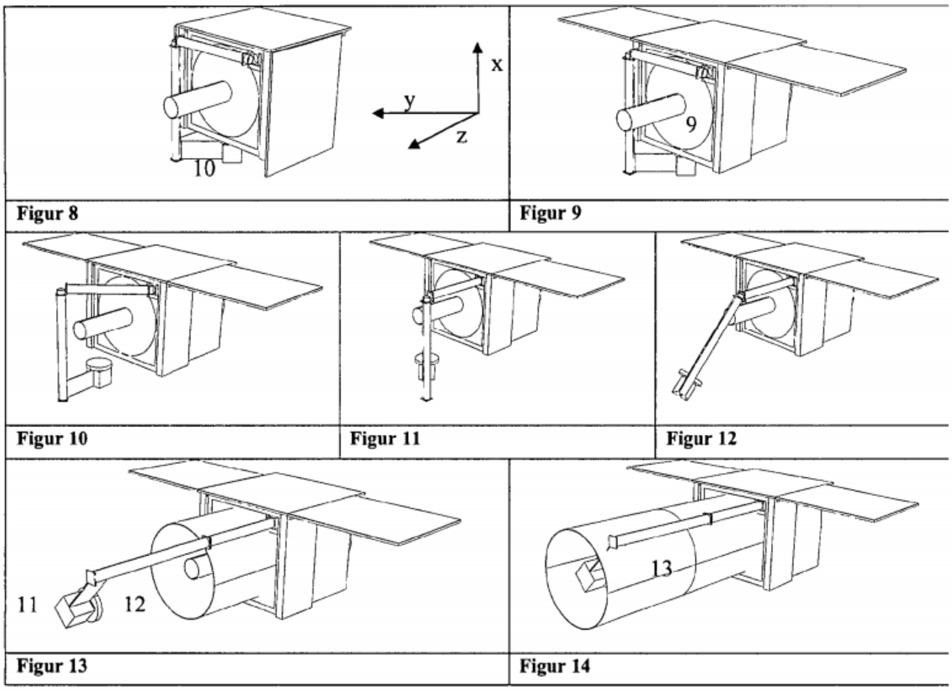

Figure 3.19: Patent drawings of deployment sequence of Dobson Space Telescope [55]

3.2. THEORY ON HINGES AND LATCHES

This section will present several types of hinges and latches that need further explanation. Where it is obvious how ball bearing hinges (fig. 2.21) and cone-in-cone latches (fig. 3.18) work, this does not hold for tape spring hinges, EMC hinges, and the JWST primary mirror wing latch. They are discussed in subsections 3.2.1, 3.2.2, and 3.2.3, respectively. Next to the theory on their working, the performance of the hinges supplied by some manufacturers are discussed as well. One thing that is not obvious by the looks of the ball bearing hinge and cone-in-cone latch are the reasons why they can achieve high precision. This is explained in section 3.3.

3.2.1. TAPE SPRING HINGES

Tape springs are already in use for a long while, for example in measuring tapes. When bending a measuring tape, one will see that it tends to go back to the original shape, in which it becomes much stiffer again. This principle is used to make tape spring hinges. These mostly metal hinges consist of thin shells and usually have a constant curvature. In recent years however, the interest of researchers moves more and more to tape spring hinges made of reinforced polymer composites. Their low Coefficient of Thermal Expansion (CTE) and high specific stiffness makes them more suitable for precision applications and adds to the other benefits that already hold for the metal versions [56]. These are the ability to self-deploy, low cost, low complexity, robustness, reasonable stiffness after deployment, and highly efficient packaging (deployed size vs stowed size) [57]. Tape spring hinges have flown in several space systems such as the Myriade satellites (metal) [58] and the MARSIS satellite (composite) [59], and will also be used in future missions such as Solar Orbiter [60] and NorSat-1 [61]. Mostly they are applied as deployable booms in non-precision applications such as solar panel and antenna deployment mechanisms.

A metal tape spring shows non-linear behaviour during deployment, as shown in fig. 3.20, but a composite tape spring also suffers from viscoelastic effects, especially due to creep and temperature variations, which cannot be neglected when predicting the repeatability [62, 63]. The nonlinear deployment is already extensively researched and can be modelled relatively accurate, but the viscoelastic effects are much harder to predict. As a result, hinges are often extensively tested before being send to space. This holds especially since the MARSIS, a satellite observing Mars, initially failed to deploy due to creep in 2005. Because of the long stowage time with changing temperatures, the hinges became unable to generate the required deployment moment. After enduring creep and a temperature drop, a small slope in line C-D of fig. 3.20 can result. As shown in fig. 3.21, this even resulted in a negative bending moment at small angles for the MARSIS satellite. With a manoeuvre that pointed the hinge in direct sun light the mission was saved [59, 64].

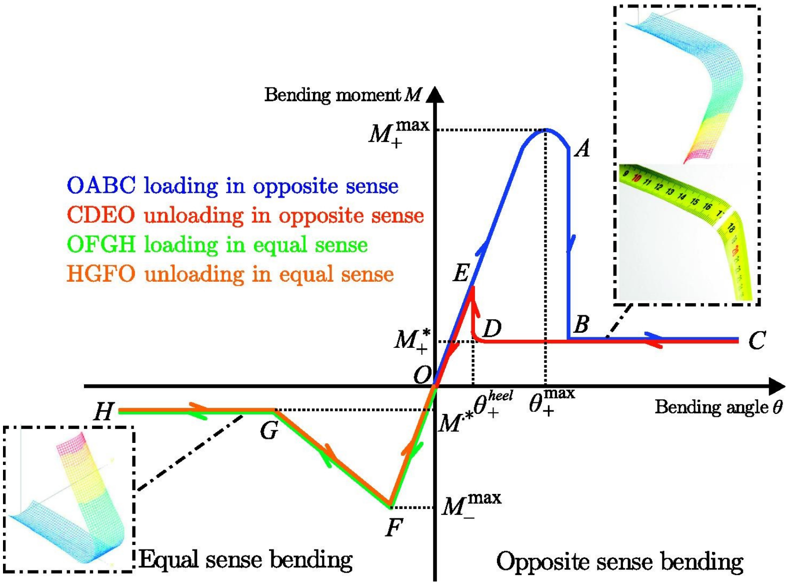

Figure 3.20: Typical theoretical curve of bending moment versus the bending angle of a tape spring hinge. Viscoelastic effects that occur in composite versions are not included [65]

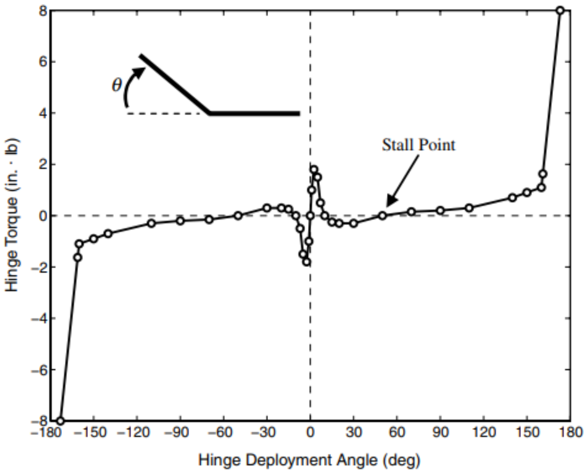

Figure 3.21: Bending moment versus bending angle curve of the tape spring hinges used in the MARSIS satellite at a temperature of -70 $^{\circ}C$. Note the negative moment at angles smaller than 50 ° that can lead to stall conditions for deployment [59]

The need to do extensive tests, together with the shock generated during the snap at full deployment, are the biggest disadvantages of tape springs. Unfortunately literature about creep and temperature effects in composite tape springs, where the effect of different materials or layups is compared, is scarce. Mostly test result are provided of a single hinge, for example in [57]. If this hinge would replace the self-latching hinge in the deployment mechanism design of Van Putten, it would result in a precision of 10.5 nm at the end of the strut that is connected to the A-frame. A recent paper [66] however does a good job at identifying creep for different composite tape springs, designed for a deployable telescope cubesat called DISCIT. The researchers used 12 different specimen with different diameter curvatures, materials, ply angles, and amount of plies in a layup. Using the data of their most precise specimen (number 6-6), again an estimate is made of the repeatability when replacing the self-latching hinge in the DST M1 deployment mechanism. This led to a repeatability of 185 nm with a standard deviation (1σ) of 41 nm at the end of the strut that connects with the A-frame. This makes this composite tape spring hinge worth considering for the DST project. It should however be mentioned that the specimen were bend to only a maximum of 135°, and that this tests took place in a controlled environment with minimal variations in temperature and humidity. The bending angle has an influence on the amount of creep. Temperature and humidity variations during stowage and deployment of the hinge also influence the repeatability. Finally it should also be investigated whether the shock during snap-through will cause any problems. Dewalque et al. [65] recently described how to test and model the dynamic evolution of the motion during, and shortly after deployment. This is useful to determine the vibrations due to the shock. On the other hand the specimen investigated was made out of metal, so it is unknown to which extend the dynamic evolution of composite tape springs will compare.

For some precision applications, hinges have been developed that use multiple tape springs that bend in different directions, such as the Maeva hinge of fig. 3.22 [58], and two other kinds of hinges for ULMAAS [67, 68], depicted in figs. 3.23 and 3.24. The Maeva hinge is made out of metal and has the advantage that, compared to a single tape spring, it has more driving torque and stability in twist during deployment. Furthermore it has a higher overall stability after deployment, due to a high end stiffness. A disadvantage of the Maeva hinge is that the deployment moment becomes very low when large bending angles are required. A comparable concept (fig. 3.23) was developed for the ULMAAS project. This hinge is made out of four short and four long composite tape springs. In this configuration the end stiffness and deployment moment under large angles are much higher. It is not described why the design team decided to switch to another design, somewhere between 2008 and 2011, but eventually they came up with the design of fig. 3.24. It is called the Ultra-light Deployment Mechanism (UDM), and looks like an adjusted version of the Maeva hinge. Although it is not explained how the directions of positioning accuracy are defined, the results of the verification tests, shown in tabs. 3.1 and 3.2, look promising, especially when looking to the rotational precision. A precision of 0.01° would translate to a precision of 3.31 nm in the current DST design. Despite the high precision, the use of multiple tape spring hinges seems to result in a mechanism that is too big and heavy to replace the self-locking hinge in the current design.

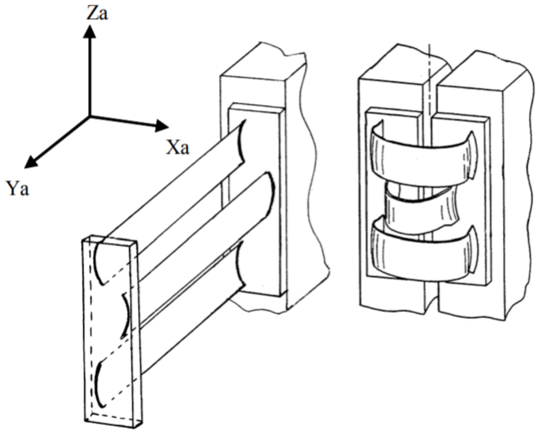

Figure 3.22: Sketch of the Maeva hinge, consisting of three metal tape springs [58]

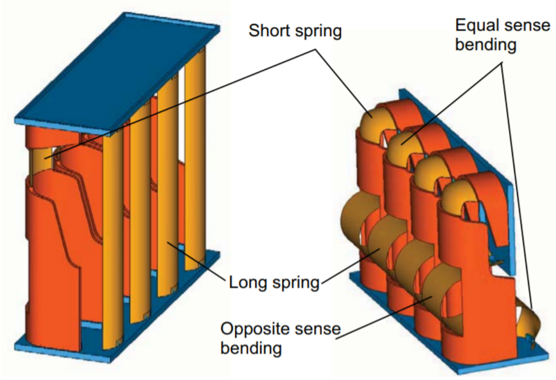

Figure 3.23: Sketch of the first ULMAAS hinge, consisting of four short and four long tape springs, of which the latter are folded in an S-shape [67]

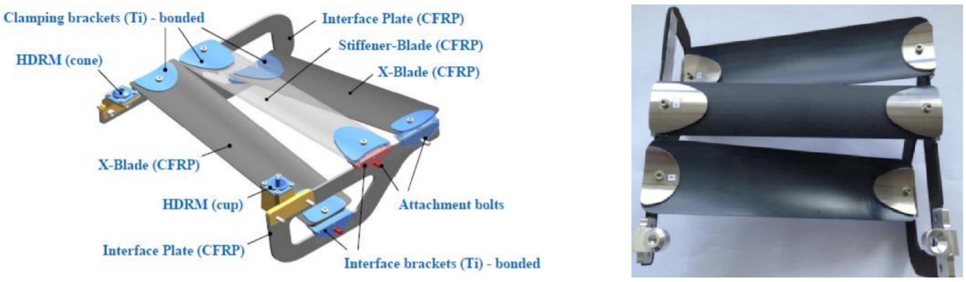

Figure 3.24: Sketch and photo of the UDM, the second ULMAAS hinge. It looks comparable to the Maeva hinge, except for the directions of the tape springs of which the axes are not parallel [68]

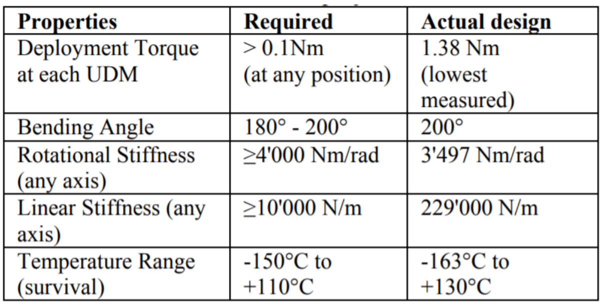

Properties	Required	Actual design
Deployment Torque at each UDM	> 0.1Nm (at any position)	1.38 Nm (lowest measured)
Bending Angle	180° - 200°	200°
Rotational Stiffness (any axis)	≥4'000 Nm/rad	3'497 Nm/rad
Linear Stiffness (any axis)	≥10'000 N/m	229'000 N/m
Temperature Range (survival)	-150°C to +110°C	-163°C to +130°C

Table 3.1: General performance table after testing the UDM [68]

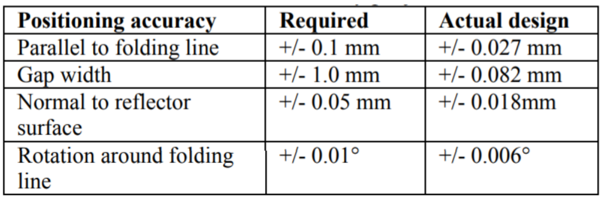

Positioning accuracy	Required	Actual design
Parallel to folding line	+/- 0.1 mm	+/- 0.027 mm
Gap width	+/- 1.0 mm	+/- 0.082 mm
Normal to reflector surface	+/- 0.05 mm	+/- 0.018mm
Rotation around folding line	+/- 0.01°	+/- 0.006°

Table 3.2: Position accuracy performance table after testing the UDM [68]

3.2.2. EMC HINGES

Elastic Memory Composite (EMC) materials are made of Shape Memory Polymers and Composites (SMPC) that fall in the class of so called 'smart materials', because they can change shape under the influence of environmental stimuli [69]. In the case of an EMC this stimulus comes from changes in temperature. After being produced in the original shape, one can heat the material above the glass transition temperature (T_g), making it a viscous material in the rubber state. At that point the material can be bend, twisted, stretched, or compressed [70]. If the material is hold in the new position and cooled down below T_g, the new shape will be kept, since the material becomes elastic again in a glass state. The strain is however stored, so when heated above T_g again, the sample will return to its original shape with high accuracy and precision. When finally cooled again the original mechanical properties are retained [69]. There are many glass transition temperatures one can design for by using different polymers. The described thermo-mechanical cycle of the shape-memory effect is visualized in fig. 3.25, and a picture of a typical EMC hinge in stowed and deployed configuration is provided in fig. 3.26.

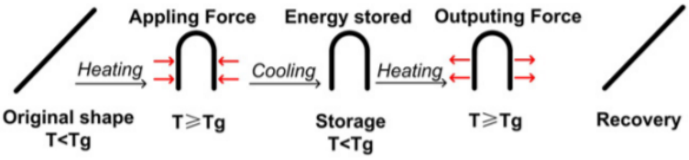

Figure 3.25: Thermo-dynamic cycle of the shape-memory effect of an EMC hinge [71]

Figure 3.26: A TEMBO CTD-BG1.3 EMC hinge with embedded heater in deployed and stowed configuration [40]

EMCs are used in many different applications. They are used as self-latching hinges, deployable STEM-booms, screw actuators, and as foams that can be compressed or expanded. In the case of the self-latching hinge the advantages are among others the low density, low production costs, high Young's modulus, good repeatability, lack of shocking during deployment, and the fact that the simple mechanism does not need motors, bearings, position sensors, or complex control electronics and software [69]. Reading [39, 40, 69, 70, 72, 73] it becomes clear that the company Composite Technology Development, Inc. (CTD) is a leader on the development of EMC actuators, with many researchers of other organizations that describe the use of products of this company. One of them was Mark Lake, one of the three main researchers that developed the NGST deployment mechanisms, discussed in subsection 3.1.1. Actually he tested an adjusted version of the deployment mechanism of the NASA lidar prototype, where the rail for the strut has been replaced by a mechanism driven by an EMC hinge, as shown in fig. 3.27. Furthermore the Cornerstone Research Group also developed some EMC products, but mostly applied in deployable skins and surfaces [72]. Unfortunately it seems that the focus of CTD has shifted to other applications of EMC actuators than self-latching hinges, since no papers about further research can be found after 2006 [39]. However, a document about experiments performed in the International Space Station (ISS) confirms successful test results in 2007, despite the fact that no publication about this results exists [41]. Another explanation for the lack of papers after 2006 may be that the further research conducted falls under International Traffic in Arms Regulations (ITAR). The properties of CTD's hinges, developed over a decade ago and described in [40, 69], are promising, especially due to the facts that they show very little microdynamic response and that their repeatability is high. Furthermore a lot of research can be found for hinges in systems that do not require high precision. Since providing precision in the form of dimensional repeatability is application specific, many calculations are needed if one wants to translate that to the dimensional repeatability in another design. Therefore manufacturers often provide the shape recovery rate, a form of repeatability that is specific to the hinge, regardless of the application. Eqn. 3.1 shows how it is calculated with parameters as explained in fig. 3.28 [73]. From this it is only one extra step to calculate the dimensional repeatability in a specific application. Most EMC hinges achieve a shape recovery rate of 96% to 99%. However, when one would replace the self-latching hinge in the current design with an EMC hinge, it is estimated that a shape recovery rate of at least 99.7% is required. Last year the Chinese company Shanghai YS Information Technology Co., Ltd. did develop a hinge to deploy an antenna reflector that meets this requirement. It has a shape recovery rate of 99.996% [74]. This would lead to a deployment accuracy in the order of nanometers.

$$R_N = \frac{\theta_0 - \theta_N}{\theta_0} \cdot 100\% \qquad [3.1]$$

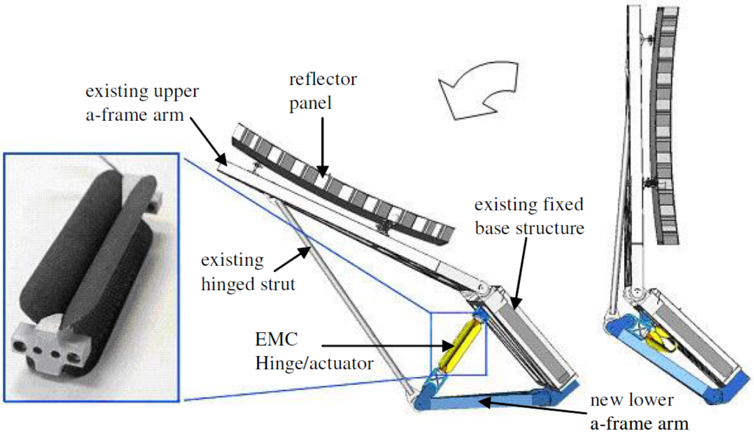

Figure 3.27: Sketch of stowed and deployed configurations of the EMC design, which is an alteration of the lidar prototype [40]

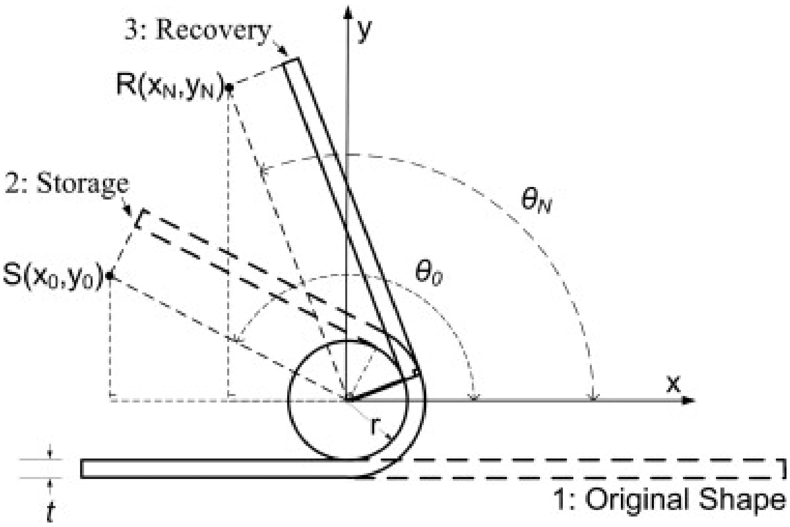

Figure 3.28: Sketch indicating the parameters to calculate the shape recovery rate [73]

Currently a lot of research goes into SMPC materials filled with carbon nanofibers. These SMPCs are not activated by an external heat source, but electrically. The carbon nanofibers are electrically conductive, but also cause resistive heating, resulting in the same phase transition as for external heating [75, 76]. However, these electrically activated SMPCs have a low TRL and have never been tested in a space environment.

A final interesting hinge to discuss is the hybrid hinge design developed by the company 'ILC Dover' for a deployable reflector antenna, as part of the NASA ESTO ACT program. It combines a SMPC, used in EMCs, with strain energy components, as used in a tape spring [77]. The SMPC part provides control over the deployment speed and increases the hinge stiffness after deployment, while the tape spring part provides deployment force and increases the deployment precision. Also the deployment shock, which is typical for tape springs and limits their suitable applications, is significantly reduced. The deployment repeatability is relatively high with a shape recovery rate of 99.9%.

3.2.3. LATCH OF THE JWST

As discussed in subsection 3.1.1, the primary mirror wing of the JWST is actuated by a motor and falls in a kinematic interface. Usually one wants to apply a constant load keep the interface together. A motor is not the most favourable mechanism to do that, because it would need to consume energy for the entire operational phase of a mission. This latch of fig. 3.29 consists of a screw that is driven by a stepper motor and a nut that floats on top of a spring. Once the screw engages with the nut, it will push back the nut against the spring without rotating. Once the panel is fully deployed, the screw is driven by the motor so the nut screws up towards its base. Since the spring will provide a constant force even during (thermal) deformations, the latch forms a compliant mechanism that will never provide a stiff load path. A disadvantage of this mechanism is that adding a motor to drive the screw may add too much weight and increases the risk of failure.

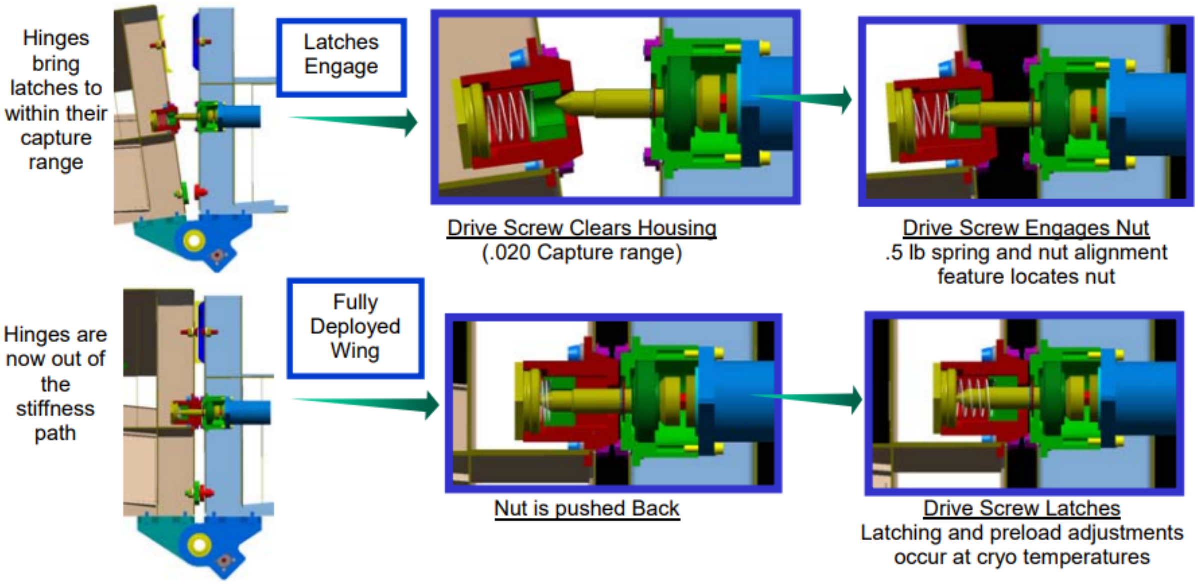

Figure 3.29: Sketch of the latching sequence of the JWST latch [42]

3.3. THEORY ON HIGH PRECISION DESIGN PRACTISES

When designing mechanisms that require high precision, there are a lot of factors to consider that would be neglected in other designs. Examples are thermal expansion, microdynamic effects, and imprecision due to manufacturing tolerances. According to [31] this can be handled best by making use of kinematic interfaces. To be able to explain how kinematic interfaces handle thermal deformations, first some theory about athermalization is discussed in subsection 3.3.1. Afterwards it is explained how precision is theoretically achieved and how these principles are applied in different types of precision interfaces 3.3.2. From the discussed topics it will become clear why kinematic interface are preferred for high precision mechanisms. When making kinematic interface designs, one will find that there is a difference between theory and practise. Subsection 3.3.3 will present some recommended design practises, including how to handle components that are per definition not manufactured perfectly.

3.3.1. ATHERMALIZATION OF PRECISION MECHANISMS

Thermal deformation of materials is the most common cause of non-repeatability [78]. Different materials have a different CTE, which means they will contract or expand with a different rate once temperature changes occur. This happens according to eqn. 3.2, which defines the new dimension of a component after a temperature change. Here L_n is the new length, L_o the old length, ΔL the change in length, α the CTE, and ΔT the change in temperature.

$$L_n = L_o + \Delta L = L_o + L_o \cdot \alpha \cdot \Delta T = L_o(1 + \alpha \cdot \Delta T) \qquad [3.2]$$

Most materials have a positive CTE, meaning they expand with increasing temperatures, but some materials have a negative CTE over a certain temperature range. This is generally referred to as negative thermal expansion rather than thermal contraction. The most well known example is water that expands when lowering the temperature below $4\ ^{\circ}C$, until it becomes ice [79]. From this one can note another important fact about the CTE: the CTE is a function of temperature. Therefore it can be assumed constant only if no major temperature changes occur during the operational life of a component.

If one does not design for thermal expansion, this may lead to either misalignments or thermal stresses. According to [80] there are four ways to increase the thermal stability. They are listed below:

- Reduce sensitivity to thermal effects by design
- Manage heat sources
- Control system environment
- Compensate for measured deviations

The list moves from passive methods to active methods and therefore it is preferred to achieve thermal stability with the higher options. For a space system it is not possible to control the most dominant heat sources, such as the sun, as suggested at the second bullet point. On the other hand there are also mechanisms within the system that generate heat, such as motors, and those can be controlled. Within the DST team the system environment is mainly controlled by the people that work on the baffle and active thermal control. On the other hand some work remains the responsibility of the people designing the deployment mechanisms, for example by thermally isolating certain components. Active compensation for thermal deviations will be applied in the DST, but this falls outside the scope of this thesis research. The deviations will be measured by an algorithm that analyzes the optical signals and the required compensation will be executed by the M1 calibration system. The algorithm only work within a certain error range and that is what led to the budgets as presented in fig. 2.8.

As explained, the lower three options of the list mostly result in tasks for other team members. The first one, reducing sensitivity by design, is on the other hand a very important part of the design presented in this thesis. The most obvious way to achieve thermal stability is to select materials with a low CTE. However, since the budgets on the thermal drift are extremely ambitious, low CTE materials alone will not lead to an acceptable design. Several other methods for athermalization by design are discussed below.

ATHERMALIZATION BY CTE COMPENSATION

A method for linear athermalization that is already applied for several centuries, is thermal balancing by using two materials with a very high difference in CTE. Two examples are shown in fig. 3.30. The upper example shows how a long bar with a slightly negative CTE compensates the expansion of its tip which is made of a highly positive CTE material. The lower example contains a long bar with a slightly positive CTE. At its end it is connected to a short, highly positive CTE bar that expands in the other direction for compensation. The lower example has been used in pendulum clocks as of 1721 [81]. It was found that pendulum clocks ran at different speeds in summer and winter. When George Graham linked this with a change in the length of the pendulum due to temperature differences, he added a mercury container at the bottom of the pendulum. When heated, the mercury expanded and moved upwards, resulting in a constant height of the center of gravity.

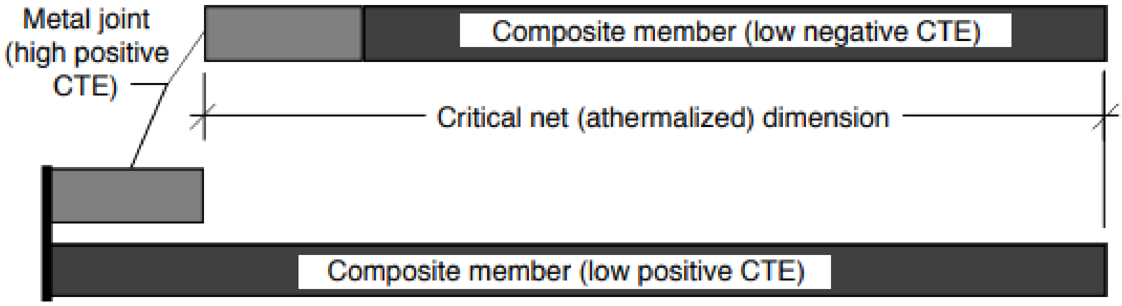

Figure 3.30: Top: CTE compensation by in-line coupling of a long component of low negative CTE with a short component of high positive CTE - Bottom: CTE compensation by coupling a long component of low positive CTE with a connection at the end from which a short component of high positive CTE expands back in the opposite direction [31]

From the two cases explained in fig. 3.30, the upper case dimensions are correct if the sum of the two ΔLs (eqn. 3.2) equals to zero, because they work in the same direction. This is shown in eqn. 3.3. In the second case the components work in opposite direction, so as long as they have the same ΔL, the distance of the end position remains constant, as shown in eqn. 3.4 [82]. The parameters are according to the illustration in fig. 3.31. In the equations α_R stands for the CTE of the long component and α_d for the CTE of the short component. Note that ΔT is a common term for the different ΔLs and is therefore dropped in eqns. 3.3 and 3.4. Fig. 3.31 illustrates an example of how to apply athermalization to a lens mount. It is assumed that the mirror has a negligibly small CTE. In such a design, it is often the case that the radius of the mirror is a given. If one would indicate this radius with M, eqn. 3.5 holds. One often also knows the materials, and so the CTEs, one is going to use. Solving for d then leads to eqn. 3.6.

$$d\alpha_d + R\alpha_R = 0 \tag{3.3}$$

$$d\alpha_d = R\alpha_R \tag{3.4}$$

$$M = R - d \tag{3.5}$$

$$d = M\frac{\alpha_R}{\alpha_d - \alpha_R} \tag{3.6}$$

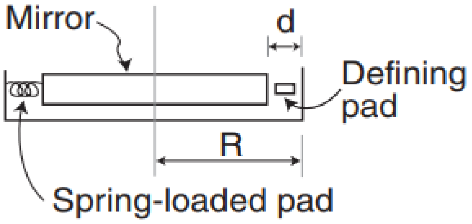

Figure 3.31: Example of athermalization by CTE compensation in a mirror mount. The mirror is assumed to be zero CTE [82]

In the story above the method is presented as a 1D problem. It can however also be used for 3D components. In this case one should calculate the distances for the athermalization material (the one represented with length d) for all 3 axes. Furthermore, one could also make a composite material that contains both positive and negative CTE materials. An example can be found in CFRPs. These composites are made out of a positive CTE resin matrix (mostly epoxy) and carbon fibers with a negative CTE in fiber direction for temperatures between roughly -200 $^\circ C$ and 400 $^\circ C$ [83, 84]. By selecting the right amount of layers and the right fiber orientation for each layer, one can design for zero CTE at a certain temperature. This then however only holds for the optimized direction, meaning athermalization may still be required in the directions perpendicular to this direction.

ATHERMALIZATION BY STEERING THERMAL DEFORMATIONS

Especially at the interface between two component of different CTE, steering the thermal deformation in a way it causes no harm is often easier to achieve than CTE compensation. The challenge with steering of the deformation is that next to avoiding misalignment, one also needs to ensure that thermal stresses (stresses resulting from thermal deformations) do not result in unwanted effects. An example of how to ensure this is provided in fig. 3.32. In this figure a connection is shown between a near zero CTE member with a highly positive CTE ball bearing hinge inside the member at one end. A cutout has been designed that was originally made to prevent bilinearity. Bilinearity means that the tang (the member in fig. 3.32) has a compression stiffness that differs from the tension stiffness. In a tang without cutouts there is generally a more direct load path in compression than in tension, leading to a higher compression stiffness. The cutout divides the load paths such that the tension and compression stiffness become equal. According to [27] the design was initially made with the assumption that the bearing-tang interface carries no radial load. A finite element analyses however showed that even with a compressive radial load from the bearing (for example due to thermal expansion), equal tension and compression stiffness are maintained when designing the tang with the relative dimensions as shown in fig. 3.33. In [31] it is explained that a tang design as explained in [27], also results in an athermalized interface.

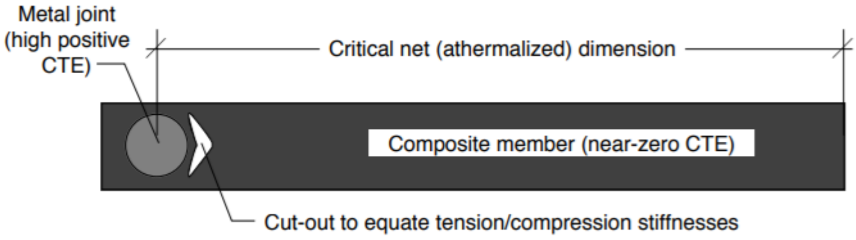

Figure 3.32: Example of athermalization by steering the deformation and preventing bilinearity [31]

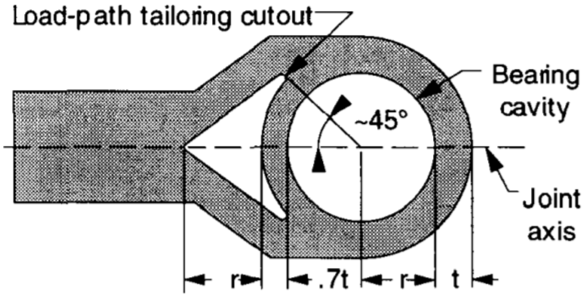

Figure 3.33: Relative dimensions that lead to a tang design with equal compression and tension stiffness, even after thermal expansion of the bearing [27]

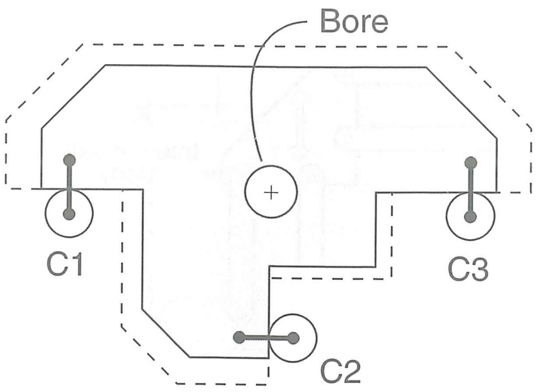

Figure 3.34: Example of a design where no rotation around the thermal center occurs after a change in temperature. The shape at an elevated temperature is indicated by the dotted line [85]

When creating an interface between two components with different CTEs, one often cares the most about maintaining alignment between the centers of the components and preventing rotations around this center. One can design for this by making the centers of the components the thermal center as well. In fig. 3.34 one can see that a thermal center is created if the constraints imposed by other components all allow for radial movement from this thermal center [85]. Kinematic interfaces always have a thermal center and allow thermal expansion without rotation around this center. Only the distance between the interfaces may change. Two examples of kinematic interfaces where it is very clear that thermal expansion will not result in rotations around the thermal center are provided in figs. 3.35 and 3.36.

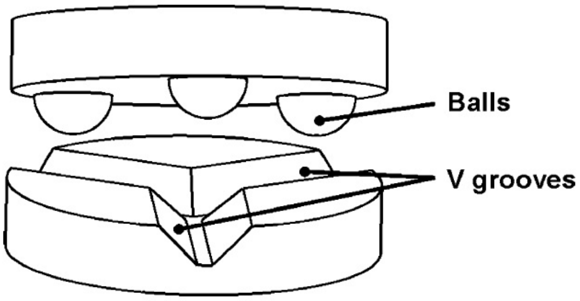

Figure 3.35: Kinematic interface with V-grooves that align with the thermal center. The balls move in radial direction over the V-grooves in case of temperature changes [86]

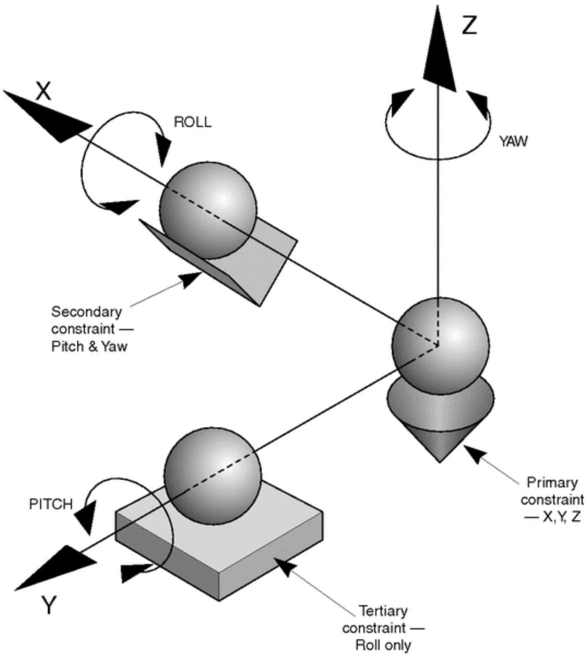

Figure 3.36: Example of a Kelvin clamp, of which the thermal center is located at the origin of the axis system. The balls are free to move radially over the V-groove and the flat plate [87]

3.3.2. THEORY FOR PRECISION INTERFACE DESIGN

Unfortunately there is no time left to write out this subsection. The main source of information for this subsection is [31] and partly [85].

3.3.3. BEST DESIGN PRACTISES FOR KINEMATIC INTERFACES

Unfortunately there is no time left to write out this subsection. The main source of information for this subsection is [85] and partly [31].

4

PRELIMINARY DESIGN FOR M1 DEPLOYMENT MECHANISM

After getting familiar with literature, the first actual step of this research is the preliminary design of the M1 deployment mechanism. This includes all parts attached to the spacecraft bus, the A-frame, and the deploying parts between the spacecraft bus and the A-frame. The components on top of the A-frame, which will most likely at least include a whiffle tree, the mirror, and the calibration actuators, will not be designed as a part of this thesis, although communication with the person in charge of this is crucial. The design of the A-frame needs to fit the wishes of the designers of both subsystems.

The first section will discuss the deployment mechanism concepts initially considered for this design, including their typical characteristics. Section 4.2 will then describe the modelled behaviour for each of them, so that in section 4.3 a trade-off can be made that leads to the best concept. Unfortunately it will turn out that none of the concepts will meet the requirements. This was the point to seek help from the outside at the department of 'Precision and Microsystems Engineering' of the 3mE faculty of the Delft University of Technology (TU Delft). A talk with Prof. dr. ir. Just Herder led to a new concept, described in section 4.4, that may be able to meet the requirements.

4.1. HINGE CONCEPTS AND THEIR CHARACTERISTICS

In the literature study many papers were assessed on deployment mechanisms that have been used in the past. Important sources of information are papers, guidelines, and production drawings, of research conducted on deployment mechanisms by mostly Lake, Peterson, and Warren (with several co-authors) [27–29, 31, 32, 35–41]. Their research led to the knowledge used to build the JWST, back then called the NGST. Other important sources of inspiration result from what is published on the DPT [43, 44, 46], developed by the Space Dynamics Laboratory of the Utah State University, and on the Dobson Space Telescope [48–51, 55], developed by a research team of the Technical University of Berlin, that continued the project as a spin-off company called 'Berlin Space Technologies GmbH'. Also the work of the previous MSc student that worked on the M1 design, Boris van Putten, served as valuable input.

Unfortunately it turned out that the design of Van Putten does not work, due to wrong assumptions about the workings of a self latching ball bearing hinge. As a starting point a step was taken back to look at the initial concepts he started with. They are presented in fig. 4.1 [25]. Note that the 'Bending Strut' was called 'Tape Spring Strut' in the original figure, but for the current purpose this name represents a concept that can unfold in the same way by making use of other types of hinges as well.

With the current knowledge about the design and after discussions with experts from ADS, both strutless concepts were discarded, because the deployed mechanisms are too vulnerable to vibrations. During Van Putten's work another student worked on the development of the M2 design and considered a telescopic boom for his deployment mechanism [22]. The lessons he learned are applicable to this design as well. The high mass and achievable precision led to discarding the extending strut option as well. The rollable strut was also discarded based on the reasoning of Van Putten. This concept had the lowest score in his trade-off with a large distance to the second lowest score.

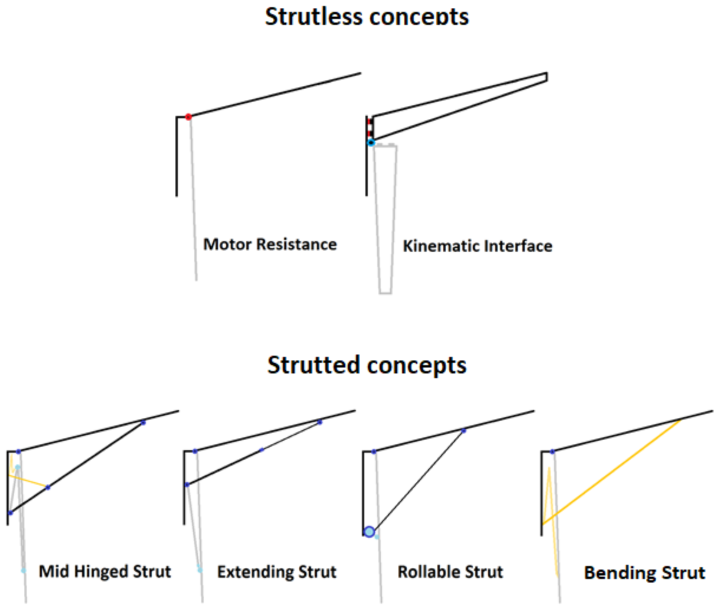

Figure 4.1: Concepts assessed in the MSc thesis of Van Putten, a predecessor for the M1 mechanism design [25]

This leaves the mid hinged strut and bending strut concepts to be investigated further. Being creative with the components and principles used in the aforementioned projects from literature, four concepts came out to be assessed in more detail. The tape spring hinge, EMC hinge, middle latch, and slider concepts will be discussed separately in the subsections below. A notable difference in the approach of assessing technology between this and Van Putten's thesis is that the availability of the assessed technology now plays a crucial factor. Next to the TRL, also the fact whether it is made by a research institute for a non-industrial project, or by a company that wants to make money is important. In a student project like this there is too little budget, too little man hours, and too little experience to develop complex components in-house. If there is no company that can or may (for example due to ITAR) sell the technology, the likelihood of finishing this project, with that component, within the planned time line is very low, even though some university research group may published a paper about a working specimen that meets this projects' requirements.

4.1.1. TAPE SPRING HINGE CONCEPT

The tape spring hinge concept (impression shown in fig. 4.2) is based on the existing design made by Van Putten [25]. The mechanism in the middle of the strut is however replaced by a tape spring hinge. The principle of a tape spring hinge is explained in more detail in section 3.2. In this design it seems like an advantageous solution due to its low mass, low complexity, low cost, low CTE, high TRL, and its ability to deploy and latch by itself without requiring additional components. Besides, tape spring have a reasonable stiffness, which will probably be enough for a deployed strut. The risks of tape spring hinges are the magnitude of the deployment shock and the risk of inability to deploy due to stress relaxation (i.e. viscoelastic creep).

Reading papers, one sees that many of the tested specimen were self made by research groups within universities or institutes. Since they are not companies, contacting them to order a suitable hinge is not an option. Two German companies however do make tape spring hinges for space applications; Hoch Technologie Systeme GmbH (HTS) and SpaceTech GmbH. HTS is known for the development of two deployment mechanism concepts, both involving tape spring hinges, in the ULMAAS project. They are describe in 3.2.1. HTS was contacted to request an offer for an UDM hinge, as shown in fig. 4.3. The company offers a downscaled version of the hinge. SpaceTech has not been found via a paper, but by contacting them after reading they are responsible for the deployment mechanism of an antenna for the JUICE project. A short brochure with information on their deployment mechanisms can be found in [88]. SpaceTech offers a boom with cut-outs, as shown in fig. 4.4, based on the same concept as the one used in the JUICE mission. They will tailor the product to meet the requirements of this project.

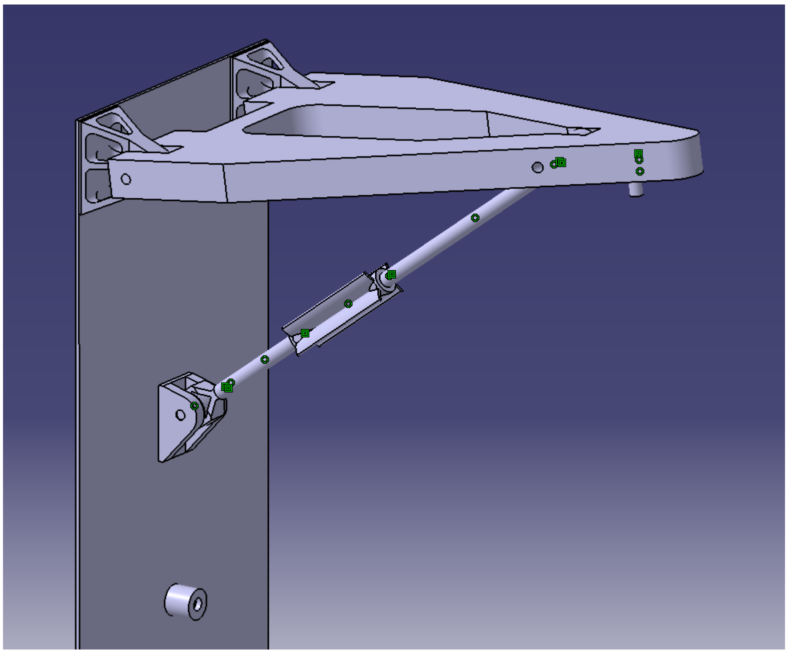

Figure 4.2: Impression of what a design with a tape spring hinge could look like

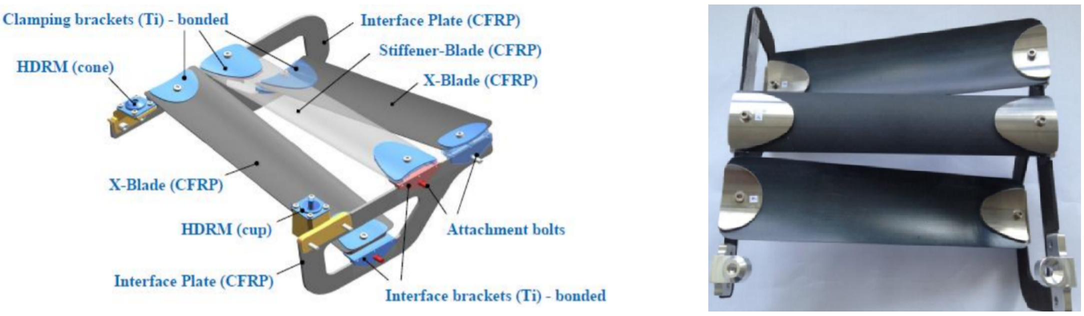

Figure 4.3: Sketch and photo of the UDM, the second hinge concept of the ULMAAS project [68]

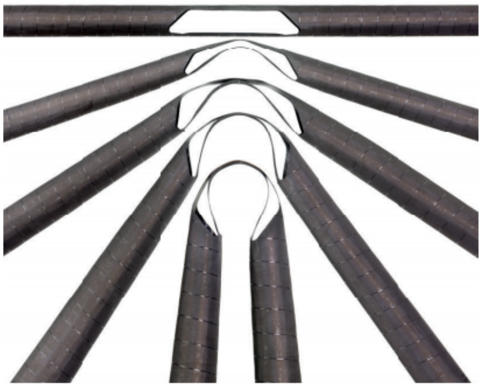

Figure 4.4: Pictures of a SpaceTech integral slotted hinge under several bending angles [88]

At the moment the trade-off in section 4.3 was made, not all desired technical information was available, since both companies required a Non Disclosure Agreement (NDA) for which the legal structure was not yet in place. The information that was taken into account for the trade-off is summarized in tab. 4.1.

Table 4.1: Properties of tape spring hinges provided by HTS and SpaceTech

Property	**HTS**	**SpaceTech**
Delivery time	Test item within 8 months, 5 more for QM*, 5 more for production and acceptance testing FM**.	Test item within 6 months, later steps unknown.
Cost	€85k for 1 hinge up to acceptance testing of the FM**.	Unknown
TRL	UDM is in TRL 5, but designed for a much larger S/C. Major rescaling to 20-25% of current size required.	Unknown at this moment, although TRL 5 or 6 is assumed based on conversations with the supplier.
Thermal properties	The UDM has a low CTE of ~1.5 $\mu m/(m-K)$. The thermal behaviour will however be discontinuous, since the device is made of a different material than the two struts around it.	A lot can be customized about this tape spring hinge by playing with the lay-up, and the shape and size of the cut-outs. The CTE can be made ~0 $\mu m/(m-K)$. Besides, the thermal behaviour is continuous over the entire length of the strut.
Creep properties	Unknown	Creep that prevents deployment only becomes a risk when enduring a temperature of >100$^\circ C$ during stowage.
End shock	Quite low due to self-damping of the opposite bending tape springs. Additional damper optional.	Somewhat higher end shock. Additional damper optional and probably required.
Stiffness	For a large design it is 10 N/mm linear stiffness and 4 kNm/rad rotational stiffness. This means the rotational stiffness will be much lower for the rescaled design.	Highly dependent on boom properties and hinge cut-outs. First approximation: take 80% of boom stiffness without cut-out.

*QM: Qualification Model
**FM: Flight Model

4.1.2. EMC HINGE CONCEPT

The EMC hinge concept is again similar to the tape spring hinge concept and Van Putten's concept, again with another type of hinge in the middle of the strut. The principle of an EMC hinge is explained in more detail in section 3.2. In this design it seems like an advantageous solution due to its low mass, low cost, low CTE, high TRL, high stiffness, the lack of shocks during deployment, and its ability to deploy and latch by itself, requiring only a bit of electricity. With this need for electricity this design is slightly more complex than a tape spring hinge, but it can still be regarded as simple. One thing to look out for is the low deployment force, which may result in an inability to deploy if there's too much friction in the system.

EMC hinges for space applications are mostly made by established companies, to which a lot of references are found in papers. This product is however always custom made for the specific application, so they cannot be ordered from stock. Several companies were found in the USA, Japan, and China, producing EMC hinges that have actually been tested in space. Unfortunately the Chinese company Shanghai YS Information Technology Co., Ltd could not be reached, SMP Technologies Inc. from Japan moved into Earth based applications of this technology, ILC Dover and Ladeau Manufacturing from the USA both declined to get involved in this project, and Composite Technology Development, Inc. from the USA could not achieve the required precision.

Without a company to deliver, it is not possible to make use of this technology. Therefore the EMC hinge concept will be disregarded in the remainder of this thesis.

4.1.3. MIDDLE LATCH CONCEPT

The middle latch concept involves a (sloppy) hinge outside the load path of the strut halves, an actuation device, and a latching mechanism that couples the strut halves. The advantages are the high stiffness, because the strut halves will act like they are one, and the thermal properties that are homogeneous over the whole length of the strut, possibly with only a short discontinuity at the latch. Further advantages and disadvantages are dependent on the selected mechanism.

The first of the two mechanisms that were looked at is the cone in cone connection, as used in the Dobson Space Telescope (fig. 4.5). It is shortly described in subsection 3.1.4. At first glance it seems like a simple and suitable solution, but when looking further into the technology it raises doubt. First of all, this type of latching mechanism has not been applied in any other high precision application. Second, the technology has been patented in Germany, but neither the Technical University of Berlin nor the spin-off company Berlin Space Technologies, applied for an international patent. If no other technology would be favored over this latch, this seems like a strange decision. Next to the explained indicators for doubt on the performance of this mechanism, no technical information can be found on the working it. The papers on this project [48–51] only describe the performance achieved by the deployment mechanism and the way this was tested. This means there is no public information on how to rescale this mechanism and model its characteristics. This difficult starting point, combined with the fact that there may be some vital information to make this mechanism work, that is not included in the patent or papers, led to the choice to not consider the cone in cone latch as a design option.

The second mechanism is the Articulated Boom Deployment Hinge (ABDS) developed by HTS (fig. 4.6). Next to the UDM, HTS proposed the ABDS as an alternative technology. A couple of properties are satisfying, such as the high stiffness, high reliability, and the very low latching shock. On the other hand the mechanism is quite heavy, it is only in TRL 4, and no information about the thermal properties is provided yet. Also, HTS says that rescaling is required (this mechanism was designed for a much larger satellite) and that as a result, there may be a need to use another actuation concept. This would mean that the actual TRL goes down even further. With a price of €100k the price of this mechanism is slightly more expensive than the UDM.

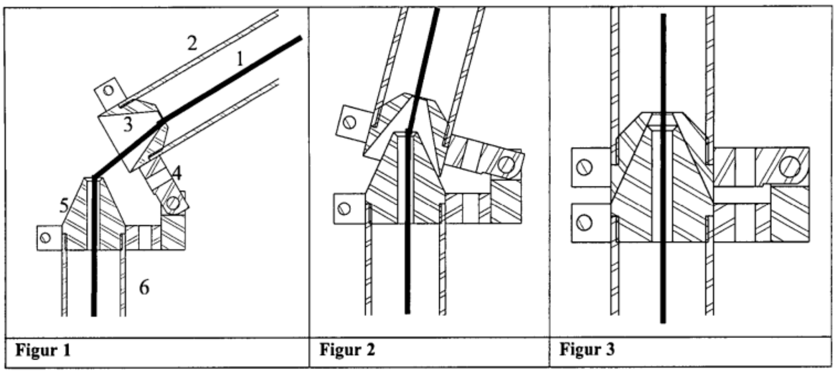

Figure 4.5: Sketch from the patent, describing the cone in cone latching mechanism used for the Dobson Space Telescope [55]

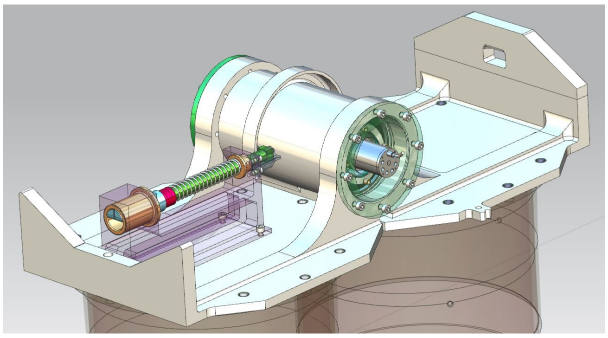

Figure 4.6: Render of the ABDS, developed by HTS [89]

4.1.4. SLIDER CONCEPT

The slider concept involves some sort of sliding mechanism, actuated by a towing line attached to a spring, that slides over the base strut (the strut half attached to the satellite bus) and is connected to an additional 'slider strut'. As shown in fig. 4.7, the sliding movement makes the slider strut push the other struts in place until it reaches its end stop. The slider strut now makes the construction much stiffer. Fig. 4.8 shows a sketch of the mechanism with the chosen terminology for the components.

This concept is inspired by the designs of the DPT [43] and a version of the Lidar Prototype Design of the NASA [32, 37]. Instead of using a precise slider to pull something along during deployment as in these projects, now a slider is used to push some parts out. This way the patent on the mechanism of the DPT [46] will not be infringed. Notice also that the cart-like mechanism riding over a V-groove in the base strut, is just an indicative way to make clear the principle. In reality a slider and guide rail design as used in the Lidar Prototype Design may lead to better performance. The assumed advantages of this concept are the high stiffness, the fact that all components can be made of the same low CTE material, the lack of creep, the low cost, and the fact that modelling the structural behaviour is more straightforward than for special material components like EMC and tape spring hinges. On the other hand the extra components add complexity. Also, properly designing the sliding mechanism in a detailed design, will probably be a much larger effort than implementing a hinge. The mass is somewhat higher compared to the other concepts, but this difference is negligible compared to the total mass of the M1 subsystem. At first it was expected that the additional components make this mechanism much more sensitive to small errors, leading to less precision. The modelled results, discussed in the next section, however lead to another conclusion.

A final note on this concept is that the dimensions, of the components that are also present in the other designs, are different. This was necessary in order to make sure that the slider fits in the stowed configuration, and that the mechanism is fully deployed when the final position is reached.

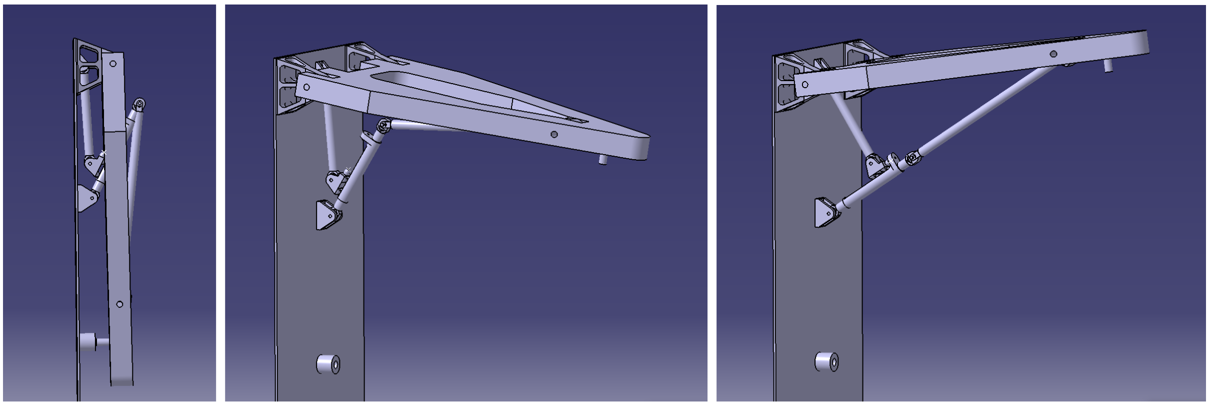

Figure 4.7: Impression of the deployment sequence of the slider concept

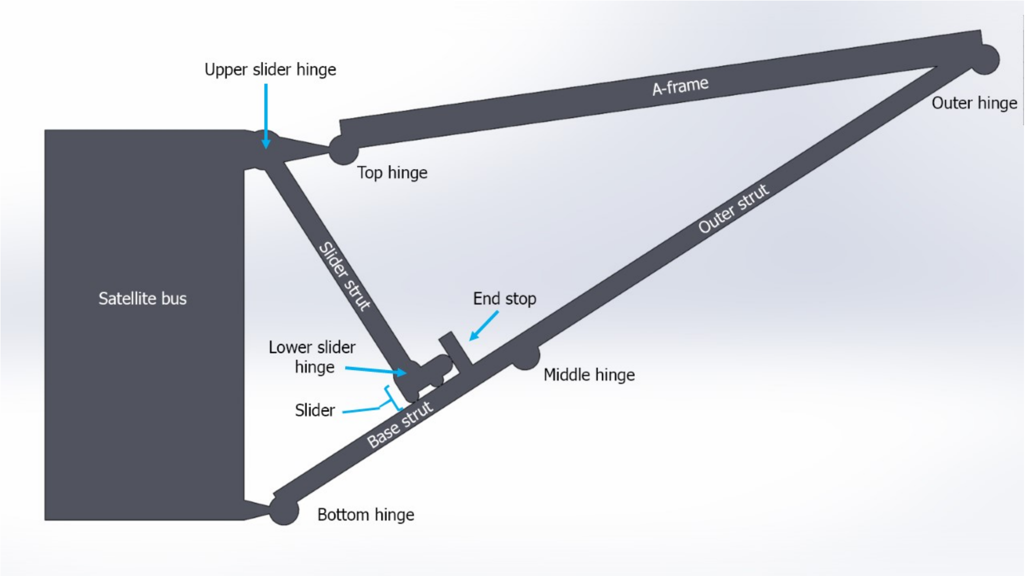

Figure 4.8: Sketch indicating the terminology for the components of the slider concept

4.2. MODELLED BEHAVIOR OF HINGE CONCEPTS

Manufacturers of hinges and latches usually provide performance characteristics, such as the deployment repeatability, on a component level. In reality you need to see this component in the context of the structure to be able to calculate the repeatability at the location of interest. Since the assessed concepts have different structures, one may find that one structure is less sensitive to deployment errors, meaning you can relax the requirement on the component level. When performing an analysis on this sensitivity to overall system errors, caused by errors in each component, one generates insights that allow identification of the most critical components and determination the maximum allowable component errors.

Since deployment repeatability and thermal behaviour are the two most critical factors in this design, a sensitivity analysis has been performed to identify how errors and thermal variations influence the system. Subsection 4.2.1 will describe what the performed sensitivity analysis actually assesses and what one can do with the results of the analysis. Afterwards subsection 4.2.2 describes how the written algorithm works. Subsection 4.2.3 will then provide the results. Finally conclusions will be drawn in subsection 4.2.4.

4.2.1. WHAT WILL RESULT FROM THE SENSITIVITY ANALYSIS

First it is important to avoid confusion between the two errors discussed in this section. The first one is the component error, an error that can occur in the length, the relative positioning, or the deployment angle of the different components. Once a component error occurs, this leads to an overall system error, at a chosen point of interest, that is usually not equal to the component error. The chosen reference point has been determined by the location for which the error budgets hold (budget reference point). The budgets of all mirrors are provided in fig. 2.8, but for ease of use it is presented again in tab. 4.2 with only the relevant data. The budget reference point is indicated in fig. 4.9. Next to the location of this point, also the angle the mirror makes is relevant. This angle, α, is equal to the angle between the A-frame and the Y-axis. The Y-axis is selected to be perpendicular to the spacecraft bus, intersecting the ideal location of the top hinge, and the Z-axis is aligned with the spacecraft bus, as indicated in fig. 4.9. Next to deviations from the reference point and α, also the Root Mean Square (RMS) of the Y- and Z-error is derived as a system error. The sensitivity analysis checks what the overall system error is, as a result of a (combination of) certain component error(s). In the analysis the chosen magnitude of the component errors was based on assumed manufacturing tolerances and on the deployment repeatabilities of less precise tape spring hinges found in literature. A second version of the model has been made where the errors are determined by temperature change rather than manufacturing tolerances, to see exactly what system errors occur if all (or single) components experience a temperature difference. This has been done for different materials.

Finally, the results of the first analysis are used to find the maximum allowable component errors. In other words, from the provided budgets on system level, new requirements on component level, indicating the allowable manufacturing tolerances and errors due to deployment, are derived. The second script provides the component and system errors due to a certain temperature change for different materials. Comparing this with the maximum allowable errors from the other script, one can see within what temperature range and with what materials, the thermal drift budgets are met. This is also done for a case with temperature gradients.

Table 4.2: Budgets for the primary mirror as defined in the requirements [21]

Position [μm]			Tilt [μrad]			Radius [%]	Shape Error [nm]
X	Y	Z	X	Y	Z		
Deployment and Coarse Alignment Tolerances							
2	2	2	2	4	50	$1*10^{-3}$	50
In-Orbit Drifts							
$2*10^{-2}$	$2*10^{-2}$	$2*10^{-2}$	$1*10^{-2}$	$2*10^{-2}$	5	$1*10^{-4}$	5
Stability Budget							
$5*10^{-3}$	$5*10^{-3}$	$5*10^{-3}$	$2.5*10^{-3}$	$1*10^{-2}$	$5*10^{-1}$	n/a	n/a

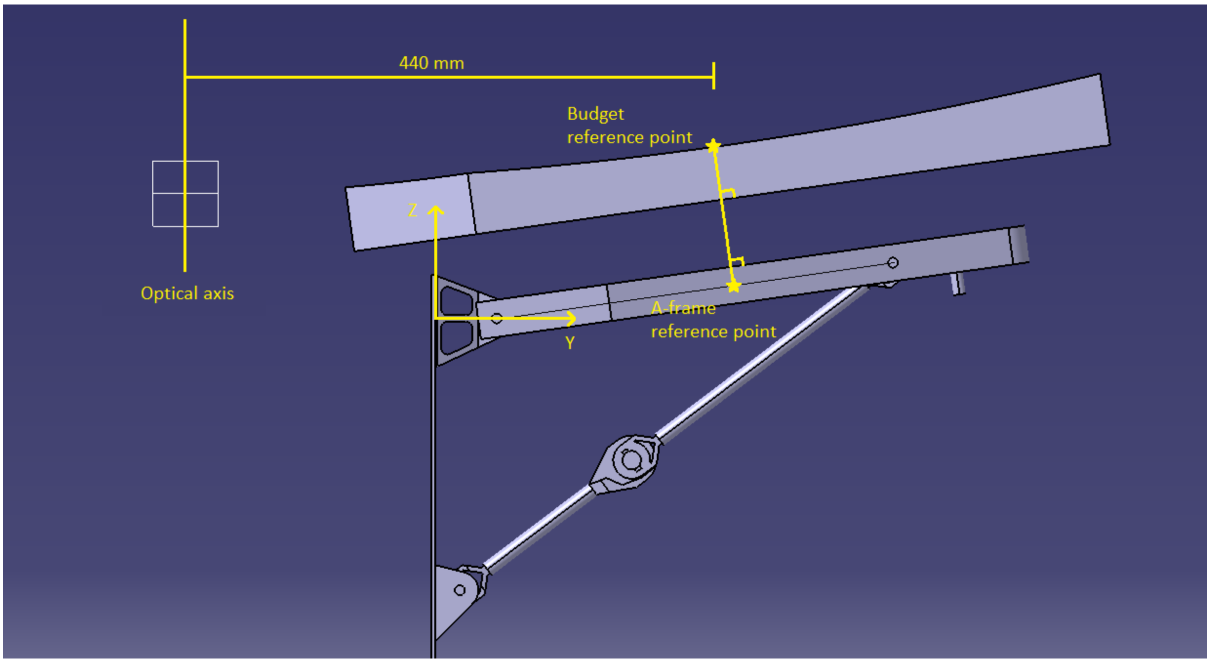

Figure 4.9: Sketch indicating the location of the budget reference point and the relative location of the A-frame reference point

4.2.2. METHODOLOGY OF THE SENSITIVITY ANALYSIS

The sensitivity analyses described in this section are very simplified estimates that only take into account geometrical changes for certain dimensional errors in a 2D plane. In the first analysis the nature of the error sources is not taken into account. Performing extensive thermal modelling, including elastic deformations in a 3D environment, on each concept will currently be too time consuming. These analyses are meant to facilitate a more complete trade-off. Once a concept has been chosen, a more extensive model is required.

As a first step to develop the model, possible errors in the parts were determined. Since the configurations differ, two separate models, with separate part lists, and different sets of corresponding component errors were made. The mid-hinge (MH) model applies to the tape spring hinge and middle latch concepts, while the slider (SL) model applies to the slider concept. The list of component errors is provided below, accompanied by a visual representation in fig. 4.10. Here all certain ideal dimensions 'X +- the specific errors' are shown.

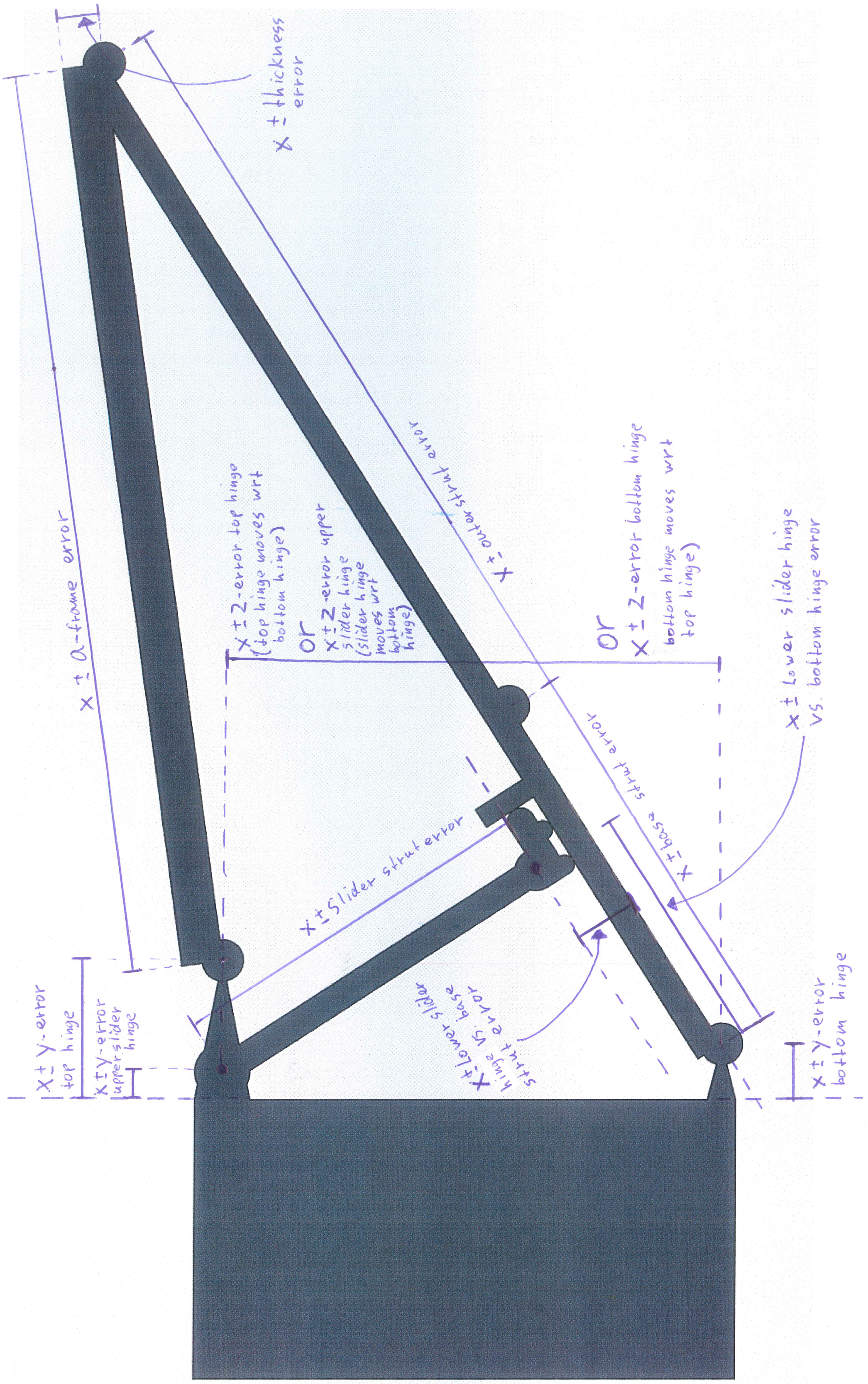

Figure 4.10: Sketch indicating the definition of each of the errors

Component errors for both models

- *Base strut error* - Error in the length of the base strut. An equal outer strut error will result in the same system errors, so the outer strut error is not presented in the results.
- *A-frame error* - Error in the distance between the top and outer hinges along the A-frame.
- *Z-error top hinge* - Error in the location of the pivot point of the top hinge in Z-direction.
- *Z-error bottom hinge* - Error in the location of the pivot point of the bottom hinge in Z-direction.
- *Y-error top hinge* - Error in the location of the pivot point of the top hinge in Y-direction.
- *Y-error bottom hinge* - Error in the location of the pivot point of the bottom hinge in Y-direction.
- *Thickness error* - Error in the thickness of the A-frame.

Component error that only applies to MH model

- *Deployment error middle hinge* - Error in the angle between the base strut and outer strut. Since the slider concept is provided in fig. 4.10, this error is not indicated in the figure.

Component errors that only apply to SL model

- *Slider strut error* - Error in the length of the strut attached to the slider.
- *Z-error upper slider hinge* - Error in the location of the pivot point of the upper slider hinge in Z-direction.
- *Y-error upper slider hinge* - Error in the location of the pivot point of the upper slider hinge in Y-direction.
- *Lower slider hinge vs. base strut error* - Error in the minimal distance between the pivot point of the lower slider hinge and the base strut axis.
- *Lower slider hinge vs. bottom hinge error* - Error in the distance between the pivot points of the lower slider hinge and bottom hinge, measured in parallel to the base strut axis. This may be the result of an error of the pivot point location on the slider or an error in the location of the end stop of the slider.

SCRIPT FOR THE SENSITIVITY TO COMPONENT ERRORS

Knowing the input arguments, the first script can be written. It includes a master script and two function files that perform the geometric calculations for the MH and SL configurations. The functional flow chart depicting this process is shown in fig. 4.12, with a legend describing the types of shapes in fig. 4.11. The arrows indicate the direction the data flows from block to block, although the script will follow the order of the block numbers.

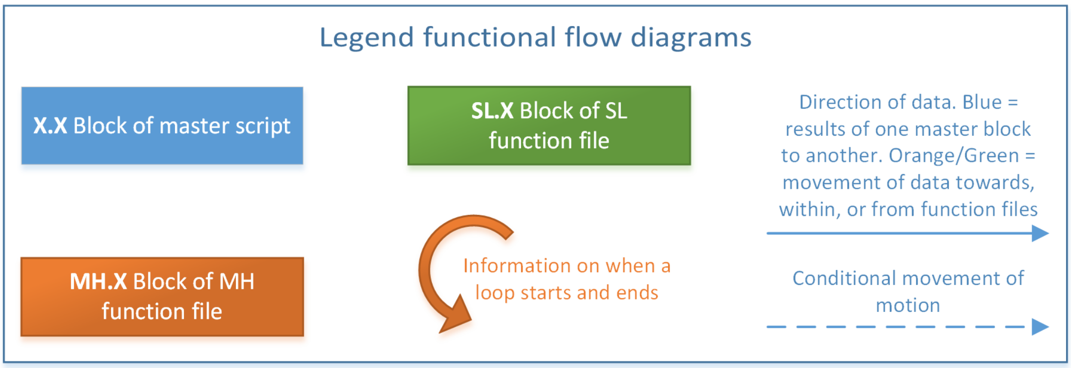

Figure 4.11: Legend used for the functional flow diagrams of figs. 4.12 and 4.13

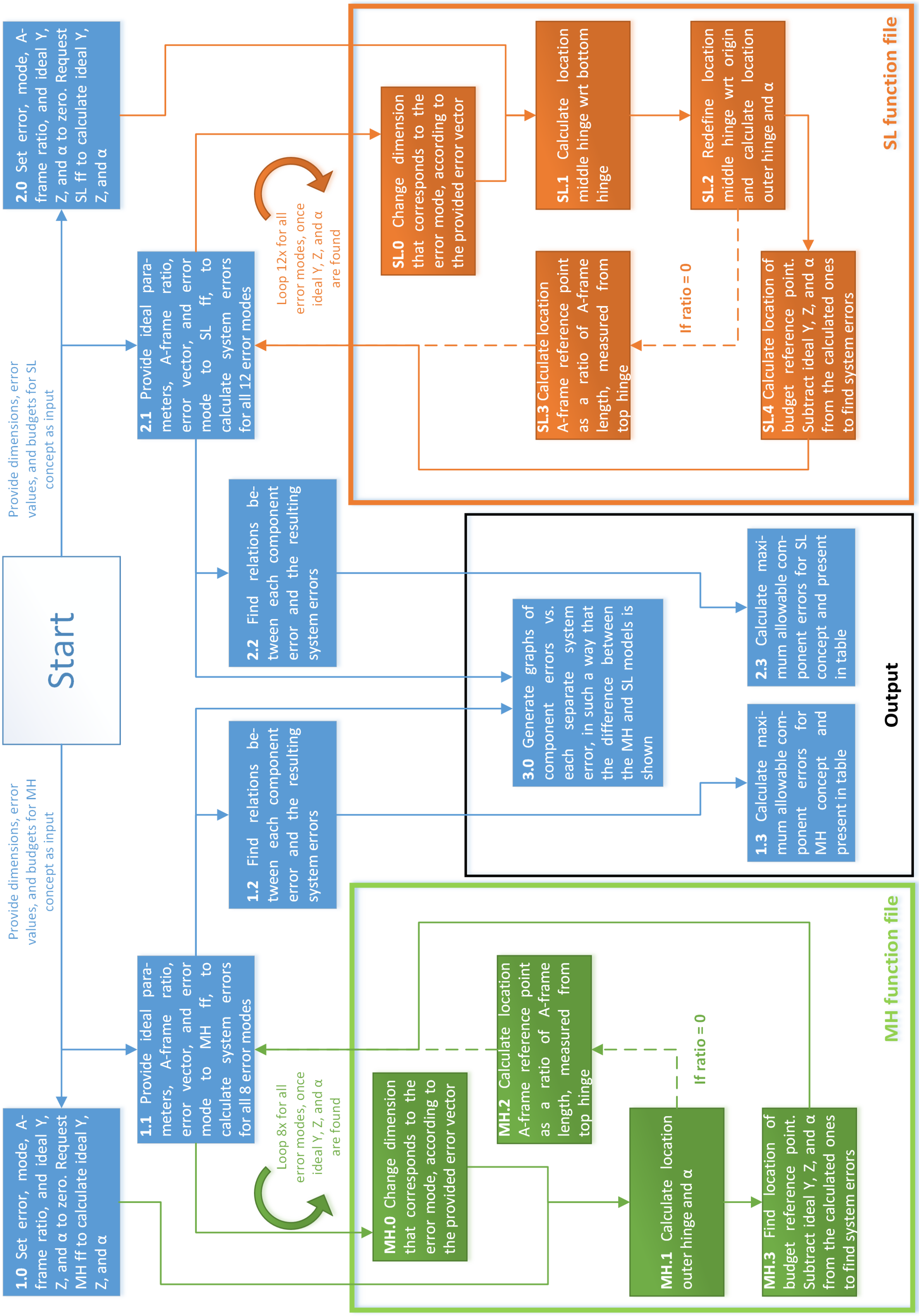

Figure 4.12: Functional flow diagram describing script of the sensitivity analysis for given component errors

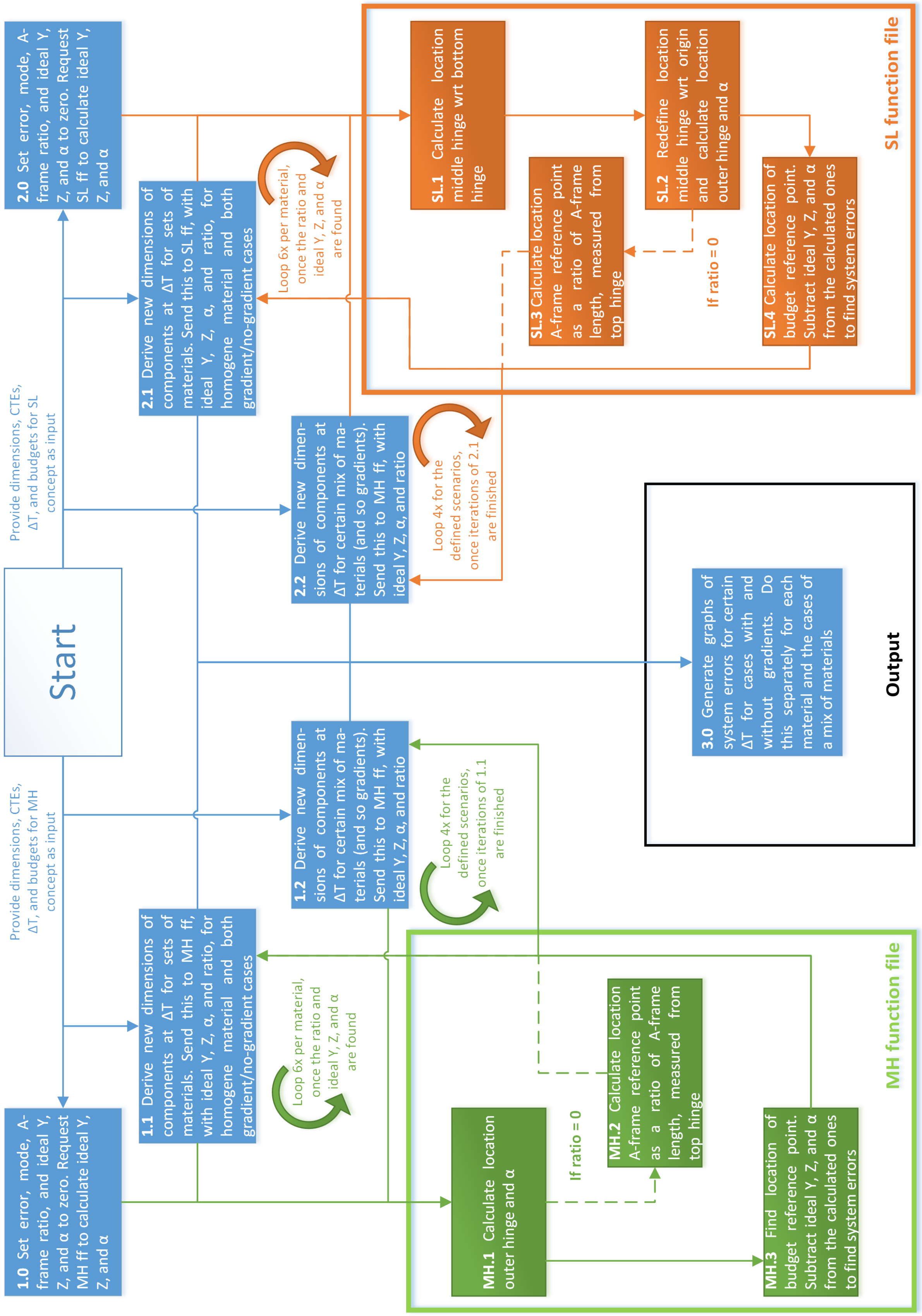

Figure 4.13: Functional flow diagram describing script of the sensitivity analysis for temperature change of +-15 *K*

The script starts by the programmer, providing the input for both models. This consists of the ideal dimension and relative locations of components, vectors providing the magnitudes of the component errors, and the error budgets provided at the budget reference point. The first run of both function files is performed to find ideal reference values. Therefore the error, A-frame ratio, and ideal Y, Z, and α are set to zero, before the function file runs in 'zero error mode'. In this mode blocks MH.0 and SL.0 are skipped. Then the location of the outer hinge and (the ideal) α are calculated. For the MH function file this is at block MH.1. For the SL function file this is at block SL.2, because first the location of the middle hinge is calculated in another reference frame in block SL.1. Since the A-frame ratio has a value of zero, the actual A-frame ratio will be calculated in block MH.2 or SL.3. This ratio represents the location of the A-frame reference point (see fig. 4.9) as a ratio between the distance from the top hinge to the A-frame reference point and the distance from the top hinge to the outer hinge. It is assumed that this ratio is constant, even with component errors. This means that the erroneous location of the budget reference point can always be calculated by taking the fixed distance to the mirror surface in perpendicular direction from the A-frame hart line (only in case of a thickness error, half this error will be added to the distance). The final blocks of both function files, MH.3 and SL.4, also produce values required in next error cases. They first calculate the Y- and Z-location of the budget reference point. These blocks normally end by subtracting the ideal Y, Z, and α values, but since they were set to zero, nothing is subtracted, and the calculated Y, Z, and α values are send to the next block in the master script as the ideal Y, Z, and α.

With the info of the zero error case, block 1.1 can now start running. It will send the ideal component dimensions and relative positions, the calculated A-frame ratio, and the calculated ideal Y, Z, and α, together with a new error vector and error mode for each case as input. This time all 8 error cases first pass block MH.0. Here the provided error vector is applied to the component that corresponds to a certain error mode. The next steps are comparable to the zero error case, except for that the subtractions in block MH.3 do now result in Y, Z, RMS, and α system errors and that block MH.2 is skipped, since an A-frame ratio that is not equal to zero is now available. The error cases at block 2.1 for the SL model follow the same system. It differs in the amount of error modes, and so the amount of cases. The SL model has 12 error modes instead of the 8 of the MH model.

For both models the next step is to find the relation between the component errors and each system error. For the MH model this is done in block 1.2. Except for the deployment error in the middle hinge, the relations between the errors are linear, so the values of the slopes are easily found. The relation between the deployment error in the middle hinge and the system errors is described by circles that touch the component error axis the origin. The radii of this circles are derived from the calculated data. In block 2.2 the component errors that the models have in common, are calculated in the same fashion. The component errors specific to the SL model have a higher order relation to the system errors, so they have been found by finding a second degree polynomial fit.

Once the relations between the component and system errors are found, it is calculated what the allowable maximum component errors are. This is done in block 1.3 for the MH model and block 2.3 for the SL model. In both cases first the budgets for the deployment precision are provided as the values for the system errors, from which the corresponding component errors are derived. Subsequently this is also done for the thermal drift budgets. The results are presented in two tables. Block 2.3 differs from 1.3 by providing a minimum and maximum allowable value for the component errors specific to the SL model. This is because the relation between the component and system errors is not symmetrical around the zero error line for these component errors.

Finally the results gathered in blocks 1.1 and 2.1 are used to generate graphs that show the effect of the component errors for each individual system error. The corresponding graphs of the two configurations are shown next to each other with the values at the edge for easy comparison.

SCRIPT FOR THE SENSITIVITY TO TEMPERATURE DIFFERENCES

The same function files are used in another model for finding errors that are caused by a certain temperature difference. To get a feeling on the system errors due to temperature difference, a case study was performed to find these errors for cases where steel, titanium, CFRP, or a mix of those materials is used in the components. The selected CTEs at a temperature of 20°C are provided in tab 4.3. Note that the choice for the CTE of CFRP is based on data sheets of the suppliers mentioned in the references. CFRP can be customized by using different materials, lay-ups, and production techniques, to obtain certain mechanical and thermal properties. Therefore the CTE can range from about -1.5, to zero, to a couple of tens $\mu m/(m-K)$ in the optimized direction (CFRP is an-isotropic with worse performance in other directions). However, only some suppliers have just one product with a close to zero CTE in the optimized direction. This is then mostly a CFRP sheet, meaning the shape needed within this project may not be available in a zero CTE version. When looking further, the suppliers mentioned above mostly offer one line of products that is designed for good thermal behaviour. Next to the rare zero CTE versions, these products mostly have a CTE between 0.6 and 1 $\mu m/(m-K)$, which resulted in the assumption that 1 $\mu m/(m-K)$ is representative for this analysis.

Table 4.3: Selected CTEs for analyzed materials

Selected CTEs for analyzed materials

	Steel	Titanium	CFRP
CTE [$\mu m/(m-K)$]	13 [90]	8.6 [90]	1 [91–93]

Another assumption made, is the temperature range the M1 system will operate in. It has been decided that a baffle will be designed to prevent large temperature differences, but the thermal model has not yet been made at this phase of the study. The person responsible for thermal modelling within the DST project, provided a temperature range of 30 K, or a +- 15 K difference from the design temperature, as a conservative estimate. Reordering eqn. 3.2 to eqn. 4.1, one can now find the multiplier, m_{temp} for each dimension, to arrive at the erroneous dimensions for the worst case scenario of the ΔT is +- 15 K assumption.

$$m_{temp} = \frac{L_n}{L_o} = 1 + \alpha \cdot \Delta T \tag{4.1}$$

Another essential assumption in this model is that the effect of temperature makes components freely expand and reach an equilibrium position. This way the effect of a thermal error is the same as for the case where components have originally been made with the erroneous dimensions.

Because of this the process is now quite similar to the other script, as shown in the functional flow diagram of fig. 4.13. An error, A-frame ratio, ideal Y, ideal Z, and ideal α of zero, together with the ideal dimensions and zero error mode, are provided to the function files in blocks 1.0 and 2.0 to calculate the A-frame ratio, ideal reference position and ideal angle. The results are again fed back to blocks 1.1 and 2.1, respectively, but then there is a significant difference. The component errors are not calculated in the function files, but in the master script. Here the temperature difference, ΔT, is used, together with the CTEs of the different materials, to calculate the erroneous length or relative position of each component for the three different materials. Note that blocks MH.0 and SL.0 of fig. 4.12 are now obsolete and that the function files keep running in zero error mode. This is done for 6 scenarios per type of material. The scenarios are:

- A gradient as a result of only heating the A-frame, which is a combination of the A-frame component error and thickness component error.
- 4 more gradients as a result of heating one component, such that one of the existing component errors of the MH and SL model will be representative for the result. A Z-error in the top hinge is however excluded, since its center is located on the Y-axis, which means it will not move in Z-direction due to thermal expansion.
- No gradient. A bulk temperature change equally affects all components, meaning that all component errors of previous two points act at the same time.

Since it is assumed a temperature change will not affect the deployment angle of the middle hinge, this component error plays no role in the calculations of block 1.1, or later on 1.2. After looking at the results of the previous script, it became clear that the system errors resulting from the component errors specific to the SL concept, are negligibly small. Since they clutter the graphs around the zero error point, they were not taken into account in block 2.1 and 2.2.

After block 1.1 and 2.1 are finished, the results for a homogeneous choice of materials has been found. In reality it is however more likely that different materials are used throughout the structure. Realistic options that were assumed, involve designs where the hinges, and possibly also the spacecraft bus, are made of a metal like steel or titanium, while the other components are made out of CFRP. Blocks 1.2 and 2.2 calculate the erroneous component dimensions for four different scenarios, that are used in the MH and SL function files, respectively, to calculate the corresponding system errors. The four scenarios are all bulk temperature changes without a gradient and are listed below:

- Hinges made out of steel, the rest out of CFRP
- Hinges made out of titanium, the rest out of CFRP
- Hinges and satellite bus made out of steel, the rest out of CFRP
- Hinges and satellite bus made out of titanium, the rest out of CFRP

After the results are found for both configurations, the data of blocks 1.1, 1.2, 2.1, and 2.2 is used to generate graphs that show the errors in Y-direction, Z-direction, and α. This results in four graphs, three describing the system errors for homogeneous use of the three chosen materials, and one describing the system errors resulting from the scenarios where a mix of materials is used.

4.2.3. RESULTS OF SENSITIVITY ANALYSIS

When looking at the results for the first time, it became clear that quite some component errors in the SL concept are negligible. For clearness purposes they have been removed from the plots. What is noticeable is that the negligible component errors were all the errors listed under 'Component errors that only apply to SL model'. Thinking about this, the reason is obvious and can be explained by a simple analogy. Fig. 4.14 shows two booms of 150 mm connected to each other. If one moves the middle hinge up by 3 mm, the new distance between the outer ends of the booms will be 299.94 mm. This means a 3 mm 'component error' results in a 'system error' of 0.06 mm, a decrease of a factor 50. Every error that could occur within the components that are specific for the slider design, will lead to a movement comparable to the 3 mm change in the example, meaning that the resulting error in the distance between the two strut ends (which eventually leads to the system error), is just a fraction of the component error value.

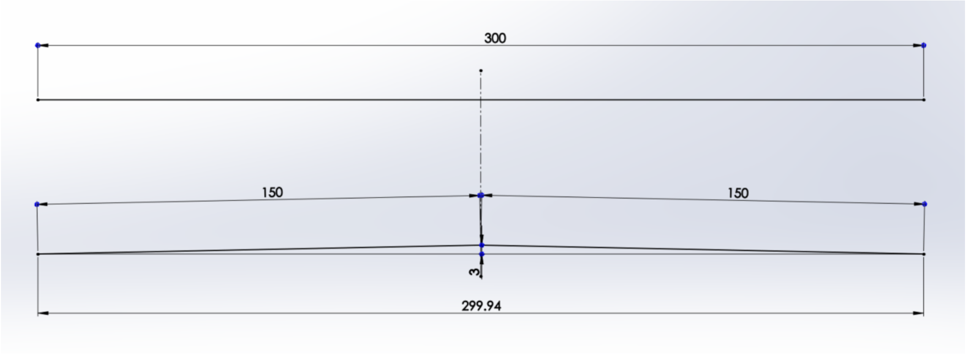

Figure 4.14: Sketch used to explain the decrease in error from component to system level for a triangle shape

The graphic results of the first sensitivity analysis look as depicted in fig. 4.15. It shows the system error in Y-direction due to certain component errors. The figures describing the system errors in Z-direction, the RMS of the Y- and Z-error, and the α angle, can be found in figs. B.1, B.2, and B.3 in appendix B. When looking to fig. 4.15 and the others in appendix B, it becomes clear that the system is most sensitive to the A-frame error, base strut error, and Z-errors in the bottom and top hinge. Looking at the slopes, the system is actually most sensitive to Y-errors in the top hinge, but since this component is small, the component error range is also smaller, and so the resulting system errors are very small compared to the other ones. An output of the script are the equations describing the relations between each component error and the different system errors. They are used to find the maximum allowable component errors to meet the deployment error budget and thermal drift budget, respectively. From these maximum allowable component errors tabs. 4.4 and 4.5 result, which present the driving maximum allowable errors. The 'driving' maximum allowable component error is the most strict value, that meets all of the Y-, Z-, and α-budgets. Note that in tab. 4.5 the first 8 component errors are provided in nm and μrad instead of μm and $mrad$, which is the case for the remaining errors in this table and all of the component errors in tab. 4.4.

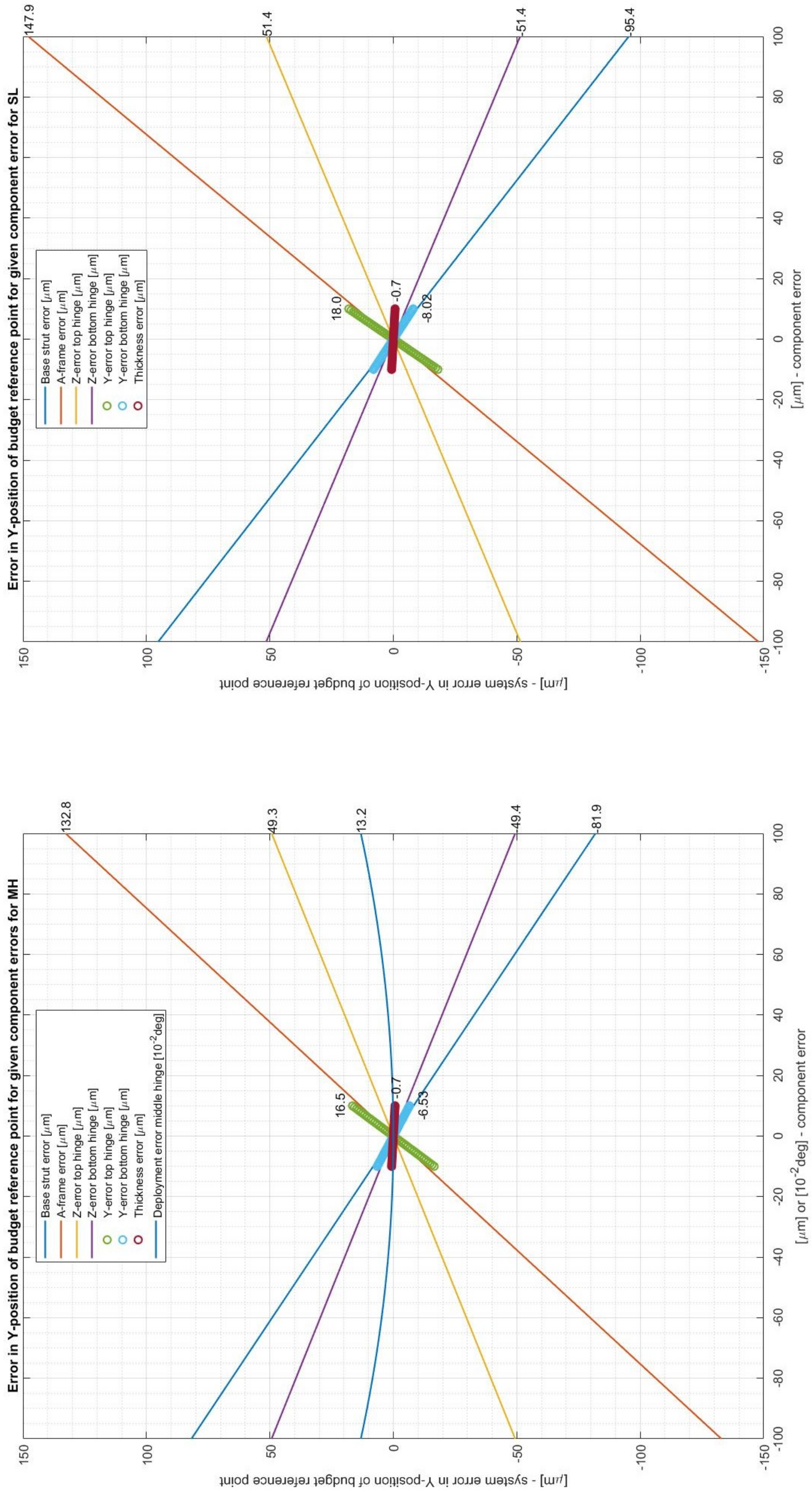

Figure 4.15: Graphs showing the system error in Y-direction as a result of different component errors, for the MH (left) and SL (right) concepts

The script that calculates the temperature errors for different materials, produced results as depicted in figs. 4.16 and 4.17. Fig. 4.16 describes the system errors in the YZ-plane and α angle when using CFRP as the component material. The effect of gradients, that are effectively individually acting component errors, are stated followed by a case without gradients, where a bulk temperature change acts. Plots like this have also been made for steel and titanium components and can be found in figs. B.4 and B.5 of appendix B. The results on a case involving components made out of different materials, is shown in fig. 4.17. It is clear that the best results are obtained when using only CFRP materials.

Finally tab. 4.6 uses the calculated component errors of a full CFRP design (best case scenario) for a 15 K temperature change and compares them to the driving maximum allowable component errors, calculated in the first script. A multiplication factor, indicating how much larger the error is than actually allowed, is provided in the last column. The results for the component errors specific to the SL concept are cut off in this table, since they are far from exceeding the budgets. In the case of a bulk temperature change, one can only look to how often the system error exceeds the budget. Dividing the system error in Y-direction of fig. 4.16 by the budget of 2 nm learns that the budget is exceeded 185 times for a 15 K temperature change in all components of a CFRP design.

Table 4.4: Driving minimum and maximum allowable component errors to meet the deployment error budget

Driving allowable component errors for:	**MH concept**	**SL concept**	
	Max (= -Min)	Min	Max
Base strut error [μm]	0.316	-0.271	0.271
A-frame error [μm]	0.362	-0.298	0.298
Z-error top hinge [μm]	0.524	-0.503	0.503
Z-error bottom hinge [μm]	0.524	-0.503	0.503
Y-error top hinge [μm]	0.396	-0.322	0.322
Y-error bottom hinge [μm]	0.396	-0.322	0.322
Thickness error [μm]	4.039	-4.039	4.039
Deployment error middle hinge [$mrad$]	2.447		
Slider strut error [μm]		-140.2	139.3
Z-error upper slider hinge [μm]		-165.4	166.5
Y-error upper slider hinge [μm]		-259.8	258.1
Lower slider hinge vs. base strut error [μm]		-140.2	139.2
Lower slider hinge vs. bottom hinge error [μm]		-140.2	139.2

Table 4.5: Driving minimum and maximum allowable component errors to meet the thermal drift error budget

Driving allowable component errors for:	**MH concept**	**SL concept**	
	Max (= -Min)	Min	Max
Base strut error [nm]	1.58	-1.36	1.36
A-frame error [nm]	1.81	-1.49	1.49
Z-error top hinge [nm]	2.62	-2.51	2.51
Z-error bottom hinge [nm]	2.62	-2.52	2.52
Y-error top hinge [nm]	1.98	-1.61	1.61
Y-error bottom hinge [nm]	1.98	-1.61	1.61
Thickness error [nm]	40.4	-40.4	40.4
Deployment error middle hinge [μrad]	173		
Slider strut error [μm]		-10.3	9.46
Z-error upper slider hinge [μm]		-11.2	12.3
Y-error upper slider hinge [μm]		-19.2	17.4
Lower slider hinge vs. base strut error [μm]		-10.4	9.41
Lower slider hinge vs. bottom hinge error [μm]		-10.4	9.41

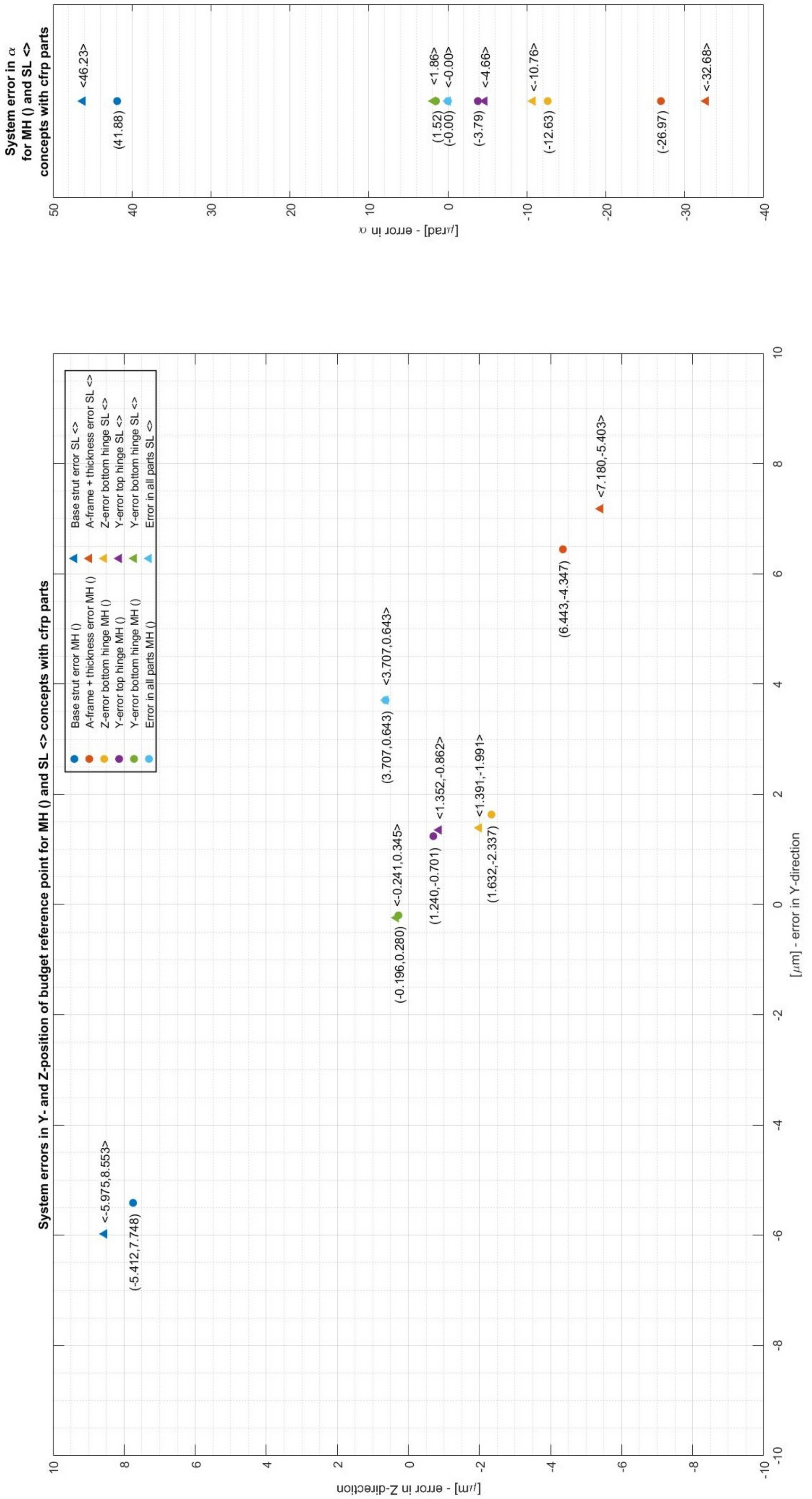

Figure 4.16: Graph showing the system errors in Y-direction, Z-direction, and α-angle due to gradients (represented as component errors) or a complete rise in temperature of 15 K. The structure is made completely out of CFRP materials in this analysis.

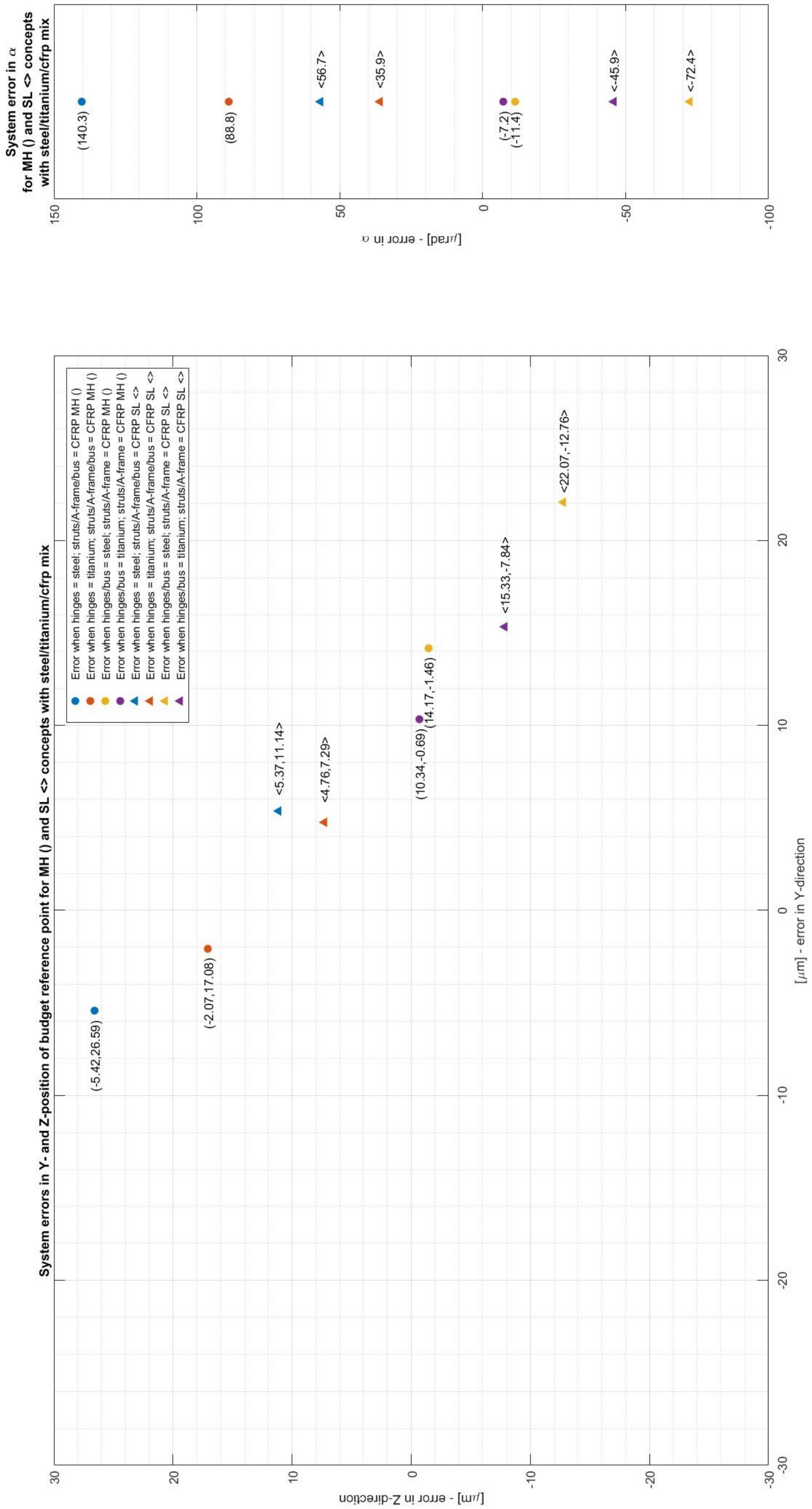

Figure 4.17: Graph showing the system errors in Y-direction, Z-direction, and α-angle for a rise in temperature of 15 K. In this analysis the structure is made up out of different mixes of materials, as indicated in the legend.

Table 4.6: Table indicating how much times the component errors exceed the ones allowed by the provided budget, in case the designs are made out of CFRP and experience a temperature change of 15 K

Temperature error results for CFRP designs at a ΔT of 15 K	**Allowed error** [nm]		**Actual error** [μm]		**Times exceeding allowed error** [-]	
	MH	SL	MH	SL	MH	SL
Base strut error	1.58	1.36	6.615	6.268	4189	4623
A-frame error	1.81	1.49	4.875	4.875	2697	3268
Z-error bottom hinge	2.62	2.52	3.310	2.704	1264	1074
Y-error top hinge	1.98	1.61	0.750	0.750	379	466
Y-error bottom hinge	1.98	1.61	0.300	0.300	152	186
Thickness error	40.4	40.4	0.225	0.225	5.57	5.57

4.2.4. CONCLUSIONS FROM SENSITIVITY ANALYSIS

Based on the results described above, discussions took place with experts of ADS that resulted in a couple of conclusions. The first comment was that taking into account manufacturing tolerances is not relevant, since component errors resulting from bad tolerances can be resolved by shimming. On the other hand, the graphs of the sensitivity analysis give a good overview on the critical (most sensitive) components.

A second conclusion is that, assuming shimming is possible up to the required precision, at this point the only relevant component error that can be assessed for meeting the deployment budgets, is the deployment error of the middle hinge for the MH concept. This error should be smaller then 2.447 $mrad$ or 0.140°. This value will go down once the microdynamic errors during deployment are added to the model.

Third, the allowed errors during deployment are really small and it is not sure if the budget can be met once microdynamic effects are taken into account. It is important to know that the deployment budgets are not defined by an assumed range a calibration actuator with a 10 nm resolution can work within. They are defined by the range in which the algorithm for optical optimization can work. If the deployment precision cannot meet the budget, two solutions are proposed; 1.) Add an extra actuation mechanism to the deployment mechanism that is able to correct in such a way that the deployment budgets are met. 2.) Use a calibration actuator with a range larger than the deployment precision. Then add sensors that can steer the mirror to a position where the optical algorithm can take over.

At the fourth place one of the most important conclusions was that meeting the thermal budgets is more complicated than expected. Probably this is more challenging than meeting the deployment budgets, so the focus of the research has to shift. Athermalization is an important next step in the design process.

A fifth conclusion is that even with a baffle, passive thermal control is not an option. The team members working on the thermal modeling and design need to come up with active thermal control solutions and provide a new temperature range to work within.

A sixth conclusion is that the different concepts have equal performance when heated without a gradient. However, once gradients are present there will be much larger system errors that are different for both concepts. Especially if only the base strut, outer strut, A-frame, or spacecraft bus (leading to Z-error in bottom hinge) are subjected to temperature change. All this means it is important to control local temperature variations in the baffle environment.

Finally, the discussion at ADS also pointed out that the slider concept brings quite some uncertainty at the moment. It is possible to properly design the sliding mechanism, but this may turn out to be more complex than expected. The need to design this will lead to a longer development time, more risk because the mechanism is not space proven, and the need of adding components that might influence the response to temperature change and the microdynamic response in a negative way.

4.3. CONCEPT TRADE-OFF

In this section a trade-off between the concepts is discussed. As usual the idea was to further develop the concept that came out best. After discussing this result with the project team and the experts of ADS, another plan was however made to continue the work. The trade-off and the reasoning behind it is discussed in subsection 4.3.1. The discussion and new plan that resulted from the trade-off are described in subsection 4.3.2.

4.3.1. RESULT OF TRADE-OFF ANALYSIS

In the original plan the idea was to perform a trade-off on the criteria shown in the left column of tab. 4.7. It however turned out that it was not possible to retrieve all the required information within the given amount of time. Also, not every criterion is relevant anymore, because it is comparable for the few design options left. The deleted criteria and the weight of the remaining ones are provided in the second and third column, respectively. An explanation for each of the criteria is provided below:

Table 4.7: Original and remaining trade-off criteria with their weight

Original criteria	Deleted criteria	Weight
Delivery time	X	
Price	X	
Repeatability	X	
Thermal properties		5
Complexity		4
Stiffness		3
Mass		3
TRL		3
Deployment shock		2

- **X - Delivery time** This was supposed to be a go/no-go type of criteria, since long delivery times lead to discontinuity in the project that is hard to handle with a team of MSc students. All the concepts in the trade-off table require components of which test specimen can be delivered in at most 6 to 9 months.

- **X - Price** This was supposed to be a go/no-go type of criteria. A financial budget is not provided yet, but discussions with the team manager and ADS were planned to assess whether the price for the components is reasonable, since the project mostly lives from subsidies. In the end it was concluded that the prices were not that high for space graded components.

- **X - Repeatability** The repeatability was supposed to be the most important criterion. Although the thermal properties seem more crucial after drawing the conclusions described in section 4.2, repeatability is still important. For now it is however not possible to assess the repeatability other than looking into the deployment repeatability of the middle hinges for the MH concepts. Since the sensitivity for errors is comparable for both models, the difference is also not a factor to differentiate upon in this trade-off. More research is needed that takes into account microdynamic effects.

- **Thermal properties (5)** The thermal properties form the most important criterion in this trade-off. This involves looking into the sensitivity of the different concepts to temperature change, the likelihood of gradients, and the risk of creep.

- **Complexity (4)** Complexity in this case means the effort required by the team to further develop this mechanism. How hard is it to implement a chosen tape spring hinge in the design? Is there a company that can produce characteristic components, that is also able to alter the component to the provided requirements? Or do you have to design and model special components by yourself? With the work force available, complex problems will probably result in delay of the project and brings the risk of mistakes, because MSc students graduate and the resulting discontinuity may lead to loss of knowledge.

- **Stiffness (3)** It is important to stay within the vibration stability budget and to have a high enough eigenfrequency. Since the eigenfrequency of the M1 mechanism (no matter which configuration) will most likely be quite a bit higher than the one of M2 mechanism, the M2 mechanism will probably set the requirements for the maximum vibration. On the other hand the stability budget for M1 is three orders of magnitude more strict and therefore the stability still has a weight of 3.

- **Mass (3)** Mass is of course always an important criterion for a space system. However, since this design is very challenging, it has been decided that good thermal properties and a low complexity are more important than finding the most optimal mass.

- **TRL (3)** The TRL is also an important factor. It not only gives an indication of the further development and testing that is required from the DST team, but it also indicates a certain risk since you only know if a new system actually works after testing.

- **Deployment shock (2)** The deployment shock can shake up a system in such a way that unwanted small displacements take place in certain components. This makes a low end shock favorable. The weight of this criterion is however low, because a damper can be added to reduce the shock. The need to add a damper reduces the score.

With these criteria, the information found in literature, the information received from manufacturers, and the analyses of section 4.2, a trade-off could be made as shown in tab. 4.8. The mechanism with the tape spring hinge of SpaceTech GmbH comes out best with quite a distance to the other concepts, although the stiffness and the deployment shock do not score very high for this mechanism. An elaboration on the reasoning for the grading per criterion is provided below:

Table 4.8: Trade-off for selecting the M1 deployment mechanism concept

Property (weight)	HTS tape spring	SpaceTech tape spring	HTS actuated latch	Slider
Thermal properties (5)	3	5	4	4
Complexity (4)	3	4	2	1
Stiffness (3)	3	2	4	5
Mass (3)	4	5	1	4
TRL(3)	4	4	4	2
Deployment shock (2)	4	2	5	5
Total score	68	78	65	67

- **Thermal properties** A point to start for the grading, is looking into the results of the analysis on the effects of temperature change. The conclusion was that all concepts perform equally well when heated/cooled without a gradient, but that the slider performs slightly worse for most gradients. Now one should think of the likelihood of the presence of these gradients. The slider mechanism and the mechanism with the SpaceTech tape spring hinge have a relatively low likelihood of gradients since these mechanisms can be made out of mostly the same material. The SpaceTech hinge is even an integral part of the strut, so no component in between breaks the conductive heat flow, which is why it is graded with a 5. The slider concept has an interruption in the middle of the strut, but possibly the middle hinge can be made of the same material as the struts, leading to less gradients. Since the sensitivity of the slider to gradients is larger than for the SpaceTech hinge, this concept is graded with a 4. Since the actuated latch of HTS also has only a fraction of the total strut length made out of another material, it is also graded with a 4. The HTS tape spring hinge actually leads to larger gradients than suggested in the thermal analysis. This hinge takes up a much larger part of the total strut length than the hinges in the slider and actuated latch concepts do. Also, this hinge is made of another material than the strut halves, making a gradient between the two strut halves more likely. The exact CTE of the HTS hinge is not provided, although it is stated that *"Excellent thermo-elastic stability is ensured by the intrinsically very low coefficient of thermal expansion (CTE) of the basic materials."* [94]. For now it is assumed that this CTE is worse than the CTE of the struts. This leads to a grade of 3.

- **Complexity** The foreseen complexity and required effort of the team to finish the design, differs for all concepts. The slider scores a 1, because a lot of thought still needs to go in the design of the slider. It is only slightly comparable to existing mechanisms, but a lot of creativity needs to come from the designer. Also this concept has the most components, leading to a lot of work. Both tape spring hinge concepts and the actuated latch concept are technologies that will be produced by companies that can alter the design to meet provided requirements. This saves a lot of work for the team, because designing these hinges with the required performance is a science on its own. From conversations with the companies it however seems that it will be easier to rescale the SpaceTech hinge to the required size than it is for the two HTS hinges. Also, the SpaceTech hinge is integrated in the strut, while the HTS hinges are placed between the two strut halves. This means more design work is needed to develop a proper interface. Finally the actuated latch may need another actuation mechanism when rescaled, leading to even more complexity. This leads to a grade of 2 for the HTS actuated latch, a 3 for the HTS tape spring hinge, and a 5 for the SpaceTech tape spring hinge.

- **Stiffness** When evaluating the stiffness, the slider concept is clearly the best, since this one is made up out of two triangles once deployed. This leads to a grade of 5. With the available data it is not possible to compare the other hinges based on quantitative data, so this has to be done in a qualitative way. It is hard to compare the linear stiffness of the tape spring hinges, but the torsional stiffness will be higher for the HTS hinge, due to the way the three tape springs are configured. Therefore the HTS hinge is graded with a 3, and the SpaceTech hinge with a 2. Since the actuated cone hinge is not made out of a tape spring, but a stiff latch, it is grade with a 4.

- **Mass** Concerning the mass, one can say that the actuated latch performs much worse than the other concepts. It is hard to say what the rescaled weight will be, but the existing design, made for a system that is quite a bit larger weights 3.5 kg. This makes it over 5 times more heavy than the comparable tape spring hinge. Therefore it is graded a 1. The other hinges are much more lightweight. The SpaceTech tape spring hinge is graded a 5 since this hinge does not add mass to the system that is not already there. The HTS tape spring hinge adds only a small amount of weight, relative to the overall M1 mechanism weight. The same holds for the extra components required for the slider concept. Therefore the latter two concepts are graded 4.

- **TRL** The score of 2 for the slider concept, rather than 1, is based on the fact that although this slider configuration has never been used before, sliding mechanisms have been used in existing satellites. An adopted version of one of these will probably be incorporated in the design when choosing this concept. The TRLs for the remaining hinges are at a level that gives confidence. They are not used in a space environment yet, but have reached TRL 5 to 6 as part of ESA programs that are still running. This leads to a grade of 4 for these 3 hinge concepts.

- **Deployment shock** The deployment shock will be lowest for the slider and actuated latch concepts. Even without dampers the end shock of both design will be low compared to the ones of the tape spring hinges. Besides, it will be fairly easy to add a damper to the end stop of the slider concept if required. This leads to a grade of 5 for these two concepts. Heavy end shocks are a typical feature of tape spring hinges. Dampers are available for both concepts, but are more complex and heavy than the ones that may be used for the slider. The HTS tape spring hinge however damps itself for quite a bit, since the bending directions of the tape three tape springs are opposite and cancel each other out to a certain extend, when simultaneously trying to snap in their own bending direction. A damper can be added if the low remaining shock load is still too large. Due to the self-damping, the HTS tape spring hinge is graded with a 4, while the SpaceTech hinge is graded with a 2.

4.3.2. DISCUSSION ON TRADE-OFF

The last discussion with Henk Cruijssen and Guus Borst, both experts of ADS, took place when the trade-off table was not completely finished. Even though the author had some preliminary results, the script for the sensitivity analysis was not finished. The rest of the picture concerning the trade-off was already quite clear. Back then the experts really pushed towards the SpaceTech hinge and in the end their feeling was proven right in the trade-off. That holds however for their feeling that the SpaceTech hinge was the best of the suggested concepts. Later, when the results of the sensitivity analysis were known, it was found out that even this concept is not good enough.

The data presented in tab. 4.6 indicates that the worst gradient of a concept with the SpaceTech hinge, exceeds the budget 4189 times. Also, this is a best case scenario where all components are made out of CFRP. Based on the results the team agreed that active thermal control is required. A new and challenging requirement was made, stating the maximum fluctuation in temperature should be +- 1 K. Since the errors scale linear with ΔT, this means the error would still be exceeding the budget by 279 times, in case of an ideal scenario regarding material choice.

At this point it was decided that help from the outside may be a good idea. That lead the team to Prof. dr. ir. Just Herder from the department of 'Precision and Microsystems Engineering' of the 3mE faculty of the TU Delft. The whole DST team had a couple of meetings with him, because other team members also got stuck on precision aspects of their design. The discussions lead to a new concept, described in the next section.

4.4. FINAL CONCEPT DESCRIPTION

Before the discussions with Just Herder took place, research was conducted into athermalization methods. Based on these findings and the discussions, a very different concept came out that is worth designing in more detail. This section first explains the train of thought that led to this concept. Afterwards the concerns that need to be looked into in a detailed design are discussed.

4.4.1. REASONING BEHIND FINAL CONCEPT

To find a concept that works, it is important to start by defining what the actual problem is. In this case that means finding the reason why the assessed concepts show bad thermal behavior, especially for gradients. The answer lays in the fact that all the concepts form a triangular structure. If one side of this triangle changes length, or the location of one corner changes slightly, it changes the shape of the whole triangle. In such a network of components athermalization mechanisms are difficult to incorporate.

One can get rid of the triangular shape by eliminating the strut. This leaves one with the strutless concepts described by Van Putten in fig. 4.1. The motor resistance concept still does not look attractive. The kinematic interface was rejected due to the higher mass and the vulnerability to vibrations. The extra mass comes from the need to create a kinematic interface, but is no deal breaker. The problem for this concept was that the A-frame is supported only at its root, while it carries a relatively heavy mirror. The stability budget in terms of vibration would not be met. On the other hand this concept is very attractive due to the high repeatability (highest of all concepts), the low complexity, and the high TRL. With the current knowledge it also seems that it is possible to implement athermalization, since it only needs to act in one component and thermal movement is simply derived.

The bad rating for the stability is however based on the assumption that the preload device is located at or near the kinematic interface. During one of the discussions with Just Herder, the question whether it was possible to apply the preload at the tip of the A-frame, instead of at the root led to a new way of thinking. If this is possible, a high repeatability, high stability, and athermalization, required to meet the three provided budgets, are possible.

It seems obvious that something will need to push up at the tip. This means a strut will be added again. The big difference with the previous one is that it is now not connected via a hinge that will deploy to a certain location, but that the strut now only should provide a constant force that preloads the kinematic interface. Soon the idea came up that a tape spring hinge that will not completely deploy is most suitable, since its bending moment only varies near full deployment, but is constant for all larger bending angles. An additional idea was that the concept of the SpaceTech tape spring hinge with the cut outs, could be applied multiple times at the root, tip, and in the middle of the strut. Now one saves mass by not requiring ball bearing hinges at the root and tip. Fig. 4.18 shows a sketch of the concept.

Brainstorming further, also considering the challenges of the mechanisms of other team members, the final idea came along. The M2 deployment mechanism has a very big challenge in achieving the right stiffness for acceptable repeatability and resistance to vibrations. Spanning lines from the top of the booms to a location more outward from the center of the satellite bus would be very beneficial. There is however an import limitation that discards a lot of options: the lines cannot cross the path along the optical axis that hits the primary mirror segments. This leaves the area shown in fig. 4.19. Considering this reasoning an idea came up that kills two birds with one stone. The A-frame can have extensions on both sides of the tip that are slightly wider than the mirror width. From these extensions a line can be spanned towards the top of the booms. A winch mechanism that starts pulling after the deployment of the M2 mechanism can now deploy the M1 mechanism and in the end provide the preload needed to both stiffen up the M2 structure and mate the two sides of the kinematic interface of the M1 mechanism. A render of the first version of this concept is shown in fig. 4.20. **An important note is a that in the remainder of this thesis, the 'A-frame' will be called the 'support frame', since it will lose its A-shape.**

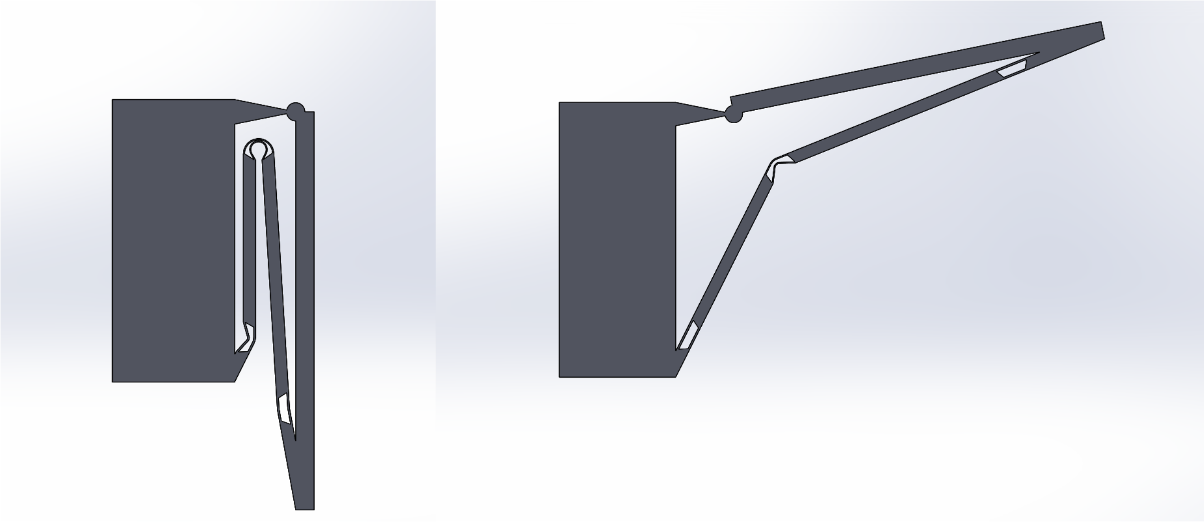

Figure 4.18: Sketch of a stowed (left) and deployed (right) kinematic interface concept with cut-outs that form tape springs to create a preload. The kinematic interface is not present in the sketch.

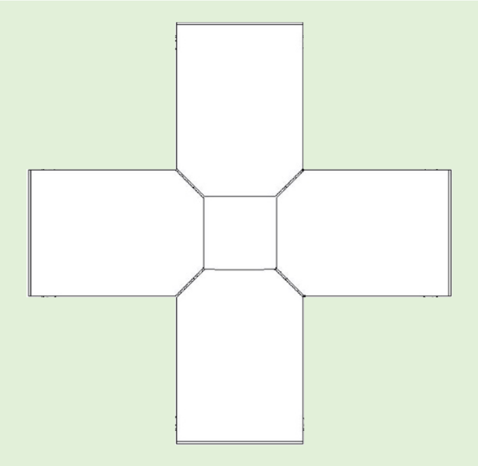

Figure 4.19: Top view of the M1 subsystem in deployed configuration. The green areas mark where the lines can extend through without disturbing the light path.

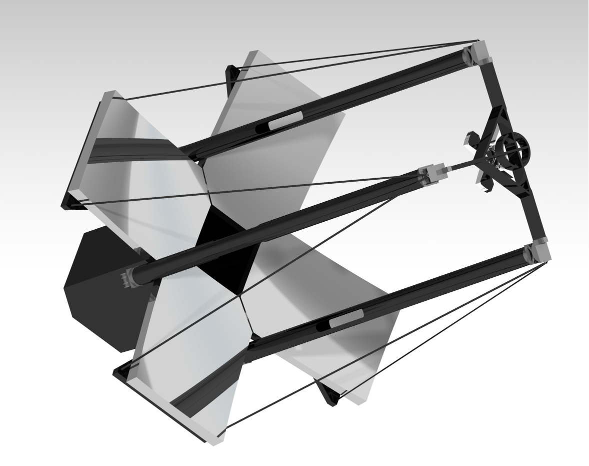

Figure 4.20: Render of the first iteration design of the final concept

4.4.2. CONCERNS OF THE FINAL CONCEPT

The concept with the preloaded line is great for both the M1 and M2 subsystems from a structural point of view. The idea however also raised some concerns. They did not seem impossible to solve, but did need a more detailed look into it. The concerns are listed below. The solutions to solve them are discussed in the next chapter on the detailed design of the mechanism.

- Lines may lead to an unacceptable amount of straylight. The round shape makes straylight scatter in a very unpredictable way. A ribbon (i.e. line with rectangular cross section) is proposed as a better alternative, but the optical engineers of the team first need to assess whether this solution is feasible.
- The loads imposed by the lines on the support frames should be symmetrical, which does not match with the current M2 mechanism design. At the moment this concept was developed, the M2 mechanism consisted of three booms (as in fig. 4.20), because four booms would make the system overconstrained. The developer of the M2 mechanism should assess how big of a problem a fourth boom would form. It would be too hard for the calibration mechanism on top of the support frame to correct for the motion induced by a line preload on only one side of the mechanism.
- The extensions of the support frame would move into the space reserved for the M2 booms in stowed configuration. A way needs to be found for both systems to coexist when stowed.
- A winch system with a high holding torque is required that does not require electrical energy once the pretension is at the required value. Also the winch needs to pull in a lot of line length. The line needs to retract roughly 0.5 m between the stadium where only the M2 mechanism is deployed and the stadium where both systems are deployed. Finding a mechanism with the right torque and winding capability that fits in the small space of 35 mm between the satellite bus and the stowed support frame is quite a challenge.

5

DETAILED DESIGN OF THE M1 MECHANISM

As discussed in section 4.4, the chosen concept offers a lot of advantages, but also requires a deeper look into some potential problems. During the detailed design phase the potential problems are mitigated and care is taken for the athermalization of the mechanism.

Two of the concerns listed in section 4.4 need to be investigated by other team members. Section 5.1 discusses their findings. Afterwards section 5.2 will present a solution where the M1 and M2 mechanisms can share the available volume in stowed configuration, since they would interfere in the current design. Next, the design of the support frame will be discussed, including the kinematic interface, in section 5.3. Then a deeper look is taken into the design of a winch mechanism in section 5.4. Finally section 5.5 describes how the support plate is athermalized.

5.1. CONCEPT FEASIBILITY CONCLUSIONS OF OTHER TEAM MEMBERS

There were two concerns about the new concept that were investigated by other team members. First the team members focused on optical design, noted that a circular line in the space between the M1 and the entrance plane of the light in the baffle environment, would lead to random and unpredictable scattering of straylight. This straylight is a serious concern, because direct light from the optical target will hit the line. A proposed solution was to make use of ribbons. The wide sides will now scatter the light against the baffle wall, and if the cross section of the ribbon would be a rectangle with sharp, non curved corners, the scattering at the thin side will may be negligible. An analysis was performed that indicated this was indeed the case, if a suitable coating is used.

The second problem concerns the overconstraining of the M2 mechanism. An overconstrained design has more than one constraining devices devices that constrain the same degree of freedom. This generally results into reduced performance (material binding, stresses, sloppiness, or imprecision), higher cost (tight tolerances or special assembly techniques needed), or both [85]. The new concept requires the use of four booms for symmetrical loads on the support frames. This makes the M2 system, which had three booms in the current design, overconstrained. It is hard to determine the effect of adding the fourth boom, because this requires a vibration analysis of ideally the spacecraft bus, M1 mechanism, and M2 mechanism. However, one can get an order of magnitude estimate by analyzing only the M2 mechanism. At the time the choice had to be made whether to proceed with four booms, it was not possible to perform this analysis yet. Another discussion with Prof. Just Herder lead to the qualitative conclusion that an overconstrained design is not necessarily bad, as long as a mechanism is symmetrical. Since this is the case, it is for now assumed that a four boom concept is feasible. It has been decided that the stability of the booms will be assessed for a three boom and four boom configuration, but at the moment of writing this thesis it is not possible to perform the vibration analysis yet.

To conclude this section, as long as the ribbon has the right coating, the introduced straylight is acceptable. Also, the four boom design is assumed feasible due to the symmetry of the system. The confirmation on whether this assumption is correct can however not be provided yet. This means that the new concept is assumed feasible at this point.

5.2. DESIGN ADJUSTMENTS FOR STOWED CONFIGURATION

When brainstorming about the ideal concept one is primarily concerned with the performance in operation. This means most of the thinking is about the system in deployed configuration. In terms of available volume there is much possible over there, but adding material may lead to problems with the limited available volume in stowed configuration. Challenges mostly come from the available space between the satellite bus and the support frame (fig. 5.1), between the support frame and the mirror (see fig. 5.1), and the available space in the corners between the mirrors (see fig. 5.2). To assess the challenges, they are investigated in two stages. First design options are formulated that only consider the M1 mechanism in subsection 5.2.1. Since extensions per definition interfere with the space that is currently reserved for the stowed M2 mechanism, solutions to this interference are discussed in subsection 5.2.2.

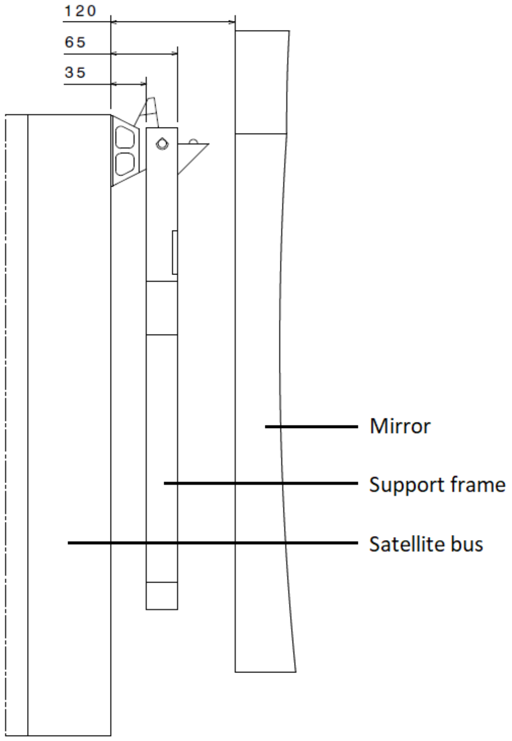

Figure 5.1: Side view of mirror segment in stowed configuration with dimensions indicating the available space in mm

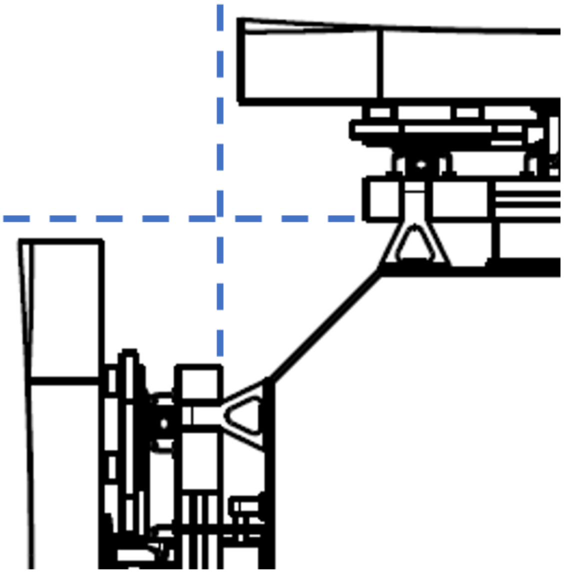

Figure 5.2: Top view of a corner of the M1 subsystem in stowed configuration with blue lines indicating where extensions of the support frame would run into each other

5.2.1. STOWED VOLUME OPTIMIZATION CONSIDERING ONLY THE M1 MECHANISM

A first thing that was found is that there is actually very little space for the extensions of the support frame, because they will interfere with the extensions of the neighbouring support frames (fig. 5.2). A screenshot and drawing of the first design are shown in fig. 5.3. With a clearance of 2 mm, only 13 mm of extension outside the mirror width is possible before the extensions interfere. This may be a too small extension to properly incorporate a pulley for the ribbon. A first potential solution that was investigated, was to make the neighbouring extensions at a slightly different height along the optical axis. This should be done in such a way that both extensions of one support frame are at one height, so that symmetry will be achieved over the XZ-, and YZ-planes of the spacecraft bus. This is shown in fig. 5.4.

Another solution is proposed where the support frame is not a flat plate in one plane, but a plate that makes out of plane steps that move towards the bottom of the mirror near the tip. It has been taken into account that there should be enough space left for the movements that the mirror will make due to the calibration mechanism. Screenshots of the single frame and the total assembly are shown in figs. 5.5 and 5.6, respectively. One sees that there is now much more room for the extensions on the support frame.

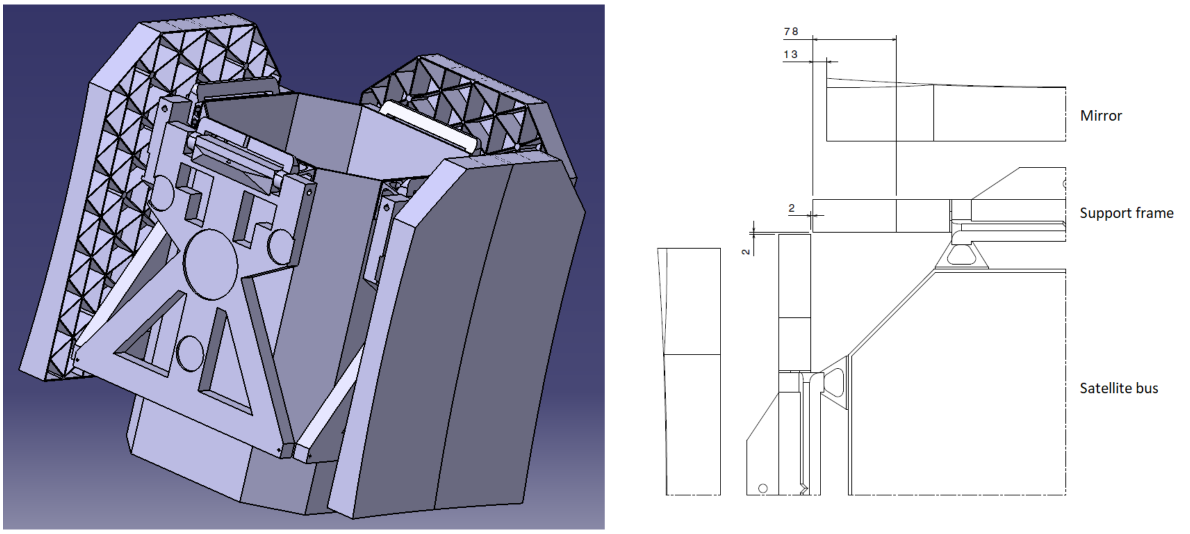

Figure 5.3: Left: screenshot of first iteration design with extensions for the ribbons. One mirror is hidden for a clear view - Right: drawing indicating the dimensions of the extension, the clearance between the extensions, and the remaining width to attach the ribbon to

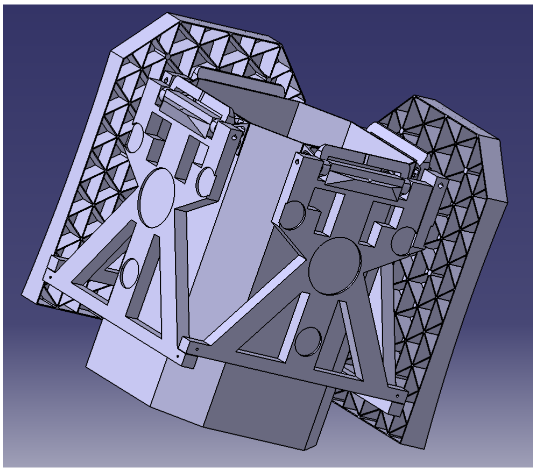

Figure 5.4: Screenshot showing a design where the extensions of two opposing support frames are at another height than the extensions of the other opposing support frames to create a fit

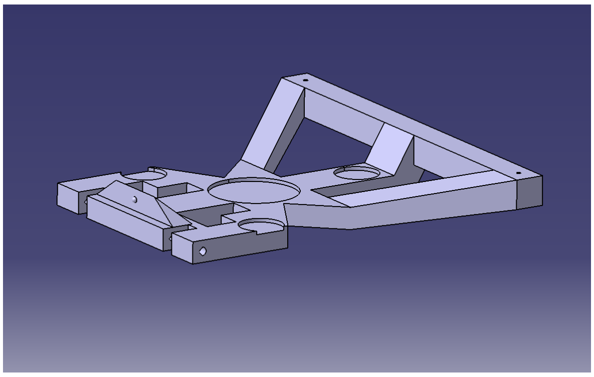

Figure 5.5: Support frame of which the end is out of plane, allowing it to become wider

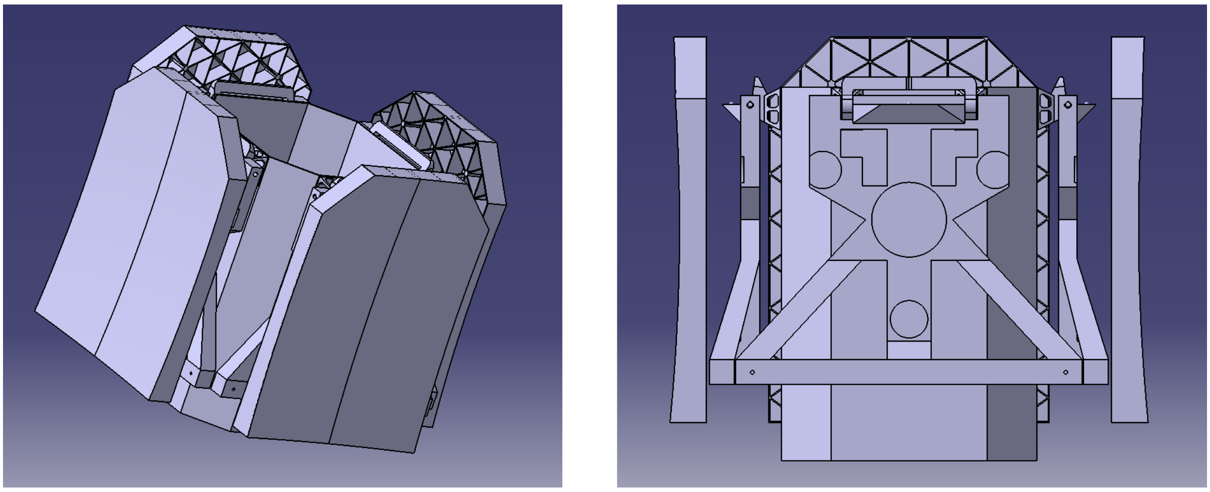

Figure 5.6: Left: screenshot with geometric view of the full assembly containing the out of plane support frame - Right: screenshot with side view of the same assembly, where one can clearly see the out of plane movement towards the mirror

5.2.2. STOWED VOLUME OPTIMIZATION CONSIDERING M1 AND M2 MECHANISM INTERFERENCE

So far, the proposed solutions only took into account the M1 mechanism. Once the M2 mechanism is considered as well, new challenges pop up. The first one concerns the proposal of the extensions with different heights along the optical axis, and its effect on the M2 mechanism. As discussed in section 5.1, overdetermination can potentially only be acceptable if the system is symmetrical. This should then also hold for the preload exerted by the ribbons on each boom. For the booms the symmetry planes of the loads should lay along the diagonals of the satellite bus, rather than the XZ- and YZ-plane. A difference in the height of the neighbouring extensions would mean that the symmetry is lost. Therefore this option is discarded.

Extending the width of the support frame outside of the original width, means one invades the space that is reserved for the stowed M2 mechanism. Currently the plan is to make the two boom halves of this mechanism align in lines nearly parallel to the optical axis. If this remains the case it is impossible to create the extensions. Discussions with the student responsible for the M2 mechanism led to the thought that it should be possible to make the first boom stow with a slight angle away from the satellite bus. If the extensions are far away from the hinges attached to the satellite bus, the angle should be small, meaning little compactness is lost. Therefore the next step was to think thoroughly about the way structural stiffness will be provided to the extensions, because the current design provides little of it with a triangular structure from the middle of the support frame. From a structural point of view the best option is to make the triangular structure right from the root of the support frame. This however means that the triangle would push the boom further outward. As a solution, one bar of the support frame will extend towards the tip on the edge of the area that should not be interfered. From there the triangular structure will be made close to the extension, so that only locally the area for the M2 boom is invaded.

Another way to keep the angle of the M2 boom small is to keep the support frame in plane and neglect the suggestion of previous subsection. The resulting support frame and the full assembly are shown in figs. 5.7 and 5.8.

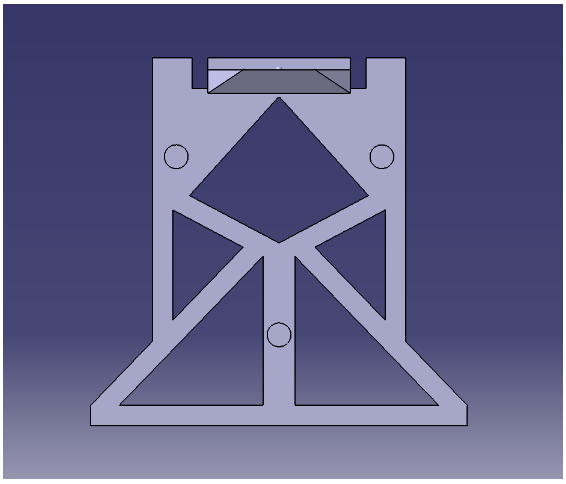

Figure 5.7: Screenshot of the support frame design, made to interfere the M2 boom area only near the ribbon attachment

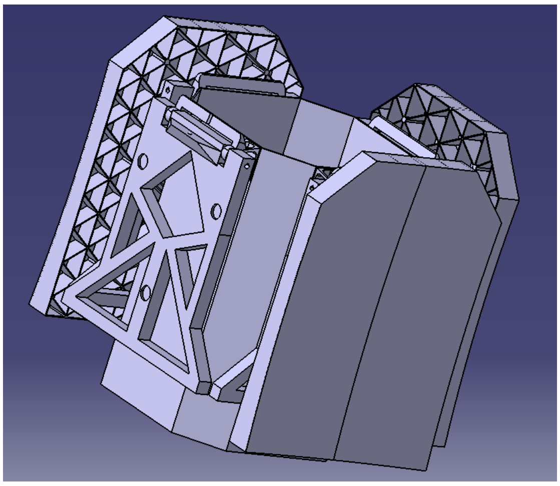

Figure 5.8: Screenshot of full assembly including the support frame of fig. 5.7, where it becomes clearly visible how little space of the M2 booms is occupied

The design decisions on how to adjust the support frame to be able to share the space with the M2 booms were made in a quick brainstorm. There was a lot of research and design work to do after these brainstorm sessions, where all the assumptions taken should have been verified. Recently it has been found that this has not been done yet for the assumption on the location of the stowed M2 booms. It has been found that the boom hinges extend so far outward that a vertically stowed boom will not interfere with the support frame at all. On the contrary, there is even some space left. Therefore one can make the triangular shape with the extensions straight from the root. Also there is now some room available to make the tip of the support frame move closer to the mirror. Due to time restraints it is not possible anymore to correct for this in this thesis research. Hence it is a design recommendation to correct this mistake during future work.

5.3. DESIGN OF THE SUPPORT FRAME AND ITS KINEMATIC INTERFACE

The support frame forms the core of the M1 mechanism. All other components are attached to it, and its mechanical and thermal properties play an important role to meet the budgets. Therefore subsection 5.3.1 will discuss the material choice of the support frame. Then the considerations leading to the chosen shape are discussed in subsection 5.3.2. Finally the details of the kinematic interface are explained in subsection 5.3.3.

5.3.1. MATERIAL SELECTION OF THE SUPPORT FRAME

Selecting the right material for the support frame is an important, but difficult task. One wants a material with a high specific stiffness, low CTE, high thermal conductivity, low outgassing, and low sensitivity to creep, that can be processed into the shape of the support frame. According to the MSc thesis of Van Putten [25] and several discussions with experts of ADS, a CFRP material optimized for good thermal properties is the best fit for these requirements. One can find general information on CFRP materials in literature and some more detailed specifications on the websites of manufacturers, but there are quite some properties that are not publicly available, or unknown because they depend on the specific geometry and environmental conditions. Therefore all considerations regarding the material choice and the assumed properties are discussed below.

COEFFICIENT OF THERMAL EXPANSION

In section 4.2 the products of some manufacturers are compared to find representative values for the CTE, which was required for modelling the thermal behaviour of the M1 mechanism concepts. Although some products have a zero CTE in the optimized direction ($CTE_{cfrp-opt}$) at room temperature, these products are rare. Since the DST team has no material experts, there are a lot of unknowns such as cost, manufacturability, and possibly other unknown factors that one has to take into account when finally selecting the material and manufacturer. To broaden the available materials, low CTE CFRPs were taken into account to end up with the assumption that 1 $\mu m/(m-K)$ is a representative value for the CTE in optimized direction at room temperature. Since CFRP is an-isotropic, the CTE in the directions perpendicular to the optimized direction ($CTE_{cfrp-per}$) is different. Unfortunately only one of the investigated companies, Mitsubishi Chemical Carbon Fiber and Composites, Inc.[91], offers product data in perpendicular direction. With a CTE that is between 3.5 to 10 times higher in perpendicular direction for their products, a conservative assumption is chosen to take a CTE according to eqn. 5.1, or in this case 10 $\mu m/(m-K)$. This is fair because the products with interesting Young's moduli have a value that is 8.5 to 10 times worse in perpendicular direction, except for the zero CTE variant, which comes very close with a value of 11 $\mu m/(m-K)$. Since the support frame is part of a high precision device and CTE is a function of temperature [95], it is important one picks a CFRP material with zero or low CTE at the operational temperature. Since this temperature is not known yet, room temperature is assumed for now. Furthermore the temperature variation will be low (+-1 K, see section 4.3.1), but it should be investigated whether this is low enough to assume a constant CTE and still meet the precision requirements. For now it is assumed that the CTE is constant. If it turns out this is not the case, one has to redesign the athermalization devices described in section 5.5.

$$CTE_{cfrp-per} = 10 \cdot CTE_{cfrp-opt} \qquad [5.1]$$

THERMAL CONDUCTIVITY

Another important thermal property is the thermal conductivity. It is beneficial to have a high conductivity, because this means that a temperature change will quickly spread over the whole component. If this is not the case, gradients will commence that lead to shape changes that are hard to predict and not constant. This means one cannot apply passive athermalization methods, which are required to meet the budgets. In general products made out of pure carbon have a high thermal conductivity, and in some forms the highest of all materials. Graphite has a thermal conductivity of 300 $W/(m-K)$, whereas diamond has a value between 900 and 2300 $W/(m-K)$ and Carbon Nano Tube (CNT)s are theoretically predicted to have values up to 6000 $W/(m-K)$ [96]. This compares to other materials with values from 13.4 $W/(m-K)$ (AISI 316 stainless steel) to 429 $W/(m-K)$ (pure silver) for metal alloys, from 0.02 $W/(m-K)$ (Polyurethane) to 0.51 $W/(m-K)$ (Polyethylene) for plastics, and from 0.1 $W/(m-K)$ (lightweight concrete) to the discussed 2300 $W/(m-K)$ for non-metallic ceramics [97, 98]. CFRP materials can have very different thermal conductivities, depending on the amount of resin matrix used. The carbon fibres have a high conductivity, but due to the plastic resin, one often ends up with a low conductivity. This especially holds for low CTE CFRPs, because a certain amount of resin is required to compensate the negative CTE of the carbon fibers. The thermal conductivity values for the researched materials are between 2.5 and 115 $W/(m-K)$ in the optimized direction. Like the CTE, also this value is different in the direction perpendicular to the optimized direction, and again only Mitsubishi provides this data. The perpendicular conductivity is similar for all products with values between 1 and 1.3 $W/(m-K)$.

To conclude the thermal considerations it will be discussed how the material will be applied to the support frame design. Considering that the longest dimension of the support frame is the one from the root to the nose, the optimized direction shall be put in this Y-direction as seen in the XY-plane of the support frame reference system (fig. 2.9). First of all, because a low CTE offers the most notable effect in this direction, and second, because there are quite long dimensions of material that need to be crossed in this direction once temperature changes occur, requiring high conductivity. The CTE in the other directions will be compensated by athermalization devices, as discussed in section 5.5. The low conductivity in these directions is also less of a problem, because the energy transfer during a temperature change does not have to go very deep due to the small thickness of the plate.

SPECIFIC STIFFNESS

So far the material discussion was mainly about the thermal properties, but there are more factors that play an important role in the material selection. A very important one is the specific stiffness, a measure to indicate how stiff a material is with respect to its weight by dividing the Young's modulus by the density. Fig. 5.9 shows a chart with the Young's moduli and the densities of different material classes. The upper left corner represents a high specific stiffness. Note that the scales are logarithmic for both axes, but that the Young's modulus increases much faster in value. Therefore CFRP has a much higher specific stiffness than the high modulus wooden products, especially compared to the ones on the far left. With this it becomes clear that certain ceramics are the best choice for a high specific stiffness and that CFRP comes in as the second best choice. Therefore an extra look has been taken into ceramic materials. Their thermal properties differ a lot, but for one type they look promising: boron nitride.

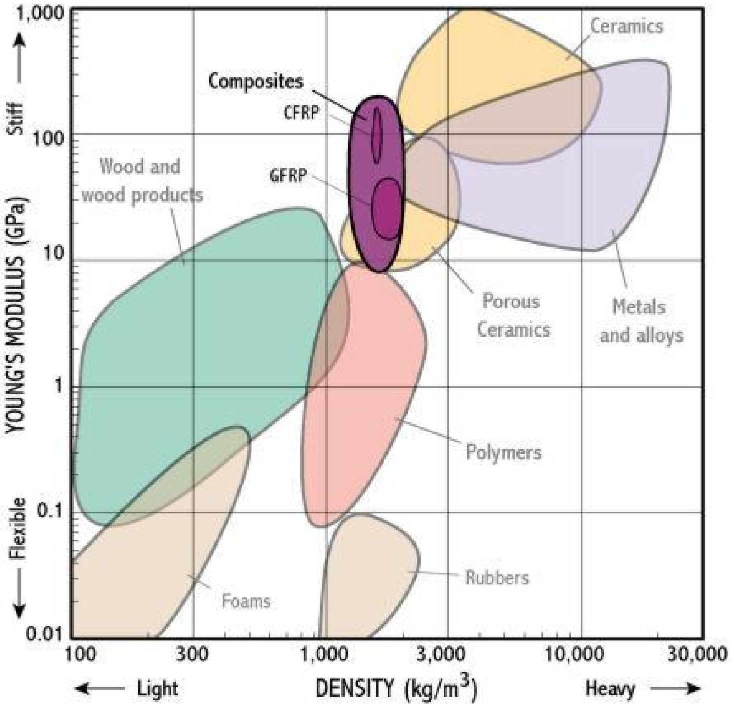

Figure 5.9: Chart indicating the Young's modulus versus the density for different material classes. The upper left corner represents a high specific stiffness, whereas the lower right corner represents a low specific stiffness [99]

Boron nitride is a ceramic that can come in different molecular structures with different properties. In this case research was performed on hexagonal boron nitride (H-BN), which is an an-isotropic form of boron nitride that is produced by hot-pressing. This leads to different properties in the pressing direction and the plane perpendicular to this. For the so called AX05 grade, the CTE and thermal conductivity are 1.0 $\mu m/(m-K)$ and 78 $W/(m-K)$, respectively, in pressing direction and 0.3 $\mu m/(m-K)$ and 130 $W/(m-K)$, respectively, in the perpendicular plane [100, 101]. This means that the preferred properties actually act in a plane and that the worse properties now only act in one direction, which is better than is the case for CFRP. The specific stiffness is however 2.5 to 5 times lower than the investigated CFRP materials. The required extra mass is the main driver for not selecting H-BN, together with the fact that the European Cooperation for Space Standardization (ECSS) engineering handbook [100] suggests that due to the brittleness it is preferable to choose another material unless it is used for high temperature environments. In that case, elaborate reviews on selection, design, and verification are required according to ECSS standard ECSS-Q-70-71.

OUTGASSING

Another factor to be aware of is outgassing. Plastics always contain a certain amount of water and when exposed to a vacuum environment this water tends to outgas from the material. Metals and ceramics usually do not lose internal material, but can outgas contaminants that nested on the surface after production. As a result two problems arise. First, the gasses tend to condensate on cold surfaces. If this surface is a lens or mirror, it lowers the image quality. Both ESA and NASA have standards describing the allowed outgassing rates to minimize problems with contamination of optical surfaces for most cases, although sometimes more stringent requirements are needed. For ESA projects the acceptance limits are described in section 5.5.3 of ECSS standard ECSS-Q-ST-70-02C [102]. The second problem of outgassing is that the mechanical properties and shape of the material will change. The change in mechanical properties is probably negligible, but a change in shape can be problematic, since the support frame is part of a high precision mechanism. None of the investigated CFRP suppliers provide information about the outgassing properties of their products. Although it seems likely they meet the standards, since they have all flown on space missions, it is highly recommended to still discuss the properties to find out how much the shape will change. If this turns out very critical one may reevaluate the choice of CFRP over H-BN.

CREEP

A final factor to take into account is creep. This is the time-dependant and permanent deformation of a material when subjected to a constant load or stress [103]. Different forms of creep exist and for polymeric materials like CFRP the most dominant form is viscoelastic creep. During viscoelastic creep stress relaxation occurs when applying a constant stress well below the yield strength. The stress causes the molecular structure to rearrange in order to lower the stress, which is seen as strain in the material. The strain rate increases at higher temperatures or higher loads. Since the ribbons will apply a constant load over the whole operational phase of the satellite, it is important to investigate the resulting amount of creep. Unfortunately none of the suppliers provides creep properties, but it is highly recommended to request this data once they are contacted.

An initial concern of the author was that the outgassing may influence the creep behaviour as well. For CFRP in a vacuum environment an analogy can be found to the creep of concrete. Concrete has unique creep properties, because it contains molecules that interact with water. Drying or hydrating concrete not only results in expansion or shrinkage of the concrete (which is not equal to creep), but also the creep properties will change. Knowing that CFRP will also lose water in vacuum, it was hypothesized that this may also influence the creep behaviour of the support frame. No literature has been found on the combined effects for outgassing and creep, except for a technical document of the company Paroscientific, Inc. [104]. The document describes a root cause analysis of drift in a Quartz Sensor of the company Quartz Seismic Sensors, Inc. The conclusions is that drift is caused by a combination of outgassing and viscoelastic creep. When looking at the graph describing the drift due to outgassing, the drift due to creep that starts at different moments in time, and the combined drifts at those moments (fig. 5.10), one can clearly see that the drift due to creep is equal at all placed, regardless of the amount of outgassed materials. Therefore the effects behave independently and can simply be added to end up with the combined drift. Possibly a quartz crystal is not representative for a combined case with CFRP, but since no other literature has been found describing a dependability of creep on the outgassing, it is assumed that this is not the case.

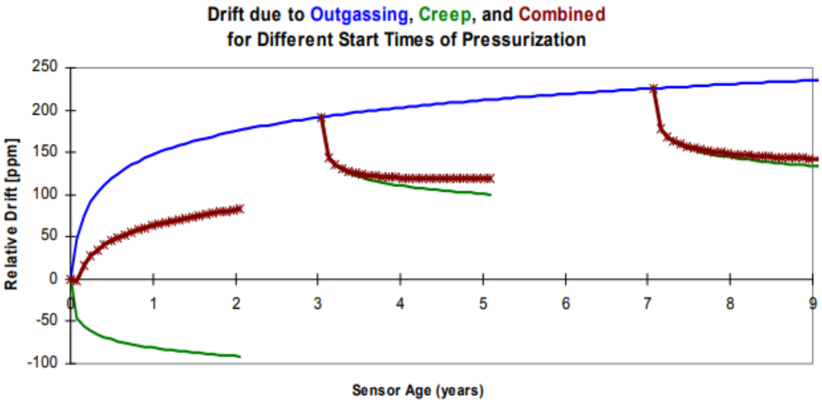

Figure 5.10: Graph showing drift in a Quartz Sensor over time for a case where only outgassing is present, for the case where only creep occurs after starting to apply pressure for three different time intervals, and for the combined cases [104]

5.3.2. DIMENSIONING OF THE SUPPORT FRAME

When looking at the final design of the support frame (fig. 5.19), it immediately becomes clear that it has a very specific shape that is optimized for weight savings. The development of this shape started however with the A-frame of the design made by the previous student working on the M1 mechanism. From there it has iteratively been updated by adding certain elements to the support frame design, adjusting the shape to the elements mounted on it, and designing appropriate cutouts for weight optimization. Since the support frame has not been developed during a dedicated design phase, but was rather updated when needed after making other design steps, this subsection will summarize how it evolved by shortly mentioning all the factors that influenced the design. Most of them are discussed more thoroughly in their own dedicated section or subsection.

It all started with the A-frame as shown in fig. 5.11. When it was already known that the initial trade-off concepts were all unfeasible, and help was still sought from the outside, a start was made with the athermalization of the A-frame. This is shown in fig. 5.12 and described in section 5.5. Here it was still assumed that the calibration mechanism would look the same as in the design of the student previously working on the M1 mechanism. Another MSc student, Sean Pepper, however started working on the calibration mechanism in the meantime. He decided to make a new concept trade-off that did not include the old mechanism as one of the options. Therefore, the next design iterations of the support frame do not include the athermalization mechanisms, because it was still unknown what they were going to look like.

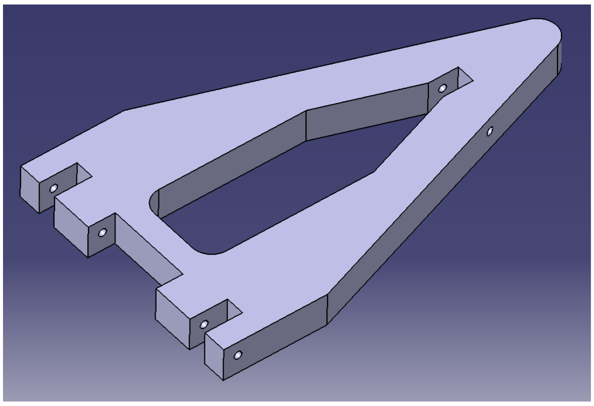

Figure 5.11: Screenshot of the original support frame (then still called A-frame), made by Van Putten [25]

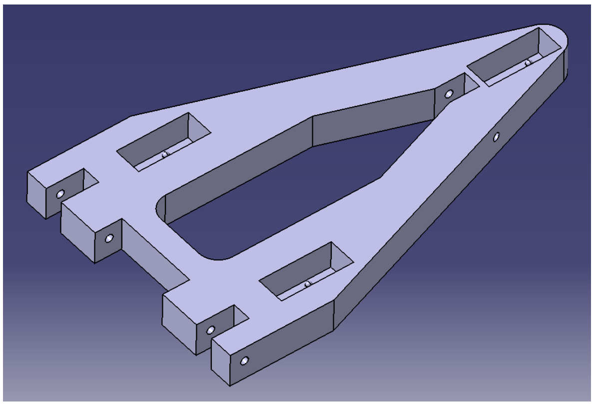

Figure 5.12: Screenshot of A-frame where athermalization design practises have been applied

Once the final concept came out of a brainstorm session, first the kinematic interface was designed as shown in fig. 5.13 and discussed in section 3.3. Afterwards the A-frame made a complete make-over to what is now called the support frame, by incorporating the extensions of fig. 5.14. In this figure one can see that there are four pockets to indicate the calibration actuator locations, because Pepper assumed that another type of actuator would be used than the one that was chosen eventually. Then several design options were explored that allow the support frame and M2 mechanism booms to coexist in stowed configuration. This led to the design of fig. 5.15, as discussed in more detail in section 5.2. In the figure one can see that only three calibration actuator locations are indicated, because a final decision on the concept had been made in the meantime.

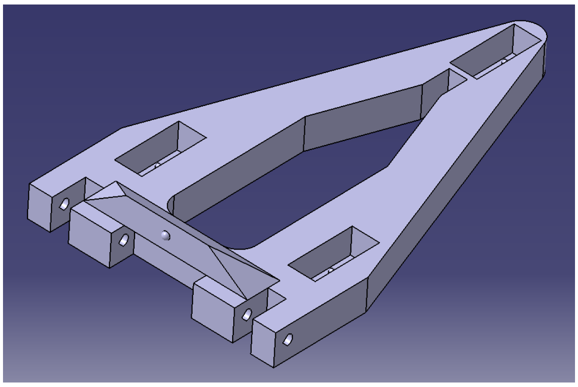

Figure 5.13: Screenshot of A-frame with kinematic interface

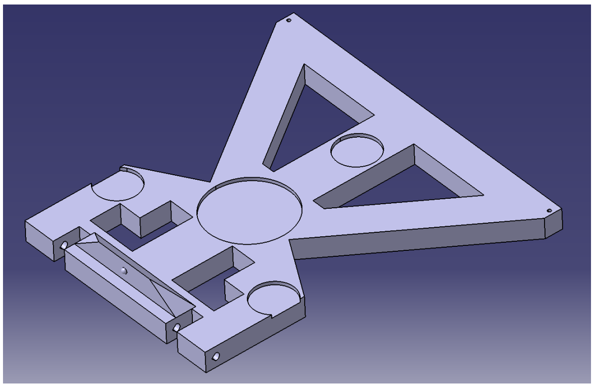

Figure 5.14: Screenshot of first iteration support frame with extensions

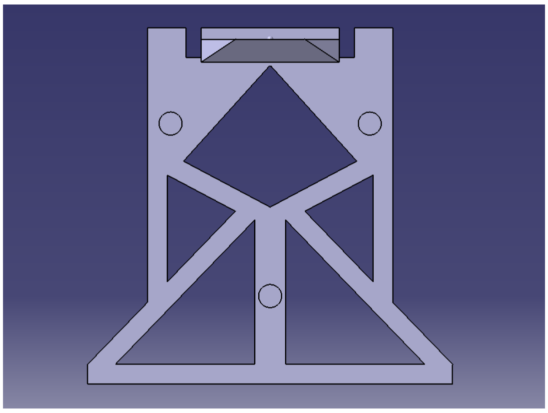

Figure 5.15: Screenshot of the support frame design, optimized for as little interference with the M2 booms as possible (copy of fig. 5.7)

After creating the extensions, an actuator assembly involving a constant force spring was made. Soon after it was found that the concept would not work as intended, so further development of this idea was not continued. The interface with the support frame was however already created and can be recognized in some of the intermediate support frame concepts. The constant force spring assembly required a big area on the back of the support frame for attachment. Also a cutout with a shallow depth is created to fit the mechanism in the available space, as shown in fig. 5.16.

Next to providing a concept for the calibration actuators, Pepper also looked into ways to hold the M1 structure in place during launch. It is preferred to connect the center of the mirror to the bus via an HDRM. It is assumed that it needs to survive quasi static accelerations of 30 g (requirement M1-MEC-09-01) acting on only the mirror, since the support frame will also be connected to the spacecraft bus in another to be determined way. With an estimated mirror mass, m_{mirr}, of 5.9 kg [25] this leads to a required hold down force, F_{hd}, of 2.43 kN according to eqn. 5.2. Here the a_{launch} is the 30 g acceleration that translates to 294.3 m/s^2 and FS_u the safety factor of 1.4 for static ultimate loads, as defined in the DST Requirements Document [21]. Looking for HDRMs at supplier websites, one sees that it is hard to find a mechanism with a rated load close to the required one [105–107]. The closest ones are designed for 4.45 kN (1000 lbf), 6 kN, and 5 kN, at the companies Glenair, NEA Electronics, and Arquimea, respectively. Although the mechanisms of the former two companies have a lower mass and probably smaller dimensions than the latter company, this cannot be stated with certainty. The brochures of both companies use both metric and imperial units, without clearly stating which units are used in the technical drawings. Therefore the HDRM of Arquimea is selected as a conservative measure. The diameter of this device is 47 mm. The support frame of fig. 5.16 takes into account that a clearance is needed to fit the HDRM mechanism, as seen in fig. 5.17. The diameter of the device has been rounded to 50 mm and the structure is designed around this circle with a clearance of 5 mm. The remainder of the material that is cut out has been removed for mass optimization. Note that in a later design stage material may need to be added again to conform strength or athermalization requirements.

$$F_{hd} = m_{mirr} \cdot a_{launch} \cdot FS_u \qquad [5.2]$$

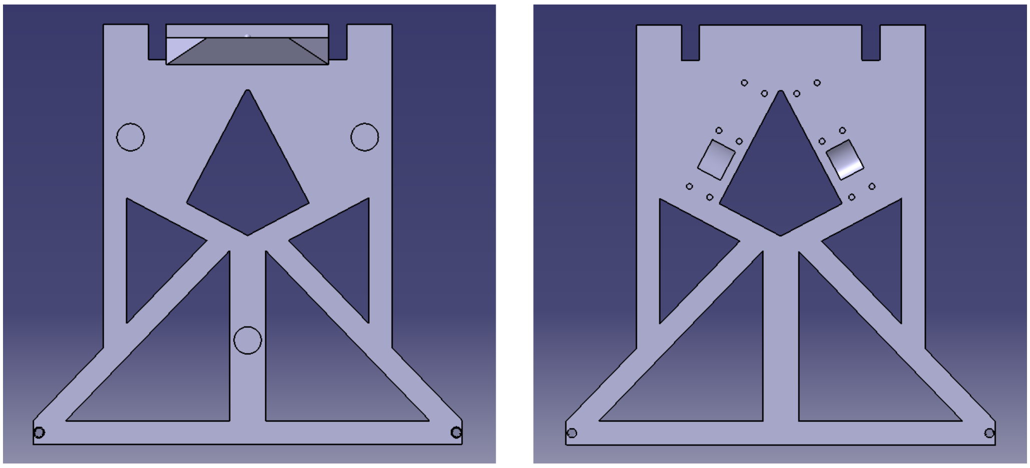

Figure 5.16: Left: screenshot in top view of the support frame designed for a constant force spring mechanism to retract the ribbon - Right: screenshot in bottom view of the support frame designed for a constant force spring mechanism to retract the ribbon

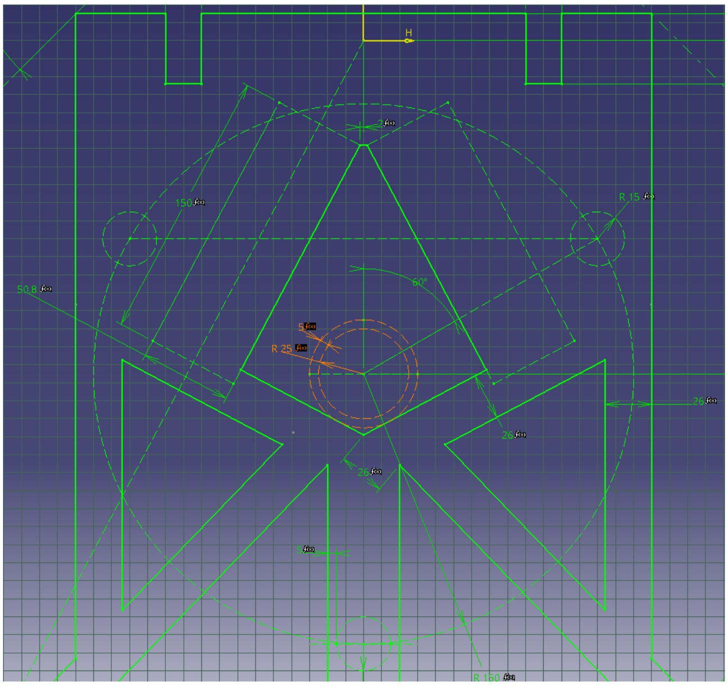

Figure 5.17: Part of the sketch that describes the shape of the support frame. The orange circles and dimensions represent the diameter of the selected HDRM and an additional clearance that need to be kept free to make space for the HDRM

In the next version of the support frame, athermalization was applied by creating an interface for plates that apply thermal expansion compensation. This is discussed in more detail in section 5.5. The result is the design of fig. 5.18, where especially the calibration actuator near the tip is visible due to the wider connection between the center and the tip edge of the support frame. Additional material has been cut from the support frame in this figure.

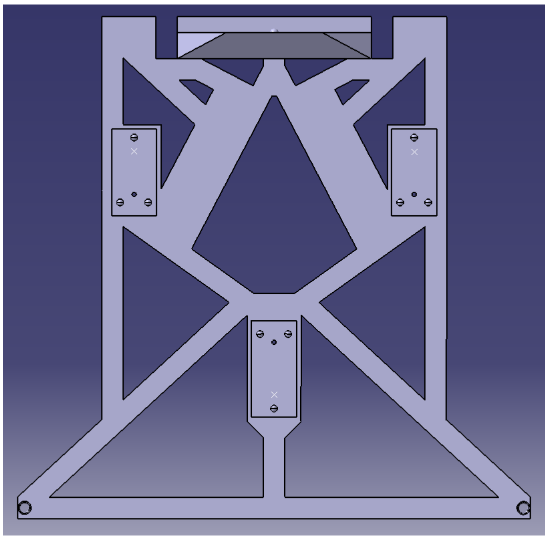

Figure 5.18: Screenshot of the athermalized version of the support frame of fig. 5.16

In a later design stage it was decided to preload the ribbon with another winch design. This design is attached via a differently shaped mount, leading to the design of fig. 5.19. Another addition in this design is the adjustment of the upper edge of the ribbon hole and a wedge that is added to the lower edge of this hole to prevent unwanted twisting effects in the ribbon. This is discussed in the end of section 5.4.

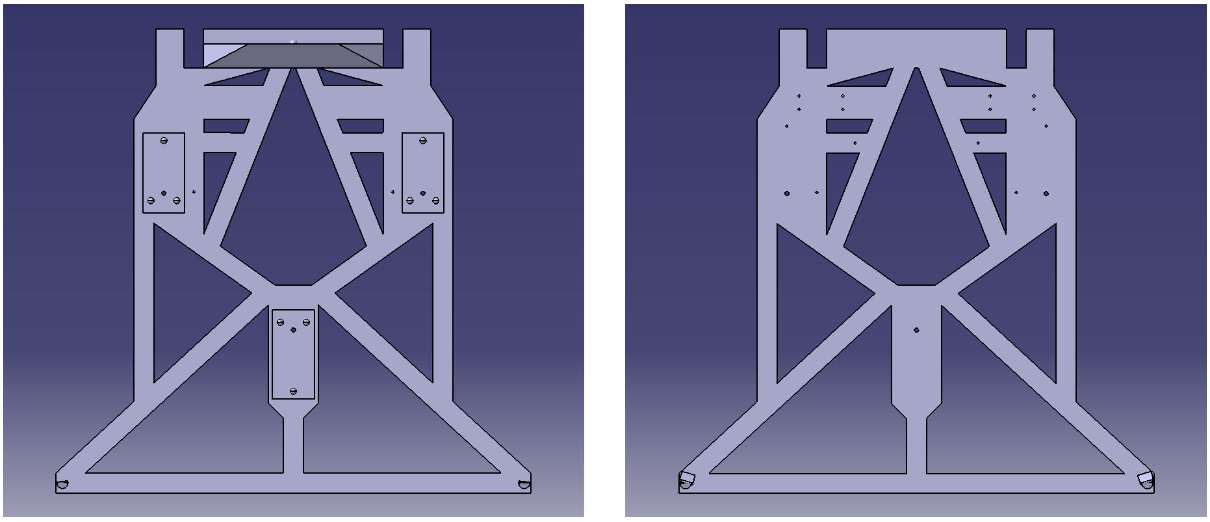

Figure 5.19: Left: screenshot of top view of the final support frame design - Right: screenshot of bottom view of the final support frame design

At the moment there are still quite some open ends in the design of the support frame. This leads to the following list of recommendations:

- The support frame is currently flat with with triangular structures that go from the center of the frame towards the extensions. This has been done to save room for the stowed M2 mechanism booms. As explained in the end of section 5.2, it has been found that the initial assumption regarding the available space was incorrect. There is actually some space left, but due to time constraints this will not be corrected in this thesis work. This leads to the recommendation to start the triangular structure towards the extension from the root and to give the frame a bend profile where the tip is located closer to the primary mirror.
- The ribbon hole on the mirror side of the support frame is rounded such that the ribbon is perfectly aligned for twisting effects, when being (nearly) fully retracted only. The angle between the edge of the hole and the top of the M2 mechanism boom is different in other phases of the retraction. It is recommended to find out how big the difference is and whether this difference may leads to problems. If yes, it is probably necessary to make an edge on top of a bearing that will rotate towards the ideal angle automatically.
- The wedge for the ribbon near the ribbon hole on the winch side of the support frame is accidentally designed as part of the support frame, rather than a component on its own. The manufacturing process is expected to be much easier and cheaper when the wedge is a separate component. This component may become more complex due to the same reason as the one of the previous bullet. Now the change in angle is the result of the effective winch diameter, which becomes larger while retracting the ribbon.
- The sides of the triangular structures that the support frame is made out of have a width of 20 mm. This dimension has been chosen quite arbitrarily with an engineering gut feeling. By performing static force and vibrational analyses with the expected disturbances of the reaction wheels and the preload applied by the winch as inputs, one can optimize for this width. One should find the width that gives the structure just the right stiffness and strength to not bend too far or deform plastically due to either the preload or vibrations.
- All edges are currently sharp. It has not been investigated yet how the material is manufactured and whether it is more complex to make rounded shapes. Also, the material properties are an-isotropic, meaning it has certain properties in the thermally optimized direction and different properties in the directions perpendicular to the optimized direction. It is not investigated whether round edges in the material are the result of finishing a sheet where the fibers all point in the same direction, or the result of fibers that bend along with the curve. Mass will be saved when adding round edges, but if the latter situation holds it needs to be confirmed what the resulting thermal behaviour of the support frame will be.

5.3.3. DESIGN OF THE KINEMATIC INTERFACE

The kinematic interface is an important feature of the support frame. It allows to achieve a high deployments precision by making use of the ribbon preload. Based on the theory of section 5.3, it has been chosen to make an interface with 3 grooves that point to the same thermal center. This thermal center is located in the symmetrical plane of the support frame at the center of rotation. Since there would be little space available for the interface if the support frame would be rotated by a sloppy hinge, it was determined that the hinge should become part of the interface. This leads to a design where two V-grooves are located on the support frame, and one is located on a bridge that is created between the support hinges. Fig. 5.20 shows how the support frame has a groove that fits an axis with the same diameter as the ball that will fall in the V-groove of the support hinge. Fig. 5.21 shows the support hinge where the V-groove in the middle is clearly visible.

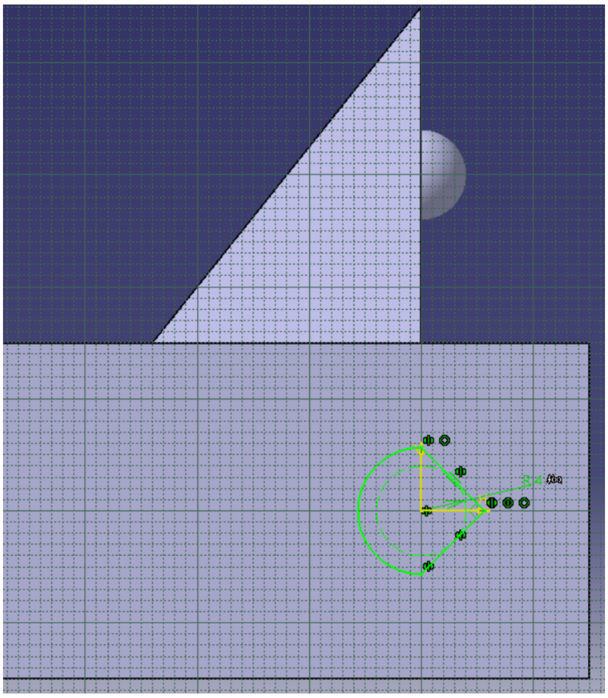

Figure 5.20: Kinematic interface on the support frame side. The hemisphere will fit the V-groove of the support hinge and the V-groove of the support frame shows that it will fit an axis with the same diameter as the shown hemisphere

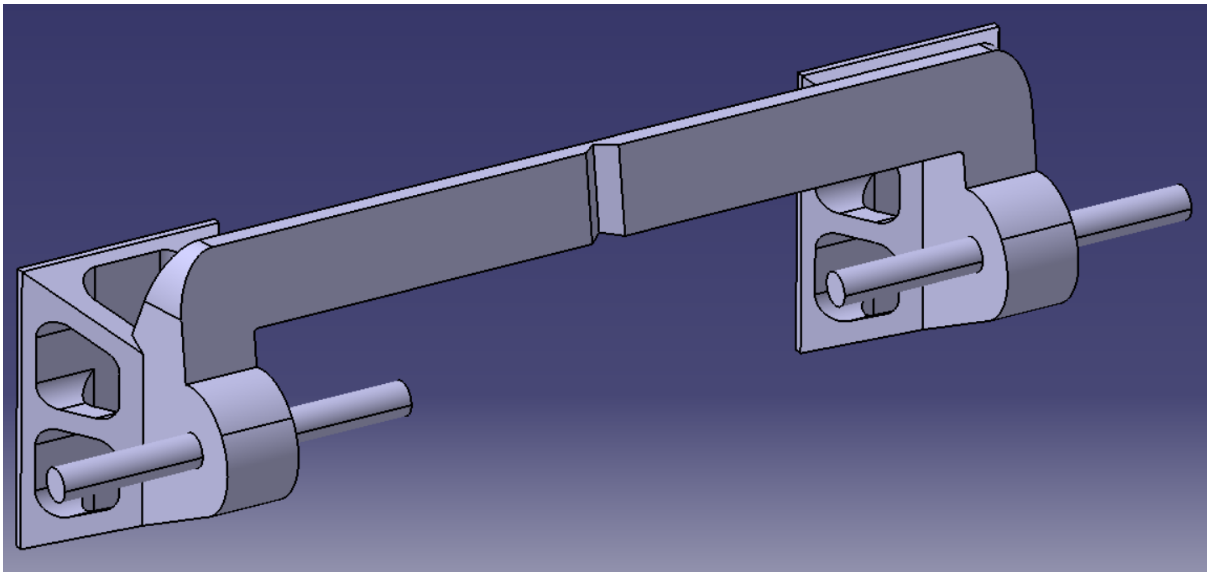

Figure 5.21: Support hinge with a bridge that has a V-groove in the middle. The axes will mate the V-grooves of the support frame

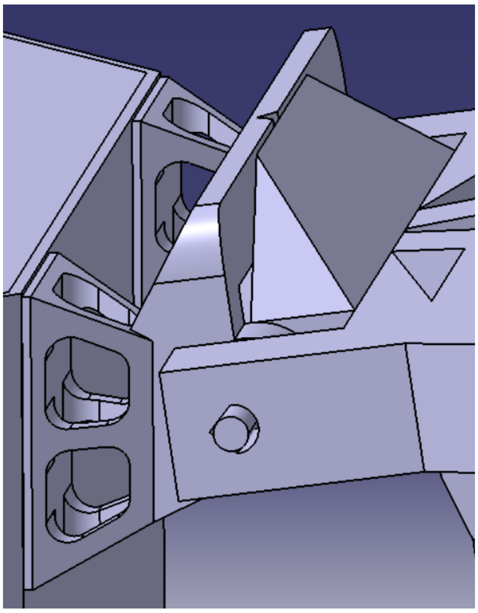

Figure 5.22: 3D view of kinematic interface when brought together

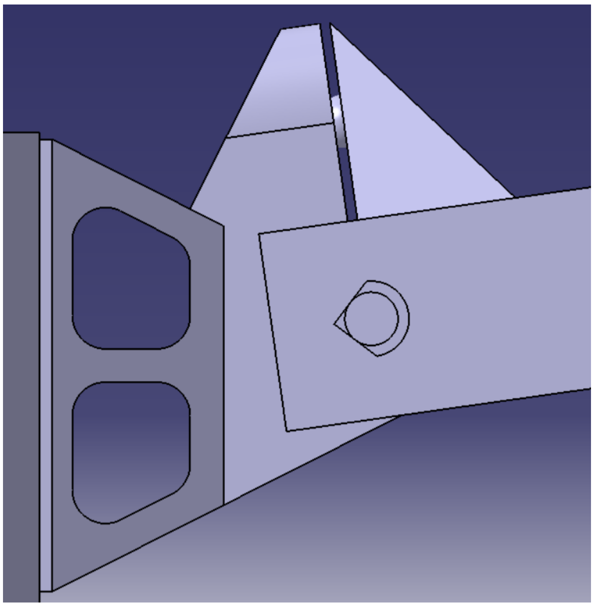

Figure 5.23: 2D view of kinematic interface when brought together. It is clearly visible how the interface elements match

Due to time constraints it is not possible to elaborate on the kinematic design in much detail. Figs. 5.22 and 5.23 show how the interface looks when it is engaged. The considerations about the design are summarized below:

- The precision of the kinematic interface cannot be estimated yet. It is explained in section 6.1 what the next steps are to make this estimate. Currently it is assumed that the required precision can be achieved, because this has been shown in several kinematic interface designs in the past.
- The current design is actually not kinematic nor semi-kinematic. It is overconstraint because there are 4 axes coming out of the support hinge. Dropping two of them will result in a semi-kinematic interface since the axes provide line contacts. It should be investigated whether this is possible.
- It should be researched what lubrication is needed for the hinge to work. Once an estimation of the friction coefficient can be made, a method for analyzing the allowable preload directions is provided in [85].
- The interface will work from a thermal point of view if the support frame hemisphere and the support hinge axes are made out of the same material, and if the remainders of the support frame and support hinge are made of the same material.
- Since the connection with the hinge fits loosely when no preload is applied, a way of preventing vibrations during launch has to be found. Possibly an HDRM can be used to pull the stowed support frame in negative Z-direction. This way a preload is applied that suits the kinematic interface. It should be remembered that the mirror is kept in place with an HDRM as well. Therefore a way needs to be found to connect the two components while being able to handle the stresses resulting from the launch loads.

5.4. DESIGN OF THE WINCH MECHANISM

The design of the winch is one of the more challenging aspects of this research. In the first place, because it involves moving components. In the second place, because it actuates the ribbon that connects two different subsystems that both need to be positioned very precisely, which was already a challenge when they were still standalone systems. This leads to a need of frequent discussions between the persons involved with designing the two subsystems, because it is crucial to understand each others needs.

Subsection 5.4.1 starts by discussing the required properties of the ribbon, from both the viewpoints of the M1 and M2 mechanisms. Then subsection 5.4.2 will discuss the actuation mechanism and gearing of the winch. In the end subsection 5.4.3 discusses the integration of the winch mechanism with the support frame. An important focus here lays on the alignment of the ribbon path.

5.4.1. PROPERTIES OF THE RIBBON

The ribbon connects the M1 and M2 subsystems and plays a role of structural importance in both subsystems. This means requirements flow down from both of these subsystems. Unfortunately the preferences of the systems contradict, so an optimal balance needs to be found. From vibration analyses performed on the M2 mechanism, it turned out that the ideal ribbon has a high stiffness and a low preload. Fig. 5.24 shows six curves indicating the frequencies of the first six eigenmodes of the M2 subsystem as a function of ribbon stiffness. All curves initially grow exponentially, until they move to an asymptote. Based on this graph it has been decided that the stiffness of the ribbon should be at least 1000 N/mm. The low preload is preferred, because the M2 mechanism makes use of tape spring hinges that may bend if the loads become too high.

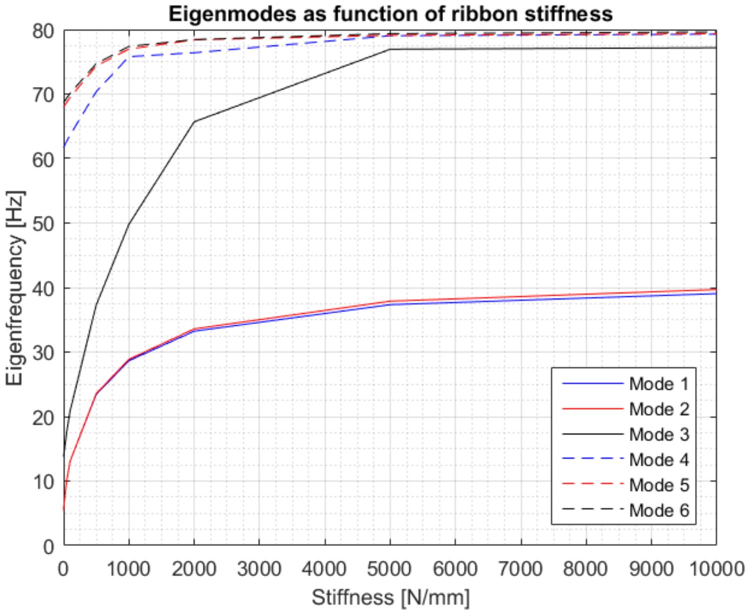

Figure 5.24: Graph providing the relation between the stiffness of the ribbon and the frequencies of the eigenmodes of the M2 mechanism [108]

Where the biggest challenge of the M2 mechanism is to improve the height of the eigenfrequency, the biggest challenge of the M1 mechanism is to achieve high precision while thermo-mechanical loads are endured. Using a kinematic interface, this means one wants to keep the preload as constant as possible with a preload device that will not transfer operational loads due to (thermal) deformation. This is generally achieved by using high preloads on compliant (i.e. low stiffness) linkages [31].

At the moment the discussion took place on the requirements of the ribbon, it was forgotten to take the need for a compliant linkage along in the considerations of the M1 mechanism. Therefore it was decided to aim at the high stiffness of 1000 N/mm. The contradicting wishes regarding the preload were recognized, but since it was expected that it would be hard to find a strong winch mechanism that fits in the available space, it was decided that the winch should be designed with the highest possible preload. Once the preload is known it can then be checked whether it exceeds the maximum loads for the tape springs of the M2 mechanism. The preload should also at least be high enough to stretch the ribbon to the point that it is still stretched after thermal expansion. This becomes easier if the chosen material has a low CTE, which is a requirement that was agreed upon from both sides.

The stiffness of the ribbon can be calculated via eqn. 5.3 [103]. The length, L_{r-fin}, is assumed to be roughly 2250 mm. After a couple of iterations the other parameters are defined as shown in tab 5.1. For high stiffness, a larger w_r and t_r are beneficial, but they are limited by the available space on the support frame extensions and the power of the motor. The motor is a limiting factor, because a higher thickness will result in a larger radius of the outer winding around the winch. This radius times the preload forms the torque that should be overcome by the motor. The chosen material of the ribbon is 'Kevlar 49'. This, because of the high modulus of elasticity, E_{kev} = 131 GPa, in fiber direction, the low CTE of -2.0 $\mu m/(m-K)$ in fiber direction, the fact that Kevlar is known for use in cables due to its capabilities to bend without damage, and the fact that cables of this material have been in space [103, 109]. According to eqn. 5.3 the discussed properties lead to a tension stiffness of 582 N/mm.

$$k_s r = \frac{w_r t_r E_{kev}}{L_{r-fin}} \tag{5.3}$$

As discussed in section 4.3.2, the temperature will fluctuate within a range of +- 1 K. With the CTE of Kevlar 49, this means that a temperature variation over the full range (2 K) will result in a longitudinal expansion of the ribbon of 9 μm. This has an effect on the preload, but how much of an impact it has depends on the winch mechanism.

To conclude this subsection, the properties of the ribbon are shown in tab. 5.1. As discussed, the choice of tension stiffness is mostly based on what is suitable for the M2 subsystem. It is assumed that it will also be good for the properties of the M1 subsystem from a vibrations perspective. Furthermore it is not yet determined what the effect of the stiffness is on the variation of preload, and thus the precision of the kinematic interface. The positive influence of high stiffness on the vibrational stability is an assumption because it has not yet been investigated what the relation between ribbon stiffness and the coupling of vibrations of the M1 and M2 systems is. It is recommended to model the relation between spring stiffness and preload variations in ANSYS and to look into literature to find more information about the coupling of vibrations through cables and the relation of this phenomenon to cable stiffness. Only then it is possibly to make a well-advised trade-off between the desires of the M1 and M2 subsystems to find the most optimal ribbon stiffness.

Table 5.1: Table summarizing the properties of the Kevlar 49 ribbon

Kevlar 49 ribbon properties

Property	Symbol	Value	Unit
Maximum length winch to boom (only M2 deployed)	L_{r-max}	2725	mm
Final length winch to boom (M1 and M2 deployed)	L_{r-fin}	2250	mm
Width	w_r	10	mm
Thickness	t_r	1	mm
Young's modulus	E_r	131	GPa
Tension stiffness	$k_s r$	582	N/mm
CTE	CTE_r	-2	$\mu m/(m-K)$
Change in length for 2 K change in temperature	ΔL_{r-dT}	9	μm

5.4.2. ACTUATION MECHANISM OF THE WINCH

The actuation mechanism of the winch is the device that creates the preload on the ribbon. Its major task is to provide a preload that is as constant as possible and at least overcomes the 9 μm of stretch in the ribbon that may result from thermal expansion. Concerning the location, it should be attached to the support plate, rather than the spacecraft bus, to limit the amount of components that can influence the tension on the line. Furthermore it should be placed on the bottom of the support frame or at a location where it can go through a cutout in the support frame.

Before considering actuation devices it is important to know that it should be able to retract a relatively long part of the ribbon. This is a result of the deployment sequence. The M2 mechanism is the first one to be deployed, because the part between the booms that holds the secondary mirror, is located such that the primary mirror segments cannot fully deploy. Hence, once only the M2 mechanism is deployed, the length of the ribbon is 475 mm longer as compared to a state where also the M1 mechanism is deployed. This is shown in fig. 5.25.

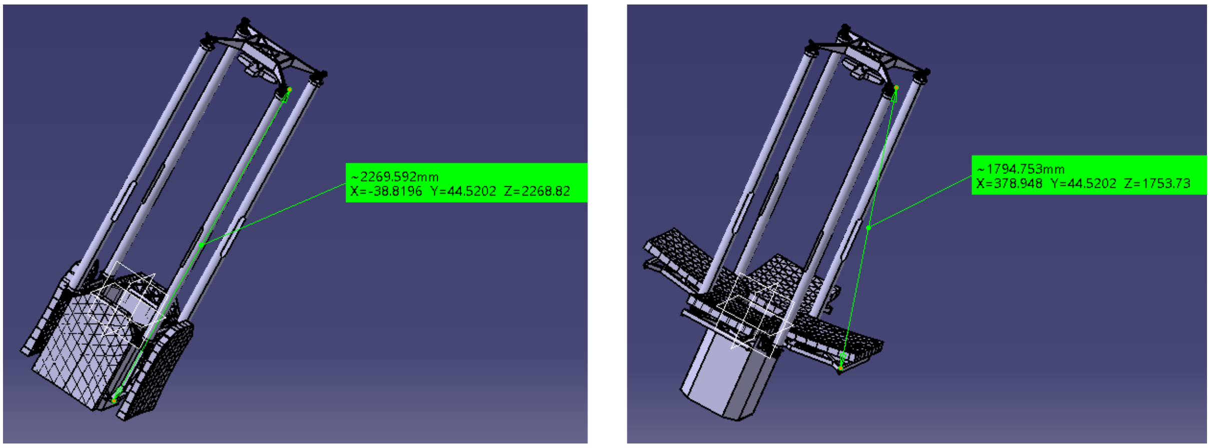

Figure 5.25: Length of the ribbon when only the M2 mechanism is deployed versus the length of the ribbon when the M1 and M2 mechanisms are deployed. The difference is 475 mm

In the first place it is preferred to have a passive winch mechanism, i.e. it should act once the HDRM releases the M1 mechanism and keep everything in place without further active control. The only device able to do that after pulling in a ribbon is a mainspring. Unfortunately the mainspring would store so much potential energy that it snaps back too hard, once the M1 mechanism is released. Also, the tape spring of the M2 mechanism may be too weak to fully deploy as the mainspring load grows during its deployment.

The only alternative option is to make use of a motor. It has the benefit of good control over the deployment, but also brings some disadvantages:

- 1. Motors are a heavy solution compared to springs.
- 2. The torque capacity of a motor scales with size and power usage. This means that the available torque will probably be limited, considering that there is little available space, and that eight of them will need to work, and thus consume electrical power, simultaneously.
- 3. Motors such as a stepper motor can have a relatively high holding torque, but that requires electrical energy. If a motor contains permanent magnets, a so called 'detent torque' remains after the motor is turned off. This is however very low and will not be suitable for preloading the ribbon.

The first disadvantage is something one simply needs to accept to make this concept work. The second and third disadvantages can be counteracted by using certain kind of gears. Gears and gearboxes are generally used to increase the torque capacity of a motor in return for losing speed. This is not a problem, since there is no time limit on the deployment sequence. On the contrary, it is even beneficial since the release speed of the ribbon determines the deployment speed of the M2 booms. This way the winch can serve as a damper for the M2 deployment mechanism. The 'gear ratio' is the multiplication factor that indicates how much more torque there is on the output side with respect to the input side, or how much slower the output side rotates with respect to the input side [110]. This is shown in eqn. 5.4. In general gear ratios are expressed as [multiplication factor]:1, but in equations like eqn. 5.4 one applies the multiplication factor.

$$GR = \frac{T_{output}}{T_{input}} = \frac{\omega_{input}}{\omega_{output}} \qquad [5.4]$$

By increasing the torque capacity with gears one may see how problem two can be counteracted, but this is not a solution to problem three. This problem can only be solved when worm gears are the type of choice. Fig. 5.26 shows a picture of a worm gear, consisting of a worm and a worm wheel. The major advantages of a worm gear are the fact that it can be put in motion via the worm, but not via the worm wheel, and that it allows a very high gear ratio. This means that the motor can actuate by turning the worm, but that the ribbon cannot rotate the worm wheel, and that the torque of the motor possibly can be increased to the required value. The disadvantage of a worm gear is the low transmission efficiency, which is the result of the large sliding surfaces at the interface between the worm and worm wheel.

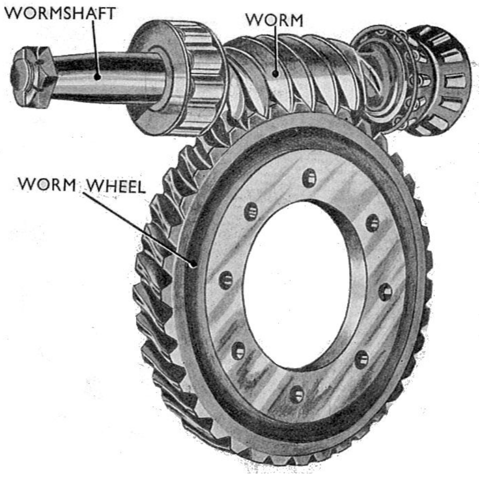

Figure 5.26: Drawing of a worm gear with the basic terminology [111]

Since no other option has been found, a worm gear with motor will be used to actuate the winch. There is a lot to consider when picking the right motor and worm gear. This is done separately below.

Motor selection

According to experts in the field, one should always use Direct Current (DC) motors in space. To be more precise, either a brushless DC motor with permanent magnets or a stepper motor [112, 113]. Comparing the characteristics of several suppliers of the two types of motors, a stepper motor comes out as the best solution [114–117]. Brushless DC motors are designed for continuous rotation at medium to high speed, while stepper motors perform good at low speed and are suitable to move one step at a time. Comparing the characteristics it was obvious that for same size, same stall torque motors, stepper motors consume way less power.

Two suppliers of stepper motors with space heritage are CDA InterCorp (CDA) and Avior Control Technologies, Inc (ACT). They both provide stepper motors with a size that fits in the available space. As a starting point a motor will be selected that fits between the satellite bus and the support frame, a distance of 35 mm. Although it was stated above that the motor may be positioned such that it goes through the support frame, doing this will limit the design space for the mirror calibration actuators and the athermalization mechanisms. Although it seems like it is clear what space will be used in the next section, this is based on a very early estimate of the person developing the calibration mechanism. The location of the calibration actuators may need to shift in the future and that becomes a lot harder if the motors already occupy parts of the available space.

The 35 mm space cannot be used in its entirety by the motor. First a 5 mm clearance goes off, to leave space for deformations due to launch loads. Furthermore, there needs to be space for a motor mount, and it was found that the axis should be slightly further away from the support frame than the center of the remaining 30 mm. This, because the winch will be placed in between the worm wheel and the support frame. Therefore the smallest motors of CDA and ACT, both with a diameter of 19.1 mm, were assessed more thoroughly to decide which motor will be selected.

Although the diameters are equal, the motors differ a lot in their other dimensions and characteristics. Where the CDA motor comes with a provided length and four options for the required stall power (and so the available torque), ACT provides a choice between three different lengths, with for each length the choice between three different stall powers. The options are summarized in tab. 5.2. In this table the 'holding torque' is the torque the motor generates when standing still. This is the highest torque it can deliver, but it also requires the most power, 'stall power', compared to other states. During the retraction of the cable, little torque is required, so this data was presumed irrelevant for this table. However, providing preload at the end of the retraction is important. This can be done at a low speed, where the highest torque can be generated for an operational state. This is called the 'low pulse rate torque'. To conclude it should be mentioned that the apparent difference in motor performance is the result of integrated gearboxes in the ACT motors. The longer lengths of the three different sizes are the result of larger gearboxes with higher gear ratios. The 'N##' part of the motor codes provides the gear ratio of either 8, 64, or 216. When dividing the provided torques by the corresponding gear ratios, one finds that the torque values of the ACT motors are similar to the ones of the CDA motors with comparable stall power.

Table 5.2: Table presenting characteristics of the 19.1 mm diameter motors of CDA and ACT. The selected motor has a bold font

Supplier	Motor code	Length	Mass	Stall power	Holding torque	Low pulse rate torque
		$[mm]$	$[g]$	$[W]$	$[mNm]$	$[mNm]$
CDA*	**12-2P6-06**	**19.81**	**37.00**	**6**	**15.7**	**11.1**
CDA*	12-2P6-10	19.81	37.00	10	20.3	14.3
CDA*	12-2P6-20	19.81	37.00	20	28.7	20.3
CDA*	12-2P6-30	19.81	37.00	30	35.1	24.8
ACT⁺	B62S-08N08-06	52.50	58.97	6	120	70
ACT⁺	B62S-08N08-12	52.50	58.97	12	170	100
ACT⁺	B62S-08N08-18	52.50	58.97	18	210	120
ACT⁺	B62S-08N64-06	71.00	86.18	6	960	490
ACT⁺	B62S-08N64-12	71.00	86.18	12	1350	750
ACT⁺	B62S-08N64-18	71.00	86.18	18	1660	940
ACT⁺	B82S-08N216-06	89.50	104.33	6	3230ˣ	1550ˣ
ACT⁺	B82S-08N216-12	89.50	104.33	12	4570ˣ	2350ˣ
ACT⁺	B82S-08N216-18	89.50	104.33	18	5590ˣ	2970ˣ

* [116]
⁺ [117]
ˣ Theoretical torque ratings. Brochure is from 2014, so possibly verified in meantime

Since no motors without integrated gearbox are found in the ACT catalog, it is clear that CDA provides the most compact and lightweight motors, but that the provided torque is very low compared to the ACT motors. This also means that the power usage for a given torque is much lower for the ACT motors. When looking to the final winch design in fig. 5.27, one sees that there is plenty of space left for a longer motor, but in the first design iterations extra length did give problems. Therefore it was decided to go with the 12-2P6-06 CDA motor.

It was hard to find an appropriate worm gear that provided an acceptable torque in combination with this motor, but a possible solution has been found. The design is left as it is right now, because there are too many unknowns to select the right motor. It is however good to know that all CDA motors and the smallest size motors of ACT would fit. Also the middle size can fit with a minor design change where 3 mm extra space is added between the motors. Once the power budget is defined and the design is mature enough to know how influential the motor choice is for meeting the mass budget, the right motor can be selected. Keep in mind that all winches will need to work at the same time, so the total required power should be eight times the stall power.

WORM GEAR SELECTION

As explained before, a worm gear is used if one wants to make sure motion can only be generated via the input side. This is exactly what one needs to pull in a ribbon with a motor, of which you want to shut off the power once the ribbon is in place. The other benefit is that one can create high gear ratios fairly easy. This comes from the fact that for each full rotation of a single start worm (most common type), the worm wheel will rotate by one tooth. In other words, the gear ratio is equal to the amount of teeth on the worm wheel.

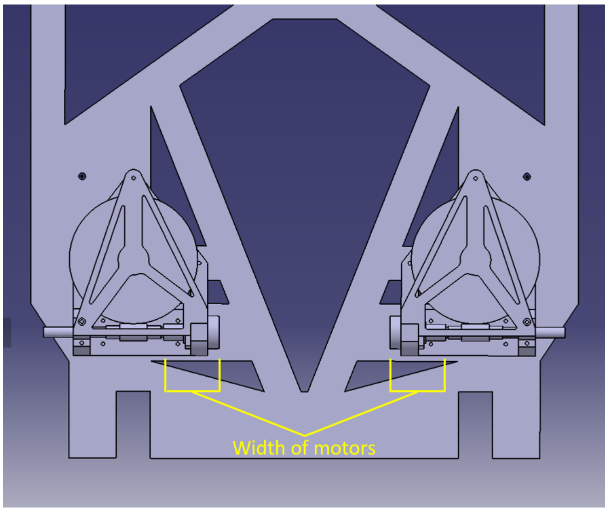

Figure 5.27: Final winch actuator assembly mounted on the support frame. The width of the selected motor is indicated in yellow

Unfortunately it is not possible to simply pick a size for the worm wheel and come up with a certain amount of teeth. The teeth of the worm and the worm wheel need to match. The industry therefore uses a unit called the module [118]. Imagine the teeth taken of a gear to lay them down in a straight line, as shown in fig. 5.28. The pitch is then the distance between corresponding points on adjacent teeth, and the module is this pitch, multiplied by π. The radius of the worm wheel is determined by the modulus and gear ratio and scales linear with both of them.

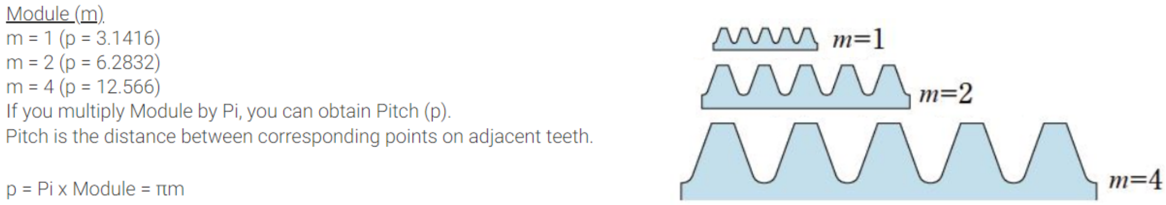
Module (m)
m = 1 (p = 3.1416)
m = 2 (p = 6.2832)
m = 4 (p = 12.566)
If you multiply Module by Pi, you can obtain Pitch (p).
Pitch is the distance between corresponding points on adjacent teeth.

p = Pi x Module = πm

Figure 5.28: Figure explaining the meaning of the module of a gear [118]

The selection of the right gear is an iterative process, because for most of the properties there are only a couple of standardized values. It is a matter of finding a mix of available values that lead to a good result when putting them into eqn. 5.5:

$$F_{pl} \cdot r_{win} = T_{in} \cdot GR \cdot \eta \qquad [5.5]$$

Here F_{pl} stand for the preload force, r_{win} for the radius of the winch when the ribbon is fully rolled in, T_{in} for the input torque (the low pulse rate torque of the motor) GR for the gear ratio, and η for the efficiency of the worm gear. When looking to the equation, it equals the torque created by the preloaded ribbon on the left side to the motor torque that remains after passing the worm gear on the right side. T_{in} is provided in tab. 5.2 as 11.1 mNm (in the right column). This is the only parameter that is already known.

η needs to be estimated, since most suppliers provide little information about it. This is also because the efficiency is dependant on factors such as the rotational speed, the module, and the chosen lubrication. The only supplier that provides information on this is Kohara Gear Industry Co.,Ltd. [119]. In the tables provided on their website, it becomes clear that lower rotations per minute (rpm)s and lower modules lead to lower efficiencies. At the end of deployment, the rotational speed will be very low to generate a high torque, which is not beneficial from an efficiency point of view. The closest value in the reference table for an approximation is an efficiency of 30 % at a rotational speed of 100 rpm for a gear with a modulus of 0.5 (the modulus of the final design). Since the motor may rotate slower and one wants to keep a conservative estimate, an efficiency of 27.5 % is chosen.

The minimum required preload force follows from the ribbon properties described in subsection 5.4.1. Due to temperature variations the ribbon will stretch 9 μm in the assumed worst case scenario. With a stiffness of 582 N/mm this means the required preload for compensating this motion is 5.238 N. However, when looking for the right worm gear, the dimensional limitations of the ribbon where not known yet, so it was still assumed the stiffness of the ribbon was 1000 N/mm. This leads to a compensating preload of 9 N. This would however mean that after the expansion in the worst case scenario, the line is on the edge of being in tension at a preload of exactly 0 N. Since it was not known yet what preload is required for the kinematic interface, the twofold of the calculated corrective preload was selected as a starting point. This is a value of 18 N.

With the values derived so far, eqn. 5.5 can be rewritten as eqn. 5.6:

$$GR = \frac{F_{pl} \cdot r_{win}}{T_{in} \cdot \eta} = 5.9 r_{win} \tag{5.6}$$

r_{win} is mostly an open design parameter that can be made fit to the available gear ratios, but there is a minimum diameter that can be calculated. First, the winch should fit around the hub of the worm wheel (smaller disk of the worm wheel without the gear teeth) that forms the first part of the radius. The second part comes from the thickness of the winch part. The third part comes from the ribbon itself. The high torque is needed once the ribbon is retracted. This means multiple layers of ribbon will add to the effective radius of the torque. At first it was assumed the worm wheel hub will have a radius of at least 7.5 mm. The actual winch connected to it is assumed to have a thickness of 4 mm, considering a connection to the shaft needs to be made and that the end of the ribbon should be connected properly as well. The additional thickness can be found by trying different values for N in eqn. 5.7:

$$L_{r-retN} = \sum_{i=1}^{N} 2\pi (r_{hub} + t_w + t_r (i - \frac{1}{2}) \tag{5.7}$$

Here L_{r-retN} stand for the retracted ribbon length after N windings, r_{hub} for the radius of the hub of 7.5 mm, t_w for the thickness of the winch of 4 mm, and t_r for the thickness of the ribbon of 1 mm. The $i - \frac{1}{2}$ is because one should measure the radius towards the center of the outer winding, which is half the ribbon thickness inwards as seen from the outside. Trying this formula for different amounts of winding, one need to look for the first value after a retracted line length of 450 mm. This is found to be after 6 windings with a retracted length of 547 mm. When $i = N$, the part between brackets of eqn. 5.7 represents the minimum value of r_{win}, which is 17 mm. According to eqn. 5.6 this means the gear ratio must be higher than 100.3:1.

Looking on the websites of worm gear suppliers, the closest standard gear ratio is 100:1. This is however below the calculated value, so the next standard value of 120:1, or for two of the suppliers 125:1 [120–125], seems more suitable. For all companies, except for 'Ondrive', the smallest module for which this gear ratio is available is 1. With a module of 1, the diameter of the worm wheel is equal to the amount of teeth, or 120 mm. This is not necessarily too big, but the space it requires will definitely limit the design freedom. Therefore it was chosen to look into the worm wheels offered by Ondrive [125]. This company produces backlash free worm wheels with a module of 0.5 with gear ratios that go up to 250:1.

Looking at their 120:1 worm wheel with a 0.5 modulus, one notices that the hub diameter is actually 30 mm. Filling this into eqns. 5.7 and 5.6, one finds that one now actually requires a gear ratio of 133:1. Even reducing the thickness of the winch by half does not lead to a required gear ratio below 120:1. After a couple of calculations with the available Ondrive worm gears, it was found that the paradox could not be solved. If one picks a worm wheel with a higher amount of teeth, it also has a wider hub, meaning a higher gear ratio than the amount of teeth is required. Playing around with the available gear dimensions, the values of the parameters in eqns. 5.6 and 5.7, and considering the available space, a compromise has been made. The 150:1 'ABPWG0.5-150-1' gear with a 45 mm diameter hub and a 75 mm diameter was selected, together with a decreased winch thickness of 2.5 mm. This leads to a preload of 16.65 N. The worm that mates with this worm wheel is called the PSW0.5-1.

5.4.3. INTEGRATION OF WINCH MECHANISM WITH THE SUPPORT FRAME

Now that the properties of the ribbon, the type of motor, and the type of worm gear are determined, they need to be integrated with the rest of the design. There are many factors that influence the integration options. Both the design of the actuator mounting and the design of the ribbon path bring their own challenges. They are discussed separately below.

INTEGRATION OF THE WINCH ACTUATOR

As a first step it is useful to make an assembly file in Catia where the motor, worm, and worm gear are connected. This allows one to play around with the location of this assembly with respect to the support plate, to find suitable locations more easily. A suitable location meets the following requirements:

- The actuator assembly shall stay out of the clearance circle of the HDRM.
- The actuator assembly shall stay as close as possible to the root of the support frame for a better resistance against vibrations.
- The ribbon shall be winded via the outer side of the worm wheel to generate as little twist in the ribbon as possible.
- The outer side of the worm wheel shall be located near the edge of the support frame to generate as little twist in the ribbon as possible.
- The actuator assembly shall be located such that the axis of the worm wheel, plus an additional clearance for a bearing, are not located at the same location as the athermalization pockets (see section 5.5), as seen in the XY plane of the support frame.

Taking these requirements into account, an initial location for the actuator assembly was chosen as shown in fig. 5.29. The motor and worm wheel are placed close to the root to move the weight as far as possible towards the satellite bus. This location gives no problems by interfering with the HDRM mechanism or the athermalization pockets.

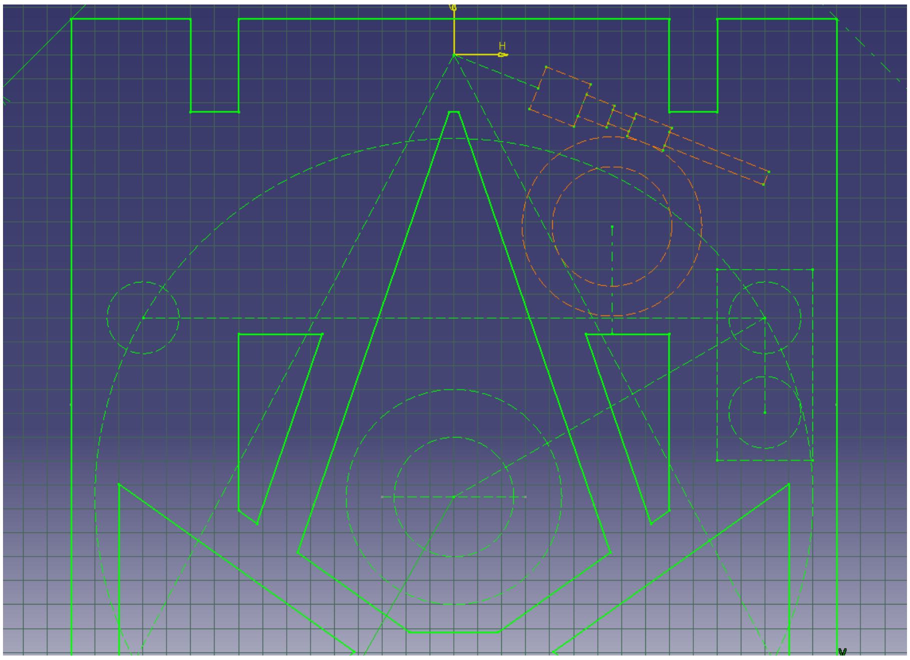

Figure 5.29: Sketch of support frame shape with athermalization pockets (dashed box with 2 circles in it) and the initial positioning of the winch assembly, indicated in orange

From here the mount of the actuator can be designed. The mount should hold the motor, worm, and worm wheel in place, both during launch and operations. To survive the launch loads, it is best to make a ring surrounding the motor at its long end, that is attached to the support frame. From there the bottom of the plate can be extended to do the same for the end of the worm. Assuming the axes of the motor and worm are connected before they are put into the mount, two full rings would make it impossible to insert the motor and worm in the construction. Therefore it has been decided to divide the mount in a bottom and a top part that can be bolted together. The bottom part designed thus far is shown in fig. 5.30.

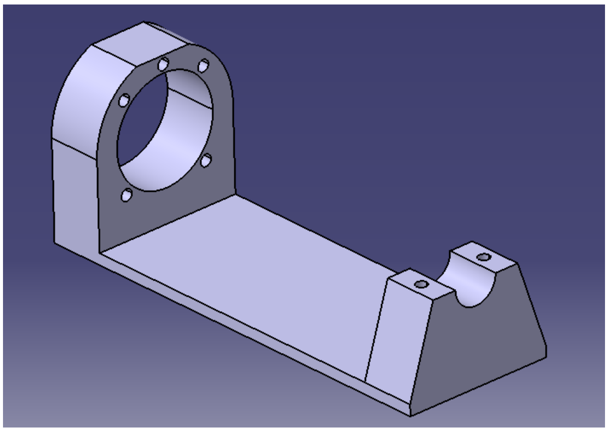

Figure 5.30: Part of the bottom mount that holds the motor and (bearing of) the worm. The holes in the worm holder and the upper hole on the motor side are for the bolts to the top mount. The four remaining holes on the motor side fit the interface plate of the motor.

The more difficult part is to make the mount hold the worm wheel, since it is relatively big and needs to be kept in place by the mount at the top. The bottom of the worm wheel can be connected to the support frame with a bearing. It is assumed that making a triangular structure between the end of the worm wheel axis, the worm axis, and the motor is too weak to keep everything in place. Therefore a pillar is created on the bottom mount that forms a triangle around the worm wheel with the worm and the motor. This is shown in fig. 5.31. The pillar connects both the top and bottom part of the mount.

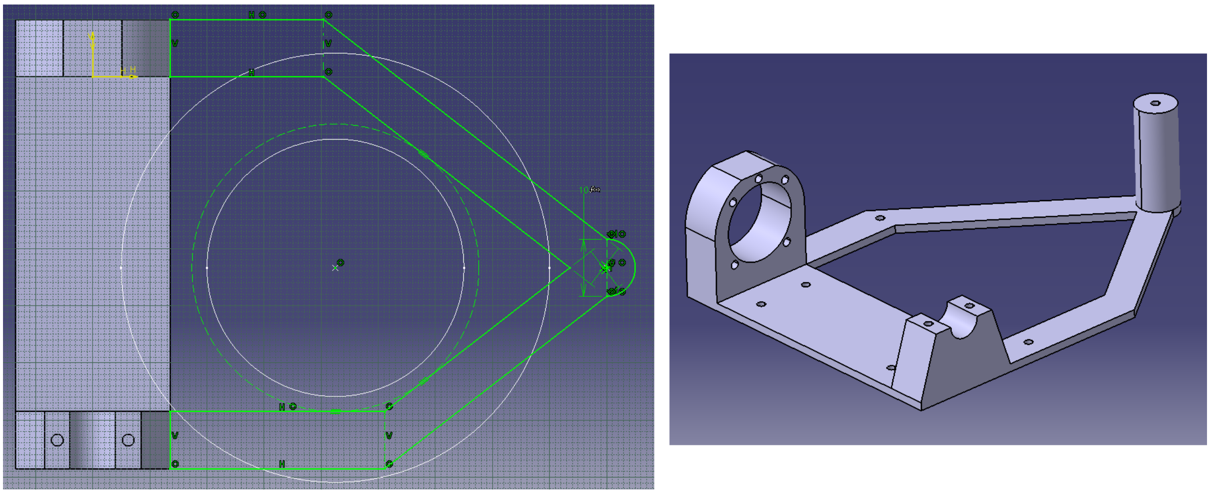

Figure 5.31: Left: sketch indicating how the structure of the bottom mount moves around the hub of the worm wheel (inner white circle) - Right: final design of bottom mount, including holes for bolts to the support frame

From the tree corners, the top mount makes a triangle again, as well as three direct connection to the top of the worm wheel, as shown in fig. 5.32. This figure shows the final design of the top mount.

In figs. 5.31 and 5.32, final designs of the two mount parts have been shown. In reality first the height of the mount parts was tuned to arrive at the current design. As discussed before, the maximum height of the mount is 30 mm. The further dimensions are determined by the worm wheel and ribbon dimensions. The width of

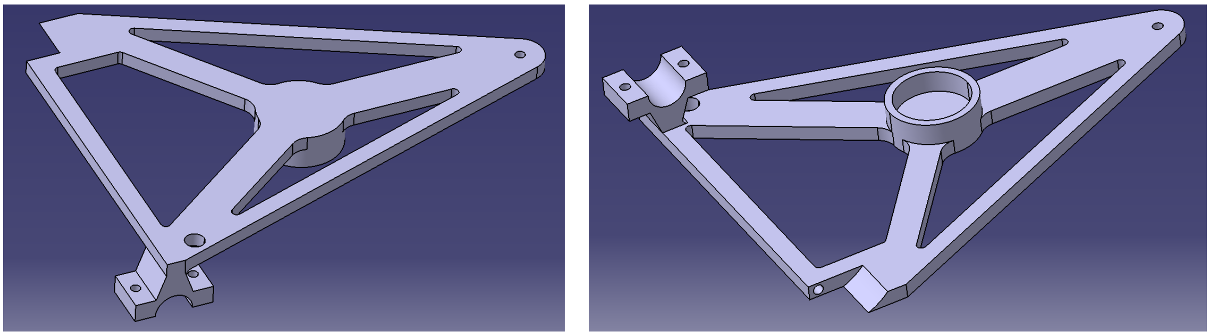

Figure 5.32: Left: isometric view showing the top of the final top mount design - Right: isometric view showing the bottom of the final top mount design

the hub is 10 mm. The winch surrounding it should however be wider, since the ribbon with a width of 10 mm should fit in. One wants to create two guidance walls around the ribbon, to prevent frictional contact with the worm wheel or the bottom part of the mount. For this a thickness of 1 mm has been chosen. This leads to a required width of 12 mm. However, one needs some additional space, because the winch may not touch the support frame and because there needs to be room to fit a bearing at the interface with the support frame. Therefore a width of 15 mm has been chosen between the support frame and the worm wheel part with the teeth.

This part with the teeth has a so called face width of 5 mm. The axis should stick out a bit on top of that to fit a bearing, which is on its turn covered by the top part of the mount. It has been decided to extend the axis for 5 mm on top of the worm wheel. In total that makes 25 mm. Fig. 5.33 shows these dimensions and the resulting height of center of the toothed part of the worm wheel of 17.5 mm. This naturally also becomes the height of the worm and motor axes.

The thickness of the top mount is determined by the available room between the top of the motor interface and the 30 mm boundary. As shown in fig. 5.33 this leads to a thickness of 2.975 mm, meaning that a 2.025 mm distance remains between the axis and the mount to fit a bearing.

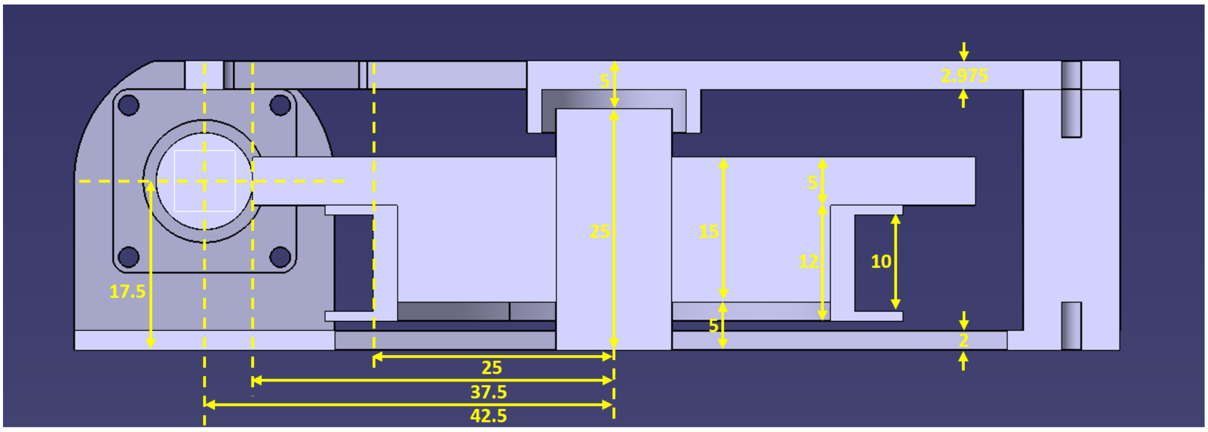

Figure 5.33: [Section view of the winch assembly, indicating the most important dimensions

The final design step to conclude the winch assembly is to define the connection with the support frame. Now the shape of the mount is known, it is re-positioned to a location where it can be bolted into the support frame without interfering with the athermalization pockets or the HDRM clearance. The isometric view of the final winch assembly is shown in fig. 5.34 and the new support frame design that matches it is shown in fig. 5.35. Fig. 5.27 shows what an assembly of the support frame and the winch looks like.

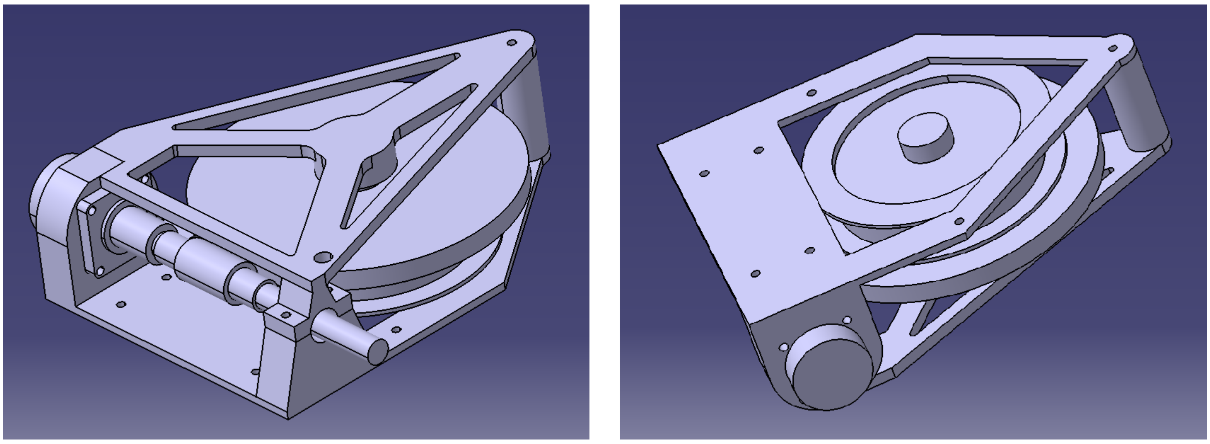

Figure 5.34: Left: isometric view showing the top of the final winch actuator assembly - Right: isometric view showing the top of the final winch actuator assembly

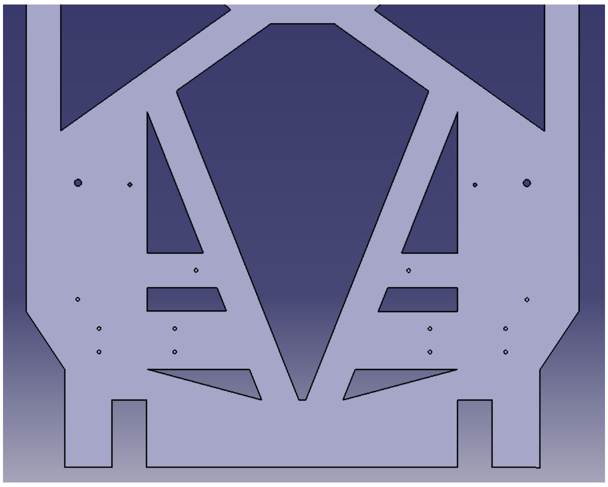

Figure 5.35: Bottom view of the support frame design that includes an interface to bolt the winch actuator assembly

INTEGRATION OF THE RIBBON

Designing a proper path for the ribbon is harder than it seems. Rather than just running it from the winch to a hole in the support frame and further to the top of a secondary mirror boom, one needs to think about how to achieve exact constraints. An overconstrained design will lead to friction between the edge of the ribbon and the guidance rails or will lead to derailing of the ribbon. To prevent this a look has been taken into exact constraint web design, the theory applied to conveyor belt design. The web is another word for the conveyor belt, or in this case the ribbon.

The book of Blanding on exact constraint design [85] devotes a whole chapter on the constraint web design theory with many examples of how to apply the theory in practise. Relevant terminology from this book are the *rollers*, the round shaped objects that steer the direction of the web, the *Web Plane Diagram (WPD)*, a 2D representation of the web and the elements it interacts with (see fig. 5.36), and *gimballing*, allowing a roller to pivot freely about an axis parallel to the incoming span of the web (see fig. 5.37).

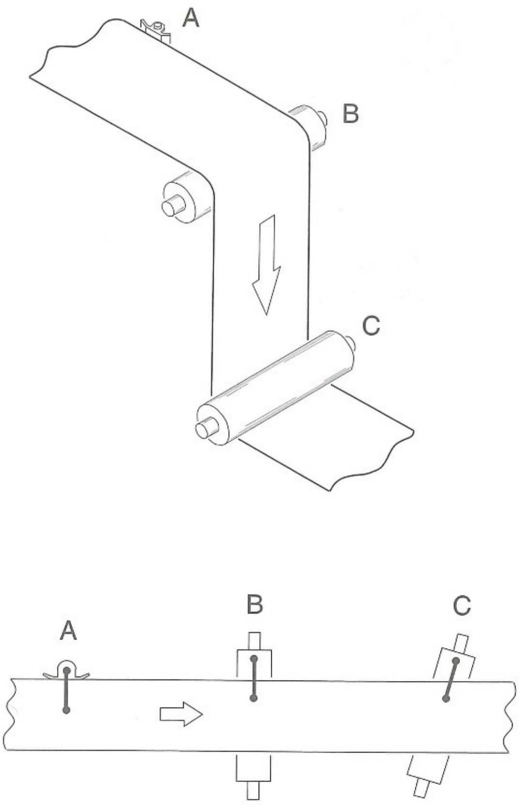

Figure 5.36: 3D sketch of a web design constrained by an edge guide (A), a perpendicular roller (B), and a misaligned roller (C), accompanied by a 2D representation in the form of a WPD [85]

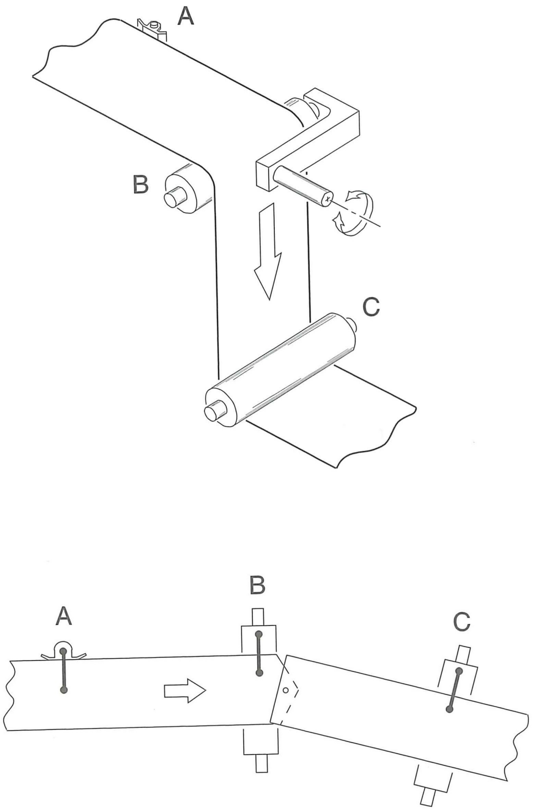

Figure 5.37: Web design of fig. 5.36, but now with a gimballed roller B, accompanied by the corresponding WPD where one can see that roller B effectively becomes a hinge [85]

Blanding explains that the constraints do not change if a web is twisted around its longitudinal axis and that one only has to take into account the roller angle with respect to the longitudinal web axis in the plane of the web: "*... we are not concerned with constraints that control where the plane of the web is, only with those controlling where the web is in its plane.*" [85]. This is convenient for two reasons. First this means that a design can be represented in 2D in the form of a WPD (bottom sketches of figs. 5.36 and 5.37). A second advantage of Blanding's observation is that one is only has to be concerned about controlling three Degree Of Freedom (DOF), X-translation (longitudinal direction of web), Y-translation (cross-track direction of the web), and Z-rotation (in plane rotation of the web). In practise one actually wants to allow free movement in X-direction, meanings only 2 DOFs need to be constrained.

In the WPDs the black lines with the dots on both ends indicate the direction of constraint imposed on the web. For an edge guide the imposed constraint is per definition in Y-direction (see book for explanation) and for rollers this is in the direction of the roller axis, which is preferred to be in Y-direction since one does not want to constrain in X-direction. The claim that the rollers impose a constraint in the direction of their axis comes from the assumption that the web is pressed against the rollers, which exert a radial force that generates enough friction to prevent the web from moving in Y-direction. Assuming a rigid web and two rollers or edge guides, the instant center of rotation can be found at the intersection of the two constraint lines, as shown in fig. 5.38. If one wants to prevent rotation, one needs to make the axes parallel, so the instant center of rotation is located at an infinite distance. This would be the case if roller C is removed from fig. 5.36. When using more than two rollers or edge guides, the system will be exactly constraint as long as all constraint lines point to the same instant center of rotation (preferably at infinity). In practise it is impossible to align all elements perfectly, meaning that a design with more than two constraining elements is per definition overconstraint, because now multiple instant centra of rotation are defined. This is the case in fig. 5.36 with an exaggerated misalignment of roller C, leading to different centra of rotation for the A-B, B-C, and A-C constraint pairs.

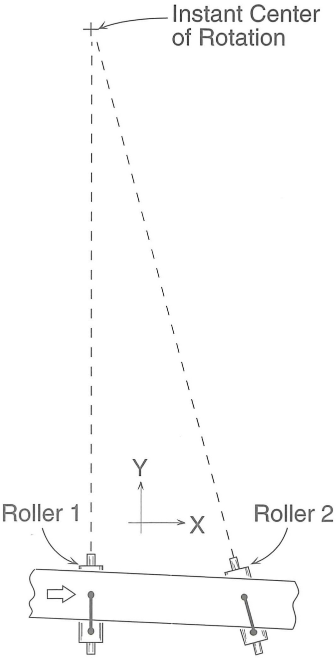

Figure 5.38: Sketch of two misaligned rollers. The intersection of their constraint lines forms the instant center of rotation [85]

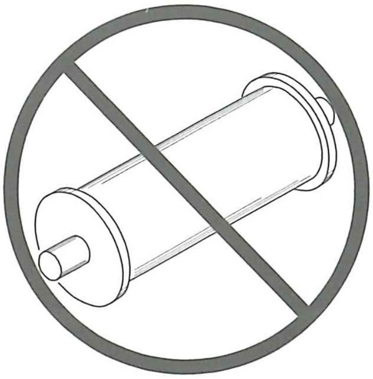

Figure 5.39: Example of a flanged roller. Flanged roller should not be used since they are per definition overconstrained [85]

This can be counteracted by gimballing one of the rollers, as shown in fig. 5.37. By gimballing one adds an extra DOF that can be represented in a WPD as a joint just downstream of the rolling element. The gimball rotation does not provide problems, because as said before, twist does not affect the constraintness of the web. The center of rotation of span A-B in fig. 5.37 will now be determined by the constraint lines of edge guide A and roller B. Span B-C is now laterally constraint at roller B, and rotationally by roller C. Since every gimballed roller provides one degree of constraint, but also one additional DOF, a series of gimballed rollers can be made while keeping the design exactly constraint. There is however one important note: only if the upstream and downstream direction of the gimballed roller are orthogonal, it can be represented as a perfect joint in the WPD. A 0° or 180° wrap would not work at all. Blanding suggests a rule of thumb that gimballing only works for wraps of 90 +- 45°.

Between two constraining elements it is also impossible to create perfect alignment and therefore an instant center of rotation is always present at a finite distance. If the axes are nearly perfectly aligned one can imagine that the web will need to roll a very long distance before it will rotate such that it glides of the roller. For conveyor belts this is a serious concern, because they are usually designed to roll in the same direction for their entire operational life. For an application like the ribbon winch this may not be a concern, because the rolling distance is relatively short, which means the misalignment may not cause a significant web rotation over the length of this motion yet. If the rotation is a concern there are ways to prevent this. One's first instinct would probably be to use flanged rollers to guide the web back if it wants to rotate. This is however a wrong though since a flanged roller is per definition overconstraint, because the flanges act as two edge guides, adding two more constraints that are superimposed. An example of a flanged roller is provided in fig. 5.39 with a prohibition sign to emphasize it should not be used. The only exception where flanges can work is the case where the web is allowed to slip due to a low web tension and/or low wrap angle. In fact it is technically not a roller anymore, but a so called non-rotating shoe. A non-rotating show falls in the category of zero-constraint web supports, but is usually the worst choice of the available options. As the name implies, zero-constraint web supports impose no constraints, which allows one to use edge guides or flanges. Other types are air bearings, axially compliant rollers, and castered rollers. They are not discussed in this thesis, but more information is available in [85].

When the ribbon design was made, the theory of the book of Blanding was not yet known. A discussion with prof. Just Herder led to the knowledge that twisting is not a problem as long as the rollers are perpendicular to the rolling direction of the ribbon in the local ribbon plane. This led to the design philosophy that the path of the ribbon should conform to the first and third design practises of fig. 5.40.

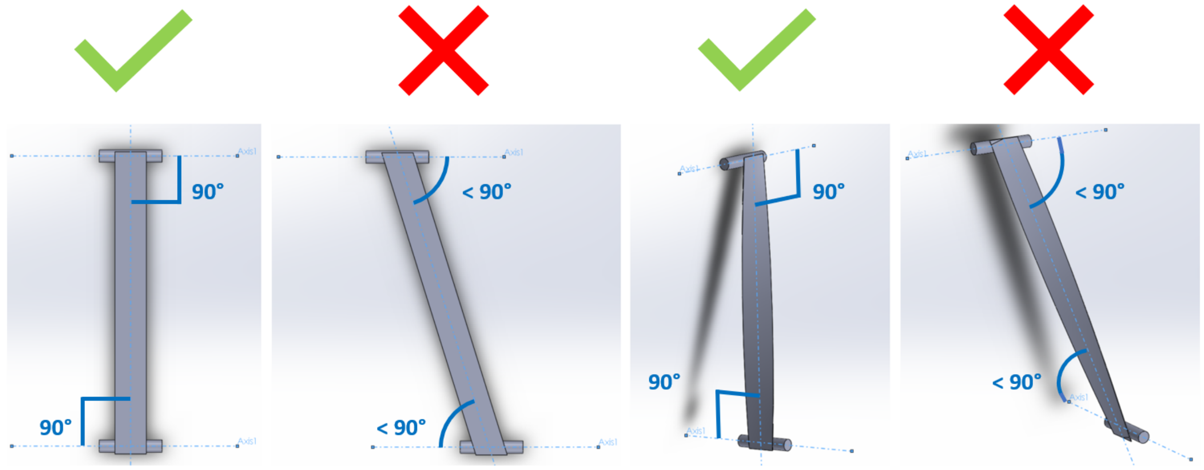

Figure 5.40: Four cases of a ribbon brought in tension between differently located rollers
1. Straight connection between two parallel rollers that are perpendicular to the ribbon center line
2. Straight connection between two parallel rollers that are not perpendicular to the center line, resulting in unwanted shear forces
3. Ribbon is twisted 90°, which is no problem since the roller axes are perpendicular to the center line of the ribbon
4. Equal to case 2, but with one roller twisted by 90° (around the vertical axis of the figure), which again results in unwanted shear forces

Following the design philosophy, one finds that at the bottom side of the support frame, a wedge is needed with a height that matches the winch. The direction of the axis of the edge on top of the wedge has been determined by making it perpendicular to a line drawn from the winch, as shown in fig. 5.41. The 'effective radius' of the winch of 27.5 mm is chosen to be the one that goes to the center of the outer ribbon after it is fully retracted (so with three windings). As a result the wedge axis does not have a perfect perpendicular angle if the ribbon is rolled out. With the current knowledge it is recommended for the next researcher to find out whether the rotation will lead to problems over the limited distance that the ribbon will roll. If yes, it is suggested to look into gimballing the wedge.

The wedge is made such that the round edge stops at half the ribbon thickness from the axis of the ribbon hole, because one should align the center line of the ribbon. This leads to the wedge design of fig. 5.42 with the alignment as shown in fig. 5.43.

With the same reasoning, the other side of the hole is shaped. A line has been drawn from the top of the M2 boom to derive the direction of a perpendicular axis for the rounding into the ribbon hole. This time the round edge is cut out of the support frame, since no wedge is needed to match heights. Looking at the hole alignment as seen from the top of the support plate in fig. 5.44, one can clearly see how the ribbon will twists in the hole.

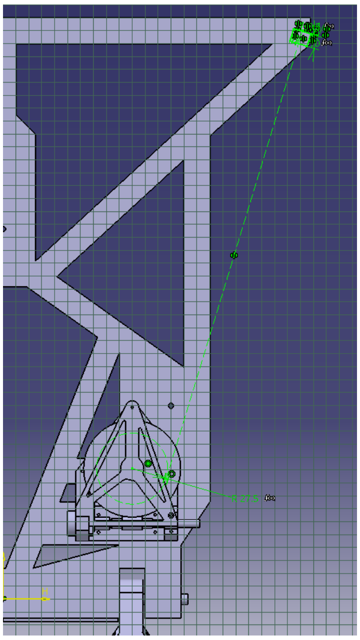

Figure 5.41: Sketch to create the right angle of the wedge to prevent shear force in the ribbon

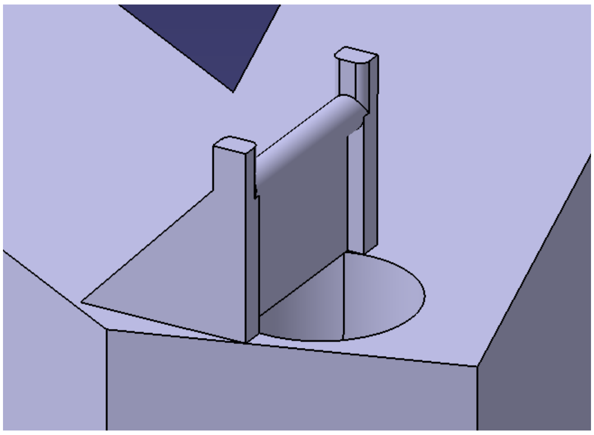

Figure 5.42: Wedge to guide the ribbon trough the hole. Note that the wall on the ribbon side does not go down straight after the rounding, because that would obstruct the twist towards the other end of the hole

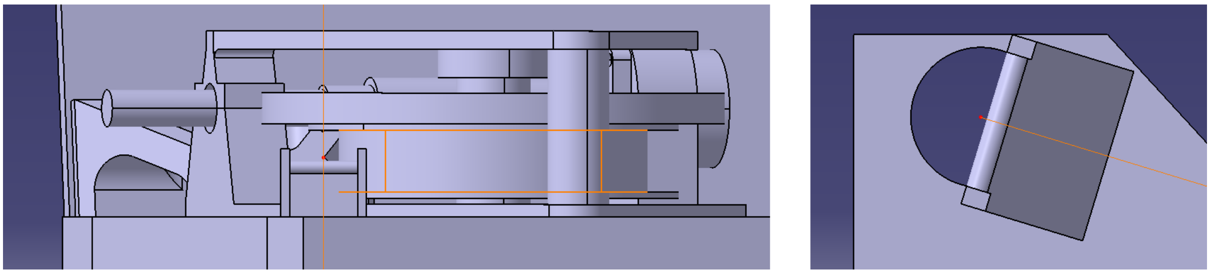

Figure 5.43: Left: figure showing the alignment of the wedge height with the winch - Right: figure showing the alignment of the wedge edge with the ribbon hole

Since the angle of the ribbon will change slightly with respect to the round edge, it is again recommended to find out whether gimballing is required.

A final note is that at this point the wedge contains self-made flanges and that the edge into the ribbon hole has flanges imposed by the edge of the hole. As discussed in the theory this leads to an overconstraint design. Therefore it is recommended to either get rid of the wedge flanges and insure that the ribbon does not rotate away from the wedge or against the side of the edge of the ribbon hole over the required rolling distance. If this is not possible the two elements should be made such that they act as zero-constraint web supports.

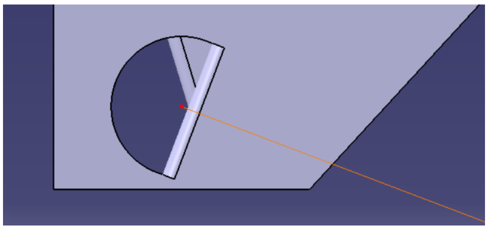

Figure 5.44: Figure showing the alignment of the edge on the top side of the support frame with the M boom and the wedge on the other side of the ribbon hole

5.5. ATHERMALIZATION OF THE M1 MECHANISM

Athermalization is a crucial factor in the design of the M1 mechanism. The budgets are very tight with an allowed deviation due to thermal effects of 20 nm in X-, Y-, and Z-direction per orbit (see tab. 4.2). With a measuring tool in the drawing software Catia, a distance between the bus and the outer calibration actuator of 385.49 mm has been measured, as seen from the XY-plane of the support frame reference system (fig. 2.9). With an assumed CTE of 1 $\mu m/(m-K)$ (section 4.2), this would mean the actuator will expand 385 nm/K. To stay within the budget of 20 nm this means that the temperature should be controlled with a 52 mK precision. Temperature control to this degree is unfeasible within this project and therefore athermalization is needed. Note that in the remainder of this section all dimensions are located in the support frame reference system.

Subsection 5.5.1 will explain how athermalization was initially applied by making use of simple CTE compensation. After the new design of the support frame was made and a calibration actuator concept had been chosen, it was possible to finish the athermalization. It is however found that the previous method cannot compensate thermal expansion in all directions. Subsection 5.5.2 explains how a circular expansion solution is able to do this. Finally subsection 5.5.3 provides remaining considerations and recommendations for further research.

5.5.1. ATHERMALIZATION BY CTE COMPENSATION

From the theory discussed in subsection 3.3.1, the idea came to keep the location of the calibration actuators in place by using an aluminum plate to compensate for the motion of the support frame. It is assumed that the support frame has a 1 $\mu m/(m-K)$ CTE in Y-direction, while aluminum has a CTE of 23 $\mu m/(m-K)$. Fig. 5.45 is a version of the bottom example of fig. 3.30 with the numbers that apply for the support frame and the aluminum plates. Here L_0 is the distance between the satellite bus and the desired actuator location in Y-direction. This value is provided by the current design. The connection point between the aluminum plate and the CFRP support frame (right side of fig. 5.45) will be called the 'plate-frame connection'. According to eqn. 3.6 the length of the aluminum plates between the desired actuator location and the plate-frame connection (L_2) should be 1/22 of L_0. From this it follows that L_1 equals 23/22 of L_0. At the bottom of fig. 5.45 a scenario is sketched where the aluminum plate and the support frame undergo thermal expansion. The formulas describing $DeltaL$ on the right side correspond with the ΔL of eqn. 3.2.

Note that there are two important assumptions on which the athermalized design is based. First it is assumed that the satellite bus itself does not expand. Now design effort went into the satellite bus, other than making some thin walls around a volume that fits the internal part of the optical system. Since the internal optical system is extremely sensitive to small misalignments, it is expected that the satellite bus will be designed such that it is athermalized by passive or active means. Second it is assumed that the support hinge is made out of the same CFRP material as the support frame with the optimized direction in the Y-direction of the support frame reference system. In other words, the optimized direction makes an 8° angle with the line perpendicular to the wall of the satellite bus and in the representation of fig. 5.45 it is included in length L_1, since it now has a CTE of 1 $\mu m/(m-K)$ in this direction as well.

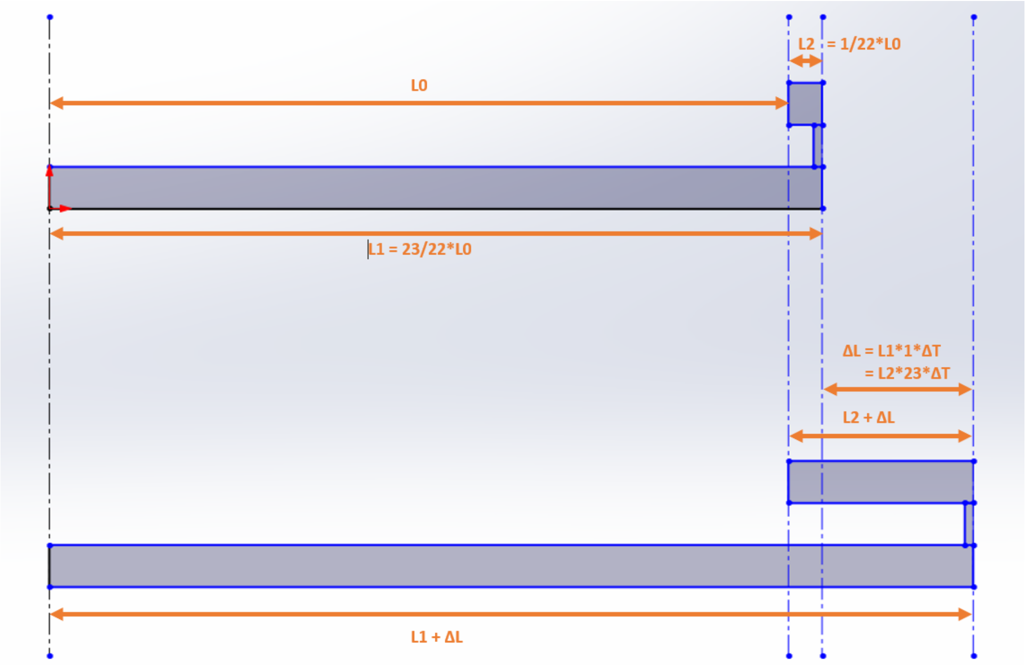

Figure 5.45: The upper construction shows the initial dimensions for the CFRP and aluminum frames, connected on the right side. The lower construction shows the same construction after a temperature increase, from which it becomes clear that L_0 is not influenced by temperature changes

Since the direction of thermal expansion needs to be controlled with high precision to meet the budgets, an interface is needed that can achieve such precision. A kinematic interface is the most likely option to achieve this. Inspired by the kinematic interface of fig. 3.35, the aluminum plates that carry the actuators are made with three grooves that fall on three spherical elements that are connected to the support plate. This is shown in fig. 5.46. Rather than using a physical plate-frame connection for the alignment of the two components at L_1, the kinematic interface is designed such that this location forms the thermal center of the components. The thermal centers are indicated by a single orange cross (without a white line intersecting them) in the figure.

If the temperature increases, the support frame will expand, moving the kinematic interfaces further towards the nose. The aluminum frame will expand radially from the thermal center in the opposite direction, to maintain the location of the actuator. This actuator location is represented by the orange crosses with intersecting white lines in fig. 5.46.

The reason that this principle is shown on the A-shaped support frame, is because athermalization in the described way is only applied in this version of the support frame. Thermal expansion happens in all directions, so not only in Y-direction. The athermalized design was not yet finished when the concept was changed to the final one. Therefore it was not yet found that this method does not work for compensation in X-direction. The final method is discussed in subsection 5.5.2, but first the correction in Z-direction is discussed, since this is the same for both methods.

Fig. 5.46 shows how a correction in Z-direction is applied by sinking the kinematic interface into the support frame to a location where the expansion of the support frame (downward if below the center line of the support frame) compensates the expansion of the aluminum plates. As a starting point it has been decided to make the radius of the spherical surfaces, r_{sph}, 3 mm. To be able to fit the grooves, the plate thickness, t_{ap}, is made 8 mm. Also a clearance gap, d_{gap}, of 1 mm is kept between the aluminum plate and the support frame. These dimensions are visualized in fig. 5.47. It is assumed that only the plate is made out of aluminum and that the rest is all made out of CFRP, including the spheres. As discussed in section 5.3, it is initially assumed that

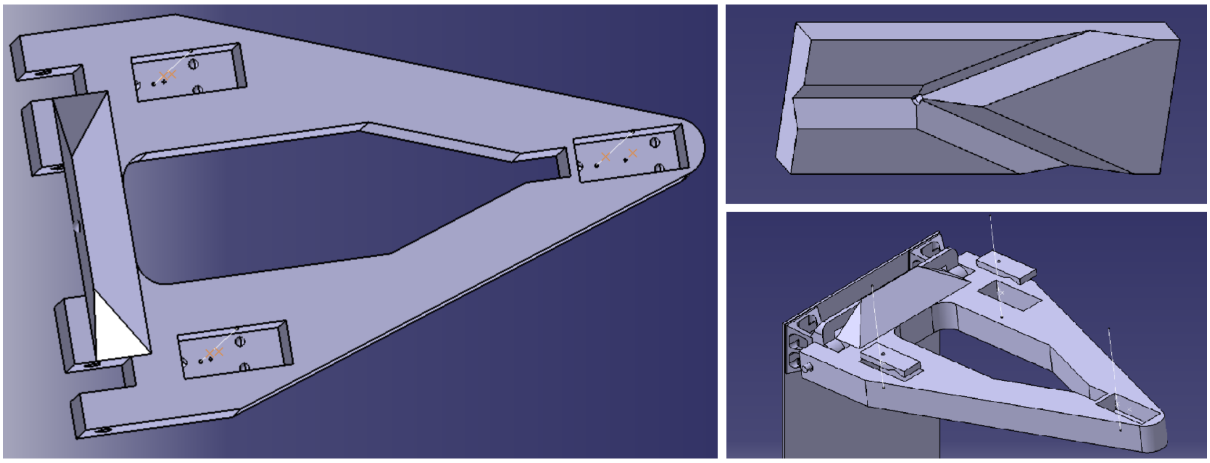

Figure 5.46: Left: A-frame with pockets containing three spheres each to create a kinematic interface. The orange crosses intersecting the white lines indicate the actuator locations (L_0), whereas the other orange crosses indicate the thermal centers of the kinematic interfaces (L_1) - Upper right: aluminum actuator plate with V-grooves that fall over the spheres - Lower right: assembly with the A-frame and the aluminum plates, in which the plates near the root are lifted

$CTE_{cfrp-per} = 10 \cdot CTE_{cfrp-opt}$ (eqn. 5.1), or in this case 10 $\mu m/(m-K)$. Note that the provided dimensions are arbitrarily chosen dimensions that fit the available space. Since it is not known what the dimensions of the actuators will be, the task to optimize the interface and aluminum plates is postponed. By then hopefully more is known about the actual thermal and mechanical properties of the CFRP so that the design can be optimized right in one go. Finishing this optimization is a highly recommended task for the future.

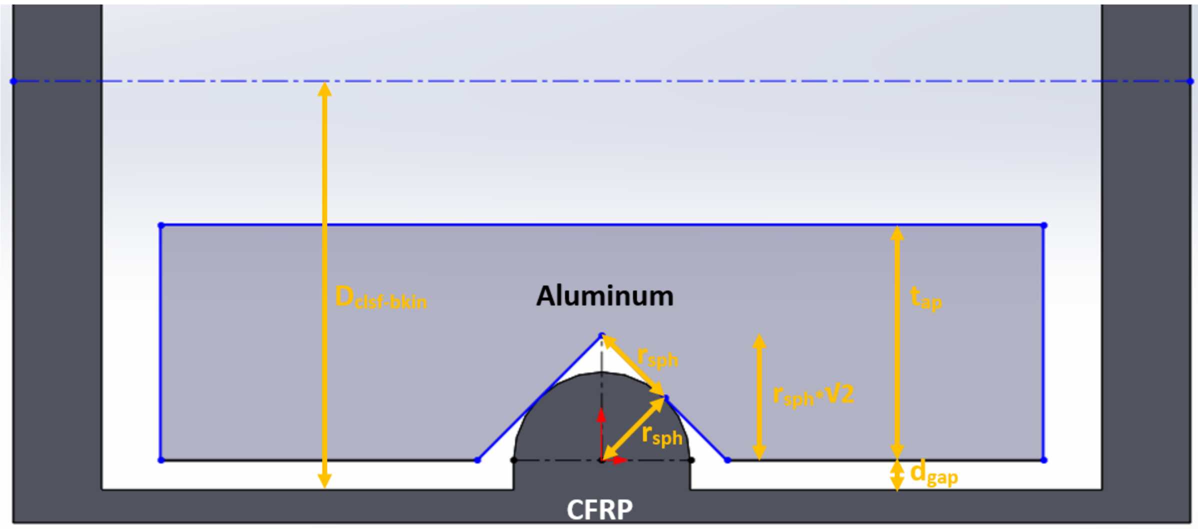

Figure 5.47: Drawing indicating the dimensional parameters and materials of the athermalized kinematic interface

With fig. 5.47 and the provided CTEs, one can now calculate how deep the kinematic interface should sink into the support frame. As seen from the center line of the support frame, the bottom of the kinematic interface will expand downwards when heated. The spheres and the aluminum plate will from there expand upwards when heated. These thermal expansions need to be equal to keep everything in place. The change in the distance between the center line of the support frame and the bottom of the kinematic interface, $d_{clsf_{b}kin}$, due to a temperature change can be calculated via eqn. 5.8. The change in distance from the top of the aluminum plate to the bottom of the kinematic interface, $d_{tap-kin}$, is described in eqn. 5.9. When equalizing these two equations the ΔT term drops. Solving for $d_{clsf-bkin}$, as shown in eqn. 5.10, leads to a value of 13.88 mm. Including the half of the support frame above the center line, this means that the pockets for the kinematic interface will need to be 28.88 mm deep, as was shown in fig. 5.46.

$$\Delta d_{clsf-bkin} = d_{clsf-bkin} \cdot CTE_{cfrp-per} \cdot \Delta T \tag{5.8}$$

$$\Delta d_{tap-bkin} = (d_{gap} + r_{sph}\sqrt{2}) \cdot CTE_{cfrp-per} \cdot \Delta T + (t_{ap} - r_{sph}\sqrt{2}) \cdot CTE_{alu} \cdot \Delta T \tag{5.9}$$

$$d_{clsf-bkin} = \frac{(d_{gap} + r_{sph}\sqrt{2}) \cdot CTE_{cfrp-per} + (t_{ap} - r_{sph}\sqrt{2}) \cdot CTE_{alu}}{CTE_{cfrp-per}} \tag{5.10}$$

5.5.2. ATHERMALIZATION BY STEERING TOWARDS CIRCULAR EXPANSION

The design described above has been made for the A-frame, before it was known what the final concept would be. In the meantime a new support frame has been designed and the person in charge of the calibration mechanism design has chosen a concept with preliminary dimensions. Before moving on with the improved athermalization, it is useful to understand the basic workings of the calibration actuators. It has been decided that a circular disk will stick out of the bottom of the mirror to connect it with the actuators. The disk will be parallel to the support frame and its center will be aligned with the budget reference point (see fig. 4.9). Three actuators will be connected as shown in fig. 5.48 [126]. Due to the flexures in the metering rod near the mirror attachment, it does not matter if the actuators at the bottom move in radial direction from the thermal center due to thermal expansion, as long as the three of them move point symmetrically around the center line of the disk. As a first estimate it is expected that the line on which the actuators will be located is a circle of 150 mm. The space required for the actuators is now estimated as a circle with a diameter of 30 mm. This can be seen in fig. 5.49.

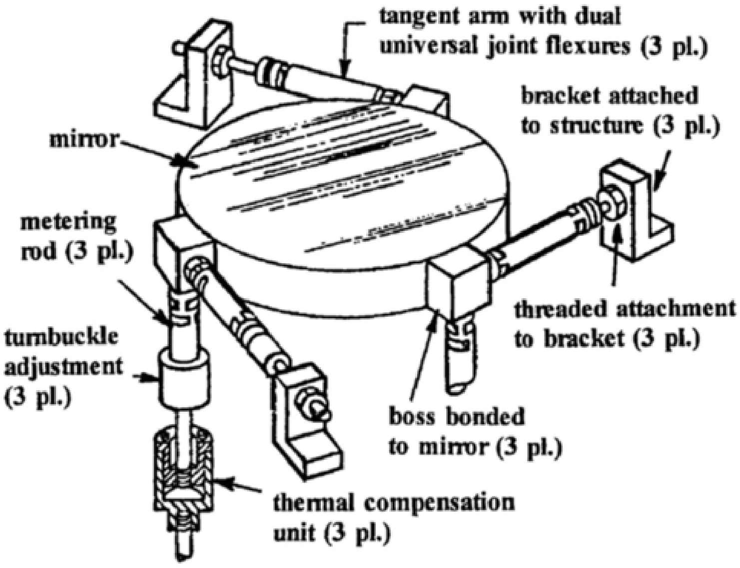

Figure 5.48: Sketch of chosen concept for M1 calibration mechanism [126]

With this knowledge one would expect to be able to apply the same athermalization mechanisms as used before. One important element was however not taken along yet in this design: the support frame also expands in X-direction. The X-direction is perpendicular to the optimized direction of the CFRP, meaning a CTE of 10 $\mu m/(m-K)$ applies. Using the same principles of fig. 5.45 again, L_0 now has a value of 130 mm, as measured from the YZ-plane of the support frame reference system. This is already very close to the edge of the support frame. It also means that L_0 is 13/23 of L_1, which has a value of 230 mm. According to these numbers the thermal center would have to be located far outside of the support frame boundaries, which is unacceptable with the provided dimensional constraints.

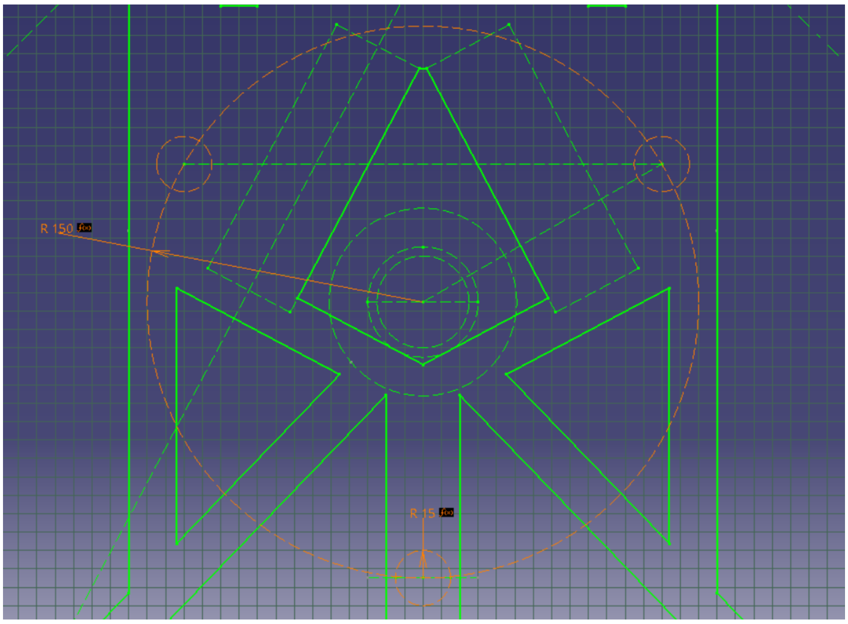

Figure 5.49: Sketch showing the locations of the calibration actuators on the reference frame

Therefore a new strategy has been devised. It makes use of the property of the calibration mechanism that the actuators are allowed to move in radial direction, as long as they are all spread with 120° angles on a circle with the same center point as the original location. Figs. 5.50, 5.51, 5.52, and 5.53 show a series of drawings that visualize the steps to come to the right thermal correction by steering towards a circular expansion around the initial center point. The figures help for deriving equations that indicate the location of the thermal centers of the aluminum plate kinematic interfaces. The first figure shows the initial situation. The second one visualizes the thermal expansion. Fig. 5.52 describes the required correction in Y-direction to end up at the original Y-location in a way similar to the previous design. This however leads to an angle of more than 120° between the actuator locations near the root of the support frame. Fig. 5.53 finally shows what additional thermal correction is required to solve this.

This method allows to solve the problems with the expansion in X-direction by only applying corrections in Y-direction. By using the figures one can derive the equations that define the locations of the thermal centers. They are described below in eqns. 5.11 and 5.12. Here dY_{b-tc} and dY_{n-tc} are the distances required between the actuator locations and the thermal centers of the kinematic interface (L_2) for the base plates (the ones near the root of the support frame) and the nose plate, respectively. dY_{b-bus} and dY_{n-bus} are the Y-distances between the satellite bus, and the base actuators and nose actuator, respectively (L_0). dX_{b-yz} is the distance between the YZ-plane and the location of the base actuator in X-direction. The values of dY_{b-bus}, dY_{n-bus}, and dX_{b-yz} can be derived from the values that created fig. 5.49 and are 160.49 mm, 385.49 mm, and 129.90 mm, respectively.

$$dY_{b-tc} = \frac{dY_{b-bus} \cdot CTE_{cfrp-par} + dX_{b-yz} \cdot CTE_{cfrp-per}\, tan(30)}{CTE_{alu}} = 39.59 mm \qquad [5.11]$$

$$dY_{n-tc} = \frac{dY_{n-bus} \cdot CTE_{cfrp-par} - dX_{b-yz} \cdot CTE_{cfrp-per} / cos(30)}{CTE_{alu}} = -48.46 mm \qquad [5.12]$$

As one can see, the location of the thermal center of the nose plate is negative, meaning it should be place between the root of the support frame and the nose actuator location. Here it actually pushes the actuator location with an even bigger distance towards the tip when heated. Fig. 5.53 also visualizes the push outwards. This can be explained by the fact that the thermal movement of the base actuators is mainly dictated by the movement in X-direction, since the CTE is 10 times higher than in Y-direction. With the dimensions in use, this means that the movement in X-direction is over 8 times bigger than the movement in Y-direction. The

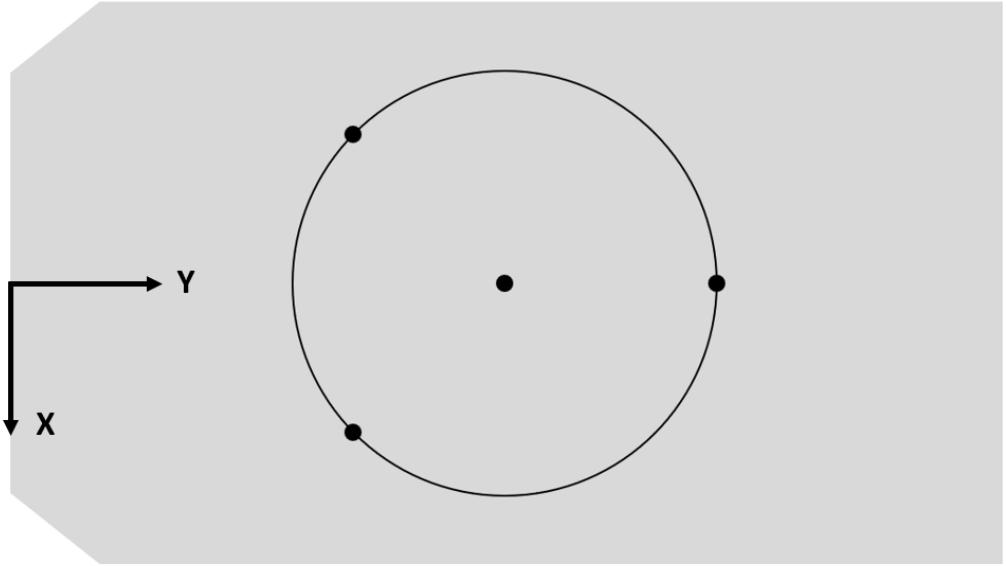

Figure 5.50: Circular athermalization 1/4: Initial state of the support frame with the location of the actuators and the center of the circle they describe

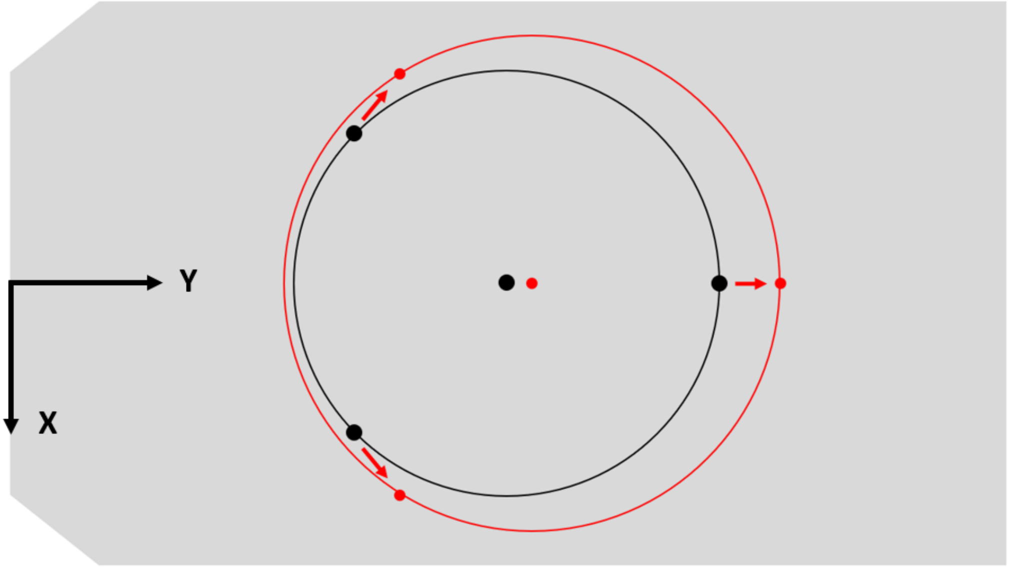

Figure 5.51: Circular athermalization 2/4: Movement of actuator locations due to thermal expansion, leading to a new circle with its center to the right of the starting point state

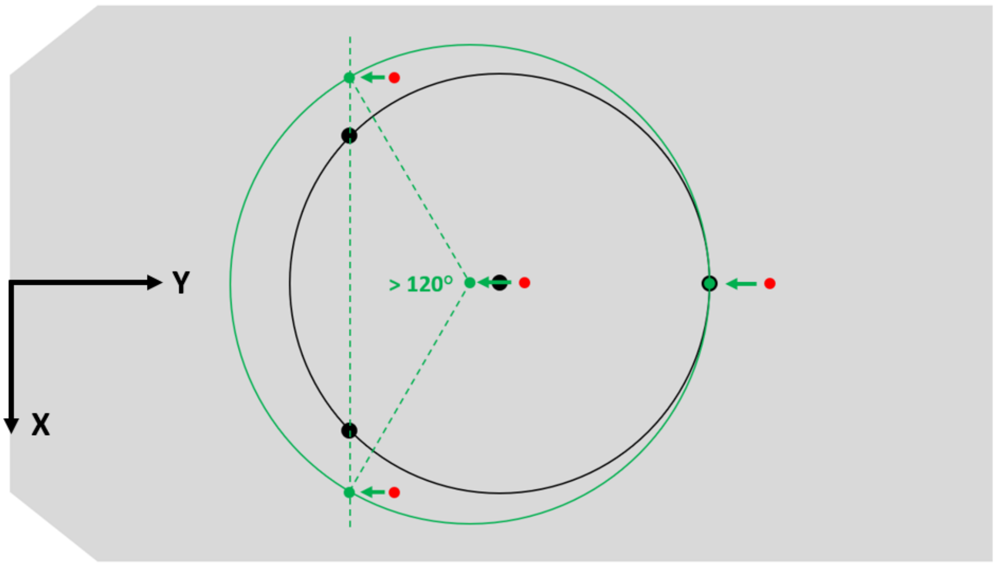

Figure 5.52: Circular athermalization 3/4: Required movement for athermalization in Y-direction, until every actuator is at the original Y-location. The point symmetry is lost now, because the indicated angle is larger than 120°

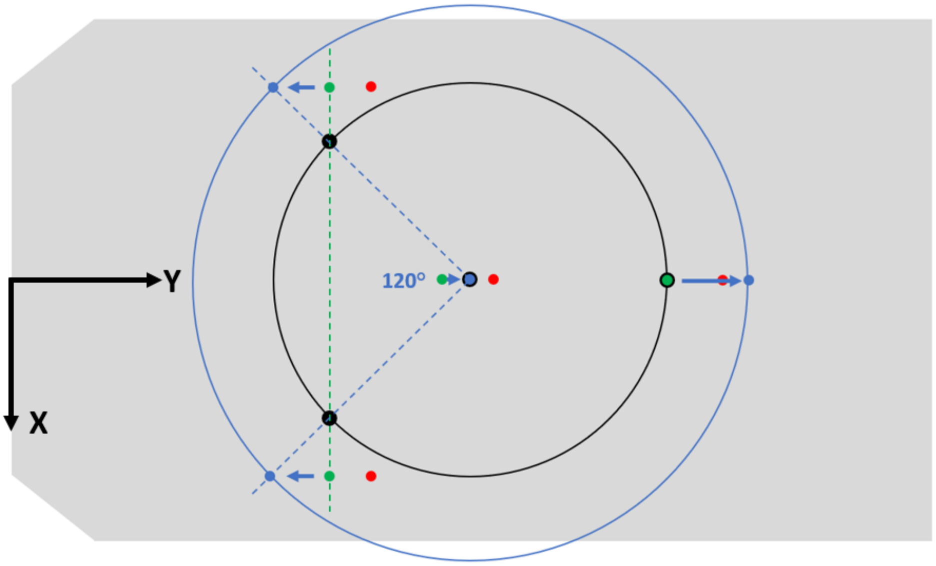

Figure 5.53: Circular athermalization 4/4: Required movement for additional thermal correction. The 120° angle is taken from the original center to find where the angle lines intersect an Y-vector applied to the actuator locations. Finally the actuator location at the tip is corrected for the new circle

corrected actuator location will therefore be on a circle with a radius that the nose actuator cannot reach, because it expands only in Y-direction where the low CTE applies.

Taking the results into account, new pockets, aluminum plates, and kinematic interfaces have been made. This leads to the design as shown in fig. 5.54. Note that the circular shapes on top of the aluminum plates are an indication of the actuator location. These circles where created by cutting away a thin layer of the plate, and so the top of this circle represents the top of the actual aluminum plate.

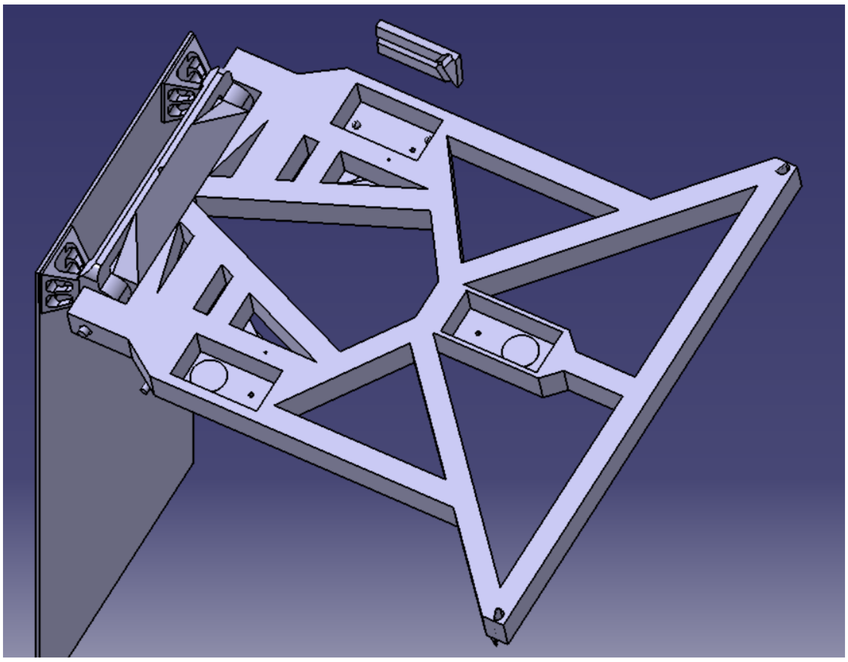

Figure 5.54: Figure of assembly with final athermalization design

5.5.3. REMAINING CONSIDERATIONS AND RECOMMENDATIONS FOR ATHERMALIZATION

With the described design changes, some factors arise that require a deeper look. The most important one relates to the kinematic interface between the support frame and the aluminum plates. A kinematic interface only works if a preload is applied to keep the interface together. The most suitable location to add a preload device is at the thermal center of the kinematic interface, because the support frame and aluminum plate will only move in a direction perpendicular to the interface at this location. Two options to consider as preload devices are a preloaded spring and a bolt with a CTE over its length that is equal to the CTE of the support frame in the direction perpendicular to the optimized direction. To make the right choice one should consider the required precision and the launch environment.

During launch high loads and high frequency vibrations occur. By applying a high enough preload one can prevent vibration damage that leads to loss in precision. The easiest way to apply a high preload is by using the option with the bolt. It can keep the interface sides pressed together during launch. Besides it will keep the preload constant when enduring thermal effects, because the expansion behaviour is equal to that of the interface if it has a CTE equal to $CTE_{cfrp-per}$. On the other hand it holds that precision at interfaces is acquired by using low stiffness devices. Based on this consideration one would prefer using a spring. This however may form a risk during launch, because applying a high preload on a low stiffness spring requires a relatively long stretch length for which there is probably too little room.

At the moment no analyses have been performed to find the right solution. It is therefore recommended to look into preload devices for the kinematic interfaces of the actuator plates. It should be taken into account that this also depends on the choices that will be made regarding the HDRMs of the complete M1 subsystem. An initial choice has been made for the attachment of the mirror to the satellite bus, but as recommended in section 5.3, one still needs to find out how to attach the support frame to the satellite bus. A separate HDRM for the support frame is required to protect its kinematic interface with the top hinge. If the support frame and the primary mirror are separately connected to the satellite bus during launch, it is preferred that the connection between them, formed by the calibration actuator and its actuator plates, has a low stiffness to prevent high launch stresses.

Two other recommendations for further research relate to the parts of the support frame surrounding the athermalization pockets. First, the thickness of the support frame between its bottom and the kinematic interfaces is only 1.12 mm. It should be investigated whether this is thick enough to not bend under the preload. Otherwise the support frame should be locally stiffened. Second, one can see in fig. 5.54 that the pockets currently are surrounded by a wall of at least 5 mm thick. Since the preload applied to the support frame by the ribbon cannot propagate through the pockets, it should be investigated whether this thickness is sufficient to prevent bending of the support frame. It is advised to optimize the thickness if this proves to be the case.

5.6. SUMMARY OF M1 SUBSYSTEM PROPERTIES

In this chapter a lot of detailed information is provided about the design features of the M1 deployment mechanism. The information is scattered and therefore the most important properties of the design are summarized in this section.

First a list of components is provided in tab. 5.3. For each component a mass estimate is provided. If applicable/known the material, manufacturer, and product code is provided as well. In the current design stage it is decided that a 20% margin should be added to the mass estimates. Therefore the total estimated system mass is 25 kg.

With materials assigned, the components in Catia are colored appropriately. This leads to the renders shown in figs. 5.55 and 5.56, where the different design feature can clearly be distinguished.

Table 5.3: Table listing the components of the M1 deployment mechanism with some of their properties

Component name	**Amount**	**Discussed in**	**Supplier**	**Product code**	**Material**	**Mass single component** [g]	**Total mass** [g]	**Comments**
Support frame	4	Sec. 5.3	TBD (Mitsubishi Chemical assumed for reference)	NA (DIALEAD 320 assumed for reference)	CFRP	3728	14912	Little mass optimization applied. Still much to gain
Support hinge	4		TBD (Mitsubishi Chemical assumed for reference)	NA (DIALEAD 320 assumed for reference)	CFRP	277	1108	
Athermalization base plate	8	Sec. 5.5	TBD	NA	Aluminum	49	392	
Athermalization nose plate	4	Sec. 5.5	TBD	NA	Aluminum	54	216	
Stepper motor	8	Subsec. 5.4.2	CDA InterCorp	12-2P6-06	NA	37	296	
Worm	8	Subsec. 5.4.2	Ondrives	PSW0.5-1	817M40T Steel	26	208	Mass not provided, estimated from dimensions
Worm wheel	8	Subsec. 5.4.2	Ondrives	ABPWG0.5-150-1	Bronze CA104	276	2208	
Worm wheel axis	8	Subsec. 5.4.2	TBD	NA	Bronze CA105	23	184	Bronze assumed for mating with worm wheel
Winch tube	8	Subsec. 5.4.2	TBD	NA	Bronze CA106	19	152	Bronze assumed for mating with worm wheel
Winch mount	8	Subsec. 5.4.2	TBD	NA	Titanium	108	864	Shape probably too complex for CFRP, therefore titanium assumed for now
Bearing worm wheel axis	16	Subsec. 5.4.2	TBD (SKF assumed for reference)	NA (W 61701 assumed for reference)	NA	3	48	Not discussed in detail, although space is left for bearings in design
Bearing worm	8	Subsec. 5.4.2	TBD (SKF assumed for reference)	NA (DW R168 assumed for reference)		1	8	Not discussed in detail, although space is left for bearings in design
Ribbon	8	Subsec. 5.4.2	TBD	NA	Kevlar 49	40	320	
Total	**100**						**20,916**	

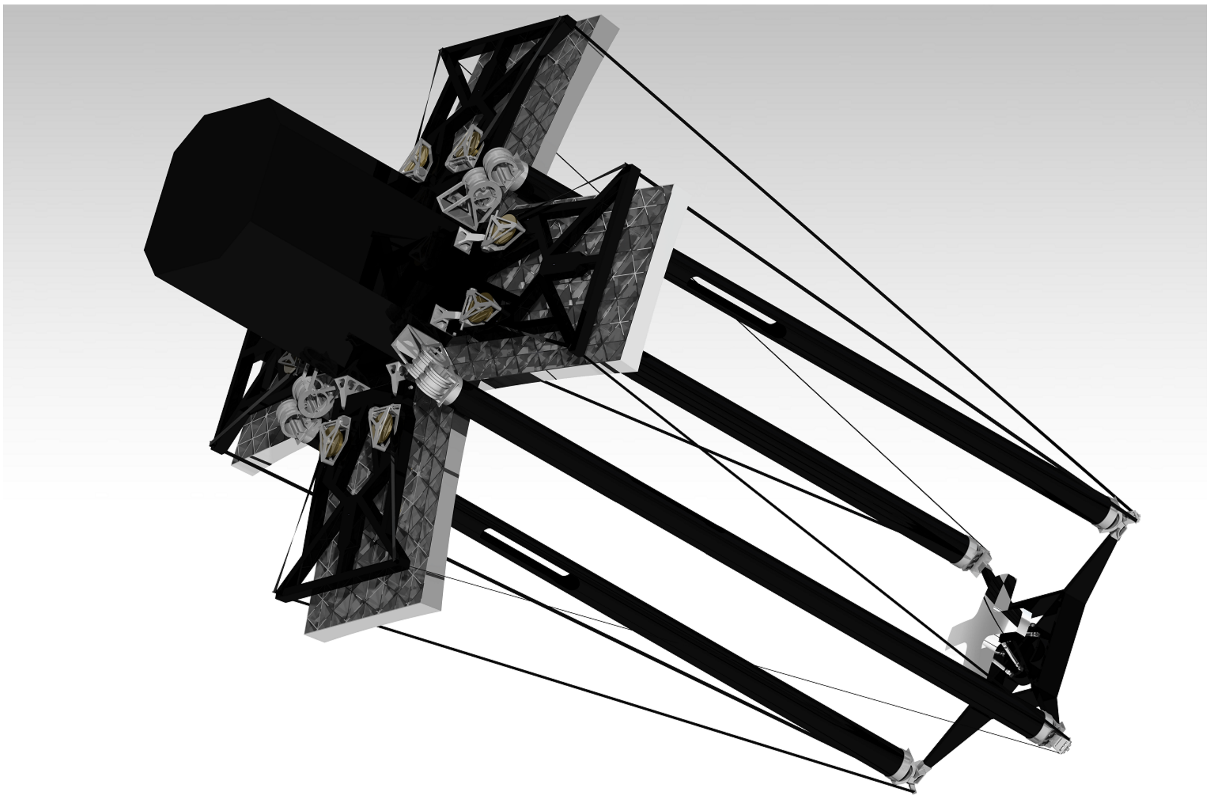

Figure 5.55: Render of an isometric view that shows the bottom side of the full satellite design. Courtesy André Krikken

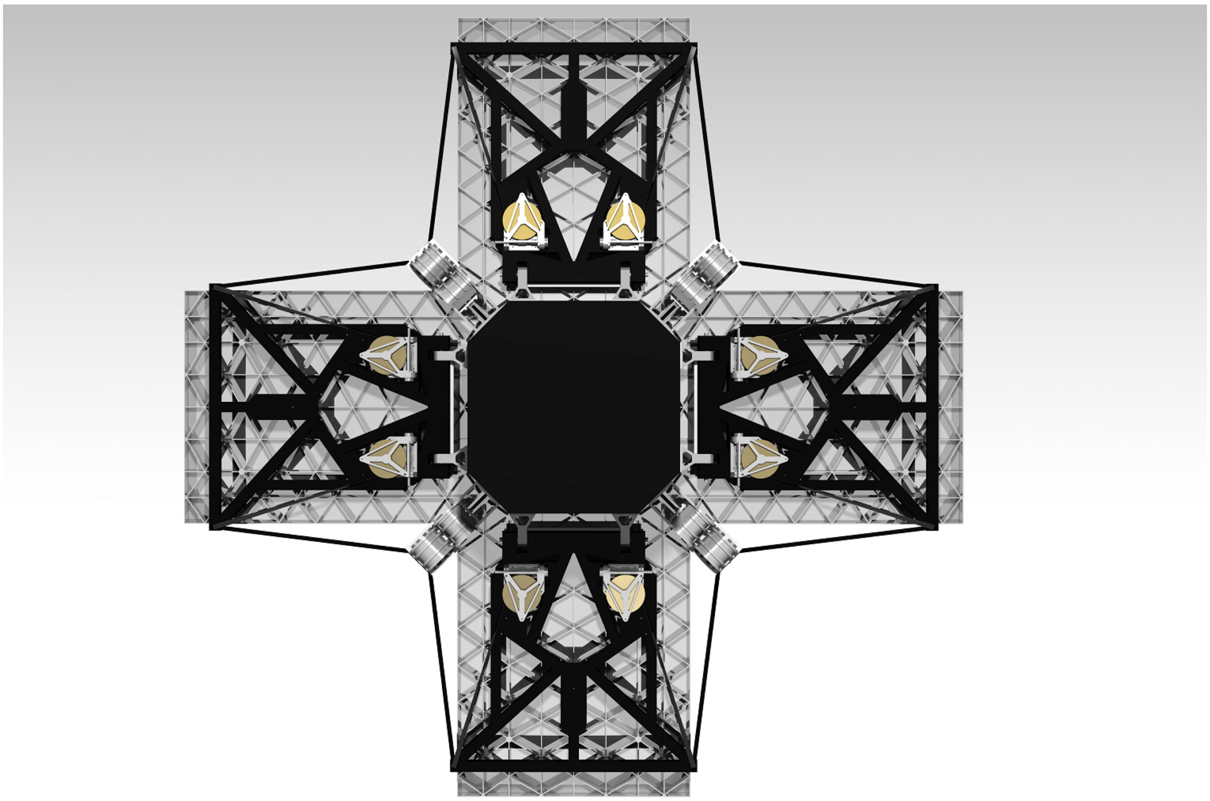

Figure 5.56: Render of a bottom view that clearly shows the design features discussed in this thesis. Courtesy André Krikken

6

UPCOMING DESIGN STEPS

Throughout this thesis it is indicated per component where the design activities stopped. Based on this recommendations are provided, which are summarized in tabs. 7.3, 7.4, and 7.5. As explained in section 2.5, the main short term goal regarding the M1 deployment mechanism is to work towards a breadboard design. The current design is almost at a point where a breadboard design can be derived, but a couple of steps still need to be made. Rather than providing detailed and specific steps as provided in the recommendation tables, the general outline of the steps up to the breadboard design are discussed in 6.1. Before a breadboard design can be made, a risk assessment needs to be performed to indicate what one wants to test for. Since the full scale M1 deployment mechanism is not designed to a level where a breadboard prototype can be derived, the risk assessment is not conducted yet. Some potential risks are however identified and discussed in section 6.2.

6.1. NEXT DESIGN STEPS FOR FULL SCALE M1 DEPLOYMENT MECHANISM

There are two major design steps that need to performed before one can move towards a well informed risk assessment. First a vibration and static structural analysis should be performed where the M2 booms are not moving. This way one can find the optimal combination of preload and ribbon stiffness to ensure that the kinematic interface stays connected and that the vibration stability budgets (requirement M1-MEC-07) are met. Furthermore the support frame can now be optimized for mass such that it can just carry the preload without deflecting to an unacceptable level. This provides the knowledge required to make a well considered trade-off between the preload and stiffness values desired for the M1 subsystem on the one hand and the M2 subsystem on the other hand. Now two processes can be started in parallel. The first process is to analyze the combined M1 and M2 subsystems for vibrations. This is a time-consuming task that requires an ANSYS license without node limits and a powerful computer.

The second process is the next major design improvement: both the kinematic interfaces of the support hinge and the athermalization plates, discussed in sections 5.3 and 5.5 respectively, need to be designed in detail. Only then it can be estimated how precise the deployment is. One can afterwards also think of how to apply shimming to compensate for errors due to manufacturing tolerances. A more detailed design approach for the described steps is provided in separate subsections below.

6.1.1. STATIC STRUCTURAL AND VIBRATION ANALYSES

Static structural and vibration analyses are crucial to make a design that can handle vibrations and the preload provided by the ribbon. Furthermore the results of the analyses are a first step to verify compliance with the requirements. Unfortunately it was not possible to include an analysis of the final design in the research due to time constraints. A first vibration model has however been made for the first iteration design of the support frame of the current deployment mechanism concept (fig. 5.14). At the moment it became clear that none of the initial concepts worked, a search for external help started. In the time between this moment and the first conversations with professor Just Herder, the author started to familiarize himself with ANSYS to apply the gained knowledge to the first iteration design of the new concept. Although the model does not work properly, it is recommended to look into this model before building one yourself, because some lessons can be learned.

ANSYS is able to perform different kinds of analyses. A modal analysis is for example used to determine the eigenfrequencies of a structure, while a random vibration or response spectrum is used to find a structure's response to vibrations. As shown in fig. 6.1, these analyses can be coupled. In the case of fig. 6.1 it was even necessary, because the eigenfrequencies calculated in the modal analysis are required as an input to calculate the response to random vibrations. The model made for these analyses is shown in fig. 6.2. Here one sees that the ribbons are represented by springs of which the stiffness and preload can be provided as input. There was however one problem that could not be fixed in the model: not all edges of materials were detected as interfering. This results in deformations as shown in fig. 6.3. In the meantime a vibration model for the M2 mechanism has been build and there it was found that this is a problem specific to the modal analysis. The bore in the support frame is not fixed to the axis of the support hinge. Their connection is determined by the ribbon preload, while the ribbon is vibrating in this analysis. A. Krikken found that if first a static structural analysis is performed, the output provides the relation between preload and the interfacing of the frame with the hinge. This output should be inserted in the modal analysis to yield better results. This approach is stated in recommendation Rec-61-01.

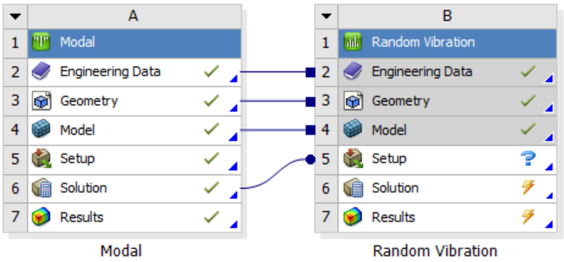

	A	
1	Modal	
2	Engineering Data	✓
3	Geometry	✓
4	Model	✓
5	Setup	✓
6	Solution	✓
7	Results	✓

Modal

	B	
1	Random Vibration	
2	Engineering Data	✓
3	Geometry	✓
4	Model	✓
5	Setup	?
6	Solution	⚡
7	Results	⚡

Random Vibration

Figure 6.1: ANSYS workbench with coupled modal and random vibration analyses

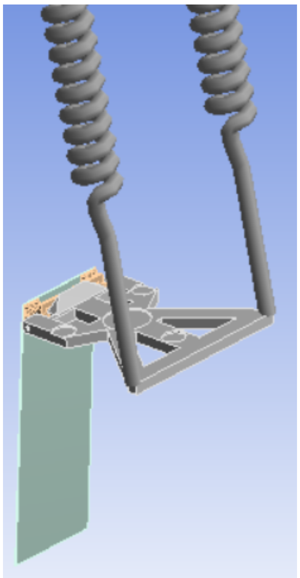

Figure 6.2: Model used for modal analysis of M1 deployment mechanism. The ribbons are represented by preloaded springs

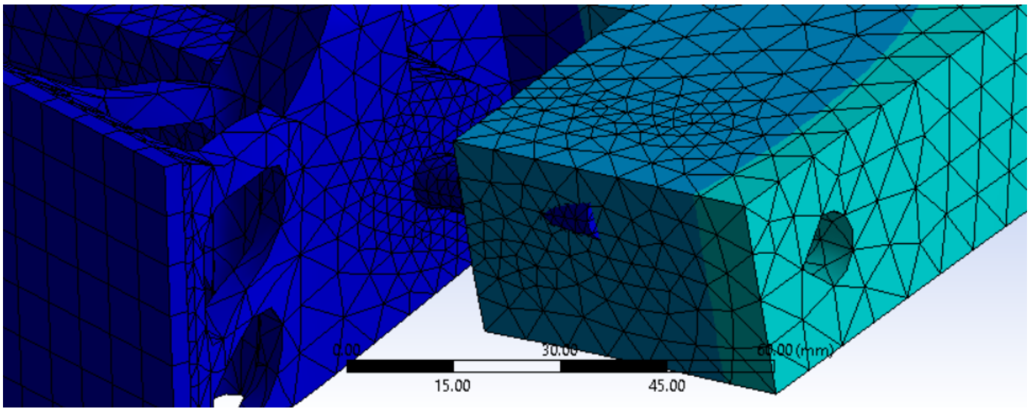

Figure 6.3: Exaggerated deformation of the third eigenmode. ANSYS is unable to detect interference between the support hing and support frame

Once the modal analysis is performed it is suggested to analyze the effect of the vibrations induced by the reaction wheels. Since the reaction wheels are not yet selected, a model has been made by A. Krikken that is based on the frequency spectrum of a reaction wheel used in a satellite with a size comparable to the DST. This model should be applied to find if the eigenfrequency of the structure is high enough and to find whether the amplitude of the vibrations meets the budgets. One should investigate how different preloads and spring stiffnesses affect the results. These results should be compared with the effects they have on the M2 design to find a preload and ribbon stiffness that suit both subsystems.

Next a static structural analysis will have to show how the chosen preload bends the support frame. Bending of the extensions around the Y-axis will lead to a lower preload, but will not cause other problems. Bending around the X-axis however leads to errors in the locations of the calibration actuators. There is no requirement telling what bending is acceptable, but deviations due to this bending fall in the 'Deployment and Coarse Alignment Tolerances' budget. This means that a smaller error is allowed for misalignments in the kinematic interfaces. It is relatively easy to increase the stiffness of the support frame, but this leads to additional mass. Once the kinematic interfaces are designed, it is expected that several iterations are required to find the optimal balance.

6.1.2. DETAILED KINEMATIC INTERFACE DESIGN OF THE SUPPORT HINGE

As explained in section 3.3 a kinematic interface is exactly constraint by making use of non-conforming interfaces (point contacts). This however leads to very low stiffness and local deformations at the interface. Since precision is required this could mean that overconstraining the design might by needed to counteract the local deformations. This can only be assessed once the preload has been determined. As defined in the DST requirements document [21], a safety factor of 1.25 should be applied to the preload. ANSYS can then calculate the stresses at the kinematic interfaces to find out if they are below the yield stress. If not, a first step to increase the stiffness is to replace the point contacts with line contacts. The interface is then referred to as semi-kinematic. The current design actually already contains line contacts between the support hinge axis and the support frame V-grooves. As discussed in section 5.3 this is however illustrative, because it is preferred to make the connection non-conforming. If line contacts do not provide the required stiffness as well, it is recommended to create more non-conforming interfaces that distribute the loads.

Once the interface is designed such that no stresses above the yield stress occur, one should analyze how large the local deformations are. This information can then be combined with the manufacturing tolerances, provided by a supplier, to calculate the expected positioning errors of the calibration actuators. If these errors exceed the budget one can estimate the amount of shimming that is required and think about convenient ways to apply shims.

6.1.3. DETAILED KINEMATIC INTERFACE DESIGN OF THE ATHERMALIZATION PLATES

For the design of the athermalization plates the same principles hold as discussed in previous subsection. There is however a big difference in the applied loads. Depending on the choice whether the mirror will hold down the whole stowed M1 subsystem or whether the support frame and mirror will have separate HDRMs, the athermalization plates may need to transmit launch loads. In the first case the plates form the connection between the mirror and the other M1 subsystem components. The connection would then need to be very stiff. Considering the size of the plates it seems unlikely that six point contacts can handle all these loads. At this point an alternative solution should be found to connect the mirror and the support frame, because the kinematic interface of the plates is required to ensure precise athermalization.

During operation the vibrations and loads from the calibration actuators should be considered next to the vibrations induced by the reaction wheel. Once these are known, the optimization strategy is equal to the one described in previous subsection.

6.2. RISK IDENTIFICATION

Even though no extensive risk assessment has been performed, some risks have been identified during the design process. A property of the design is indicated as a risk if there is a certain likelihood that it endangers the systems capability to meet the requirements. A lot of assumption are made throughout this work. Some are based on theory from literature, some are based on an engineering gut feeling, and some assumptions are taken out of convenience (mostly the negligence of certain phenomena), because the information to define a somewhat reliable assumption is not available. The four major foreseeable risks are described below:

- Viscoelastic creep is an effect that forms a major risk for achieving the required deployment precision over the entire course of the mission. Other than for materials that are subjected to other forms of creep, there is no database with properties of viscoelastic creep for different materials, because the properties are very design specific. Therefore creep in CFRP components can only be characterized by testing. Especially if it turns out that a high ribbon preload is required, there is a high risk of a deformation in the support frame that slowly exceeds the budgets.

- It has been decided to control the temperature up to +-1 K accurate from the nominal temperature. This is great, but there is still a major concern once gradients occur. The design will lose its symmetry and since the M1 and M2 subsystems are connected, it is hard to predict the impact of a gradient on the complete system. It is recommended to test for gradients and their impact on the system performance as a whole.

- The conflicting preferences of the M1 and M2 subsystems concerning the ribbon properties form are another risk. For the M1 subsystem a low stiffness and high preload is preferred, while the M2 subsystem prefers a high stiffness. For the M2 mechanism the preload is less of a concern, as long as it allows the booms to deploy. Since the whole structural integrity of the current design is based on the ribbon connections, the impact will be catastrophic if it turns out that no ribbon can be made such that its properties satisfy the requirements of both subsystems. For the M1 mechanism there is an alternative concept to apply the required preload (fig. 4.18), but the design of the M2 mechanism will be set back to a conceptual brainstorm stage.

- The current mass estimate leads to a M1 deployment mechanism mass of 25 kg, including a 20% margin. Requirement M1-MEC-11 allows for a combined system mass of this mechanism and the calibration system of 16 kg. This means the mass of the calibration system should be added before it is known how far the budget is exceeded. 75% of the 25 kg comes from the support frames, it is expected that their mass will become significantly lower once the two optimization strategies, described in recommendations Rec-53-02 and Rec-53-03 (tab. 7.3), are applied. A support frame mass reduction of roughly 50% is however needed to meet the budgets and it is unlikely that this will be the result of the suggested mass optimization. Therefore there is a high likelihood that requirement M1-MEC-11 cannot be met, but the technical impact is very low. The impact is mostly a financial concern and since there is no customer yet, it cannot be estimated how critical the additional costs are.

7

CONCLUSIONS AND RECOMMENDATIONS

In this chapter, the results of this thesis research are discussed to draw the main conclusions. This is described in section 7.1. During the thesis some questions arose to which an answer could not be provided yet. Furthermore some design tasks are not completely finished. Section 7.2 presents the remaining questions and suggests how to proceed with the uncompleted tasks in the form of recommendations.

7.1. CONCLUSIONS

Looking back to the research objective, research questions, and research framework presented in section 2.5, it becomes clear that not all of the planned research activities are executed. This is shown in fig. 7.1.

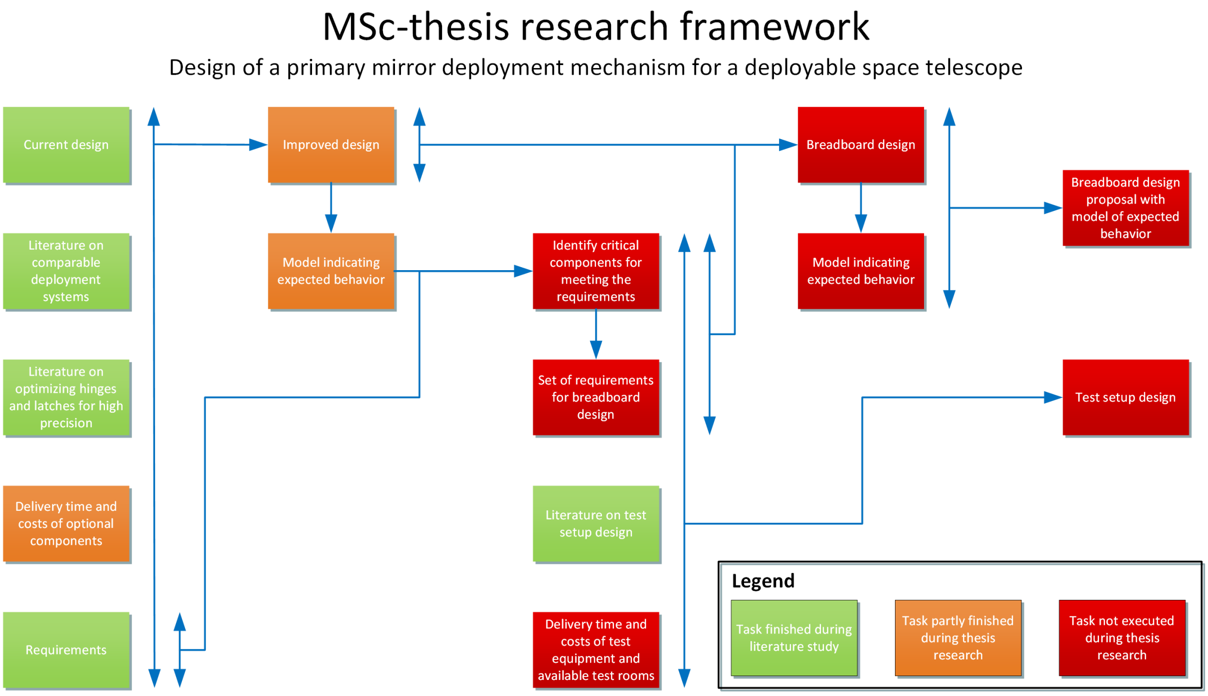

Figure 7.1: Thesis framework of fig. 2.26, but now with a color scheme indicating the tasks finalized during this thesis

The major reason for not being able to execute the complete research framework is that halfway the research it had to be concluded that none of the proposed concepts would lead to a feasible design. It was planned that the three orange blocks of fig. 7.1 would take half the time of the thesis research. The other, smaller tasks would follow in the second half. This means that the unfortunate conclusion was drawn almost halfway the research. The concept phase had to start all over and additional literature research was required for implementing the recommended design practices in the new concept.

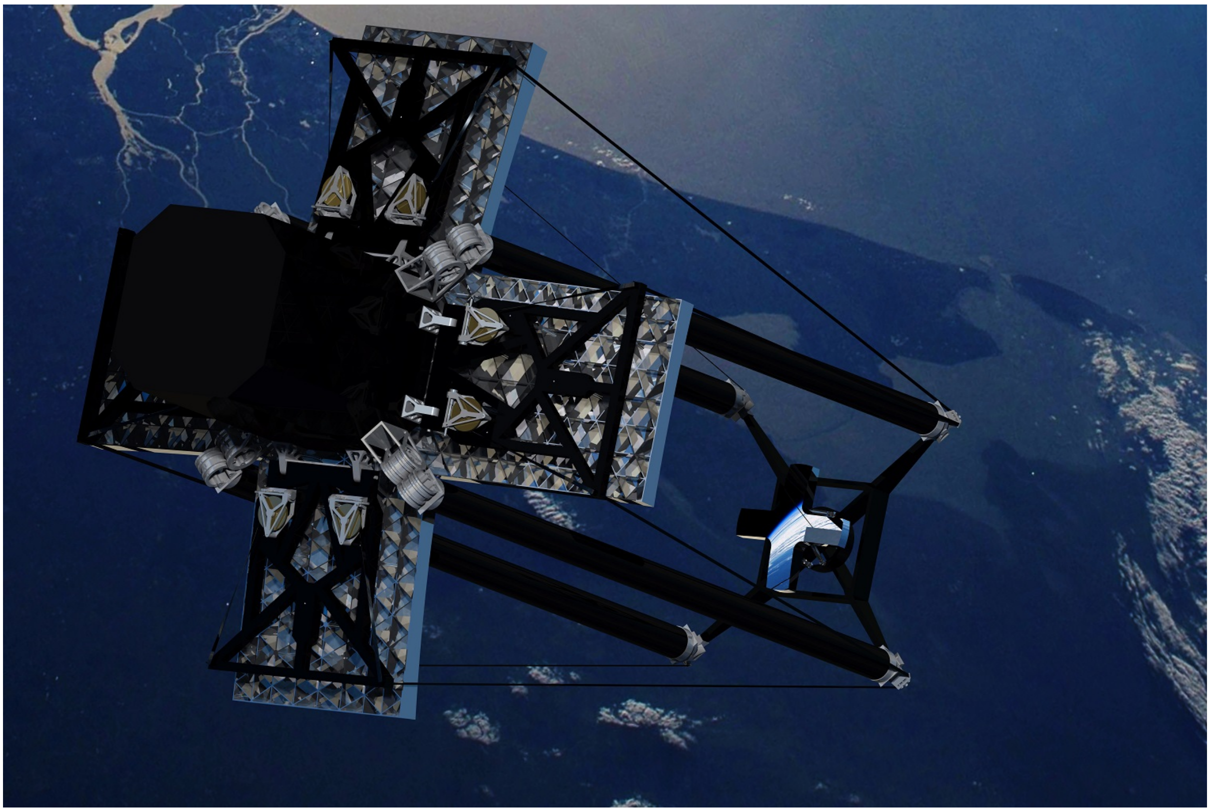

Figure 7.2: Render of the most recent DST design. Courtesy André Krikken

In the end the design efforts led to the system of fig. 7.2. In literature no example has been found of a concept like this that has flown in space. Satellites of which both the primary mirror and secondary mirror unfold do exist, but none of them use lines with the dual functionality to provide stability to the secondary mirror, while providing a preload to mate the kinematic interface of the primary mirror. With this design only the first research question can be partially answered. It is stated below:

Central research question 1
What improvements of the primary mirror deployment mechanism are needed to meet the requirements?

With the conclusion that the concepts presented in chapter 4 all lead to unfeasible designs, one can start the answer to the research question by mentioning that an 'improvement' is an euphemism for what was needed to get to the current design, since a completely new concept had to be developed. The favourable answer to the research question would be to say that the current design allows to meet most of the requirements. The other requirements have not been designed for yet, but feasibility is expected.

However, until the performance of a component is verified by testing, one cannot know for sure whether a component meets the requirements, unless the requirement imposes a design feature that is inherent to the design (e.g. a dimension). With (mathematical) reasoning one can however qualitatively argue why feasibility is assumed. Therefore the reasoning behind the feasibility of each subsystem requirement (see appendix A) is provided below:

M1-MEC-01, M1-MEC-02, and M1-MEC-03
These three requirements relate to the deployment and coarse alignment tolerance budget of the deployment mechanism and the calibration system, as presented in tab. 7.1. In this table, the daughter requirements of M1-MEC-01 correspond to the first six columns, M1-MEC-02 corresponds to the seventh column, and M1-MEC-03 corresponds to the last column. Currently it is not possible to calculate a first estimate of the deployment precision, since there are too many unknowns. It is described in section 6.1 what steps are required to be able to make this estimate. For now it is expected that the requirements can be met as long as the ribbon preload can be kept constant, since kinematic interfaces with the required precision have been made in the past.

Table 7.1: Budgets for the primary mirror as defined in the requirements (copy of tab. 4.2) [21]

Position [μm]			Tilt [μrad]			Radius [%]	Shape Error [nm]
X	Y	Z	X	Y	Z		
Deployment and Coarse Alignment Tolerances							
2	2	2	2	4	50	$1*10^{-3}$	50
In-Orbit Drifts							
$2*10^{-2}$	$2*10^{-2}$	$2*10^{-2}$	$1*10^{-2}$	$2*10^{-2}$	5	$1*10^{-4}$	5
Stability Budget							
$5*10^{-3}$	$5*10^{-3}$	$5*10^{-3}$	$2.5*10^{-3}$	$1*10^{-2}$	$5*10^{-1}$	n/a	n/a

M1-MEC-04, M1-MEC-05, and M1-MEC-06
These three requirements relate to the in-orbit drift budget due to temperature changes, as presented in tab. 7.1. In this table the daughter requirements of M1-MEC-04 correspond to the first six columns, M1-MEC-05 corresponds to the seventh column, and M1-MEC-06 corresponds to the last column. Since it initially turned out that these requirements formed the toughest challenge, a lot of effort has been put in passive athermalization of the design. The calculations described in section 5.5 provide confidence that the requirements will be met as long as the thermal design team creates an environment according to M1-MEC-15 with negligible gradients.

M1-MEC-07
The daughters of this requirement correspond with the values in the bottom row of tab. 7.1 and form the vibrational stability budget. At the moment it cannot be determined whether this budget is met, but as explained in section 6.1, it will be an iterative optimization process to find the ribbon preload and stiffness that allow for meeting the requirement. It is expected that a feasible solution exists.

M1-MEC-08
Requirement rejected

M1-MEC-09
This requirement demands that the stowed deployment mechanism survives launch. Its daughter requirements define the assumed loads and vibrations that occur during the launch event. In this thesis little effort has been put in optimizing the deployment mechanism for this phase, because it is assumed that meeting this requirement is much less of a challenge than meeting M1-MEC-01 to M1-MEC-07, and therefore more time has been spent in accomplishing the latter. Some considerations are described in subsections 5.3.3 and 5.5.3. Although it is necessary to make a serious design effort to comply with this requirement, it is a design practise for which a lot of solutions are available, since every component that goes into space needs to meet this requirement. Therefore there are at the moment no reasons to assume it cannot be met.

M1-MEC-10
This requirement states: *The stowed mechanism shall conform with Guiana Space Centre safety regulations.* This is a concern for a later design stage. As long as the components are not potentially hazardous to people in the direct environment, there is no reason to assume this requirement cannot be met.

M1-MEC-11
This requirement states: *The combined mass of the primary mirror deployment and active optics systems shall be no more than 16 kg.* This requirement forms a major challenge, since the current mass estimate of the deployment mechanism without the active optics is already 25 kg (including a 20% margin). Although the mechanism currently exists out of 100 components (tab. 5.3), the support frames account for 75% of the mass. It is expected that a significant amount of support frame mass can be saved by rounding the edges and corners and by optimizing the mass and shape to just achieve the required bending stiffness. It is however disputable whether this would result in half the current support frame mass, which is roughly needed to meet the requirement. A way to save additional support frame mass is to move the extensions closer to the root, meaning the length becomes shorter. It is however important to involve the M2 subsystem engineer, because this has a negative impact on the stability of the booms.

If it turns out unfeasible to comply with this requirement, there is still hope. The mother requirement of M1-MEC-11 is MIS-REQ-08, stating that the mass of the instrument shall be lower than 100 kg. The mass requirements of the subsystems are a distribution of this 100 kg. Possibly one of the subsystems turns out lighter than required. It can then be discussed whether the unused mass can be added to the M1 deployment mechanism mass budget. For now it is expected that meeting the requirement is unfeasible. It is recommended to discuss revision of the mass distribution over the subsystems.

M1-MEC-12
This requirement states that the M1 subsystem shall have an operational life of at least five years. Since the deployment mechanism is protected by a baffle, no material degradation by UV radiation or thermal cycling is expected. Furthermore the ribbon preloads are assumed to be constant, meaning that fatigue is not likely to cause failure. Outgassing and viscoelastic creep however potentially limit the operational lifetime of the subsystem by gradually introducing a deployment error that grows outside of the budgets. Especially during the first months in space outgassing occurs. Next to the risk of contaminating the mirror surfaces, the shape of the support frame will slightly change when it loses mass, possibly resulting in unacceptable deformations. Over a much longer time span, viscoelastic creep may result from the preload of the ribbons, leading to unacceptable bending deformation. Both phenomena are discussed in subsection 5.3.1, where it is explained that especially creep forms a potential risk. Tests will have to verify whether this requirement can be met. Since creep will reduce with lower preloads and different materials have different sensitivities to creep, it is expected that meeting this requirement is feasible, although some optimization may be required.

M1-MEC-13
This requirement specifies that four mirror segments shall be used. This is an inherent design future and is therefore per definition feasible.

M1-MEC-14
This requirement specifies the distance between the M1 plane and the M2 plane, which is 1.6 m. It is again an inherent design feature, so it is certain the requirement can be met. On the other hand, large changes in this dimension will impact the compliance of the design with other requirements.

M1-MEC-15
This requirement defines that the M1 system shall be able to operate in a thermal environment of 298 K +- 1 K. Although it was not possible for the initially proposed concepts to operate within the drift budgets in such a thermal environment, the current design is athermalized and insensitive to the small temperature changes. This however only holds for bulk temperature changes, since gradients may result in unacceptable deformations. It is advised to model what gradients are acceptable and provide a requirement to the thermal design team to control the gradients within these bounds. There are multiple design options to improve the control on gradients and it is therefore expected this requirement will be met.

Table 7.2: Summary of expected feasibility to meet the subsystem requirements

Requirement(s)	Feasible?
M1-MEC-01 M1-MEC-02 M1-MEC-03	Likely. Condition is that the ribbon preload is constant. Argumentation based on performance existing designs.
M1-MEC-04 M1-MEC-05 M1-MEC-06	Very likely. Argumentation based on calculations that lead to an athermalized design. Condition is that no gradients are present.
M1-MEC-07	Likely. Based on assumption that a suitable combination of ribbon preload and stiffness exists that also allows compliance with other requirements.
M1-MEC-09	Likely. Argumentation based on availability of many design solutions.
M1-MEC-10	Very likely. More of a bureaucratic challenge than a design challenge.
M1-MEC-11	Unlikely. Argumentation based on calculations.
M1-MEC-12	Likely. Based on assumption that the ribbon preload can be lowered to a level where creep does not pose a threat.
M1-MEC-13	Certain. Inherent design feature.
M1-MEC-14	Certain. Inherent design feature.
M1-MEC-15	Likely. Condition is that no gradients are present.

The likelihood of the feasibility and the argumentation, conditions, and assumptions that hold to assume this likelihood are summarized in tab. 7.2. Coming back at the research question, tab. 7.2 clearly shows that for the current design it is likely that meeting all requirements is feasible, except for the one defining the mass budget. With this design, the compliance to the requirements is improved with respect to the design of Van Putten. The most favourable answer to the research question, that it is feasible to meet all requirements can unfortunately not be given. This conclusion can change if requirement M1-MEC-11 allows a higher mass. It is therefore recommended to apply the suggested mass optimization of the support frame as a next design step to determine how far the budget will actually be exceeded. Then the mass distribution over the subsystems can be evaluated to see if the M1 deployment mechanism mass budget can be increased, by decreasing the mass budgets of other subsystems.

7.2. RECOMMENDATIONS

As explained in previous section, there is still a lot of work to do to complete the design of the M1 deployment mechanism. The major upcoming design steps are discussed in detail in chapter 6, but throughout the report a lot of small recommendations are provided as well. Often they relate to questions that arise from intermediate results or to specific design details that could not be incorporated anymore due to time constraints. All these recommendations are summarized in tabs. 7.3, 7.4, and 7.5. Often a reference can be found to sections explaining the recommendation, but some relate to topics that have not been discussed in detail in this report.

Table 7.3: Table listing all recommendations resulting from this thesis research part 1/3

Relevant section	Code	Recommendation
5.2	Rec-52-01	Calculate the positioning of the stowed M2 boom and visualize this in a Catia model
	Rec-52-02	Make a triangular connection to the extensions of the support frame directly from the root. This provides a higher structural stiffness than the current triangle near the tip. This was done because it was wrongly assumed this was necessary to avoid conflicts with the stowed M2 boom.
	Rec-52-03	Make a support frame that moves closer to the mirror near the tip (out of plane). One can now make the extensions wider as shown in fig. 5.5.
5.3	Rec-53-01	Request more information about CFRPs from suppliers. Especially the following data is relevant:
	Rec-53-01-a	-Properties such as Young's modulus, CTE, and thermal conductivity in all directions. Suppliers mostly only provide data for the optimized direction.
	Rec-53-01-b	-Information with respect to outgassing. Ask specifically about deformations due to outgassing, because it is more common to request data about the amount of material that is outgassed.
	Rec-53-01-c	-Information with respect to creep. This data is crucial, because it may lead to the conclusion that only a slight amount of ribbon preload is allowed. This may conflict with what is required to achieve the required precision at the kinematic interface of the support frame hinge.
	Rec-53-01-d	-Information about the allowed complexity of the component to be able to manufacture it.
	Rec-53-02	Optimize the width of the linkages of the support frame. All linkages currently have a width of 20 mm. This is chosen quite arbitrarily. One should perform a vibration analysis to find the optimal preload of the ribbon. Then one should perform a static force analysis to see how the support frame bends under this preload. If this is within the limits, one can optimize the design by making the linkages smaller. Note that not only bending around the X-axis (tip bends upwards), but also symmetrical bending around the Y-axis (extensions bent towards each other) is a concern.
	Rec-53-03	All edges of the support frame are currently sharp, because it was initially unknown whether the appropriate production methods allow for round edges. By now it is known round edges are possible. It is highly recommended to implement them in the design, because it will save mass and because round edges lead to lower stress concentrations.
	Rec-53-04	The precision of the kinematic interface cannot be estimated yet. It is explained in section 6.1 what the next recommended steps are to make this estimate.
	Rec-53-05	Investigate whether it is possible from a load handling perspective to drop two of the support frame hinge axes. Only if this can be done the interface becomes semi-kinematic.
	Rec-53-06	Look into suitable lubricants for the hinge components. Once the friction coefficient is known, a method described in [85] should be used to find whether the ribbon points in the allowed preload direction.
	Rec-53-07	Look into a way to hold down the support frame such that it survives launch.
5.4	Rec-54-01	Model the relation between the ribbon tensional stiffness and the variation in preload when enduring vibrations. This way one will find what ribbon stiffness is preferred for the M1 mechanism, since the selected stiffness is now mostly based on the desires of the M2 mechanism.
	Rec-54-02	Find information about the coupling of vibrations for components connected by a preloaded cable. It has not yet been researched if this phenomenon occurs and what the result would be.

Table 7.4: Table listing all recommendations resulting from this thesis research part 2/3

Relevant section	Code	Recommendation
5.4	Rec-54-03	Look into the design of the ribbon hole edge on the mirror side of the support frame. The angle between the ribbon section that comes from the M2 boom and the round edge of the ribbon hole, will slightly change during retraction. It is advised to find out whether this is a problem. If it is, it is suggested to look into gimballing a roller that replaces the edge.
	Rec-54-04	Similar to the point above, one should find out whether gimballing of the ribbon wedge on the winch side of the support frame is required.
	Rec-54-05	Either get rid of the flanges of the wedge or redesign the wedge such that it becomes a zero-constraint web support. The flanges lead to an overconstraint design. If no solution can be found to keep the ribbon on track without flanges, a design can only become exactly constraint if the flanges are part of a zero-constraint web support.
	Rec-54-06	Evaluate the selected winch motor. The current motor is the weakest, but also the lightest of the available options. The other options are provide in tab. 5.2.
	Rec-54-07	Design a connection between the worm wheel and its axis. Currently it is just a cylinder in a bore. A connection between the worm wheel and the winch tube is required as well.
	Rec-54-08	Select bearings for the top and bottom of the worm wheel axis, and for the end of the worm. The suggested types of tab. 5.3 were just quick selections based on the bore diameters, because a mass estimate was needed. In reality one should contact the supplier to see if their bearings can run dry in a vacuum or contain lubricants that are space proven.
	Rec-54-09	After completing recommendation Rec-54-08 the bearings should be implemented in the design. Circular spaces around the worm and worm wheel axis are incorporated as indication, but the dimensions are not based on any reference bearing. Only the bottom of the worm wheel axis does not show where the bearing should be placed. This is because it should be mounted into the support frame as well and this feature is not yet present in the support frame design.
5.5	Rec-55-01	Optimize the design of the aluminum athermalization plates and their kinematic interface with the support frame. All dimensions were chosen arbitrarily in a way they fitted in the available space. The performance should be analyzed and optimization should be applied.
	Rec-55-02	Design an appropriate preload device for the kinematic interfaces of the aluminum plates. The relevant considerations are discussed in subsection 5.5.3.
	Rec-55-03	One should analyze whether the 1.12 mm bottom thickness of the support frame at the kinematic interfaces is enough. Otherwise the structure should be locally stiffened.
	Rec-55-04	The pockets for the athermalization plates currently have edges of at least 5 mm. Since these edges should carry the loads, one needs to find out whether this thickness is sufficient.
6.1	Rec-61-01	Before assessing the eigenfrequencies in a modal analysis in ANSYS, one should perform a static structural analysis to provide as input to the model analysis.
	Rec-62-02	Investigate what the effect of thermal gradients (within the required temperature range) will be. First do this on a subsystem level, but also make a model for the combined M1 and M2 mechanisms, since the coupled effect may be even worse. If required, discuss strategies with the thermal team to lower the gradients.
	Rec-62-03	Perform the two mass optimization strategies proposed in recommendations Rec-53-02 and Rec-53-03 to determine how far the M1 subsystem mass budget will actually be exceeded. Evaluate the mass distribution and discuss whether requirement M1-MEC-11 can be loosened to a feasible value.

Table 7.5: Table listing all recommendations resulting from this thesis research part 3/3

Relevant section	Code	Recommendation
7.1	Rec-71-01	It is recommended to continue the development by completing the unfinished research activities of the research framework presented in fig. 7.1.
NA	Rec-misc-01	Currently the vibration response spectrum of a reference reaction wheel is used to directly model the expected vibrations. The vibrations will however propagate through the satellite structure, so damping will occur. Therefore the current method is an extreme worst case scenario, leading to the recommendation to model how the vibrations of the reaction wheels will propagate through the satellite structure.
	Rec-misc-02	The current concept has never been build before. This novel technology is possibly patentable and therefore it is recommended to investigate whether this is the case.
	Rec-misc-03	To build on top of the previous recommendation, it is advised to mark every thesis resulting from this project as confidential. Furthermore it is the task of the whole team to make sure the information is not made available in the public domain, since Intellectual Property (IP) cannot be patented anymore once it has been described in the public space. This also means that no in depth details can be shared with companies until there is a signed NDA and that taking pictures should not be allowed during thesis presentations

BIBLIOGRAPHY

[1] P. Kansakar and F. Hossain, "A review of applications of satellite earth observation data for global societal benefit and stewardship of planet earth," Space Policy, vol. 36, pp. 46–54, May 2016.

[2] "VERY HIGH RESOLUTION SATELLITES." `http://www.geoimage.com.au/satellites/very-high-resolution-satellites`. [Online; accessed 12-06-2017].

[3] "Satellite Information." `https://www.digitalglobe.com/resources/satellite-information`. [Online; accessed 12-06-2017].

[4] W. J. Larson and J. R. Wertz, Space Mission Analysis and Design. Microcosm, Inc. and Kluwer Academic Publishers, 5th ed., 1992.

[5] A. Keith, "Significant Supply Expansion for EO Industry: Data Demand Driven by Defense and Emerging Markets." `http://eijournal.com/print/articles/significant-supply-expansion-for-eo-industry-data-demand-driven-by-defense-and-emerging-markets`, 2016. [Online; accessed 06-07-2017].

[6] "EO Concentration & Commercial Revenues." `http://www.nsr.com/news-resources/the-bottom-line/eo-concentration-commercial-revenues/`, 2012. [Online; accessed 06-07-2017].

[7] "Battle Lines Drawn in EO." `http://www.nsr.com/news-resources/the-bottom-line/battle-lines-drawn-in-eo/`, 2017. [Online; accessed 06-07-2017].

[8] G. Marchisio, An Overview of the WorldView-3 Sensor. Geospatial World Forum, 2014. `http://geospatialworldforum.org/2014/presentation/Sensors/WGF%202014b%20-%20Giovanni%20Marchisio%20-%20DigitalGlobe_PDF.pdf`. [Online; accessed 06-07-2017].

[9] W. Ferster, "Digitalglobe adding infrared capability to worldview-3 satellite." `http://spacenews.com/digitalglobe-adding-infrared-capability-worldview-3-satellite/`, 2012. [Online; accessed 10-07-2017].

[10] M. S. Smith, "Enhancedview news not so rosy for geoeye." `http://www.spacepolicyonline.com/news/enhancedview-news-not-so-rosy-for-geoeye`, 2012. [Online; accessed 10-07-2017].

[11] D. Werner, "Worldview-4's long road to launch about to pay off for digitalglobe." `http://www.spacenewsmag.com/feature/worldview-4s-long-road-to-launch-%E2%80%A8about-to-pay-off-for-digitalglobe/`, 2016. [Online; accessed 10-07-2017].

[12] "Welcome to rocketbuilder, atlas v, starting at $109m." `https://www.rocketbuilder.com/`. [Online; accessed 10-07-2017].

[13] P. B. de Selding, "Vega expected to be price-competitive with russian rockets." `http://spacenews.com/vega-expected-be-price-competitive-russian-rockets/`, 2012. [Online; accessed 10-07-2017].

[14] "Vega (rocket)." `https://en.wikipedia.org/wiki/Vega_(rocket)`. [Online; accessed 10-07-2017].

[15] R. E. Fischer, B. Tadic-Galeb, and P. R. Yoder, Optical System Design. McGraw-Hill, 2nd ed., 2008.

[16] "Ccd spatial resolution." `http://www.andor.com/learning-academy/ccd-spatial-resolution-understanding-spatial-resolution`. [Online; accessed 10-07-2017].

[17] "Meet worldview-4." `http://worldview4.digitalglobe.com/#/main`. [online; accessed 10-07-2017].

[18] "Frequently asked questions about worldview-4." `http://blog.digitalglobe.com/news/frequently-asked-questions-about-worldview-4/`. [Online; accessed 10-07-2017].

[19] "About the james webb space telescope." `https://jwst.nasa.gov/about.html`. [Online; accessed 14-06-2018].

[20] D. Dolkens, "A Deployable Telescope for Sub-Meter Resolutions from MicroSatellite Platforms," Master's thesis, Delft University of Technology, Feb. 2015.

[21] S. Pepper and A. Krikken, DST Requirements Document. TU Delft - DST Project Group, rev. d ed., April 2018. Internal document. Access can be requested via j.m.kuiper@tudelft.nl.

[22] J. Lopes Barreto, "Deployable Space Telescope: Optimal Boom Design for High Precision Deployment of Secondary Mirror," Master's thesis, Delft University of Technology, May 2017.

[23] D. Dolkens and H. Kuiper, "DESIGN AND END-TO-END MODELLING OF A DEPLOYABLE TELESCOPE," International Conference on Space Optics, vol. 18, pp. 21–28, 2016.

[24] S. Pellegrino, Deployable structures. Springer, 2001.

[25] B. van Putten, "Design of the Deployment Mechanism for the Primary Mirror Elements of a Deployable Space Telescope," Master's thesis, Delft University of Technology, Apr. 2017.

[26] R. M. Warden, "Cryogenic Nano-Actuator for JWST," in Proceedings of the 38th Aerospace Mechanisms Symposium, (Williamsburg), NASA, 2006.

[27] M. S. Lake, P. A. Warren, and L. D. Peterson, "A revolute joint with linear load-displacement response for precision deployable structures," in 37th AIAA/ASME/ASCE/AHS/ASC Structures, Structural Dynamics, and Materials Conference, Salt Lake City, Utah, 1996.

[28] L. Peterson, S. Bullock, J. Hinkle, M. Hachkowski, P. Warren, and M. Lake, "Micron accurate deployable antenna and sensor technology for new-millennium-era spacecraft," in IEEE Aerospace Applications Conference Proceedings, vol. 1, pp. 129–139, IEEE, 1996.

[29] M. S. Lake, J. Fung, K. Gloss, and D. S. Liechty, "Experimental Characterization of Hysteresis in a Revolute Joint for Precision Deployable Structures," in 38th AIAA Structures, Structural Dynamics, and Materials Conference, Kissimmee, Florida, (Kissimmee, Florida), AIAA, 1997.

[30] J. E. Phelps, "Fabrication and Assembly of High-Precision Hinge and Latch Joints for Deployable Optical Instruments," tech. rep., NASA Langley Research Center, Hampton, Aug 1999.

[31] M. S. Lake and M. R. Hachkowski, "Design of mechanisms for deployable, optical instruments: Guidelines for reducing hysteresis," tech. rep., NASA Langley Research Center, Hampton, 2000.

[32] M. S. Lake, J. E. Phelps, J. E. Dyer, D. A. Caudle, A. Tam, J. Escobedo, and E. P. Kasl, "A Deployable Primary Mirror for Space Telescopes," tech. rep., NASA Langley Research Center, Hampton, Virginia, Sep. 1999.

[33] G. v. Marrewijk, "Design of an aberration correction system for a deployable space telescope," Master's thesis, Delft University of Technology, May 2018.

[34] S. T. S. Institute, "History." `https://jwst.stsci.edu/about-jwst/history`. [Online; accessed 14-06-2018].

[35] M. S. Lake, L. D. Peterson, M. R. Hachkowski, J. D. Hinkle, and L. R. Hardaway, "Research on the problem of high-precision deployment for large-aperture space-based science instruments," in AIP Conference Proceedings, vol. 420, pp. 188–198, AIP, 1998.

[36] P. A. Warren, L. D. Peterson, and J. D. Hinkle, "Submicron mechanical stability of a prototype deployable space telescope support structure," Journal of spacecraft and rockets, vol. 36, no. 5, pp. 765–771, 1999.

[37] J. C. Heald and L. D. Peterson, "Deployment repeatability of a space telescope reflector petal," Journal of spacecraft and rockets, vol. 39, no. 5, pp. 771–779, 2002.

[38] J. L. Domber, J. D. Hinkle, L. D. Peterson, and P. A. Warren, “Dimensional repeatability of an elastically folded composite hinge for deployed spacecraft optics,” Journal of spacecraft and rockets, vol. 39, no. 5, pp. 646–652, 2002.

[39] R. Barrett, W. Francis, E. Abrahamson, M. Lake, and M. Scherbarth, “Qualification of Elastic Memory Composite Hinges for Spaceflight Applications,” in 47th AIAA/ASME/ASCE/AHS/ASC Structures, Structural Dynamics, and Materials Conference, (Reston, Virigina), American Institute of Aeronautics and Astronautics, May 2006.

[40] W. Francis, M. Lake, J. Hinkle, and L. Peterson, “Feasibility study of using elastic memory composites for the deployment of precision optical space instruments,” in Proc. of SPIE, vol. 5528, p. 193, 2004.

[41] C. A. Evans, J. A. Robinson, J. Tate-Brown, T. Thumm, J. Crespo-Richey, D. Baumann, and J. Rhatigan, “International space station science research accomplishments during the assembly years: an analysis of results from 2000-2008,” tech. rep., NASA, June 2009.

[42] P. Reynolds, C. Atkinson, and L. Gliman, “Design and development of the primary and secondary mirror deployment systems for the cryogenic jwst,” in 37th Aerospace Mechanisms Symposium, NASA, 2004.

[43] J. Champagne, S. Hansen, T. Newswander, and B. Crowther, CubeSat image resolution capabilities with deployable optics and current imaging technology. Space Dynamics Laboratory, 2014. `http://digitalcommons.usu.edu/smallsat/2014/AdvTechII/10/`. [Online; accessed 16-08-2017].

[44] S. D. Laboratory, “Petal telescope.” `https://www.youtube.com/watch?v=zA3GNZ6_sdc`, 2015. [Online; accessed 16-08-2017].

[45] K. Opsahl, “Space dynamics lab engineers develop unique telescope.” `http://news.hjnews.com/allaccess/space-dynamics-lab-engineers-develop-unique-telescope/article_86aaaab4-e300-11e4-880d-5fbbbcd6bdca.html`, 2015. [Online; accessed 16-08-2017].

[46] B. Crowther, T. Newswander, J. Champagne, and A. Norris, “Multiple petal deployable telescope.” Worldwide patent WO2012116366, Feb. 25 2011.

[47] P. Mazzinghi, V. Bratina, D. Ferruzzi, L. Gambicorti, F. Simonetti, A. Zuccaro Marchi, P. Salinari, F. Lisi, M. Olivier, A. Bursi, D. Gallieni, R. Biasi, and J. Pereira, “Deployable, lightweight and large aperture spaceborne telescope for lidar-based earth observations,” in Proceedings of SPIE 6750 (U. N. Singh and G. Pappalardo, eds.), International Society for Optics and Photonics, Oct 2007.

[48] T. Segert, B. Danziger, and M. Lieder, “Dobson Space Telescope - Recent Developments,” in 56th International Astronautical Congress of the International Astronautical Federation, the International Academy of Astronautics, and the International Institute of Space Law, (Reston, Virigina), American Institute of Aeronautics and Astronautics, Oct 2005.

[49] B. Danziger, T. Segert, and M. Lieder, “Dobson space telescope: Development of a laboratory model,” in 55th International Astronautical Congress, 2004.

[50] T. Segert, B. Danziger, and M. Lieder, “Dobson space telescope the future of microsat based observation,” in Fifth IAA Symposium on Small Satellites for Earth Observation, IAA-B5-0606, Berlin, 2005.

[51] T. Segert, B. Danziger, D. Gork, and M. Lieder, “Dobson space telescope-development of an optical payload of the next generation,” in Sixth International Conference on Space Optics, Proceedings of ESA/CNES ICSO 2006, vol. 621, June 2006.

[52] “Dst (dobson space telescope).” "`https://eoportal.org/web/eoportal/satellite-missions/content/-/article/dobson-2`". [Online; accessed 24-08-2017].

[53] "`http://dobson-space-telescope.com`".

[54] "`https://www.berlin-space-tech.com/`". [Online; accessed 24-08-2017].

[55] B. Danziger, M. Lieder, and T. Segert, “Vorrichtung zur raumsparenden faltung eines entfaltbaren optischen systems zum weltraumeinsatz.” DE202005020683, Dec. 31 2005.

[56] K. Kwok and S. Pellegrino, “Folding, stowage, and deployment of viscoelastic tape springs,” AIAA journal, vol. 51, Aug. 2013.

[57] J. T. Black, J. A. Whetzal, B. J. DeBlonk, and J. J. Massarello, “Deployment repeatability testing of composite tape springs for space optics applications,” in Proceedings of the 47th AIAA/ASME/ASCE/AHS/ASC Structures, Structural Dynamics, and Material Conference, (Newport, Rhode Island), pp. 1–4, May 2006.

[58] J. Sicre, D. Givois, and A. Emerit, “Application of “maeva” hinge to myriade microsatellites deployments needs,” in 11th European Space Mechanisms and Tribology Symposium/ESMATS (B. Warmbein, ed.), (Lucerne, Switzerland), pp. 243–250, Sep. 2005.

[59] M. Mobrem and D. S. Adams, “Deployment analysis of lenticular jointed antennas onboard the mars express spacecraft,” Journal of Spacecraft and Rockets, vol. 46, pp. 394–402, Mar. 2009.

[60] M. Sampl, M. Kapper, D. Plettemeier, M. Maksimovic, K. van t Klooster, and H. O. Rucker, “Wave length scaled scanning of the solar orbiter/rpw antennas: First results,” in 8th European Conference on Antennas and Propagation (EuCAP 2014), (The Hague, The Netherlands), pp. 403–404, IEEE, Apr. 2014.

[61] S. Kanji, “Mechanical aspects of design, analysis, and testing for the norsat-1 microsatellite,” Master’s thesis, University of Toronto, Nov. 2015.

[62] K. Kwok and S. Pellegrino, “Viscoelastic effects in tape-springs,” in 52nd AIAA/ASME/ASCE/AHS/ASC Structures, Structural Dynamics, and Material Conference, (Denver, Colorado), Apr. 2011.

[63] K. Kwok and S. Pellegrino, “Micromechanical modeling of deployment and shape recovery of thin-walled viscoelastic composite space structures,” in 53rd AIAA/ASME/ASCE/AHS/ASC Structures, Structural Dynamics and Materials Conference, (Honolulu, Hawaii), Apr. 2012.

[64] D. S. Adams and M. Mobrem, “Lenticular jointed antenna deployment anomaly and resolution onboard the mars express spacecraft,” Journal of Spacecraft and Rockets, vol. 46, pp. 403–408, Mar. 2009.

[65] F. Dewalque, C. Schwartz, V. Denoël, J.-L. Croisier, B. Forthomme, and O. Brüls, “Experimental and numerical investigation of the nonlinear dynamics of compliant mechanisms for deployable structures,” Mechanical Systems and Signal Processing, vol. 101, pp. 1–25, Feb. 2018. Already published online in Aug. 2017.

[66] M. J. Silver, M. A. Echter, B. M. Reid, and J. A. Banik, “Precision high-strain composite hinges for the deployable in-space coherent imaging telescope,” in 3rd AIAA Spacecraft Structures Conference, (San Diego, California), p. 0969, Jan. 2016.

[67] C. Boesch, C. Pereira, R. John, T. Schmidt, K. Seifart, H. Sparr, J. Lautier, and T. Pyttel, “Ultra light self-motorized mechanism for deployment of light weight spacecraft appendages,” in 39th Proceedings of Aerospace Mechanisms Symposium, (Huntsville, Alabama), pp. 221–234, May 2008.

[68] K. Zajac, T. Schmidt, M. Schiller, K. Seifart, M. Schmalbach, and L. Scolamiero, “Verification test for ultra-light deployment mechanism for sectioned deployable antenna reflectors,” in 15th European Space Mechanisms and Tribology Symposium - ESMATS 2013, (Noordwijk, The Netherlands), Sep. 2013.

[69] S. C. Arzberger, M. L. Tupper, M. S. Lake, R. Barrett, K. Mallick, C. Hazelton, W. Francis, P. N. Keller, D. Campbell, S. Feucht, et al., “Elastic memory composites (emc) for deployable industrial and commercial applications,” in SPIE Smart Structures and Materials + Nondestructive Evaluation and Health Monitoring, (San Diego, California), pp. 35–47, International Society for Optics and Photonics, May 2005.

[70] F. Xie, L. Huang, J. Leng, and Y. Liu, “Thermoset shape memory polymers and their composites,” Journal of Intelligent Material Systems and Structures, vol. 27, no. 18, pp. 2433–2455, 2016.

[71] X. Lan, Y. Liu, H. Lv, X. Wang, J. Leng, and S. Du, “Fiber reinforced shape-memory polymer composite and its application in a deployable hinge,” Smart Materials and Structures, vol. 18, no. 2, p. 024002, 2009.

[72] Y. Liu, H. Du, L. Liu, and J. Leng, “Shape memory polymers and their composites in aerospace applications: a review,” Smart Materials and Structures, vol. 23, no. 2, p. 023001, 2014.

[73] J. Leng, X. Lan, Y. Liu, and S. Du, “Shape-memory polymers and their composites: stimulus methods and applications,” Progress in Materials Science, vol. 56, no. 7, pp. 1077–1135, 2011.

[74] Q. Chen, Z. Yao, Y. Hou, and H. Fang, “Design and testing of a space deployable mechanism,” in 4th AIAA Spacecraft Structures Conference, (Grapevine, Texas), p. 0176, Jan. 2017.

[75] I. S. Gunes, G. A. Jimenez, and S. C. Jana, “Carbonaceous fillers for shape memory actuation of polyurethane composites by resistive heating,” Carbon, vol. 47, no. 4, pp. 981–997, 2009.

[76] H. Lu, K. Yu, Y. Liu, and J. Leng, “Sensing and actuating capabilities of a shape memory polymer composite integrated withhybrid filler,” Smart Materials and Structures, vol. 19, no. 6, p. 065014, 2010.

[77] H. Fang, L. Shook, J. K. Lin, J. Pearson, and J. Moore, “A large and high radio frequency deployable reflector,” in 53rd AIAA/ASME/ASCE/AHS/ASC Structures, Structural Dynamics andMaterials Conference 20th AIAA/ASME/AHS Adaptive StructuresConference 14th AIAA, vol. 1838, 2012.

[78] R. Donaldson, “The deterministic approach to machining accuracy,” in Society of Manufacturing Engineers Fabrication Technology Symposium, (Golden, Colorado), Nov. 1972.

[79] M. Arthur and D. Saffer, “Thermal expansion and density.” https://www.e-education.psu.edu/earth111/node/842. [Online; accessed 16-06-2018].

[80] L. Hale, Principles and Techniques for Designing Precision Machines. PhD thesis, Massachusetts Institute of Technology, Feb. 1999.

[81] C. Hellman, “George graham,” Popular Astronomy, vol. 39, pp. 186–198, 1931.

[82] P. Bely, ed., The Design and Construction of Large Optical Telescopes. New-York: Springer-Verlag, 2003.

[83] P. C. Inc., “Carbon fiber composite design guide.” http://www.performancecomposites.com/about-composites-technical-info/124-designing-with-carbon-fiber.html. [Online; accessed 16-06-2018].

[84] D. Tsang, B. Marsden, S. Fok, and G. Hall, “Graphite thermal expansion relationship for different temperature ranges,” Carbon, vol. 43, pp. 2902–2906, Nov. 2005.

[85] D. Blanding, Exact Constraint: Machine Design Using Kinematic Principles. New York: ASME Press, 1999.

[86] M. L. Culpepper, “Design of quasi-kinematic couplings,” Precision Engineering, vol. 28, no. 3, pp. 338–357, 2004.

[87] “Optical mirror mount technology guide.” "https://www.newport.com/n/optical-mirror-mount-technology-guide". [Online; accessed 04-09-2017].

[88] S. GmbH, “Deployment mechanisms - product information.” http://spacetech-i.com/images/press/downloads/Datasheets/Datasheet_DeploymentMechanisms_SpaceTech102017.pdf, 2017. [Online; accessed 26-02-2018].

[89] H. GmbH, “Deployment mechanisms.” https://www.htsdd.de/content/Raumfahrt_Deployment_Mechanisms_en.html. [Online; accessed 13-03-2018].

[90] Wikipedia, “Thermal expansion.” https://en.wikipedia.org/wiki/Thermal_expansion. [Online; accessed 28-02-2018].

[91] M. C. Corporation, “Dialead$^{\text{TM}}$ composite.” https://www.m-chemical.co.jp/en/products/departments/mcc/composite-products/product/1201233_7508.html. [Online; accessed 28-02-2018].

[92] C. S. Group, "Selector guide." http://www.cytec.com/selector-guide/. [Online; accessed 28-02-2018], in the selector guide click Aerospace Materials -> Carbon Fibre -> Aerospace. Here a list with CFRP products can be found. Thornel products are designed for thermal properties.

[93] N. G. F. Corp., "Granocyarn ys-a series (ultra high modulus and high thermal conductivity)." http://www.ngfworld.com/dcms_media/other/YSAfiber2014.pdf, 2014. [Online; accessed 28-02-2018].

[94] M. Eigenmann, M. Schmalbach, M. Schiller, T. Schmidt, and L. Scolamiero, "Ultra-light deployment mechanism (udm) for sectioned large deployable antenna reflectors," in 14th European Space Mechanisms and Tribology Symposium — ESMATS 2011, (Constance, Germany), pp. 479–481, Sep. 2011.

[95] C. Ho and R. Taylor, eds., Thermal Expansion of Solids, vol. 1-4. ASM International, 1998, 1998.

[96] P.-C. Ma, N. Siddiqui, G. Marom, and J.-K. Kim, "Dispersion and functionalization of carbon nanotubes for polymer-based nanocomposites: A review," Composites Part A: Applied Science and Manufacturing, vol. 41, pp. 1345–1367, Oct. 2010.

[97] A. Trouve and T. Minnich, "Thermal properties database," tech. rep., University of Maryland and University of Central Florida, 2012.

[98] E. ToolBox, "Thermal conductivity of common materials and gases." https://www.engineeringtoolbox.com/thermal-conductivity-d_429.html, 2003. [Online; accessed 10-06-2018].

[99] U. of Cambridge, "Young's modulus - density." http://www-materials.eng.cam.ac.uk/mpsite/interactive_charts/stiffness-density/NS6Chart.html, 2002. [Online; accessed 10-06-2018].

[100] European Cooperation for Space Standardization, ECSS-E-HB-32-20 Structural Materials Handbook, 2011.

[101] S.-G. C. Materials, "Combat boron nitride solids." https://www.bn.saint-gobain.com/sites/imdf.bn.com/files/combat-bn-solids-ds.pdf, 2017. [Online; accessed 20-05-2018].

[102] European Cooperation for Space Standardization, ECSS-Q-ST-70-02C Thermal vacuum outgassing test for the screening of space materials, 2008.

[103] W. Callister and D. Rethwisch, Materials Science and Engineering - SI Version. John Wiley and Sons, Inc., 8th ed., 2011.

[104] J. M. Paros and T. Kobayashi, "Root causes of quartz sensor drift," Tech. Rep. Doc. No. G8101 Rev. A, Paroscientific, Inc., 2016.

[105] I. Glenair, "Series 06 hold-down release mechanisms (hdrm)." https://cdn.glenair.com/catalogs/hold_down_release_mechanism_technology.pdf, 2016. [Online; accessed 04-06-2018].

[106] I. NEA Electronics, "Hold-down and release mechanisms." https://www.neaelectronics.com/products/hold-down-and-release-mechanisms/. [Online; accessed 04-06-2018].

[107] S. Arquimea Ingeniería, "Hdrm." http://www.arquimea.com/?q=products-services/actuators/hdrm. [Online; accessed 04-06-2018].

[108] A. Krikken, June 6 2018. Internal document, developed by A. Krikken. Information regarding the computation of the results will be provided in his upcoming MSc thesis. Until the moment of publication of this thesis information can be requested via a.krikken@student.tudelft.nl.

[109] DuPont, "Dupont™ kevlar® 49 aramid fiber." http://www.matweb.com/search/datasheet.aspx?matguid=77b5205f0dcc43bb8cbe6fee7d36cbb5&ckck=1. [Online; accessed 26-05-2018].

[110] Wikipedia, "Gear train." https://en.wikipedia.org/wiki/Gear_train. [Online; accessed 06-06-2018].

[111] W. Office, Manual of Driving and Maintenance for Mechanical Vehicles (Wheeled). His Majesty's Stationery Office, London, 1937.

[112] S. Murugesan, "An overview of electric motors for space applications," IEEE transactions on industrial electronics and control instrumentation, no. 4, pp. 260–265, 1981.

[113] R. Fusaro, W. Shapiro, F. Murray, and R. Howarth, "Space mechanism lessons learned study - volume i," tech. rep., NASA Lewis Research Center and Mechanical Technology Incorporated, Sep. 1995.

[114] M. M. AG, "Brushless dc motors." https://www.maxonmotor.com/maxon/view/content/Overview-brushless-DC-motors. [Online; accessed 27-05-2018].

[115] Micromo, "Brushless dc motors." https://www.micromo.com/brushless-dc-motors. [Online; accessed 27-05-2018].

[116] C. InterCorp, "Stepper motors." http://www.cda-intercorp.com/products.cfm?cid=3. [Online; accessed 27-05-2018].

[117] I. Avior Contol Technologies, "Space rated motors." http://aviorcontrols.com/space-rated-motor-modules/. [Online; accessed 27-05-2018].

[118] L. Kohara Gear Industry Co, KHK The ABCs of Gears - B Basic guide. Kohara Gear Industry Co, LTD, 2007.

[119] L. Kohara Gear Industry Co., "Technical information of worm gear." https://khkgears.net/product-category/worm-gear-pair/technical-information-of-worm-gear/. [Online; accessed 27-05-2018].

[120] L. Kohara Gear Industry Co., "Worm gear." https://khkgears.net/new/worm_gear.html. [Online; accessed 27-05-2018].

[121] SDP/SI, "Stock drive products/sterling instrument > gears > worm gears > right hand lead worm gears (metric)." https://shop.sdp-si.com/catalog/?cid=p391. [Online; accessed 27-05-2018].

[122] BeltingOnline, "Worm wheels." http://www.beltingonline.com/gears-racks-366/worm-wheels-374/. [Online; accessed 27-05-2018].

[123] AccuGroup, "Buy wheels." https://www.accu.co.uk/631-wheels. [Online; accessed 27-05-2018].

[124] Gears and Sprockets, "Metric bronze wormwheels." https://www.gearsandsprockets.co.uk/metric-bronze-wormwheels/. [Online; accessed 27-05-2018].

[125] Ondrives, "Precision anti-backlash wormwheels." https://www.ondrives.com/precision-anti-backlash-wormwheels. [Online; accessed 27-05-2018].

[126] P. Yoder, Mounting Optics in Optical Instruments. SPIE, 8th ed., 2008.

A

REQUIREMENT TABLES

The tables presented in this appendix come out of the project requirements document. The meaning of most columns do not need an explanation, but there are two that should be discussed. The first column is called 'Old ID'. Some of the requirements were provided in old thesis reports. Back then each researcher came up with his own ID tag system. This document was made, because there is a need for a uniform system. To be able to easily find the reasoning behind certain requirements that were described in the old thesis reports, the 'Old ID' column provides a way to find them quickly. If a requirement originates from an old thesis report, the source is stated in the 'Comment' column.

As one can see in the tables, discarded requirements are not deleted out of the tables, but are crossed out. This way it is easier to reconstruct when major design changes happened and what change in the requirements led to this decision.

Table A.1 provides the objectives and top level requirements. The subsystem requirements of the primary mirror deployment mechanism are split over tables A.2 and A.3.

Table A.1: Table 1 and 2 of the requirements document, containing the mission objectives and top level requirements

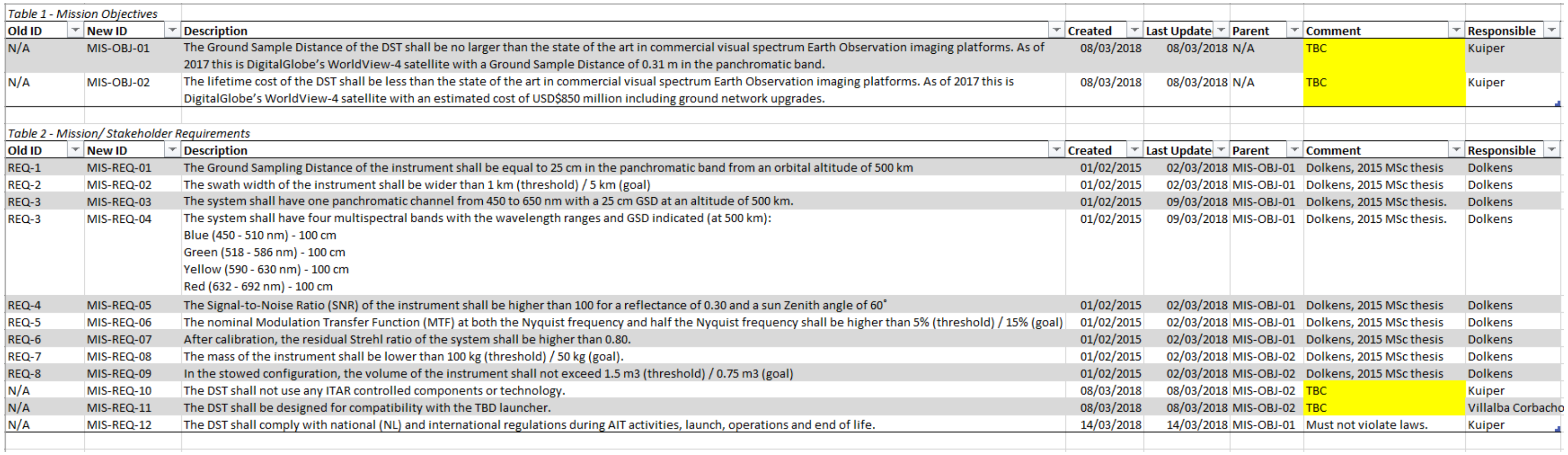

Table 1 - Mission Objectives

Old ID	New ID	Description	Created	Last Update	Parent	Comment	Responsible
N/A	MIS-OBJ-01	The Ground Sample Distance of the DST shall be no larger than the state of the art in commercial visual spectrum Earth Observation imaging platforms. As of 2017 this is DigitalGlobe's WorldView-4 satellite with a Ground Sample Distance of 0.31 m in the panchromatic band.	08/03/2018	08/03/2018	N/A	TBC	Kuiper
N/A	MIS-OBJ-02	The lifetime cost of the DST shall be less than the state of the art in commercial visual spectrum Earth Observation imaging platforms. As of 2017 this is DigitalGlobe's WorldView-4 satellite with an estimated cost of USD$850 million including ground network upgrades.	08/03/2018	08/03/2018	N/A	TBC	Kuiper

Table 2 - Mission/ Stakeholder Requirements

Old ID	New ID	Description	Created	Last Update	Parent	Comment	Responsible
REQ-1	MIS-REQ-01	The Ground Sampling Distance of the instrument shall be equal to 25 cm in the panchromatic band from an orbital altitude of 500 km	01/02/2015	02/03/2018	MIS-OBJ-01	Dolkens, 2015 MSc thesis	Dolkens
REQ-2	MIS-REQ-02	The swath width of the instrument shall be wider than 1 km (threshold) / 5 km (goal)	01/02/2015	02/03/2018	MIS-OBJ-01	Dolkens, 2015 MSc thesis	Dolkens
REQ-3	MIS-REQ-03	The system shall have one panchromatic channel from 450 to 650 nm with a 25 cm GSD at an altitude of 500 km.	01/02/2015	09/03/2018	MIS-OBJ-01	Dolkens, 2015 MSc thesis.	Dolkens
REQ-3	MIS-REQ-04	The system shall have four multispectral bands with the wavelength ranges and GSD indicated (at 500 km): Blue (450 - 510 nm) - 100 cm Green (518 - 586 nm) - 100 cm Yellow (590 - 630 nm) - 100 cm Red (632 - 692 nm) - 100 cm	01/02/2015	09/03/2018	MIS-OBJ-01	Dolkens, 2015 MSc thesis.	Dolkens
REQ-4	MIS-REQ-05	The Signal-to-Noise Ratio (SNR) of the instrument shall be higher than 100 for a reflectance of 0.30 and a sun Zenith angle of 60˚	01/02/2015	02/03/2018	MIS-OBJ-01	Dolkens, 2015 MSc thesis	Dolkens
REQ-5	MIS-REQ-06	The nominal Modulation Transfer Function (MTF) at both the Nyquist frequency and half the Nyquist frequency shall be higher than 5% (threshold) / 15% (goal)	01/02/2015	02/03/2018	MIS-OBJ-01	Dolkens, 2015 MSc thesis	Dolkens
REQ-6	MIS-REQ-07	After calibration, the residual Strehl ratio of the system shall be higher than 0.80.	01/02/2015	02/03/2018	MIS-OBJ-01	Dolkens, 2015 MSc thesis	Dolkens
REQ-7	MIS-REQ-08	The mass of the instrument shall be lower than 100 kg (threshold) / 50 kg (goal).	01/02/2015	02/03/2018	MIS-OBJ-02	Dolkens, 2015 MSc thesis	Dolkens
REQ-8	MIS-REQ-09	In the stowed configuration, the volume of the instrument shall not exceed 1.5 m3 (threshold) / 0.75 m3 (goal)	01/02/2015	02/03/2018	MIS-OBJ-02	Dolkens, 2015 MSc thesis	Dolkens
N/A	MIS-REQ-10	The DST shall not use any ITAR controlled components or technology.	08/03/2018	08/03/2018	MIS-OBJ-02	TBC	Kuiper
N/A	MIS-REQ-11	The DST shall be designed for compatibility with the TBD launcher.	08/03/2018	08/03/2018	MIS-OBJ-02	TBC	Villalba Corbacho
N/A	MIS-REQ-12	The DST shall comply with national (NL) and international regulations during AIT activities, launch, operations and end of life.	14/03/2018	14/03/2018	MIS-OBJ-01	Must not violate laws.	Kuiper

Table A.2: The first half of table 3 of the requirements document, containing the primary mirror deployment mechanism requirements

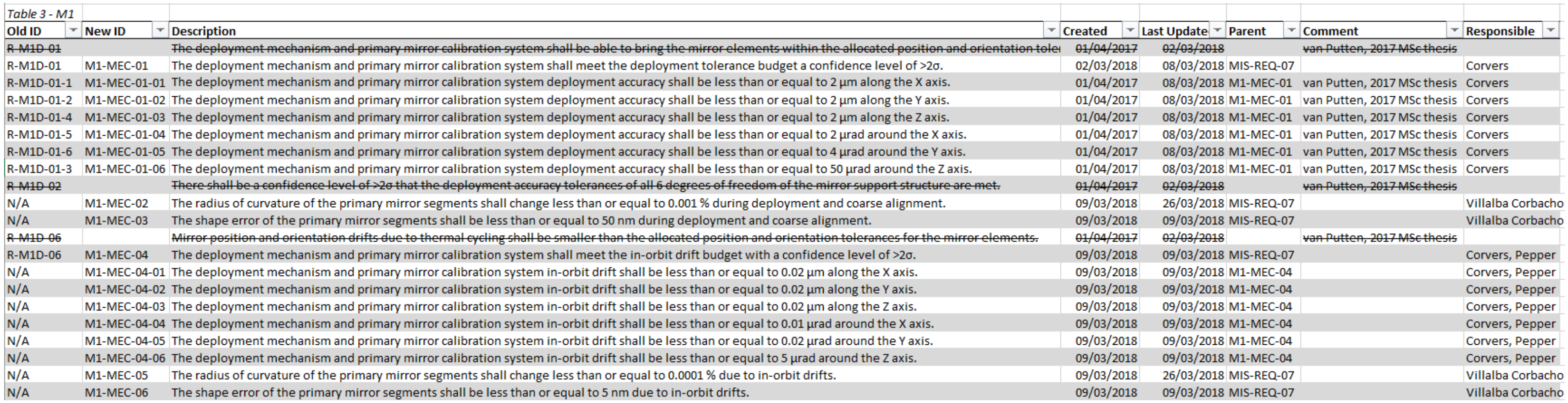

Table 3 - M1

Old ID	New ID	Description	Created	Last Update	Parent	Comment	Responsible
~~R-M1D-01~~		~~The deployment mechanism and primary mirror calibration system shall be able to bring the mirror elements within the allocated position and orientation tole~~	~~01/04/2017~~	~~02/03/2018~~		~~van Putten, 2017 MSc thesis~~	
R-M1D-01	M1-MEC-01	The deployment mechanism and primary mirror calibration system shall meet the deployment tolerance budget a confidence level of >2σ.	02/03/2018	08/03/2018	MIS-REQ-07		Corvers
R-M1D-01-1	M1-MEC-01-01	The deployment mechanism and primary mirror calibration system deployment accuracy shall be less than or equal to 2 µm along the X axis.	01/04/2017	08/03/2018	M1-MEC-01	van Putten, 2017 MSc thesis	Corvers
R-M1D-01-2	M1-MEC-01-02	The deployment mechanism and primary mirror calibration system deployment accuracy shall be less than or equal to 2 µm along the Y axis.	01/04/2017	08/03/2018	M1-MEC-01	van Putten, 2017 MSc thesis	Corvers
R-M1D-01-4	M1-MEC-01-03	The deployment mechanism and primary mirror calibration system deployment accuracy shall be less than or equal to 2 µm along the Z axis.	01/04/2017	08/03/2018	M1-MEC-01	van Putten, 2017 MSc thesis	Corvers
R-M1D-01-5	M1-MEC-01-04	The deployment mechanism and primary mirror calibration system deployment accuracy shall be less than or equal to 2 µrad around the X axis.	01/04/2017	08/03/2018	M1-MEC-01	van Putten, 2017 MSc thesis	Corvers
R-M1D-01-6	M1-MEC-01-05	The deployment mechanism and primary mirror calibration system deployment accuracy shall be less than or equal to 4 µrad around the Y axis.	01/04/2017	08/03/2018	M1-MEC-01	van Putten, 2017 MSc thesis	Corvers
R-M1D-01-3	M1-MEC-01-06	The deployment mechanism and primary mirror calibration system deployment accuracy shall be less than or equal to 50 µrad around the Z axis.	01/04/2017	08/03/2018	M1-MEC-01	van Putten, 2017 MSc thesis	Corvers
~~R-M1D-02~~		~~There shall be a confidence level of >2σ that the deployment accuracy tolerances of all 6 degrees of freedom of the mirror support structure are met.~~	~~01/04/2017~~	~~02/03/2018~~		~~van Putten, 2017 MSc thesis~~	
N/A	M1-MEC-02	The radius of curvature of the primary mirror segments shall change less than or equal to 0.001 % during deployment and coarse alignment.	09/03/2018	26/03/2018	MIS-REQ-07		Villalba Corbacho
N/A	M1-MEC-03	The shape error of the primary mirror segments shall be less than or equal to 50 nm during deployment and coarse alignment.	09/03/2018	09/03/2018	MIS-REQ-07		Villalba Corbacho
~~R-M1D-06~~		~~Mirror position and orientation drifts due to thermal cycling shall be smaller than the allocated position and orientation tolerances for the mirror elements.~~	~~01/04/2017~~	~~02/03/2018~~		~~van Putten, 2017 MSc thesis~~	
R-M1D-06	M1-MEC-04	The deployment mechanism and primary mirror calibration system shall meet the in-orbit drift budget with a confidence level of >2σ.	09/03/2018	09/03/2018	MIS-REQ-07		Corvers, Pepper
N/A	M1-MEC-04-01	The deployment mechanism and primary mirror calibration system in-orbit drift shall be less than or equal to 0.02 µm along the X axis.	09/03/2018	09/03/2018	M1-MEC-04		Corvers, Pepper
N/A	M1-MEC-04-02	The deployment mechanism and primary mirror calibration system in-orbit drift shall be less than or equal to 0.02 µm along the Y axis.	09/03/2018	09/03/2018	M1-MEC-04		Corvers, Pepper
N/A	M1-MEC-04-03	The deployment mechanism and primary mirror calibration system in-orbit drift shall be less than or equal to 0.02 µm along the Z axis.	09/03/2018	09/03/2018	M1-MEC-04		Corvers, Pepper
N/A	M1-MEC-04-04	The deployment mechanism and primary mirror calibration system in-orbit drift shall be less than or equal to 0.01 µrad around the X axis.	09/03/2018	09/03/2018	M1-MEC-04		Corvers, Pepper
N/A	M1-MEC-04-05	The deployment mechanism and primary mirror calibration system in-orbit drift shall be less than or equal to 0.02 µrad around the Y axis.	09/03/2018	09/03/2018	M1-MEC-04		Corvers, Pepper
N/A	M1-MEC-04-06	The deployment mechanism and primary mirror calibration system in-orbit drift shall be less than or equal to 5 µrad around the Z axis.	09/03/2018	09/03/2018	M1-MEC-04		Corvers, Pepper
N/A	M1-MEC-05	The radius of curvature of the primary mirror segments shall change less than or equal to 0.0001 % due to in-orbit drifts.	09/03/2018	26/03/2018	MIS-REQ-07		Villalba Corbacho
N/A	M1-MEC-06	The shape error of the primary mirror segments shall be less than or equal to 5 nm due to in-orbit drifts.	09/03/2018	09/03/2018	MIS-REQ-07		Villalba Corbacho

Table A.3: The second half of table 3 of the requirements document, containing the primary mirror deployment mechanism requirements

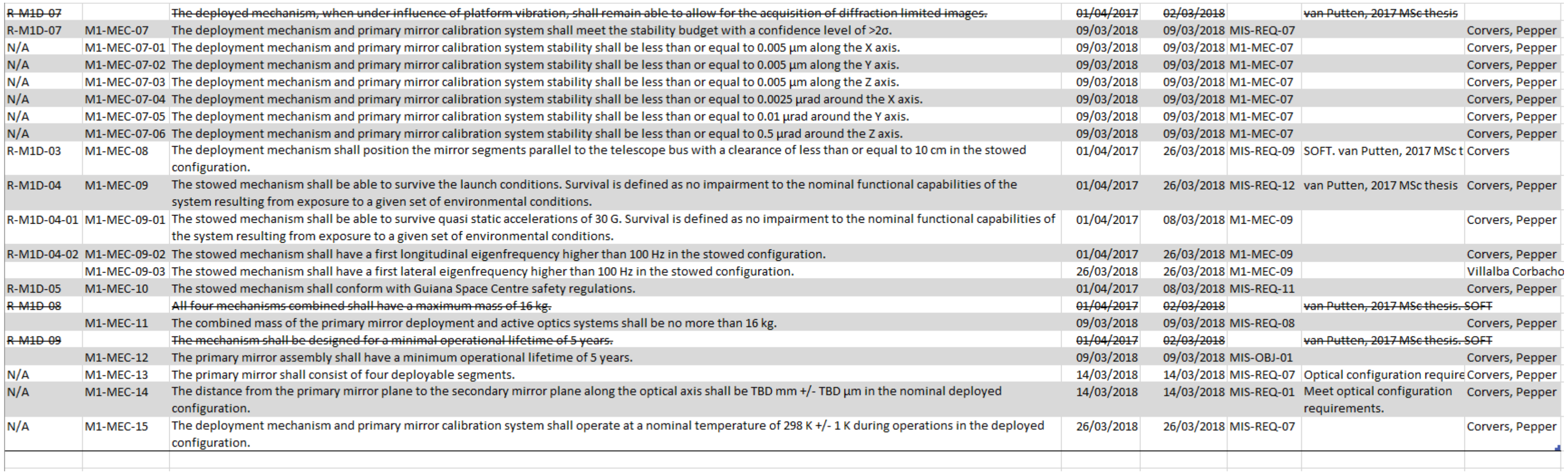

~~R-M1D-07~~		~~The deployed mechanism, when under influence of platform vibration, shall remain able to allow for the acquisition of diffraction limited images.~~	~~01/04/2017~~	~~02/03/2018~~		~~van Putten, 2017 MSc thesis~~	
R-M1D-07	M1-MEC-07	The deployment mechanism and primary mirror calibration system shall meet the stability budget with a confidence level of >2σ.	09/03/2018	09/03/2018	MIS-REQ-07		Corvers, Pepper
N/A	M1-MEC-07-01	The deployment mechanism and primary mirror calibration system stability shall be less than or equal to 0.005 μm along the X axis.	09/03/2018	09/03/2018	M1-MEC-07		Corvers, Pepper
N/A	M1-MEC-07-02	The deployment mechanism and primary mirror calibration system stability shall be less than or equal to 0.005 μm along the Y axis.	09/03/2018	09/03/2018	M1-MEC-07		Corvers, Pepper
N/A	M1-MEC-07-03	The deployment mechanism and primary mirror calibration system stability shall be less than or equal to 0.005 μm along the Z axis.	09/03/2018	09/03/2018	M1-MEC-07		Corvers, Pepper
N/A	M1-MEC-07-04	The deployment mechanism and primary mirror calibration system stability shall be less than or equal to 0.0025 μrad around the X axis.	09/03/2018	09/03/2018	M1-MEC-07		Corvers, Pepper
N/A	M1-MEC-07-05	The deployment mechanism and primary mirror calibration system stability shall be less than or equal to 0.01 μrad around the Y axis.	09/03/2018	09/03/2018	M1-MEC-07		Corvers, Pepper
N/A	M1-MEC-07-06	The deployment mechanism and primary mirror calibration system stability shall be less than or equal to 0.5 μrad around the Z axis.	09/03/2018	09/03/2018	M1-MEC-07		Corvers, Pepper
R-M1D-03	M1-MEC-08	The deployment mechanism shall position the mirror segments parallel to the telescope bus with a clearance of less than or equal to 10 cm in the stowed configuration.	01/04/2017	26/03/2018	MIS-REQ-09	SOFT. van Putten, 2017 MSc t	Corvers
R-M1D-04	M1-MEC-09	The stowed mechanism shall be able to survive the launch conditions. Survival is defined as no impairment to the nominal functional capabilities of the system resulting from exposure to a given set of environmental conditions.	01/04/2017	26/03/2018	MIS-REQ-12	van Putten, 2017 MSc thesis	Corvers, Pepper
R-M1D-04-01	M1-MEC-09-01	The stowed mechanism shall be able to survive quasi static accelerations of 30 G. Survival is defined as no impairment to the nominal functional capabilities of the system resulting from exposure to a given set of environmental conditions.	01/04/2017	08/03/2018	M1-MEC-09		Corvers, Pepper
R-M1D-04-02	M1-MEC-09-02	The stowed mechanism shall have a first longitudinal eigenfrequency higher than 100 Hz in the stowed configuration.	01/04/2017	26/03/2018	M1-MEC-09		Corvers, Pepper
	M1-MEC-09-03	The stowed mechanism shall have a first lateral eigenfrequency higher than 100 Hz in the stowed configuration.	26/03/2018	26/03/2018	M1-MEC-09		Villalba Corbacho
R-M1D-05	M1-MEC-10	The stowed mechanism shall conform with Guiana Space Centre safety regulations.	01/04/2017	08/03/2018	MIS-REQ-11		Corvers, Pepper
~~R-M1D-08~~		~~All four mechanisms combined shall have a maximum mass of 16 kg.~~	~~01/04/2017~~	~~02/03/2018~~		~~van Putten, 2017 MSc thesis. SOFT~~	
	M1-MEC-11	The combined mass of the primary mirror deployment and active optics systems shall be no more than 16 kg.	09/03/2018	09/03/2018	MIS-REQ-08		Corvers, Pepper
~~R-M1D-09~~		~~The mechanism shall be designed for a minimal operational lifetime of 5 years.~~	~~01/04/2017~~	~~02/03/2018~~		~~van Putten, 2017 MSc thesis. SOFT~~	
	M1-MEC-12	The primary mirror assembly shall have a minimum operational lifetime of 5 years.	09/03/2018	09/03/2018	MIS-OBJ-01		Corvers, Pepper
N/A	M1-MEC-13	The primary mirror shall consist of four deployable segments.	14/03/2018	14/03/2018	MIS-REQ-07	Optical configuration require	Corvers, Pepper
N/A	M1-MEC-14	The distance from the primary mirror plane to the secondary mirror plane along the optical axis shall be TBD mm +/- TBD μm in the nominal deployed configuration.	14/03/2018	14/03/2018	MIS-REQ-01	Meet optical configuration requirements.	Corvers, Pepper
N/A	M1-MEC-15	The deployment mechanism and primary mirror calibration system shall operate at a nominal temperature of 298 K +/- 1 K during operations in the deployed configuration.	26/03/2018	26/03/2018	MIS-REQ-07		Corvers, Pepper

B

RESULTS SENSITIVITY ANALYSIS FOR CONCEPTUAL TRADE-OFF

The two sensitivity analyses described in section4.2 determine the sensitivity of the system to certain component errors and to certain temperature changes with or without gradients, respectively. The analyses are performed with two models, the mid-hinge (MH) model and the slider (SL) model. The MH model applies to the tape spring hinge and actuated latch concepts and the SL model applies only to the slider concept.

The graphical results of the first analysis show the relation between certain component errors and the resulting system errors, which are the Y-error, Z-error, the RMS of the Y- and Z-error, and the α-error. This is then done for the MH model on the left and the SL model on the right. The relation between the component errors and the Y-error has been shown in fig. 4.15. The relation between the component errors and the Z-error, RMS-error, and α-error are shown below in figs. B.1, B.2, and B.3, respectively.

The second analysis found what happens when heating single components (gradients) or the whole structure (no gradient) by 15 K. This has been done for cases where the structure was made out of (mixes of) different materials. The resulting figures show only the Y-error, Z-error, and α-error that result from the temperature changes. The results for a case where every component is made out of CFRP and a case where mixes of different material components are used, were already provided in figs. 4.16 and 4.17, respectively. The results for a structure made out of only steel and a structure made out of only titanium are provided in figs. B.4 and B.5, respectively.

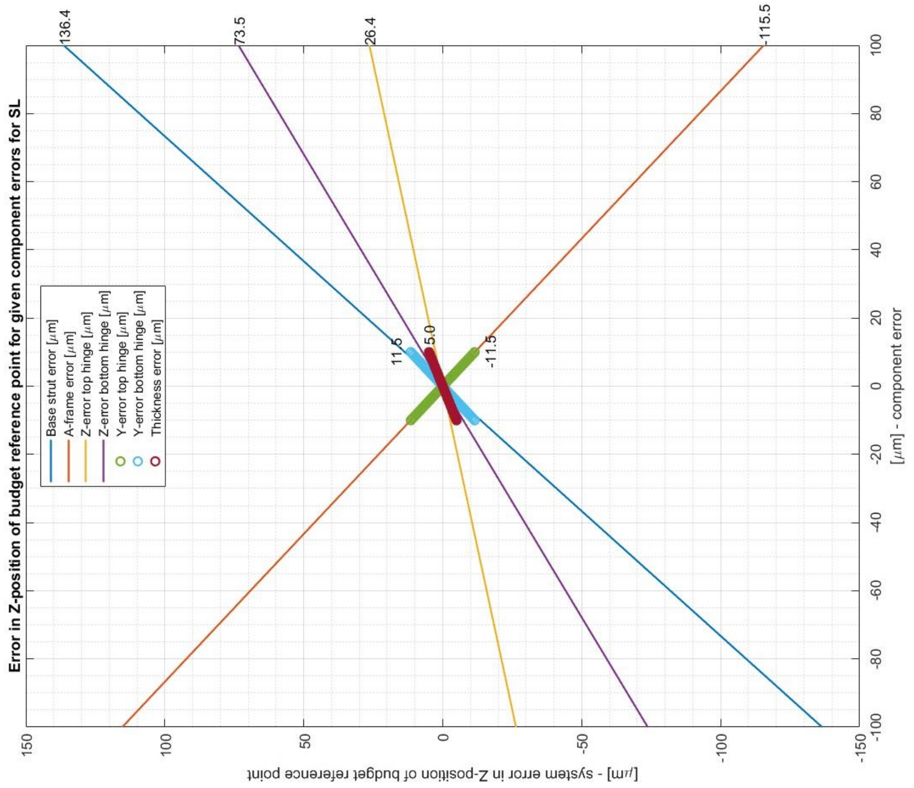

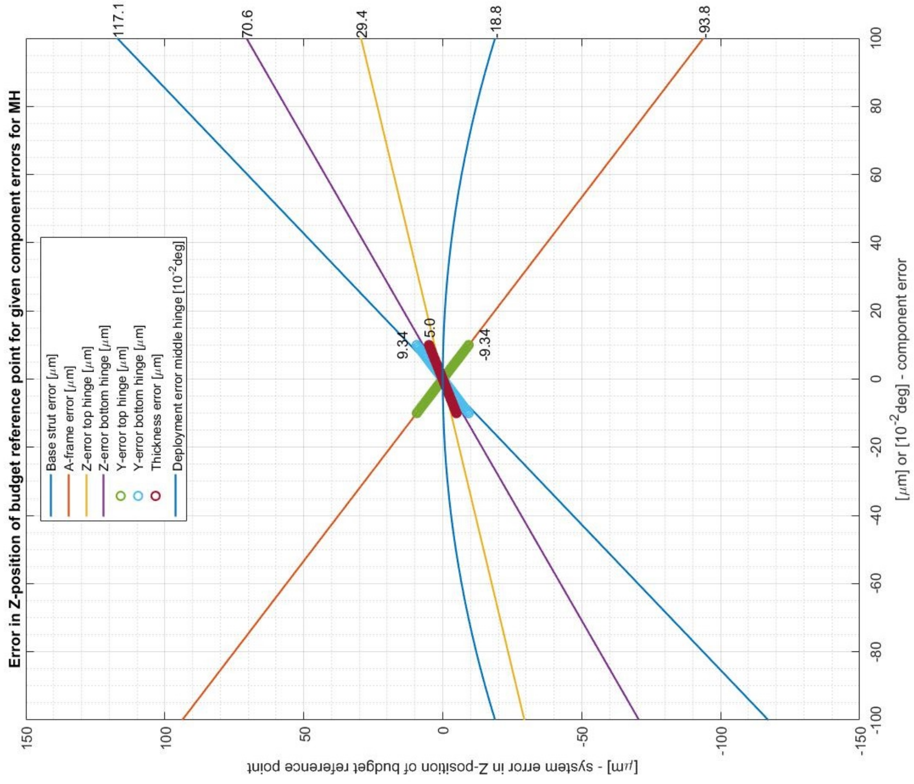

Figure B.1: Graphs showing the system error in Z-direction as a result of different component errors, for the MH (left) and SL (right) concepts

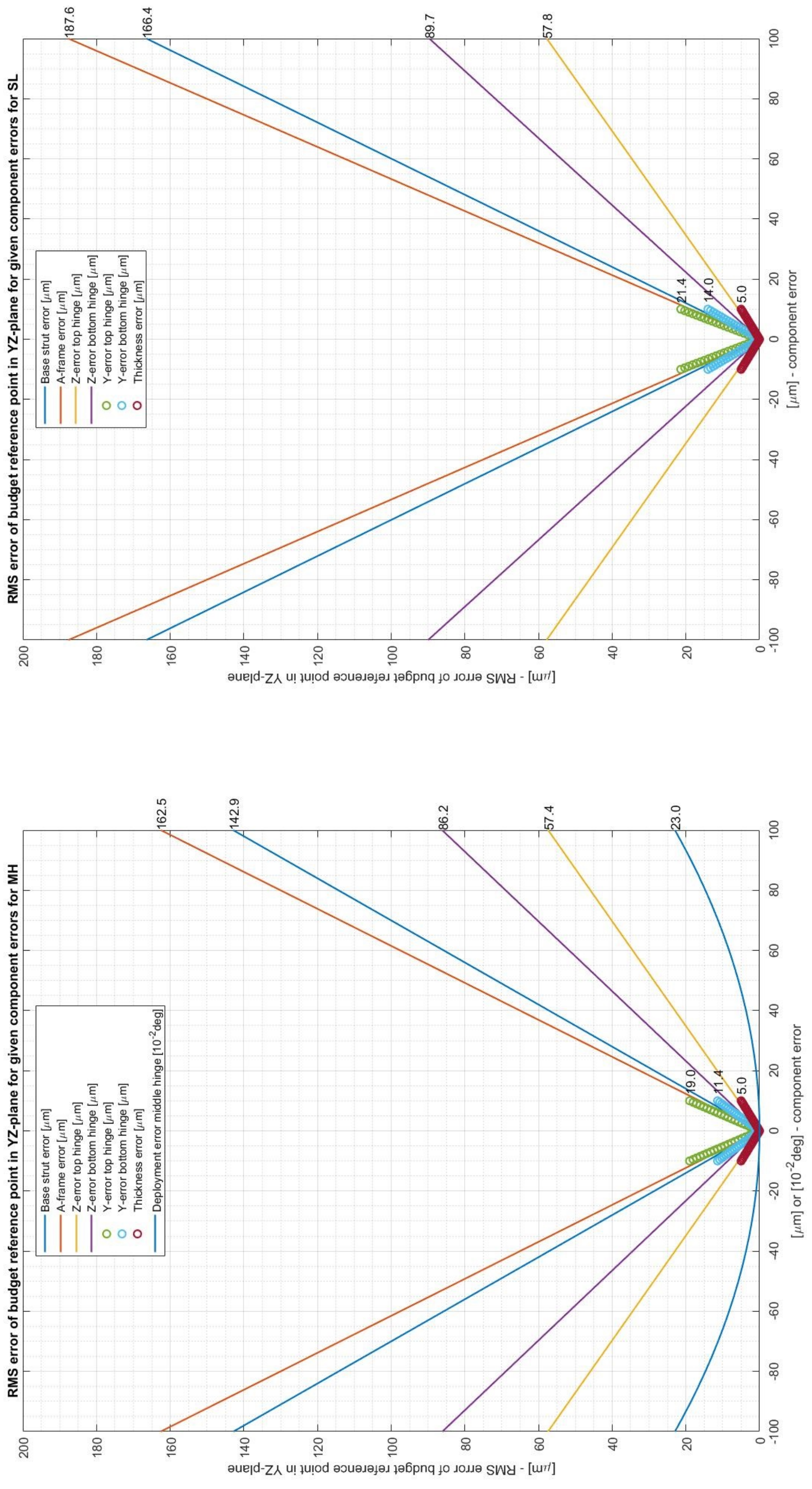

Figure B.2: Graphs showing the RMS system error of the system errors in Y- and Z-direction as a result of different component errors, for the MH (left) and SL (right) concepts

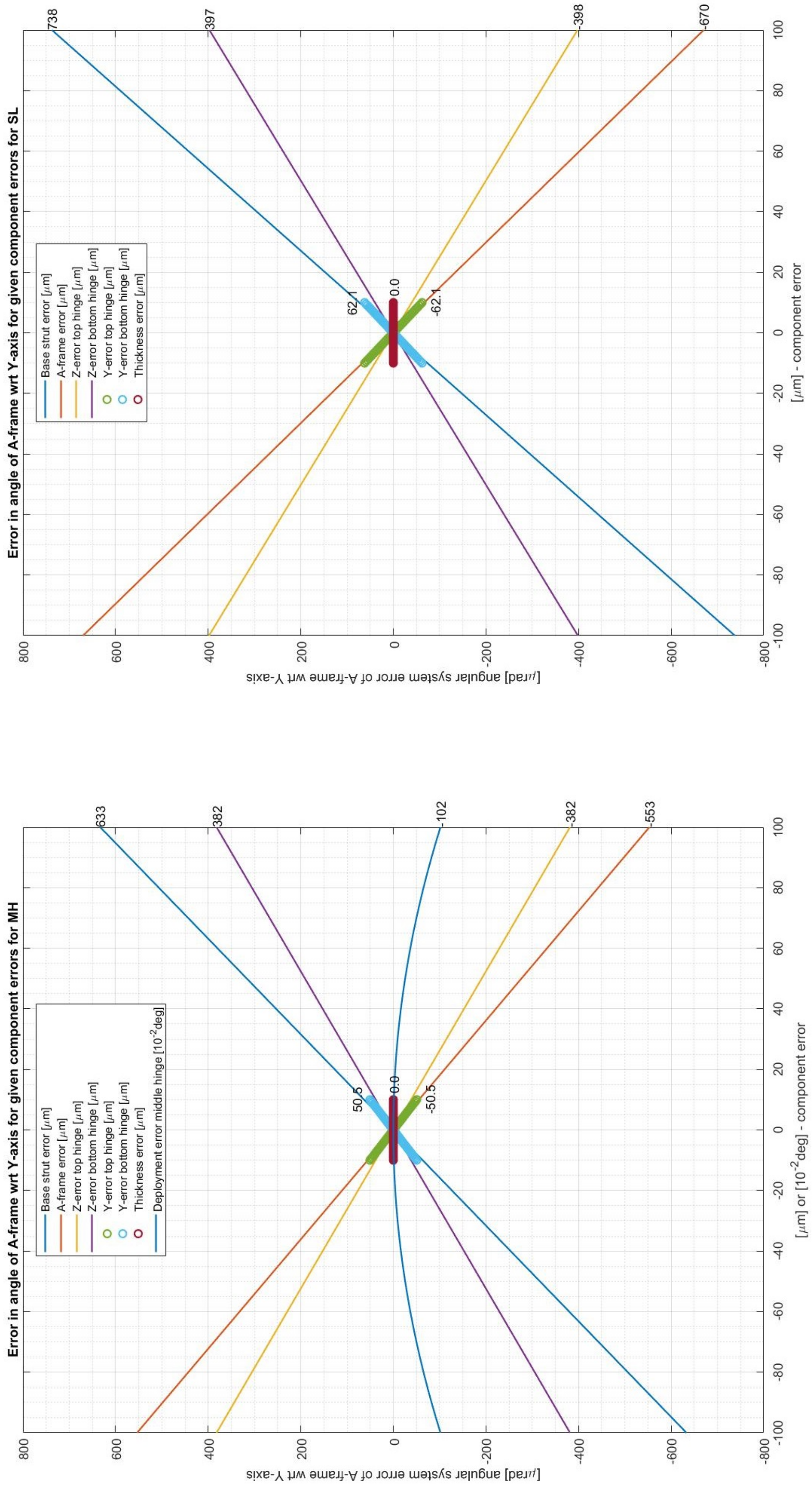

Figure B.3: Graphs showing the system error in α-angle as a result of different component errors, for the MH (left) and SL (right) concepts

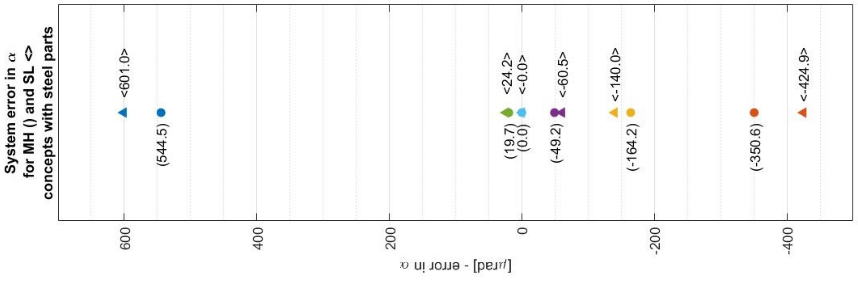

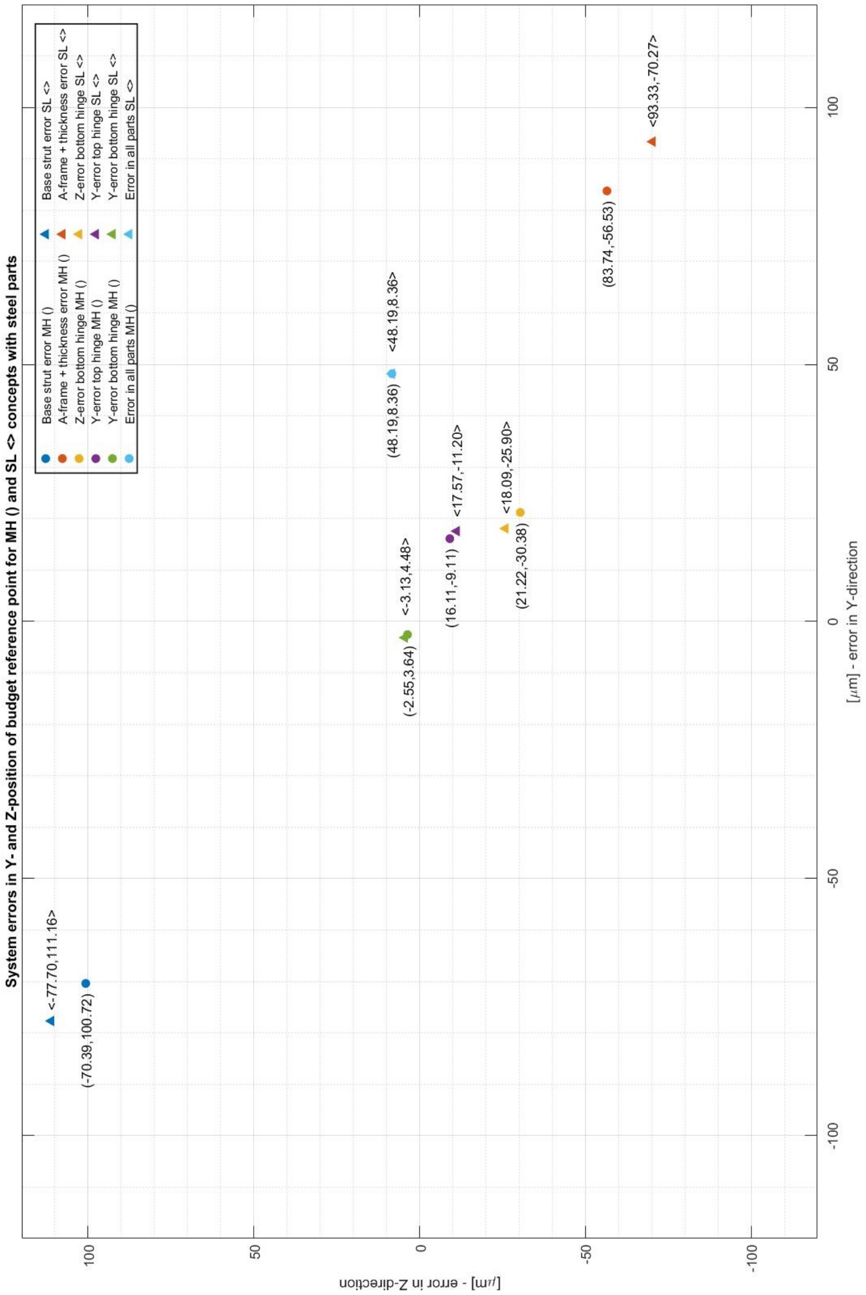

Figure B.4: Graph showing the system errors in Y-direction, Z-direction, and α-angle due to gradients (represented as component errors) or a complete rise in temperature of 15 K. The structure is made completely out of steel in this analysis.

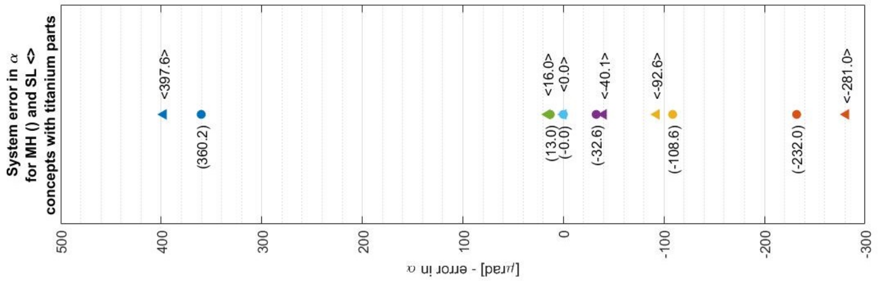

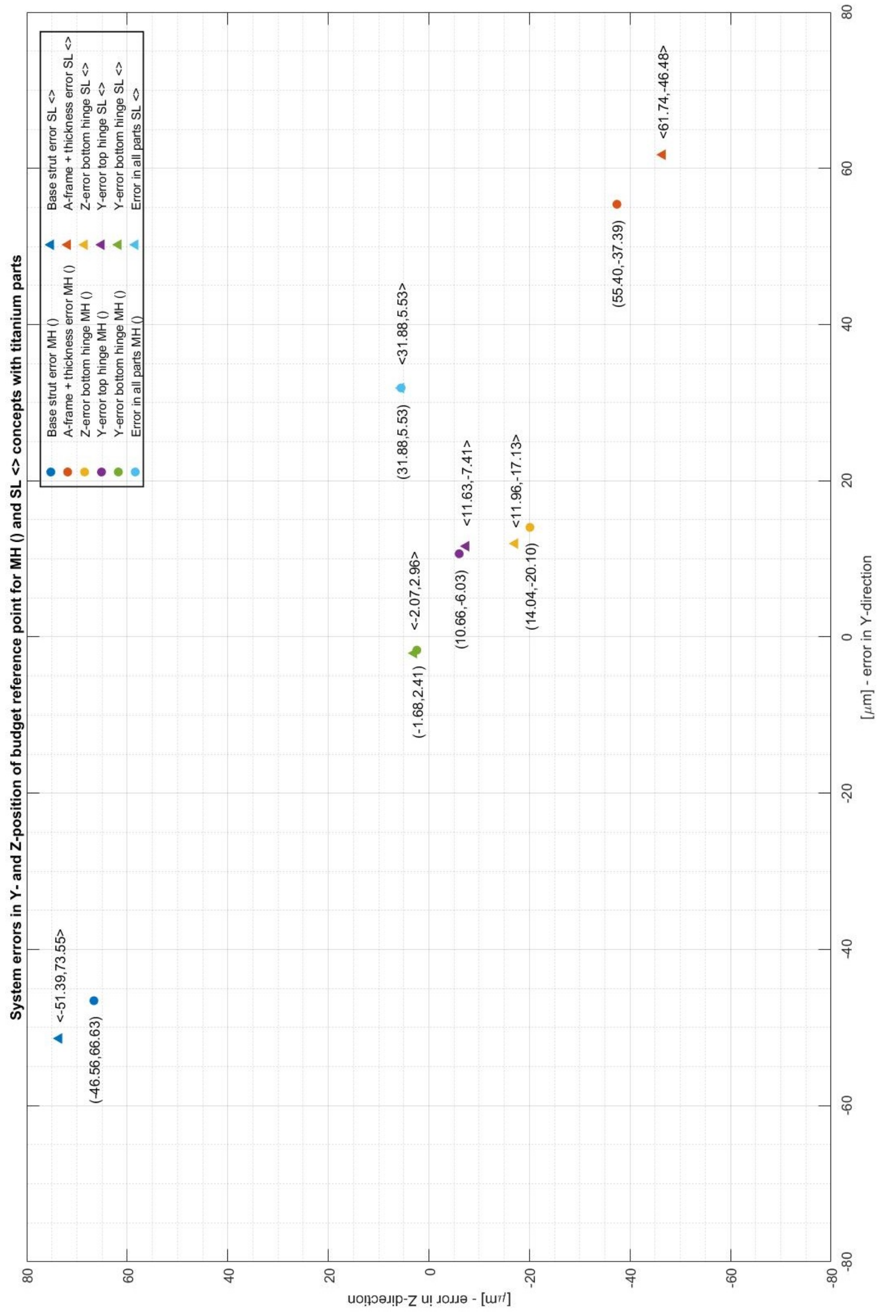

Figure B.5: Graph showing the system errors in Y-direction, Z-direction, and α-angle due to gradients (represented as component errors) or a complete rise in temperature of 15 K. The structure is made completely out of titanium in this analysis.